

Physical Modelling of Brass Instruments using Finite-Difference Time-Domain Methods



Reginald Langford Harrison-Harsley

Doctor of Philosophy
University of Edinburgh
2018

Abstract

This work considers the synthesis of brass instrument sounds using time-domain numerical methods. The operation of such a brass instrument is as follows. The player's lips are set into motion by forcing air through them, which in turn creates a pressure disturbance in the instrument mouthpiece. These disturbances produce waves that propagate along the air column, here described using one spatial dimension, to set up a series of resonances that interact with the vibrating lips of the player. Accurate description of these resonances requires the inclusion of attenuation of the wave during propagation, due to the boundary layer effects in the tube, along with how sound radiates from the instrument. A musically interesting instrument must also be flexible in the control of the available resonances, achieved, for example, by the manipulation of valves in trumpet-like instruments.

These features are incorporated into a synthesis framework that allows the user to design and play a virtual instrument. This is all achieved using the finite-difference time-domain method. Robustness of simulations is vital, so a global energy measure is employed, where possible, to ensure numerical stability of the algorithms.

A new passive model of viscothermal losses is proposed using tools from electrical network theory. An embedded system is also presented that couples a one-dimensional tube to the three-dimensional wave equation to model sound radiation. Additional control of the instrument using a simple lip model as well a time varying valve model to modify the instrument resonances is presented and the range of the virtual instrument is explored. Looking towards extensions of this tool, three nonlinear propagation models are compared, and differences related to distortion and response to changing bore profiles are highlighted. A preliminary experimental investigation into the effects of partially open valve configurations is also performed.

Declaration

I do hereby declare that the following thesis was composed by myself and that the work described within is my own work, except where explicitly stated otherwise.

Reginald Langford Harrison-Harsley

March 2018

Acknowledgements

Throughout the course of my Ph.D. studies I have received support from various sources. First I would like to thank my main supervisor, Stefan Bilbao, for his constant support with all aspects of this research. Thanks also to my second supervisor, Michael Newton, for various discussions on all things acoustics over the years.

I would like to thank my other colleagues in the Acoustics and Audio Group for their support throughout my studies: John Chick, Murray Campbell, Charlotte Desvages, Brian Hamilton, Amaya López-Carromero, Alberto Torin, and Craig Webb. Additional thanks go to collaborating researchers whose discussions have been vital to the development of this research: J  el Gilbert, Jonathan Kemp, Bruno Lombard, and Christophe Vergez.

Thanks to the members of the Edinburgh Parallel Computing Centre who worked on the NESS project: Paul Grahame, Alan Gray, Kostas Kavoussanakis, and James Perry.

Additional thanks to James Perry who ported the brass instrument environment from MATLAB to C, allowing for use by composers including: Chris Chafe, Gordon Delap, Gadi Sassoon, and Trevor Wishart.

Funding was gratefully received from the European Research Council under grant number ERC-2011- StG-279068-NESS.

I'd like to thank my parents for their support throughout the various stages of my life.

Finally, I'd like to thank my wife, Kim, who has supported me in so many ways during the period of this research.

List of publications

- [A] S. Bilbao and B. Hamilton and R. Harrison and A. Torin. Finite Difference Schemes in Musical Acoustics: A Tutorial. For Inclusion in *Handbook of Systematic Musicology*, Editor: R. Bader, Springer, Heidelberg, 2017.
- [B] R. Harrison and B. Hamilton and A. López-Carromero. Finite Difference Time Domain Simulation of Hybrid 1D/3D Brass Instrument Model and Comparison to Measured Radiation Data. In *24th International Congress on Sound and Vibration*, 2017.
- [C] S. Bilbao and R. Harrison. Optimisation techniques for finite order viscothermal loss modelling in acoustic tubes. In *Proceedings of the International Symposium on Musical and Room Acoustics*, 2016.
- [D] Stefan Bilbao and Reginald Harrison. Passive time-domain numerical models of viscothermal wave propagation in acoustic tubes of variable cross section. *The Journal of the Acoustical Society of America*, 140(1), 2016.
- [E] R. Harrison and S. Bilbao. Comments on travelling wave solutions in nonlinear acoustic tubes: Application to musical acoustics. In *Proceedings of the 22nd International Congress on Acoustics*, Buenos Aires, Argentina,, 2016.
- [F] R. Harrison and S. Bilbao. Coupling of a one-dimensional acoustic tube to a three-dimensional acoustic space using finite-difference time-domain methods. In *Proceedings of the International Symposium on Musical and Room Acoustics*, La Plata, Argentina,, 2016.
- [G] Stefan Bilbao, Reginald Harrison, Jean Kergomard, Bruno Lombard, and Christophe Vergez. Passive models of viscothermal wave propagation in acoustic tubes. *The Journal of the Acoustical Society of America*, 138(2), 2015.
- [H] R. Harrison, S. Bilbao, and J. Perry. An algorithm for a valved brass instrument synthesis environment using finite-difference time-domain methods with performance optimisation. In *Proceedings of the 18th International Conference on Digital Audio Effects*, Trondheim, Norway, 2015.
- [I] R. L. Harrison, S. Bilbao, J. Perry, and T. Wishart. An environment for physical modeling of articulated brass instruments. *Computer Music Journal*, 29(4):80–95, 2015.
- [J] R. L. Harrison and J. Chick. A single valve brass instrument model using finite-difference time-domain methods. In *Proceedings of the International Symposium on Musical Acoustics.*, Le Mans, France, 2014.

Contents

Abstract	i
Declaration	i
Acknowledgements	ii
List of publications	iii
List of Figures	xviii
List of Tables	xx
1 Introduction	1
1.1 Acoustics of brass wind instruments	1
1.2 A brief history of physical modelling	2
1.3 Passive time-domain modelling	2
1.4 Accuracy and efficiency	3
1.5 Thesis objectives	4
1.6 Thesis outline	4
1.7 Main contributions	7
I Linear Acoustics	8
2 Wave propagation in acoustic tubes	9
2.1 Introducing notation: Étude I	10
2.1.1 Partial differential equations and differential operators	10
2.1.2 Integral relations and identities	10
2.1.3 The Laplace transform and the frequency domain	11
2.2 The wave equation	12
2.2.1 Dispersion analysis	14
2.2.2 Energy analysis: A conserved quantity	15
2.2.3 Boundary conditions	16
2.2.4 Modes of the system	17
2.2.5 Input impedance	18
2.3 The horn equation	19
2.3.1 Dispersion analysis	21

2.3.2	Energy analysis	23
2.3.3	Modes of the system	24
2.3.4	Input impedance	26
2.3.5	The Transmission Matrix Method	26
2.4	Viscous and thermal losses	29
2.4.1	The Zwikker and Kosten model	29
2.4.2	Approximations of the model and positive real functions	30
2.4.3	Circuit representation of the Zwikker and Kosten model	34
2.4.4	Cauer and Foster forms of RL and RC circuits	34
2.4.5	Cauer structure representation of loss model	37
2.4.6	Foster structure representation of loss model	38
2.4.7	Time domain system of the Foster structure	40
2.4.8	Energy analysis of Foster structure	41
2.4.9	Numerical optimisation procedures	42
2.4.10	Reusing Z_v coefficients for \hat{Y}_t	46
2.4.11	Generalising for different tube radii and temperatures	47
2.4.12	Restricting optimisation ranges	49
2.4.13	Comparisons of viscothermal models	50
3	Finite-difference time-domain methods: Applications to acoustic tubes	52
3.1	Numerical methods for solving PDEs	53
3.1.1	Previous numerical methods applied to the horn equation	53
3.1.2	Passive numerical methods	54
3.1.3	The finite-difference time-domain method	55
3.2	Basics of FDTD methods: Étude II	55
3.2.1	Grids	55
3.2.2	Finite-difference operators	57
3.2.3	Accuracy of discrete operators	59
3.2.4	Inner products and useful identities	60
3.2.5	Discrete frequency transforms	62
3.2.6	The bilinear transform	64
3.3	Scheme design: The wave equation	64
3.3.1	An explicit scheme	65
3.3.2	Numerical dispersion	65
3.3.3	Stability and von Neumann analysis	66
3.3.4	Bandwidth of scheme	66
3.3.5	Energy analysis	67
3.3.6	Boundary conditions	68
3.3.7	Modes of the system	69
3.3.8	Implementation	70
3.3.9	An implicit scheme: Variation on a scheme	72
3.3.10	Numerical dispersion analysis	73
3.3.11	Energy analysis	73
3.3.12	Implementation	74
3.3.13	Explicit vs implicit schemes	75

3.3.14	Schemes for PDEs using first vs. second derivatives	78
3.4	Scheme design: the horn equation	79
3.4.1	An explicit scheme	79
3.4.2	Boundary conditions	81
3.4.3	Implementation	81
3.4.4	An implicit scheme	82
3.4.5	Implementation	83
3.4.6	Explicit vs. implicit scheme	84
3.4.7	A note in defence of the bilinear transform	85
3.5	Scheme design: the horn equation with losses	86
3.5.1	Model with fractional derivatives	86
3.5.2	Complete models for Zwikker and Kosten: Foster structure	92
3.5.3	Frequency warping in Foster structure	96
3.5.4	Comparison of loss models	99
3.6	Conclusions	103
4	Modelling radiation of sound from an acoustic tube	105
4.1	Radiation impedance models	105
4.1.1	Network representation of radiation model	107
4.1.2	Energy analysis	108
4.1.3	Numerical scheme	109
4.1.4	Discrete energy analysis	111
4.1.5	Simulation results	112
4.2	Coupling to a 3D acoustic field	113
4.2.1	Partial differential equations and integrals in higher dimensions: Étude IIIa	115
4.2.2	The 3D wave equation	116
4.2.3	Energy analysis	116
4.2.4	Boundary conditions	117
4.2.5	Coupling the systems: Continuous case	118
4.2.6	Finite-difference operators and inner products in higher dimensions: Étude IIIb	119
4.2.7	The simple scheme for the 3D wave equation	121
4.2.8	Boundary conditions	123
4.2.9	Matrix implementation	124
4.2.10	Coupling the systems: Discrete case	125
4.2.11	Numerical scheme	127
4.2.12	Simulation results	127
4.3	Modelling a full instrument	130
4.4	Conclusions	132
II	Virtual Instrument	134
5	Towards a complete instrument	135
5.1	The lip reed model	136
5.1.1	A simple model	137

5.1.2	Energy analysis	138
5.1.3	Numerical scheme	139
5.1.4	Simulation	141
5.2	Valves	142
5.2.1	Numerical scheme	146
5.2.2	Update for coupling	147
5.2.3	Recombining tubes	148
5.2.4	Junction coupling using lossy propagation	150
5.2.5	Simulation results	150
5.2.6	Time varying valves	153
5.3	Conclusions	156
6	A brass instrument synthesis environment	157
6.1	Structure of code	157
6.1.1	Input files	158
6.1.2	Precomputation	158
6.1.3	Main loop	159
6.1.4	Output sounds	160
6.2	Control of instrument	160
6.2.1	The instrument file	160
6.2.2	The score file	161
6.2.3	Sound examples	162
6.2.4	Playability space	166
6.3	Conclusions	168
III	Nonlinear Acoustics	169
7	Comparison of nonlinear propagation models	170
7.1	History of nonlinear propagation and brassiness	171
7.2	The Euler equations	172
7.2.1	Adiabatic approximation	173
7.2.2	Riemann invariants	173
7.3	Uni-directional models	175
7.3.1	Burgers model	175
7.3.2	Generalised Burgers model	175
7.4	Propagation behaviour in different models	177
7.4.1	Numerical methods	177
7.4.2	Simulation results	179
7.5	Effect of varying bore profile on linearised models	181
7.5.1	Dispersion analysis	183
7.5.2	Input impedances	184
7.6	Effect of coupling of forwards and backwards waves in a cylinder	185
7.6.1	Simulation results	186
7.7	Conclusions	191

IV	Finale	193
8	Conclusions and future work	194
8.1	Summary	194
8.2	Future work	195
A	Circuit elements	197
B	Foster network element values	201
B.1	Element values for continuous case	201
B.2	Element values for discrete case	203
C	Experiments on brass instrument valves	206
C.1	Experimental set up	206
C.1.1	Results	207

List of Figures

1.1	Functional diagram of a musical instrument.	1
1.2	Schematic of how energy is transferred between different elements in the system. Over time, all of the energy must be accounted for to determine stability.	3
2.1	Left: Undisturbed volume of air of length dz . Right: Air has been disturbed, changing its overall length to dz' . The shaded area denotes the previous volume the air occupied.	12
2.2	Left: Initial conditions to the wave equation. Forwards wave, $\psi_+(t - z/c_0)$, (dashed red); backwards wave, $\psi_-(t + z/c_0)$, (dotted yellow); sum of forwards and backwards solutions (solid blue). Right: Solution to the wave equation at a later time. The waves now occupy different domains but preserve the shape they had at $t = t_0$	13
2.3	Top: Input impedance for the wave equation with Dirichlet termination. Bottom: Input impedance for the wave equation with Neumann termination. The cylinder has a length $L = 1$ m, and radius $r_0 = 0.005$ m. The values for air density and speed of sound are $\rho_0 = 1.1769 \text{ kg} \cdot \text{m}^{-3}$ and $c_0 = 347.23 \text{ m} \cdot \text{s}^{-1}$ corresponding to a temperature of 26.85°C	19
2.4	Profile of an acoustic tube with variable cross-sectional area, $S(z)$, that changes along the axial length, z	20
2.5	Plots of the real part of the spatial solution to the horn equation, $\text{Re}(e^{j\beta z})$ at different frequencies. Left: ω is less than the cutoff frequency goes to zero. Middle: ω is at the cutoff frequency and the solution still goes to zero but less severely. Right: ω is above cutoff frequency and waves can propagate.	23
2.6	Top: Profile of an exponential horn of length 1 m, opening radius $r(0) = 0.005$ m and flare parameter $\alpha = 5 \text{ m}^{-1}$. Bottom: Input impedance for this horn with an open end. $c_0 = 347.23 \text{ m} \cdot \text{s}^{-1}$ and $\rho_0 = 1.1769 \text{ kg} \cdot \text{m}^{-3}$. Dashed vertical lines show the resonances of a cylindrical tube with corresponding boundary conditions.	26
2.7	Top: A general acoustic tube. Bottom: An approximation of an acoustic tube using a series of concatenated cylinders.	27
2.8	Schematic of an element in the TMM.	28
2.9	Top: Real (left) and imaginary (right) parts of Γ calculated using the Zwicker and Kosten Model for a tube of radius 0.005 m. Bottom: Fractional error of the real and imaginary parts of Γ from the expansions given by Benade (blue), Keefe (red), Caussé <i>et al.</i> (yellow), Bilbao and Chick (purple) and Webster-Lokshin (green). Note that the small and large expansions have been connected around $r_v = 1$ and $r_t = \nu$	33

2.10	Left: Magnitude of Z in the complex plane. Right: Magnitude of Y in the complex plane. Poles are bright yellow and zeros are green/blue. Note that surfaces have been plotted using a logarithmic plot to accentuate the poles and zeros. A tube of radius 0.03 m has been used to highlight the poles and zeros in a reasonable range.	35
2.11	Top: First form of Cauer RL circuit. Bottom: Second form of Cauer RC circuit.	35
2.12	Top: First form of Foster RL structure. Bottom: Second form of Foster RC . Both structures have M branches.	36
2.13	Cauer structures. Top: Impedance structure. Bottom: Admittance structure.	38
2.14	Fractional error of impedance calculated using the Cauer structure for a tube of radius 0.005 m. Left: Error in real part of impedance. Right: Error in imaginary part of impedance.	38
2.15	Fractional error of admittance calculated using the Cauer structure for a tube of radius 0.005 m. Left: Error in real part of admittance. Right: Error in imaginary part of admittance.	39
2.16	Left: Magnitude of Z_v in the complex plane. Right: Magnitude of Y_t in the complex plane. Poles are yellow and zeros are dark blue. Note that surfaces have been plotted using a logarithmic plot to accentuate the poles and zeros. The tube radius is 0.03 m	39
2.17	Top: Z_v Foster structure. Bottom: Y_t Foster structure.	40
2.18	Fractional error of Foster model optimised to Z_v using E_R for a tube of 0.005 m over a frequency range 0 Hz to 10 kHz. Left: Error in real part. Right: Error in imaginary part.	45
2.19	Fractional error of Foster model optimised to Z_v using E_M for a tube of 0.005 m over a frequency range 0 Hz to 10 kHz. Left: Error in real part. Right: Error in imaginary part.	45
2.20	Fractional error of Foster model optimised to Z_v using E_R for a tube of 0.005 m over a frequency range 0 Hz to 10 kHz when it is applied to admittance \hat{Y}_t . Left: Error in real part. Right: Error in imaginary part.	47
2.21	Fractional error of Foster model optimised to Z_v using E_M for a tube of 0.005 m over a frequency range 0 Hz to 10 kHz when it is applied to admittance \hat{Y}_t . Left: Error in real part. Right: Error in imaginary part.	47
2.22	Fractional error of the impedance using the element values in (2.142) for a fourth order filter. The original impedance was optimised using E_M for a tube radius of 0.005 m and a temperature of 26.85°C. Left: Error in real part. Right: Error in imaginary part.	48
2.23	Fractional error of the impedance using the element values in (2.143) for a fourth order filter. The original impedance was optimised using E_M for a tube radius of 0.005 m and a temperature of 26.85°C. Left: Error in real part. Right: Error in imaginary part.	49
2.24	Fractional error of Foster model optimised to Z_v using E_R for a tube of 0.005 m over a frequency range 20 Hz to 3 kHz. Left: Error in real part. Right: Error in imaginary part. The shaded area shows the frequency range that optimisation was performed over.	49

2.25	Fractional error of Foster model optimised to Z_v using E_M for a tube of 0.005 m over a frequency range 20 Hz to 3 kHz. Left: Error in real part. Right: Error in imaginary part. The shaded area shows the frequency range that optimisation was performed over.	50
2.26	Fractional error of the impedance for the Foster model, optimised using E_R (solid lines) over a frequency range 0 Hz to 10 kHz, and for Cauer model (dashed lines) for a tube of 0.005. Left: Error in real part. Right: Error in imaginary part. . . .	51
2.27	Fractional error of the impedance for the Foster model, optimised using E_M (solid lines) over a frequency range 0 Hz to 10 kHz, and for Cauer model (dashed lines) for a tube of 0.005. Left: Error in real part. Right: Error in imaginary part. . . .	51
3.1	Discretised domain for a finite-difference scheme. The temporal domain is sampled at intervals of time k s and labelled using integers n . The spatial domain is sampled at intervals of length h m and labelled using integers l . Black circles denote the grid function f at each temporal and spatial point.	56
3.2	Left: Grids that are interleaved only in space. Right: Grids that are interleaved in time and space. Dashed lines show the original grid labelled by the integers n and l . Dotted lines show the interleaved grid. Black circles denote the locations of the grid function, f , on the integer field. White circles denote the locations grid function, g , on the interleaved grids.	57
3.3	Stencils of temporal difference operators, labelled at top, when applied to a grid function at time step n (highlighted in green). Black circle denotes the grid functions that are used, white circles are unused by the operator.	58
3.4	Stencils of temporal difference operators, labelled at left, when applied to a grid function at spatial step l (highlighted in red). Black circle denotes the grid functions that are used, white circles are unused by the operator.	59
3.5	Left: Geometric visualisation of inner product. Right: Geometric visualisation of weighted inner product. At the boundaries of the domain, the weighted inner product uses only half a spatial step. Black circles denote the values of f on the spatial grid.	61
3.6	Effect of bilinear transform on frequency mapping at different sample rates. At high frequencies, the bilinear transform warps the frequency away from where it is supposed to be represented. This is improved with a higher sample rate but never truly goes away.	64
3.7	Left: Dispersion for scheme (3.40) for different values of λ at a sample rate of 20 kHz. As λ moves away from the CFL condition, frequencies are warped. Right: Bandwidth as a function of λ for the explicit scheme. The dashed line shows the Nyquist frequency.	67
3.8	Solutions calculated using scheme (3.42) at two time instants. The sample rate is 20 kHz and $\lambda = 1$. The acoustic velocity potential has been initialised with an Hann pulse of width 21 steps.	71
3.9	Plot of \mathfrak{h}_{sum} for the system in Fig. 3.8. The energy is calculated using the weighted inner product form (3.64).	72

3.10	Left: Dispersion for scheme (3.78) for different values of λ at a sample rate of 20 kHz. Even for $\lambda = 1$, the dispersion deviates from the exact dispersion relation. Right: Bandwidth of implicit scheme as a function of λ . The dashed line shows the Nyquist frequency which this scheme can never fully achieve.	73
3.11	Solutions calculated using scheme (3.89) at two time instances. The sample rate is 20 kHz and $\lambda = 1$. The acoustic velocity potential has been initialised with an Hann pulse of width 21 steps. Both sides of the domain are terminated using the centred Neumann conditions.	75
3.12	Plot of \mathfrak{h}_{sum} for the system in Fig. 3.11. The energy is calculated using the weighted inner product form (3.87).	75
3.13	Input impedances calculated for a cylinder of length 0.3 m and radius 0.01 m using the explicit (blue) and implicit (green) schemes. Top: Input impedance calculated using $\lambda = 1$. Bottom: Input impedance calculated using $\lambda = 0.7972$. Dashed vertical line show the exact resonances. Sample rate is 20 kHz.	76
3.14	Bore profile and surface areas on different girds. Solid line shows the bore profile. Dashed line shows the spatial grid that \bar{S} is calculated on and dotted line shows the grid that S is sampled on.	79
3.15	Input impedances for an exponential horn of length $L = 0.3$ m, flaring parameter $\alpha = 5 \text{ m}^{-1}$, and opening radius $r_0 = 0.005$ m calculated using the exact expression (black), and explicit finite-difference scheme (blue), and an implicit finite-difference scheme (green). Sample rate is 20 kHz and simulations were run for 10 s.	85
3.16	Left: Real part of $(j\omega)^{1/2}$. Right: Imaginary part of $(j\omega)^{1/2}$. Black line shows the exact value. Coloured lines show approximations to the fractional derivative using the IIR filter of differing orders constructed from the CFE of the bilinear transform at 50 kHz.	89
3.17	Pole-zero plots for fractional derivative filter at 50 kHz. Left: Filter order of 20. Right: Filter order of 33. Poles are marked as red crosses and zeros as blue circles. Dashed vertical and horizontal lines show where the real and imaginary axes lie. Dashed circle is the unit circle.	90
3.18	Left: Real part of $(j\omega)^{1/2}$. Right: Imaginary part of $(j\omega)^{1/2}$. Black line shows the exact value. Blue, red and orange lines show approximations to the fractional derivative using the IIR filter of order 4 (blue), 8 (red), 16 (orange), and 20 (purple) constructed from the CFE of the bilinear transform at 50 kHz.	90
3.19	Errors in impedance when calculated using the bilinear transform at a sample rate of 50 kHz (solid lines) and the exact frequency (dashed) for the Foster network optimised using E_M over 0 Hz to 10 kHz. Left: Error in real part. Right: Error in imaginary part.	97
3.20	Errors in impedance when calculated using the bilinear transform at a sample rate of 50 kHz (solid lines) and the exact frequency (dashed) for the Foster network optimised using E_M over 20 Hz to 3 kHz. Left: Error in real part. Right: Error in imaginary part. Grey box shows optimisation range.	97
3.21	Errors in impedance calculated using the bilinear transform at 50 kHz for the Foster network optimised using E'_M over 0 Hz to 10 kHz with pre-warped frequencies. Left: Error in real part. Right: Error in imaginary part.	98

3.22	Errors in impedance calculated using the bilinear transform at 50 kHz for the Foster network optimised using E'_M over 20 Hz to 3 kHz with pre-warped frequencies. Left: Error in real part. Right: Error in imaginary part. Grey box shows optimisation range.	98
3.23	Input impedance calculated using the loss model of Bilbao and Chick for different filter orders. Top left: Input impedance magnitude. Bottom left: Input impedance phase. Top right: Absolute percentage error in input impedance peak position relative to TMM. Bottom right: Absolute percentage error in input impedance peak magnitude.	100
3.24	Input impedance calculated using the Foster network with coefficients acquired by optimising of E'_M from 0 Hz to 10 kHz. Top left: Input impedance magnitude. Bottom left: Input impedance phase. Top right: Absolute percentage error in input impedance peak position relative to TMM. Bottom right: Absolute percentage error in input impedance peak magnitude.	100
3.25	Input impedance calculated using the Foster network with coefficients acquired by optimising of E'_M from 20 Hz to 3 kHz. Top left: Input impedance magnitude. Bottom left: Input impedance phase. Top right: Absolute percentage error in input impedance peak position relative to TMM. Bottom right: Absolute percentage error in input impedance peak magnitude.	101
3.26	Input impedance of an exponential horn calculated using the Bilbao and Chick loss model using different filter orders. Top left: Input impedance magnitude. Bottom left: Input impedance phase. Top right: Absolute percentage error in input impedance peak position relative to TMM. Bottom right: Absolute percentage error in input impedance peak magnitude.	102
3.27	Input impedance of an exponential horn calculated using the Foster network with coefficients acquired by optimising of E'_M from 0 Hz to 10 kHz. Top left: Input impedance magnitude. Bottom left: Input impedance phase. Top right: Absolute percentage error in input impedance peak position relative to TMM. Bottom right: Absolute percentage error in input impedance peak magnitude.	102
3.28	Input impedance of an exponential horn calculated using the Foster network with coefficients acquired by optimising of E'_M from 20 Hz to 3 kHz. Top left: Input impedance magnitude. Bottom left: Input impedance phase. Top right: Absolute percentage error in input impedance peak position relative to TMM. Bottom right: Absolute percentage error in input impedance peak magnitude.	103
4.1	Circuit representation of approximation to the Levine and Schwinger radiation model.	107
4.2	Left: Radiation reflection magnitude for a tube of radius 0.05 m calculated using the Levine and Schwinger model (blue) and the network approximation. Right: Radiation length correction.	108
4.3	Left: Error in reflection magnitude of network when using the bilinear transform (dashed red) at 50 kHz. Right: Error in length correction.	110
4.4	Top: Total stored energy (blue), stored energy in the tube (red), stored energy in the radiation model (yellow), and energy lost by the radiation model (purple). Bottom: Energy balance showing numerical precision of machine.	112

4.5	Top: Input impedance of a lossless cylinder of radius 0.05 m and length 1 m calculated using an FDTD simulation with lossy radiating end (solid black) and a frequency domain calculation terminated with the Levine and Schwinger radiation impedance (dashed red). Bottom: Absolute error in peak position of FDTD simulation relative to frequency domain calculation.	113
4.6	Top: Input impedance of a lossless cylinder of radius 0.1 m and length 1 m calculated using an FDTD simulation with lossy radiating end (solid black) and a frequency domain calculation terminated with the Levine and Schwinger radiation impedance (dashed red). Bottom: Absolute error in peak position of FDTD simulation relative to frequency domain calculation.	114
4.7	Schematic of an embedded system. The cylindrical, or slowly varying, portion of the instrument bore is modelled using a one-dimensional wave propagation model. In the flaring portions of the instrument, a three-dimensional wave propagation model is used. The dashed line shows the boundary between the two sections of the instrument.	114
4.8	Schematic of embedded system. Energy is transferred between the cylinder, at left, and the enclosed volume of air, at right, via the point at the end of the tube and the surface Ω	118
4.9	Illustration of the vectorisation of the three-dimensional grid function.	124
4.10	Staircased fitting applied to the interior of a circle, indicated by a blue line. Dots indicate grid points and black lines denote the area they approximate. Red centres denote grid points that lie within the circle, empty centres are those that lie without. The perimeter of the staircased approximation to the circle is indicated by a green line.	125
4.11	Layout of simulations. Left: Wave propagation in one-dimensional model of cylinder. Right: Cross-section of volume of air for the two simulation scenarios. Top: Only the surface Ω_d is positioned in the air box. Bottom: A cylindrical profile is positioned behind the surface Ω_d . Curved lines are a representation of sound leaving Ω_d	128
4.12	Input impedance magnitudes of two cylinders calculated using the frequency domain expression terminated with the Levine and Schwinger radiation impedance (solid blue) and using the embedded FDTD system with only the plane in the air box (dashed red) and the cylinder in the air box (dotted yellow). Top: Tube radius of 0.05 m. Bottom: Tube radius of 0.1 m.	129
4.13	Fractional differences in peak frequency of embedded system using just a plane (red) and with a cylinder in the enclosed volume (yellow) relative to the exact solution terminated with the Levine and Schwinger radiation impedance. Top: Results for a tube of radius 0.05 m. Bottom: Results for a tube of radius 0.1 m.	129
4.14	Top: Energy evolution of the embedded FDTD system with only the plane Ω_d in the enclosed volume of air. Bottom: Deviation in the total stored and lost energy over time.	130
4.15	Bore profile of Smith Watkins trumpet.	130

4.16	Input impedances of the Smith Watkins trumpet with Kelly Screamer mouth-piece; measured (black), simulation terminated with network approximation to Levine and Schwinger radiation impedance (blue), simulation of embedded system (red).	131
4.17	Top: Fractional error in peak position of input impedance of simulations relative to experimental measurement. Bottom: Fractional error in peak magnitude of impedance impedance of simulations relative to experiments. Error in simulation terminated with network approximation shown in blue, error in embedded system shown in red.	132
5.1	Schematic of lip reed.	137
5.2	Displacement of the lip reed from equilibrium when no self sustained oscillation occurs.	141
5.3	Energy balance of the system when no oscillation occurs.	142
5.4	Displacement of the lip reed from equilibrium in the case of self sustained oscillation.	142
5.5	Energy evolution of the system when self sustained oscillation occurs. Stored energy in the reed (blue) and tube (red), summed power dissipation in reed (orange) and summed power input at reed (purple).	143
5.6	Energy evolution of the system when self sustained oscillation occurs. Stored energy in the reed (blue) and tube (red), summed power dissipation in reed (orange) and summed power input at reed (purple).	143
5.7	Energy balance for self sustained oscillating system.	143
5.8	Schematic of a brass instrument valve. Three pieces of tubing are combined at J . The pressure at the junction is the same in each piece of tubing and the total volume velocity flow over the junction is conserved.	144
5.9	Overlapping circles representing the junction of a valve. The default (green) and bypass (red) tubes overlap the main tube (blue). However, it is clear that that the total area of the main tube is not covered by the other tubes.	145
5.10	Schematic of the valve junction on the discrete grids. The pressure at the valve junctions is the same in each tube. There are velocities outside the domain, but these can be removed using continuity of volume velocity over the junction. . . .	148
5.11	Schematic of a tube system that splits into two and then recombines back into one tube. Note that modelling of the bypass tube is done by assuming it is straight, its bent appearance in the figure is to show how the default and bypass tubes reconnect.	149
5.12	Profile of the default tube. Black dotted lines show the pressure spatial grid, grey dotted lines show the particle velocity grid, solid black lines show the bore profile.	149
5.13	Top: Energy evolution of the system with $q^{(d)} = 0.5$: total energy (blue), main tube energy (red), default tube energy (yellow), bypass tube (purple), recombined tube (green). Bottom: energy balance for the whole system.	151
5.14	Input impedance calculations for the lossy valved tube system for different opening configurations. Top to bottom: Decreasing value of $q^{(d)}$ from 1 to 0 in increments of 0.25.	152

5.15	Top: Energy evolution of the valved system with time varying openings. Bottom: Energy balance of the system.	156
6.1	Structure of the brass instrument synthesis environment. Users specify instrument and score files (in blue rectangle) that are inputs to the code. These input files are then used in the precomputation stage (green rectangle) to calculate system parameters and control streams used in the main loop (red rectangle) where the system variables (acoustic pressure, particle velocity, lip position) are computed. The output (purple rectangle) is generated as a WAV file from the pressure at the end of the instrument.	158
6.2	Example of an instrument constructed using the custom instrument function. Section (a) is the mouthpiece defined using a cosine, (b) a cylindrical segment, (c) is a bulge defined using the square of a sinusoid, (d) a converging conical section, and (e) is the flaring section defined using a power of the axial position.	160
6.3	Top: Spectrogram of output sound when the lip frequency linearly changes from 220 Hz to 1000 Hz over 3 s. Bottom: The lip frequency as a function of time.	163
6.4	Top: Time series of output when two separate notes are played. Bottom: Corresponding mouth pressure as a function of time.	163
6.5	Top: Spectrogram of output sound when vibrato is added to the note after 1 s. Bottom: Lip frequency as a function of time. Lip frequency is constant for first second then modulation is added.	164
6.6	Top: Time series of output sound when tremolo is added. Bottom: Mouth pressure as a function of time. After the initial increase, the mouth pressure remains constant for the first second, after which the tremolo is added.	164
6.7	Top: Spectrogram of output sound when noise is added after 1 s. Bottom: Corresponding mouth pressure signal, with noise added after 1 s.	165
6.8	Spectrogram of output for repeated lip frequency sweeps from 300 Hz to 700 Hz over 2 s whilst changing valve configurations. At 2 s intervals, the next valve is depressed. This corresponds to a reduction in the lowest peak frequency shown in the spectrogram.	165
6.9	Spectrum of sounds produced with valves in open configuration (blue) and partially open configuration (red).	166
6.10	Top: Spectrogram of sound produced when first valve is modulated. Bottom: Time series of the first valve opening.	167
6.11	Example of a sound that fits the acceptance criteria. It is clear that the appearance of the repeated cycle that makes up the sustained part of the note occurs before 0.07 s.	167
6.12	Playability space for Smith Watkins trumpet bore used in brass instrument environment. Points denote areas where a note is produced whose sustained part occurs in 0.07 s or less. Dashed vertical lines show where the instrument resonances lie.	168

7.1	Left: A simple wave. Right: An example of distortion applied to the wave (solid line) with the original wave profile shown as reference (dotted line). Arrows show how the wave has been distorted, with positive values sped up, and negative values slowed down.	174
7.2	Propagation of a Hann pressure pulse of width 1/300 s and amplitude 3 % of atmospheric pressure in a cylindrical tube modelled using the Euler equations (blue), Burgers equation (dashed red), generalised Burgers equation (dash-dot yellow), and the linear horn equation (dotted purple). Labels above peaks denote corresponding time steps.	180
7.3	Propagation of a Hann pressure pulse of width 1/300 s and amplitude 5 % of atmospheric pressure in a cylindrical tube modelled using the Euler equations (blue), Burgers equation (dashed red), generalised Burgers equation (dash-dot yellow), and the linear horn equation (dotted purple). Labels above peaks denote corresponding time steps.	180
7.4	Propagation of a Hann pressure pulse of width 1/300 s and amplitude 5 % of atmospheric pressure in an exponential horn with flaring parameter $\alpha = 0.5 \text{ m}^{-1}$ modelled using the Euler equations (blue), Burgers equation (dashed red), generalised Burgers equation (dash-dot yellow), and the linear horn equation (dotted purple). Labels above peaks denote corresponding time steps.	181
7.5	Propagation of a Hann pressure pulse of width 1/300 s and amplitude 5 % of atmospheric pressure in an exponential horn with flaring parameter $\alpha = 1 \text{ m}^{-1}$ modelled using the Euler equations (blue), Burgers equation (dashed red), generalised Burgers equation (dash-dot yellow), and the linear horn equation (dotted purple). Labels above peaks denote corresponding time steps.	181
7.6	Input impedances calculated using models 1-3 for an exponential horn of length 1 m and flaring parameter 1 m^{-1} terminated with a Dirichlet boundary condition. Dashed black lines show the resonance frequencies of a cylinder of similar length.	185
7.7	Top: Test case where the tube is excited with the same signal at both ends. Bottom: Test case where the tube is excited with signals of opposite signs at both ends. Dashed line shows where the output is taken.	185
7.8	Pressure signals recorded 75 % along a tube of length 3 m when excited at both ends with Hann pulses of amplitude 5 % of atmospheric pressure, with the same sign, Test 1 (blue), and opposite sign, Test 2 (red). Top: Pulse width 1/300 s. Middle: Pulse width 1/500 s. Bottom: Pulse width 1/700 s.	186
7.9	Percentage differences in magnitude of output relative to a single input. Top: Test 1 difference. Bottom: Test 2 difference.	187
7.10	Percentage differences in angle of output relative to a single input. Top: Test 1 difference. Bottom: Test 2 difference.	188
7.11	Percentage differences in magnitude of output relative to a single input for a pulse of width 1/500 s for tubes of different lengths. Top: Test 1 difference. Bottom: Test 2 difference.	189
7.12	Percentage differences in angle of output relative to a single input for a pulse of width 1/500 s for tubes of different lengths. Top: Test 1 difference. Bottom: Test 2 difference.	189

7.13	Percentage differences in magnitude of output relative to a single input for a pulse of width $1/300$ s for tubes of different lengths. Top: Test 1 difference. Bottom: Test 2 difference. For $L = 6$ m the differences go to 25 % for Test 1 and -25 % for test 2.	190
7.14	Percentage differences in angle of output relative to a single input for a pulse of width $1/300$ s for tubes of different lengths. Top: Test 1 difference. Bottom: Test 2 difference. For $L = 6$ m the differences go to 25 % for Test 1 and -25 % for test 2.	190
A.1	One-port networks. Left: Resistor network. Middle: Inductor network. Right: Capacitor network.	197
A.2	Left: Currents into and out of a node. Right: The looped sum of voltages. . . .	198
A.3	Top: Circuit with elements connected in series. Bottom: Circuit with elements connected in parallel.	199
A.4	An RLC circuit which has the same response as a simple harmonic oscillator with damping.	199
C.1	A trumpet valve in isolation.	207
C.2	Schematic of valve experiment	207
C.3	Simulated and measured input impedance with the valve fully open.	208
C.4	Simulated and measured input impedance where 9 washers are used to keep the valve partially open.	208
C.5	Simulated and measured input impedance where 7 washers are used to keep the valve partially open.	209
C.6	Simulated and measured input impedance where 5 washers are used to keep the valve partially open.	209
C.7	Simulated and measured input impedance where 3 washers are used to keep the valve partially open.	209
C.8	Simulated and measured input impedance with the valve fully closed.	210
C.9	Simulated and measured input impedance where 7 washers are used to keep the valve partially open. The value of $q^{(b)}$ has been modified in the simulation to better match the results of experiment.	210

List of Tables

2.1	Modal solutions and modal frequencies of the wave equation for different combinations of boundary conditions.	18
2.2	Resonance frequencies of 1 m horns of cylindrical and exponential profile, flaring constant being 5 m^{-1} , and percentage difference of horn resonances relative to cylinder resonances. $c_0 = 325 \text{ m} \cdot \text{s}^{-1}$	25
2.3	Angular frequencies of resonances of 1 m long exponential horn with flaring constant being 5 m^{-1} calculated using the exact expression (2.76) and the Transmission Matrix Method with element lengths of 0.1 m and 0.01 m. $c_0 = 325 \text{ m} \cdot \text{s}^{-1}$	29
2.4	List of thermodynamic constants and their calculation as a function of ΔT which is the temperature deviation from 26.85°C . Originally presented by Benade [13] and reprinted by Keefe [94]	30
2.5	Frequency domain impedance and admittances that include viscous and thermal losses in acoustic tubes	31
2.6	Propagation constants that include viscous and thermal losses in acoustic tubes.	32
3.1	Differential operators and the expansion point that gives second order accuracy in time or space.	60
3.2	Modal solutions and modal frequencies for the wave equation solved with the explicit scheme (3.40) using the uncentred and centred Neumann boundary conditions at $l = 0$ and $l = N$	69
6.1	Parameters and typical values used in score file that plays a trumpet.	161
B.1	Foster element values when optimising using E_R for a tube of radius 0.005 m at 26.85°C over the frequency range 0.1 – 10 kHz.	201
B.2	Foster element values when optimising using E_M for a tube of radius 0.005 m at 26.85°C over the frequency range 0.1 – 10 kHz.	202
B.3	Foster element values when optimising using E_R over a smaller frequency range for a tube of radius 0.005 m at 26.85°C over the reduced frequency range 20 Hz - 3 kHz.	202
B.4	Foster element values when optimising using E_M for a tube of radius 0.005 m at 26.85°C over the reduced frequency range 20 Hz - 3 kHz.	203
B.5	Foster element values when optimising using E'_M for a tube of radius 0.005 m at 26.85°C over the pre-warped frequency range 0.1 – 10 kHz at a sample rate of 50 kHz.	204

B.6	Foster element values when optimising using E'_M for a tube of radius 0.005 m at 26.85° C over the pre-warped frequency range 20 Hz - 3 kHz at a sample rate of 50 kHz.	204
B.7	Foster element values when optimising using E'_M for a tube of radius 0.05 m at 26.85° C over the pre-warped frequency range 0.1 – 10 kHz at a sample rate of 50 kHz.	205
B.8	Foster element values when optimising using E'_M for a tube of radius 0.1 m at 26.85° C over the pre-warped frequency range 0.1 – 10 kHz at a sample rate of 100 kHz.	205

Chapter 1

Introduction

1.1 Acoustics of brass wind instruments

From an audience’s perspective, the members of the brass instrument family are identified by their shining material, glistening at the back of the symphony orchestra or leading the ensemble in a jazz group. However, acoustically speaking, the material that brass instruments are constructed from is of secondary importance. In fact, some of the earliest brass instruments, such as the Serpent, are made out of wood and recently there has been a trend toward producing trumpets and trombones out of plastic [131, 133]. Instead, the defining characteristic of a brass instrument is that it is excited by the lips of the player, giving the classification of *labrosone* in the Hornbostel-Sachs taxonomy system [34]. The lips of the player interact with the instrument, the acoustics of which are determined, primarily, by the instrument’s geometry.

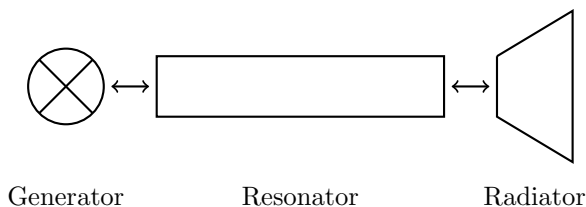


Figure 1.1: Functional diagram of a musical instrument.

A functional diagram of a musical instrument is shown in Fig. 1.1. The sound generator is the mechanism that injects energy into the system and can be considered as where the sound ‘begins’. The resonator of an instrument is the part where, usually, standing waves can be produced that determine the available range of notes produced by the instrument. The radiator defines the mechanism in which sound leaves the instrument. In the case of brass instruments, the player is the sound generator, and the resonator and radiator sections are controlled by the dimensions of the tubing. The production of sound in a brass instrument, however, is not just a cascade of processes that happen one after the other—the vibration of the player’s lips interact with the instrument’s resonances, which themselves are determined by both the internal tube profile and how it interacts with the acoustic environment. Further discussions on the acoustics of brass instruments can be found in [14, 34, 35, 63].

The conventional modelling picture of a musical instrument is that of steady state oscillations to produce a single note at a fixed pitch. In this work we intend to be more general and extend this picture beyond single tones.

1.2 A brief history of physical modelling

The history of sound synthesis and the field of physical modelling are intimately linked with developments in electronics and computing that occurred during the 20th Century. Methods such as additive, subtractive, and FM synthesis involve the manipulation of periodic signals to control the timbre of the sound. Wavetable synthesis involves the use of lookup tables to store waveforms that are then repeated at different speeds to change the pitch. Amplitude modulation can then be used to modify these sounds. These early synthesis methods are described by Roads in [141] and were applied to trumpet synthesis by Morrill [119]. These methods allow for a wide variety of sounds with minimal computational effort, but require a large and non-intuitive parameter space that is difficult to map to the perceived sounds.

As understanding of the musical instrument systems improved, researchers began using the physics of the systems to produce sounds—the beginning of physical modelling. Constructing virtual instruments using these methods gives the user an intuition over their control.

The work of Kelly and Lochbaum on vocal tract modelling [96] is considered the first physical modelling framework, and its influence is still seen today in acoustic tube modelling as an efficient simulation tool; see [81] for example. The Kelly-Lochbaum structure uses the knowledge of the physical system, mainly the scattering of waves from changes in cross-sectional area, to produce a filter that behaves in a similar manner to the vocal tract. Other methods based on travelling wave formulations have followed from this earlier work, particularly the Digital Waveguide Framework used in string [149] and brass [47] instrument synthesis. This method saw later commercial success in the Yamaha VL1 synthesiser [144].

Modal methods can be applied to simulate the individual modes of vibration present within the instrument and were applied to brass instrument synthesis in the MoReeSC framework [148] and to general synthesis in the MOSAIC system [120].

With improvements in computing hardware, it became possible to directly simulate musical instrument systems using discrete numerical methods, such as finite-difference time-domain (FDTD) methods, to solve the partial differential equations. Although applications to string modelling dates back to the 1970's [87], and even earlier to solve problems in electromagnetism [179], these methods have seen regular application in the last twenty years, spurred on by the work of Botteldooren [31, 32] and Savioja [145] in room acoustics and Chaigne [38] in musical acoustics. Recently these methods have been extended by Bilbao and colleagues [21, 74, 163], with specific applications to brass instruments shown in [22, 23]. It is these methods that will be the focus of this thesis.

1.3 Passive time-domain modelling

The steady state solutions to instrument systems show only part of the possible soundscape that virtual instruments can produce. To extend the region of possible sounds we must look to time varying systems. This is not a trivial task as time domain problems can suffer from stability issues. The modular approach to describing a brass instrument through sound

generator, resonator, and radiator also introduces problems as the connections between each section must be stable. To approach this problem, we therefore look to *passive* methods of time domain modelling that guarantee this type of growth does not occur in the global system and its connecting parts.

As we are examining a physical system, it is sensible to consider the overall energy of the system. This includes the energy stored within the propagating parts of the system and at the boundaries along with any dissipation or forcing terms; see Fig. 1.2.

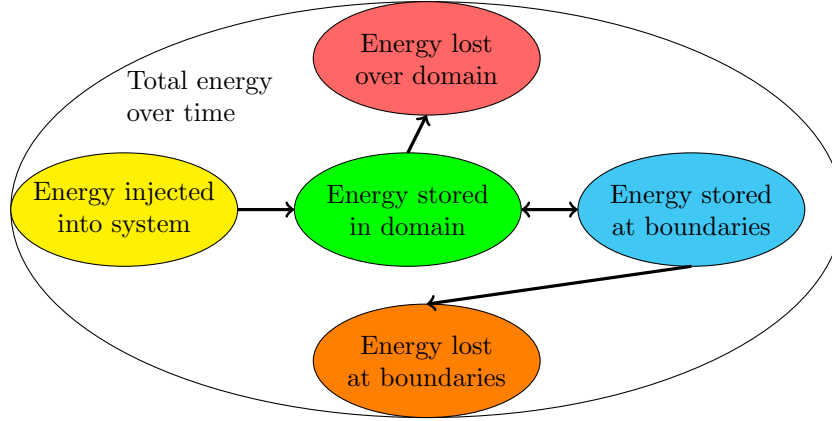


Figure 1.2: Schematic of how energy is transferred between different elements in the system. Over time, all of the energy must be accounted for to determine stability.

Energy methods [71] are constructed by taking appropriate norms over the continuous system equations to define an upper limit to the energy as the system evolves in time. This idea is related to the Port-Hamiltonian framework [164] which uses a general energy picture to construct the synthesis procedure; this will be discussed in Chap. 3. Additional non-negativity constraints on the energy bound the norms of the solution which suggests stable behaviour.

These energy methods can then be transferred into the discrete domain to determine if the numerical scheme is going to be stable. The reader may reasonably ask ‘Why not apply these methods to the discrete case immediately?’. As will become apparent in Chap. 3, there are multiple approaches to discretising schemes along with multiple approaches to constructing numerical energies for them. By already constructing an energy in the continuous time domain, we know what to aim for in the discrete case.

The discrete energy methods offer additional advantages for the algorithm designer. Discrete forms of boundary conditions are naturally suggested from the construction of the numerical energy, aiding in scheme design. In addition, a computation of the discrete energy of the system serves as a debugging tool, where deviations in the energy beyond that of machine precision would suggest incorrect implementation.

1.4 Accuracy and efficiency

Applications of numerical methods introduce inaccuracies into simulations, typically highlighted through examining the truncation order [156], which displays how accurate the scheme is with relation to how it is discretised. For audio applications, we do not require an infinite accuracy as there is an upper limit to the frequencies a human can hear. However,

additional artefacts can be introduced by the numerical method, such as inharmonicity due to frequency warping and aliasing, which must be removed.

In general, accuracy of a numerical method can be improved by increasing the resolution of the domain over which simulations are performed over. This, however, creates its own issues from a user standpoint: a finer resolution simulation requires more computational operations and therefore takes longer to complete. An ideal simulation would at best be real-time: a user would have to wait one second for a single second of sound to be produced. However, if this fast output displays significant artefacts, a user will not be satisfied with the sound. As a result, the algorithm designer must be aware of this balance between creating the correct solution within a reasonable amount of time.

1.5 Thesis objectives

The main objective of this thesis is to develop a framework for the synthesis of brass instrument sounds. This broad objective can be broken down into several smaller objectives:

- Model wave propagation in an acoustic tube, with the inclusion of boundary layer effects and those due to changes in cross-sectional area of the tube
- Inclusion of boundary conditions at the entrance and exit of the tube for accurate excitation and radiation modelling
- Enabling the changing of the instrument's resonances through the use of valves
- Incorporation of nonlinearities in the propagation models

These goals will be achieved through the application of FDTD methods. Geometric integration methods focussing on the energy of the system will be used to guarantee that the formulations are passive.

The framework described in this work has been applied in a virtual instrument environment that has been used by several musicians during the course of this Ph.D. project. The specifics of the design of the environment is outwith the scope of this work, but some discussion on how the code is structured and how such a virtual instrument is controlled is presented in Chap. 6.

1.6 Thesis outline

The outline of this thesis is as follows:

Chapter 2 - Wave propagation in acoustic tubes

We begin with an outline of the linear acoustic tube system that describes low-amplitude wave propagation in brass instruments. The wave equation is derived for disturbances within a fluid filled cylindrical tube followed by the introduction of dispersion and energy analysis of the system. Simple boundary conditions are discussed along with the concept of an input impedance, a common experimentally measured quantity. The system is then extended to a lossless acoustic tube whose cross-sectional area varies along the axial coordinate. The

Transmission Matrix Method is introduced as a ‘ground truth’ that later FDTD simulations will be compared against.

The second half of this chapter concerns losses restricted to the boundary layers of acoustic tubes—of particular interest is the model of Zwikker and Kosten. A survey of previous approximations to this model is presented, along with a discussion of positive real functions (a requirement for passivity). This then leads into a novel approximation using electrical network representations. These networks are fully explored so that a minimal choice of parameters can be applied to tubes of different radii and systems at different temperatures. The accuracy of these structures can also be improved by reducing the frequency range over which they are optimised.

Chapter 3 - Finite-difference time-domain methods: Applications to acoustic tubes

This chapter concerns the numerical problem of simulating wave propagation in acoustic tubes. The fundamentals of FDTD methods are introduced and then applied to the equations introduced in Chap. 2. Comparisons are made using explicit and implicit numerical schemes (the latter employing the bilinear transform) to simulate wave propagation in the lossless system, with focus on the construction of a numerical energy as well as frequency domain effects related to bandwidth reduction and warping.

FDTD methods are then applied to the system that includes boundary layer losses. A method for constructing an approximation to the fractional derivatives seen in the literature is presented, although stability is not proven. A numerical scheme for the network model is also presented which is proven to be stable. Frequency warping effects can be addressed in this approximation by ‘pre-warping’ the frequency variable during the optimisation procedure. The numerical schemes for the loss models are compared for the cases of a cylinder and an exponential horn.

Chapter 4 - Modelling radiation of sound from an acoustic tube

The problem of modelling the sound radiation behaviour of an acoustic tube is the subject of this chapter. The first section looks at first approximating the Levine and Schwinger radiation impedance of an unflanged cylinder using a simple equivalent electrical network and how this is translated into an FDTD scheme that is coupled to the acoustic tube.

The remainder of the chapter looks to embedding the instrument in a three-dimensional sound field. This is done by coupling the one dimensional acoustic tube model to the three-dimensional wave equation via energy conserving principles. The problem is stated in the continuous domain and then translated to the discrete domain. Comparisons against experimental measurements show greater agreement for the embedded system than the simpler equivalent network model.

Chapter 5 - Towards a complete instrument

This chapter introduces the remaining elements required to produce a virtual instrument. A review of lip reed modelling is presented and a simple model is chosen as the excitation

mechanism for the instrument. The discretisation procedure and some simple results using this model are presented.

To modify the resonances of the instrument, a valve model is presented that introduces additional paths that waves may propagate through. The model presented here is derived from energy and momentum conservation and allows for the interaction between the two paths when the valve is partially depressed, resulting in complex resonance phenomena. The scheme for the lossless system is presented, along with extensions to those where losses are included in the wave propagation model and when the valves are allowed to vary with time.

Chapter 6 - A brass instrument synthesis environment

The elements described in the previous chapters are combined to create a virtual instrument that allows the user to construct and control the instrument. The basic structure of the code is presented along with a discussion on how the user interacts with it. Examples of gestures are presented, displaying such effects as time varying modulation of parameters along with the production of ‘multiphonic’ sounds from partially open valves. A simple playability space study highlights some of issues related to control of an instrument.

Chapter 7 - Comparison of nonlinear propagation models

This chapter looks to the extension of the propagation model by including nonlinear effects that contribute to the ‘brassy’ timbre of brass-wind instruments played at high dynamic levels. A review of current models highlights the use of separable wave solutions—the effect of this assumption is explored in this chapter. Simple numerical experiments are performed to show the effect of coupling between forwards and backwards waves in an acoustic tube and linearised forms of the models help explain why such models do not accurately represent the behaviour due to changes in cross-sectional area.

Chapter 8 - Conclusions and future work

This chapter provides a summary of the work performed in this thesis and how it can be extended in the future.

Appendix A - Circuit elements

A brief introduction to the use of passive circuit representations is presented here for those unacquainted with the method. Although not extensive, this should help the unfamiliar reader with the discussions in chapters 2-4.

Appendix B - Foster network element values

This appendix presents a list of tables containing the network element values used in the Foster network approximation to the boundary layer loss model.

Appendix C - Experiments on brass instrument valves

Preliminary experiments are presented relating to the effect of partially open valve systems. A simple experimental set up is described and experimental measurements are compared to

simulations.

1.7 Main contributions

The main contributions of this thesis are

- Development of an approximation to the boundary layer loss model of Zwikker and Kosten using passive circuit representations whose parameters can be modified for use in both the impedance and admittance models, different tube radii, and simulations at different temperatures. This approximation is presented in Secs. 2.4.3 to 2.4.12
- Construction of an explicit, passive, and guaranteed stable numerical scheme for the boundary layer loss model including modification to counter frequency warping effects. This scheme is presented in Secs. 3.5.2 to 3.5.3.
- Modelling an embedded instrument system by coupling the one-dimensional model to the three-dimensional wave equation. This is presented in Secs. 4.2 to 4.2.12.
- Development of a time-varying valve model to modify the instrument's resonances that allow for production of multiphonic tones. This model is presented in Sec. 5.2
- Investigation of wave separation in nonlinear propagation models. This is presented in Chap. 7.

All results, with the exception of the nonlinear propagation models, are tied together with strict passive realisations to create explicit schemes.

Act I

Linear Acoustics

Chapter 2

Wave propagation in acoustic tubes

“Essentially, all models are wrong, but some are useful.”

— George Box

The construction of a brass instrument creates an enclosure of air within the instrument’s tubing. The diameter of the instrument is significantly less than its overall length—we can describe this as an acoustic tube. Although, strictly speaking, a brass instrument is defined in a three-dimensional space, its behaviour can be well described using a one-dimensional approximation. There are some caveats to this simplification, namely that the wavelengths of interest are longer than the diameter of the instrument bore and that the bore profile changes slowly along the length of the instrument [63, 132]. The input of the instrument is closed off by the lips of the player (or by a loudspeaker in experimental settings) and its radiating end is left open. When excited, e.g. by buzzing the lips to inject pulses of air into the system, waves are created that travel along the length of the tube. At the open end, the wave is partially transmitted out of the instrument (which becomes the sound an observer hears) and partially reflected back into it. This reflected wave combines with the other incoming waves to set up a series of resonances within the instrument—these resonances are what determine the range of available notes that can be played.

In the linear approximation, the profile of the instrument bore and associated viscous and thermal effects in air dominate the locations and widths of these resonances [63]—the dynamics of the acoustic tube in isolation are the subject of this chapter. Another attribute is that of radiation, but discussion of this is postponed until Chap. 4. See Chap. 7 for models that include nonlinear propagation—the mechanism which creates the ‘brassy’ sound at high dynamic levels [88].

This chapter is concerned with the model problem. Numerical simulation techniques will be introduced in the next chapter. To begin, the notation used for partial differential equations is introduced along with identities that will be used frequently in the analysis of the systems. Frequency domain transformations will also be covered in this section.

The rest of this chapter is then split into two parts. First the lossless problem is discussed in the case of a cylindrical tube and then with a tube of varying cross-section. The discussion of these two systems follows in a parallel manner. Dispersion analysis is discussed followed by

energy analysis on the infinite, then bounded domains. Passivity of the system is a constant theme throughout this work and the energy analysis presented here is a suitable method to show stability that later translates into the discrete case. In addition, this also allows for a convenient analysis of boundary conditions which are used to calculate the modes of the system. The concept of the input impedance is then introduced which is related to the modes of the system. A small step is taken into numerical methods at this point to cover the Transmission Matrix Method as this will be used as our “ground truth” when comparing the numerical models in later chapters.

The last section of this chapter concerns viscous and thermal mechanisms that lead to the dissipation of energy within an acoustic tube. The standard model of Zwikker and Kosten [182] is introduced; in general, this model is expressed in the frequency domain so further approximations must be made for it to be used in a time domain model, several of which are presented from the literature. The concept of positive realness [165, 174] is introduced as this is important for the construction of equivalent circuits to approximate the Zwikker and Kosten model. Two such structures are presented: Cauer and Foster [165, 174]. A brief discussion of these structures is presented before application to attenuation modelling, in which the Foster model is selected as a suitable candidate. The time domain representation of the Foster structure is introduced, along with energy analysis to show that the network is passive. Implementation of the Foster structure requires appropriate circuit element values which are found through a numerical optimisation procedure. This is briefly discussed, along with how the values can be manipulated to use for different tubes. Finally, an overall comparison of the different approximations is made.

2.1 Introducing notation: Étude I

Before discussing the model for wave propagation, some notation must first be introduced.

2.1.1 Partial differential equations and differential operators

In many branches of science, the system under examination can be described by partial differential equations (PDEs). These equations describe how some function varies with respect to its independent variables, e.g. space or time. For the majority of this work we will only consider variation in time over the positive real axis, $t \in \mathbb{R}^+ = \{0 \leq t \leq \infty\}$, and axial coordinate over the real axis, $z \in \mathbb{R} = \{-\infty \leq z \leq \infty\}$. A finite spatial domain of an acoustic tube is defined by $\mathcal{D} = \{z \in \mathbb{R} \mid 0 \leq z \leq L\}$, where L is the finite length of the acoustic tube. ∂_t and ∂_z represent differentiation with respect to t and z respectively. Higher derivatives are denoted as powers of the operators mentioned previously, e.g. ∂_t^2 , ∂_z^3 . PDEs will be labelled according to their highest derivative, e.g. second derivative PDE, first derivative PDE. This strays from the normal labelling using ‘order’ so as to avoid confusion when discussing accuracy of simulations in later chapters. In order to describe a complete physical system, a PDE must be complemented by boundary conditions and initial conditions.

2.1.2 Integral relations and identities

It is useful to define inner products along with other identities that can be used to determine passivity of the system through energy analysis. The one-dimensional L^2 inner product

between two continuous functions f and g over the generic domain $z \in \mathcal{W}$ is

$$\langle f, g \rangle_{\mathcal{W}} = \int_{\mathcal{W}} f g dz \quad (2.1)$$

The L^2 norm comes from this inner product

$$\|f\|_{\mathcal{W}} = \sqrt{\langle f, f \rangle_{\mathcal{W}}} \quad (2.2)$$

Integration by parts will be used repeatedly in the work that follows:

$$\int_{\mathcal{W}} f \partial_z g dz = |fg|_{\mathcal{W}_-^+} - \int_{\mathcal{W}} (\partial_z f) g dz \implies \langle f, \partial_z g \rangle_{\mathcal{W}} = fg|_{z=\mathcal{W}_+} - fg|_{z=\mathcal{W}_-} - \langle \partial_z f, g \rangle_{\mathcal{W}} \quad (2.3)$$

where \mathcal{W}_+ and \mathcal{W}_- denote the boundaries of the domain.

Another useful identity is:

$$f \partial_t f = \frac{1}{2} \partial_t (f^2) \implies \langle f, \partial_t f \rangle_{\mathcal{D}} = \frac{1}{2} \frac{d}{dt} \|f\|_{\mathcal{D}}^2 \quad (2.4)$$

where the d/dt is the total derivative operator¹.

2.1.3 The Laplace transform and the frequency domain

In acoustics and signal processing, it is often of use to analyse the system using the Laplace transform. This maps the function $f(t)$ of time to the complex plane $\hat{f}(s)$, where $s = \sigma + j\omega$, σ is the real frequency, ω is the imaginary or angular frequency, and $j = +\sqrt{-1}$. Frequency domain functions will be notated with the $\hat{}$ operator.

Neglecting initial conditions² the two sided Laplace transformation is defined as [39]

$$\hat{f}(s) = \mathcal{L}\{f(t)\} = \int_{-\infty}^{\infty} e^{-st} f(t) dt \quad (2.5)$$

The Laplace transform of the time derivative of a function is

$$\mathcal{L}\{\partial_t f(t)\} = s \hat{f}(s) \quad (2.6)$$

The two sided Laplace transform is equivalent to the ansatz

$$f = e^{st} \quad (2.7)$$

For multivariable functions of time and space, the Laplace transform is easily extended as the spatial coordinate is independent of time.

The Fourier transform is related to the Laplace transform. It considers only the imaginary part of the complex domain so that $s = j\omega$. This is denoted as

$$\hat{f}(\omega) = \mathcal{F}\{f(t)\} = \int_{-\infty}^{\infty} e^{-j\omega t} f(t) dt \quad (2.8)$$

¹Here the coordinate z is independent of t so that the norm of f is only a function of t . We can therefore go from the partial derivative with respect to time to the total derivative with respect to time.

²This is valid as we will consider only the steady state in this type of analysis.

The same properties hold for the Fourier transform of the time derivative as for the Laplace transform.

2.2 The wave equation

Here, we derive the one-dimensional wave equation that describes the dynamics of air contained in a cylindrical tube of cross-sectional area S_0 . The derivation here follows that of Morse [121].

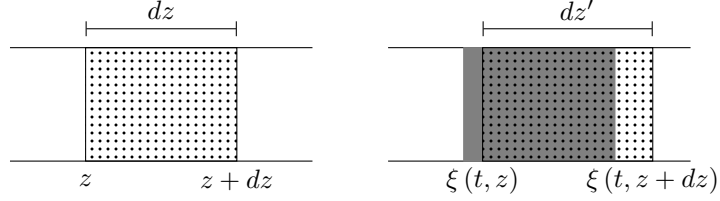


Figure 2.1: Left: Undisturbed volume of air of length dz . Right: Air has been disturbed, changing its overall length to dz' . The shaded area denotes the previous volume the air occupied.

Consider a small element of air within the tube that lies between z and $z + dz$, where dz is the length of the element; see at left in Fig. 2.1. The total volume of air is given by $V = S_0 dz$ with a total mass $m = \rho_0 V$, where ρ_0 is the static air density. As a disturbance passes through the tube, the end points of this element are displaced a distance $\xi(t, z)$ as shown at right in Fig. 2.1. This changes the total length to be

$$dz' = dz + \xi(t, z + dz) - \xi(t, z) \quad (2.9)$$

For small dz , the Taylor expansion of this expression reduces to

$$dz' = (1 + \partial_z \xi) dz \quad (2.10)$$

so that the new volume is

$$V' = S_0 (1 + \partial_z \xi) dz \quad (2.11)$$

The change in volume is given by

$$dV = S \partial_z \xi dz \quad (2.12)$$

Assuming there is no change in temperature over the element, the pressure, $p(t, z)$, generated due to the change in volume is given by

$$p = -K \frac{dV}{V} \implies p = -K \partial_z \xi \quad (2.13)$$

where K is the bulk modulus of air.

If we now examine the forces acting on the element of air, we see that the acceleration of the element is given by the pressure gradient over the two sides

$$\rho_0 S_0 dz \partial_t^2 \xi = -S_0 (p(t, z + dz) - p(t, z)) \quad (2.14)$$

For small dz this becomes

$$\rho_0 S_0 \partial_t^2 \xi = -S_0 \partial_z p \quad (2.15)$$

Taking the spatial derivative of this expression and combining with the second time derivative of (2.13) produces the one-dimensional wave equation in terms of pressure

$$S_0 \partial_t^2 p - S_0 c_0^2 \partial_z^2 p = 0 \quad (2.16)$$

where $c_0 = \sqrt{K/\rho_0}$ is the speed of sound in air.

Alternatively, the wave equation can be defined in terms of the acoustic velocity potential $\psi(t, z)$ [122]

$$\rho_0 S_0 \partial_{tt} \psi - \rho_0 S_0 c_0^2 \partial_{zz} \psi = 0 \quad (2.17)$$

where

$$\rho_0 \partial_t \psi = p, \quad \partial_z \psi = -v \quad (2.18)$$

and $v(t, z)$ is the velocity of the element. The acoustic velocity potential allows for simple treatment of boundary conditions, presented later in this chapter, and will be used in discussions on the wave equation.

The wave equation can be factored into

$$S_0 \rho_0 (\partial_t + c_0 \partial_z) (\partial_t - c_0 \partial_z) \psi = 0 \quad (2.19)$$

In this form, it is clear that the solution is made up of travelling waves

$$\psi(t, z) = \psi_+(t - z/c_0) + \psi_-(t + z/c_0) \quad (2.20)$$

where $\psi_+(t - z/c_0)$ and $\psi_-(t + z/c_0)$ are wave solutions that travel in the positive and negative axial directions respectively. The arguments signify some translation in space as time progresses, without distortion of the initial disturbance; see Fig. 2.2.

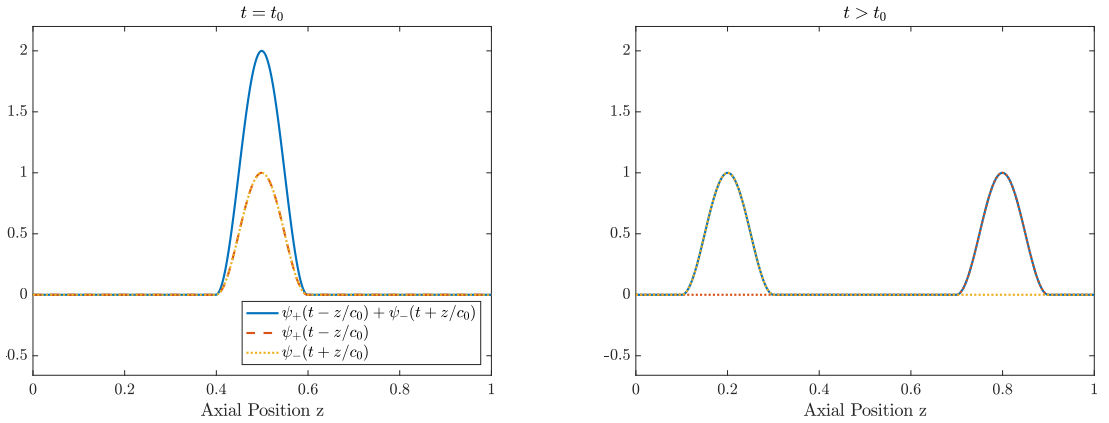


Figure 2.2: Left: Initial conditions to the wave equation. Forwards wave, $\psi_+(t - z/c_0)$, (dashed red); backwards wave, $\psi_-(t + z/c_0)$, (dotted yellow); sum of forwards and backwards solutions (solid blue). Right: Solution to the wave equation at a later time. The waves now occupy different domains but preserve the shape they had at $t = t_0$.

Digital waveguides

Although the main discussion on numerical methods is postponed until the next chapter, it is worthwhile to take a small stop here to mention digital waveguides (DWG) without disrupting the flow of the overall topic; see the reference of Julius Smith for a thorough description of the method [151].

The use of DWGs follows from the idea of travelling wave solutions—from some set of initial conditions, the forwards and backwards waves can be found and then propagated without their overall form being changed. This can be implemented computationally by moving pointers around a circular buffer—a very small computational cost which makes the method so efficient compared to methods discussed later in this work (at the cost of generality). Of course, as models of wave propagation are improved this travelling wave solution is no longer exact, so modifications, such as scattering junctions [19] to include the effect of varying the cross-sectional area of the tube, must be made which complicate the construction of the scheme. An example of this is the Kelly-Lochbaum scheme [96] but this method is a specific case of a finite-difference scheme [21].

2.2.1 Dispersion analysis

The behaviour of the wave equation can be analysed by first assuming that the temporal and spatial parts of the solution can be separated. Assuming a time harmonic dependence over an infinite spatial domain, the solution can be written in the form [140]

$$\psi(t, z) = e^{j\omega t} e^{j\beta z} \quad (2.21)$$

where β is the spatial wavenumber and is considered real at this point as we are considering bounded solutions. In this case ψ can be complex—the observed quantity is therefore $\text{Re}(\psi)$. Substituting (2.21) into (2.17) gives the characteristic equation

$$-\frac{\omega^2}{c_0^2} + \beta^2 = 0 \quad (2.22)$$

Solving for the angular frequency gives the dispersion relation

$$\omega = \pm c_0 \beta \quad (2.23)$$

From this, we can define a phase velocity, v_p , and group velocity, v_g , as [63]

$$v_p = \frac{\omega}{\beta}, \quad v_g = \frac{d\omega}{d\beta} = \left(\frac{d\beta}{d\omega} \right)^{-1} \quad (2.24)$$

It is clear that the phase and group velocity have the same value for the wave equation

$$v_p = v_g = \pm c_0 \quad (2.25)$$

Alternatively we can solve the dispersion relationship for the spatial wavenumber

$$\beta = \pm \frac{\omega}{c_0} \quad (2.26)$$

This will be used when solving for the modes of the system. It is clear from the dispersion analysis that the harmonic solutions are bounded over time.

2.2.2 Energy analysis: A conserved quantity

The wave equation describes a lossless system—as such it must be energy conserving; we will come back to the lossy system later in this chapter. This is an extremely useful way to analyse a system, both in terms of boundary conditions and later for numerical implementation.

Let us first examine the wave equation over the infinite domain $z \in \mathbb{R}$. First, we take the inner product of (2.17) with $\partial_t \psi$

$$\frac{S_0 \rho_0}{c_0^2} \langle \partial_t \psi, \partial_t^2 \psi \rangle_{\mathbb{R}} - S_0 \rho_0 \langle \partial_t \psi, \partial_z^2 \psi \rangle_{\mathbb{R}} = 0 \quad (2.27)$$

Using integration by parts, (2.3), on the second term gives

$$\frac{S_0 \rho_0}{c_0^2} \langle \partial_t \psi, \partial_t^2 \psi \rangle_{\mathbb{R}} + S_0 \rho_0 \langle \partial_t \partial_z \psi, \partial_z \psi \rangle_{\mathbb{R}} = 0 \quad (2.28)$$

where it is assumed that $\psi = 0$ at $z = \pm\infty$. This assumption is valid as we can say that any disturbances will not have travelled to $z = \pm\infty$ due to the finite phase and group velocities of the system. Using (2.4) gives

$$\frac{d}{dt} \left(\frac{S_0 \rho_0}{2c_0^2} \|\partial_t \psi\|_{\mathbb{R}}^2 + \frac{S_0 \rho_0}{2} \|\partial_z \psi\|_{\mathbb{R}}^2 \right) = 0 \quad (2.29)$$

This can be rewritten as

$$\frac{d\mathcal{H}_{we}}{dt} = 0 \quad (2.30)$$

where \mathcal{H}_{we} is the energy in the system described by the wave equation

$$\mathcal{H}_{we} = \frac{S_0 \rho_0}{2c_0^2} \|\partial_t \psi\|_{\mathbb{R}}^2 + \frac{S_0 \rho_0}{2} \|\partial_z \psi\|_{\mathbb{R}}^2 \quad (2.31)$$

Equation (2.30) describes the rate of change of energy of the system. It is clear that this system is lossless and that

$$\mathcal{H}_{we}(t) = \mathcal{H}_{we}(0) \geq 0, \quad t \in \mathbb{R}^+ \quad (2.32)$$

As the energy does not grow with time, the system can be considered passive [19]; there are no energy generating components within it. This is important in the construction of numerical schemes, which we shall return to in Chap. 3.

The energy, \mathcal{H}_{we} , is a Lyapunov function of the system [45]. The methods used in this thesis will utilise energy conserving principles as well as taking into account dissipation processes as systems become more complex, similar to the Port-Hamiltonian framework [59, 164].

Bounds on the solution

It is clear from (2.30) and (2.31) that \mathcal{H}_{we} is a) constant throughout time and b) is always a non-negative, real quantity. The phase space of this system can be defined as

$$\|\partial_t \psi\|_{\mathbb{R}}^2 + c_0^2 \|\partial_z \psi\|_{\mathbb{R}}^2 = \frac{2c_0^2}{S_0 \rho_0} \mathcal{H}_{we}(0) \quad (2.33)$$

which describes an ellipse whose dimensions are constant in time. We can consider the values $\|\partial_t \psi\|_{\mathbb{R}}$ and $\|\partial_z \psi\|_{\mathbb{R}}$ as travelling around this ellipse, the starting point being determined by the initial conditions of the system. This implies that the norms of the derivatives of the solution are bounded by

$$\|\partial_t \psi\|_{\mathbb{R}} \leq c_0 \sqrt{\frac{2\mathcal{H}_{we}(0)}{S_0 \rho_0}}, \quad \|\partial_z \psi\|_{\mathbb{R}} \leq \sqrt{\frac{2\mathcal{H}_{we}(0)}{S_0 \rho_0}} \quad (2.34)$$

although we cannot say the same about the norms of the solutions themselves³. At best, we can say that the growth of the solutions can be no more than linear. If we were to perform the same analysis in terms of the acoustic pressure and velocity so that the energy is given by

$$\mathcal{H}_{we} = \frac{S_0}{2\rho_0 c_0^2} \|p\|_{\mathbb{R}}^2 + \frac{S_0 \rho_0}{2} \|v\|_{\mathbb{R}}^2 \quad (2.35)$$

we can say that there are bounds on the norms of the solutions to p and v —there will be no linear drift in the norm of these values.

$$\|p\|_{\mathbb{R}} \leq c_0 \sqrt{\frac{2\rho_0 \mathcal{H}_{we}(0)}{S_0}}, \quad \|v\|_{\mathbb{R}} \leq \sqrt{\frac{2\mathcal{H}_{we}(0)}{S_0 \rho_0}} \quad (2.36)$$

If there were loss terms in the PDE describing the system, the trajectory of the norms would no longer be bound on an ellipse, instead they would travel on an elliptical spiral that concentrates on the origin.

2.2.3 Boundary conditions

Let us now consider the wave equation, (2.17), over the finite domain \mathcal{D} . Using the same method as in the previous subsection, (2.30) is now

$$\frac{d\mathcal{H}_{we}}{dt} + \mathcal{B}_{we} = 0 \quad (2.37)$$

where the energy is now defined over \mathcal{D}

$$\mathcal{H}_{we} = \frac{S_0 \rho_0}{2c_0^2} \|\partial_t \psi\|_{\mathcal{D}}^2 + \frac{S_0 \rho_0}{2} \|\partial_z \psi\|_{\mathcal{D}}^2 \quad (2.38)$$

and the power transfer at the tube boundaries is

$$\begin{aligned} \mathcal{B}_{we} &= S_0 \rho_0 (\partial_t \psi) (\partial_z \psi)|_{z=0} - S_0 \rho_0 (\partial_t \psi) (\partial_z \psi)|_{z=L} \\ &= -p S_0 v|_{z=0} + p S_0 v|_{z=L} \end{aligned} \quad (2.39)$$

³These solutions are described in a Sobolev space.

Two simple boundary conditions that preserve the energy of the system are [63]

$$\partial_t \psi(t, 0) = \frac{p(t, 0)}{\rho_0} = 0, \quad \partial_t \psi(t, L) = \frac{p(t, L)}{\rho_0} = 0 \quad (\text{Dirichlet}) \quad (2.40a)$$

$$\partial_z \psi(t, 0) = -v(t, 0) = 0, \quad \partial_z \psi(t, L) = -v(t, L) = 0 \quad (\text{Neumann}) \quad (2.40b)$$

Both of these boundary conditions reflect waves that are incident upon them and it is clear that $\mathcal{B}_{we} = 0$. The physical interpretation of these boundary conditions in an acoustic tube are as follows. For the Neumann boundary conditions, the particle velocity is zero at the boundaries and this corresponds to a closed tube. For the Dirichlet condition, the acoustic pressure is zero; this is a crude first order approximation to an open tube. See Chap. 4 for more realistic modelling of boundary conditions in acoustic tubes.

Lossy boundary conditions

Boundary conditions do not have to be lossless; in the case of lossy boundary conditions the energy is no longer constant over time. Integrating (2.37) with respect to time gives

$$\mathcal{H}_{we}(t) - \mathcal{H}_{we}(0) + \int_0^t \mathcal{B}_{we}(t') dt' = 0 \quad (2.41)$$

where we are now taking into account the energy transfer at the boundaries of the system.

Energy storing boundary conditions

The boundary conditions mentioned above are considered to be ‘memoryless’, that is there is no mechanism for them to store energy. When boundary conditions do have this property, the power transfer at the boundary can be considered as

$$\mathcal{B}_{we} = \frac{d\mathcal{H}_b}{dt} + \mathcal{Q}_b \quad (2.42)$$

where the energy stored and the power dissipated by the boundary condition are denoted by \mathcal{H}_b and \mathcal{Q}_b respectively. The energy of the system is then given by

$$\frac{d\mathcal{H}_t}{dt} + \mathcal{Q}_b = 0 \implies \mathcal{H}_t(t) + \int_0^t \mathcal{Q}_b(t') dt' = 0 \quad (2.43)$$

where the combined energy stored in the wave equation and the boundary condition is given by $\mathcal{H}_t = \mathcal{H}_{we} + \mathcal{H}_b$. This form will be returned to in later sections.

2.2.4 Modes of the system

The selection of boundary conditions determines the overall behaviour of the solution to the wave equation.

Since the dispersion relation gives two solutions for β , the spatial part of the wave equation can be given as a combination of sine and cosine terms. This is modified by a harmonic time component so that the solution is of the form

$$\psi = e^{j\omega t} \left(A \sin \left(\frac{\omega z}{c_0} \right) + B \cos \left(\frac{\omega z}{c_0} \right) \right) \quad (2.44)$$

where A and B are constants.

A relationship between A and B , along with constraints on the angular frequencies, can be found from the boundary conditions set at $z = 0$ and $z = L$. The angular frequencies, ω_m , are the modal frequencies of the system; see Tab. 2.1 for a list of solutions and possible frequencies.

Boundary conditions	Solution	Mode frequencies
Dirichlet $z = 0$ Dirichlet $z = L$	$\psi_m = A_m e^{j\omega_m t} \sin\left(\frac{\omega_m z}{c_0}\right)$	$\omega_m = \frac{m\pi c_0}{L}, \quad m = 1, 2, 3, \dots$
Dirichlet $z = 0$, Neumann $z = L$	$\psi_m = A_m e^{j\omega_m t} \sin\left(\frac{\omega_m z}{c_0}\right)$	$\omega_m = \frac{(2m-1)\pi c_0}{2L}, \quad m = 1, 2, 3, \dots$
Neumann $z = 0$, Dirichlet $z = L$	$\psi_m = B_m e^{j\omega_m t} \cos\left(\frac{\omega_m z}{c_0}\right)$	$\omega_m = \frac{(2m-1)\pi c_0}{2L} \quad m = 1, 2, 3, \dots$
Neumann $z = 0$, Neumann $z = L$	$\psi_m = B_m e^{j\omega_m t} \cos\left(\frac{\omega_m z}{c_0}\right)$	$\omega_m = \frac{m\pi c_0}{L}, \quad m = 0, 1, 2, \dots$

Table 2.1: Modal solutions and modal frequencies of the wave equation for different combinations of boundary conditions.

Since there are multiple modal frequencies, the total solution is a combination of all the modal shapes. This is the principle behind modal synthesis methods such as those used in the Modalys [52], MoReeSC [148], and Mosaic [120] frameworks.

2.2.5 Input impedance

The input/output behaviour of a brass instrument can be characterised by the input impedance [63] which describes the frequency response of the system to some volume flow injected at the input. The input impedance of a cylinder is given by the ratio of the acoustic pressure and volume velocity at the input of the tube

$$Z_{in}(\omega) = \frac{\hat{p}(\omega, 0)}{S_0 \hat{v}(\omega, 0)} \quad (2.45)$$

where $\hat{p}(\omega, z)$ and $\hat{v}(\omega, z)$ are the Fourier transforms of the pressure and velocity. The input impedance gives information about how waves propagate through the domain and how they are reflected at the far boundary.

The characteristic impedance of air in a cylindrical tube is defined as

$$Z_c = \frac{\rho_0 c_0}{S_0} \quad (2.46)$$

which is the input impedance of an infinitely long tube. A wave travelling in an infinitely long cylinder does not have a chance to be reflected, so the input does not see any returning waves and it ‘appears’ as if the wave has been dissipated—this is highlighted in the purely real value of the characteristic impedance.

A finite cylinder behaves in a different manner. For a Dirichlet boundary condition at $z = L$, the input impedance is

$$Z_{in} = jZ_c \tan\left(\frac{\omega L}{c_0}\right) \quad (2.47)$$

For Neumann boundary conditions at $z = L$, the input impedance is

$$Z_{in} = -jZ_c \cot\left(\frac{\omega L}{c_0}\right) \quad (2.48)$$

Both cases exhibit resonances and antiresonances, the phases of which depend on the boundary conditions. The resonances occur at frequencies where $Z_{in} = \infty$; these are the same frequencies calculated using the modal analysis. See Fig. 2.3 for plots of these impedances.

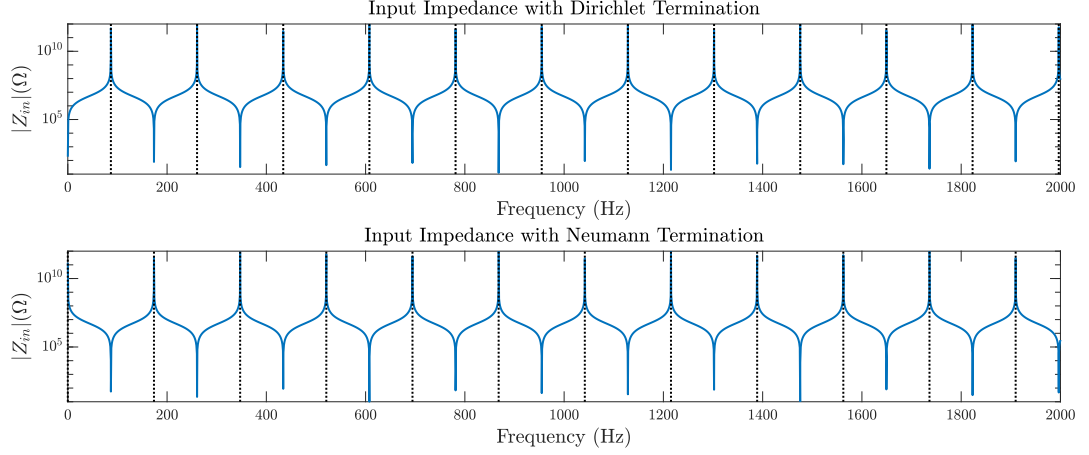


Figure 2.3: Top: Input impedance for the wave equation with Dirichlet termination. Bottom: Input impedance for the wave equation with Neumann termination. The cylinder has a length $L = 1$ m, and radius $r_0 = 0.005$ m. The values for air density and speed of sound are $\rho_0 = 1.1769 \text{ kg} \cdot \text{m}^{-3}$ and $c_0 = 347.23 \text{ m} \cdot \text{s}^{-1}$ corresponding to a temperature of 26.85°C .

2.3 The horn equation

The wave equation is a suitable description of the dynamics of a cylindrical tube system. However, if we are to describe the behaviour of brass instruments, we need to include the effect of a variable cross-sectional area, $S(z)$; see Fig. 2.4.

A suitable first derivative PDE system describing the dynamics of an acoustic tube system is

$$\frac{S}{\rho_0 c_0^2} \partial_t p + \partial_z (Sv) = 0, \quad \rho_0 \partial_t v + \partial_z p = 0 \quad (2.49)$$

This can be written in a second derivative form in terms of the acoustic velocity potential

$$S \partial_{tt} \psi - c_0^2 \partial_z (S \partial_z \psi) = 0 \quad (2.50)$$

which is traditionally called Webster's [173] or the horn equation. This equation can also be written in terms of pressure, but the acoustic velocity potential lends itself to simpler applications of boundary conditions.

Combining (2.49) gives

$$(\partial_t \pm c_0 \partial_z) \left\{ \frac{p}{\rho_0 c_0} \pm v \right\} = -\frac{c_0 v}{S} \frac{dS}{dz} \quad (2.51)$$

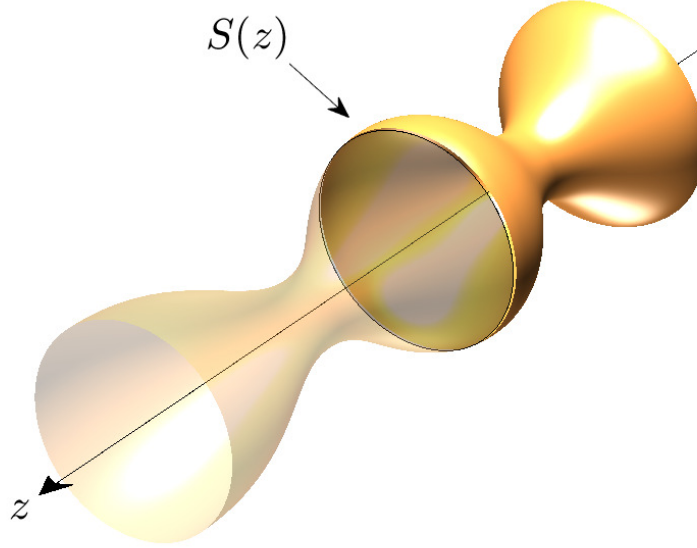


Figure 2.4: Profile of an acoustic tube with variable cross-sectional area, $S(z)$, that changes along the axial length, z .

When $S(z)$ is constant, (2.50) reduces to the wave equation and (2.51) allows for separable waves; the wave variables being the terms in $\{\}$. However, for general bore profiles this equation does not allow for separable solutions as waves are scattered by the change in cross-sectional area; the right hand side of the equation can only be written in terms of the forwards and backwards waves. We will return to this type of analysis in Chap. 7 when looking at nonlinear propagation models.

A note on one-dimensional models of brass instruments

The reader might wonder whether it is correct to use a one-dimensional model to describe three-dimensional phenomena. For the wavelengths of interest in audio applications, the one-dimensional model is suitable and has been tested in the works cited below. Although a complete model includes losses in the air, a topic that will be covered later in this chapter, the following citations do show that the one-dimensional model is suitable.

Recent work by Eveno *et al.* [56] and H  lie *et al.* [80] show good agreement between one-dimensional models and experiments on real brass instruments.

In this work, the shape of the wavefronts is assumed to be planar—the pressure and velocity fields are assumed constant over a circular cross-section of the instrument that is perpendicular to the axial coordinate. Other choices of wavefront shape are available. Benade and Jansson [15] used spherical wave fronts in their model of wave propagation. A curved, but not spherical, wavefront shape was proposed by H  lie that uses the walls of the instrument as the coordinate system [79].

Modes beyond the planar mode have been included in multimodal studies by, e.g., Amir *et al.* [6] and Kemp [99].

2.3.1 Dispersion analysis

For an acoustic tube with varying cross-sectional area, dispersion analysis is not, in general, illuminating because the PDE does not have constant coefficients. Approximations, such as the WKB method [95], can be applied but require additional assumptions. However, in certain special cases, the PDE can be rendered constant coefficient. A particular example is the exponential horn of cross-section defined by

$$S(z) = S_0 e^{\alpha z} \quad (2.52)$$

where S_0 is now the opening cross-sectional area of the tube and α is a flaring constant.

This results in the following form of the horn equation in terms of acoustic velocity potential

$$\frac{1}{c_0^2} \partial_t^2 \psi - \partial_z^2 \psi - \alpha \partial_z \psi = 0 \quad (2.53)$$

Even though the bore profile is spatially varying, the PDE has constant coefficients.

Again we can assume the solution is of the form

$$\psi = e^{j\omega t} e^{j\beta z} \quad (2.54)$$

which results in the following dispersion relation

$$-\frac{\omega^2}{c_0^2} + \beta^2 - j\alpha\beta = 0 \quad (2.55)$$

Solving for ω gives

$$\omega = \pm c_0 \sqrt{\beta^2 - j\alpha\beta} \quad (2.56)$$

We define ω as being real from its relation to s therefore the expression $\beta^2 - j\alpha\beta$ must be real and non-negative. The wavenumber β must be complex to satisfy this, although in other contexts β is restricted to be real [65, 124]. The real and imaginary parts of this expression must satisfy

$$\text{Re}(\beta)^2 - \text{Im}(\beta)^2 + \alpha \text{Im}(\beta) \geq 0 \quad (2.57a)$$

$$\text{Re}(\beta) (2\text{Im}(\beta) - \alpha) = 0 \quad (2.57b)$$

There are two solutions that satisfy (2.57b). When $\text{Re}(\beta) = 0$ then $\text{Im}(\beta)$ lies within 0 and α for (2.57a) to hold. When $\text{Im}(\beta) = \alpha/2$ then (2.57a) always holds.

This is more succinctly shown if we solve the dispersion relation for β

$$\beta = \frac{j\alpha \pm \sqrt{4\frac{\omega^2}{c_0^2} - \alpha^2}}{2} \quad (2.58)$$

where for $\omega \leq c_0\alpha/2$, β is imaginary with $0 < \text{Im}(\beta) < \alpha$ and for $\omega > c_0\alpha/2$, $\text{Im}(\beta) = \alpha/2$ and $\text{Re}(\beta) > 0$. As in the case of the wave equation, the dispersion relation shows that the solutions are bounded in time.

The phase and group velocities for waves in an exponential horn are

$$v_p = \frac{\omega}{\text{Re}(\beta)} = \pm \frac{2\omega}{\sqrt{4\frac{\omega^2}{c_0^2} - \alpha^2}}, \quad v_g = \pm \frac{c_0^2 \sqrt{4\frac{\omega^2}{c_0^2} - \alpha^2}}{2\omega} \quad (2.59)$$

where the phase velocity is defined using the real part of the wavenumber [63]. The phase and group velocities are different in the exponential horn, whereas they are equal for the free space wave equation. These velocities are also functions of frequency meaning that waves of different frequency travel at different velocities, indicating dispersion.

Cutoff frequency

Clearly the solutions of the horn equation behave differently to the those of the wave equation, as shown by the relationship between ω and β . For the wave equation, a real β always produces a real ω , therefore waves of all frequencies can propagate over the entire domain. For the horn equation, β is now complex (and sometimes imaginary) restricting wave propagation at certain frequencies. This means that waves must have a frequency above a certain cutoff if they are to propagate.

As previously stated, for $\omega \leq \frac{\alpha c_0}{2}$, β is a positive, imaginary number. In this case, the spatial part of the solution is determined by an exponential function whose argument is always negative over the positive side of the spatial domain. This means that waves of frequencies below this value have a spatial envelope that goes to zero exponentially. This is also reflected in the group and phase velocities which are imaginary numbers so waves have no real propagation speed.

When $\omega > \frac{\alpha c_0}{2}$, then β is complex so that the spatial solution can instead be described by sine and cosine functions, with some exponential envelope that corresponds to the spreading of the wave over the increasing surface area of the horn. In this case, waves are allowed to propagate—again reflected in the phase and group velocities as they now have real parts. The value $\frac{\alpha c_0}{2}$ is the cutoff frequency [132], above which waves can propagate⁴. Fig. 2.5 shows the spatial solution of the horn equation for three different cases.

Alternate forms

The horn equation can be transformed into an alternate PDE [63] by using the scaling

$$\phi = \sqrt{S}\psi \quad (2.60)$$

which gives

$$\frac{1}{c_0^2} \partial_t^2 \phi - \partial_z^2 \phi + \left(\frac{1}{2} \frac{\partial_z^2 S}{S} - \frac{1}{4} \left(\frac{\partial_z S}{S} \right)^2 \right) \phi = 0 \quad (2.61)$$

Using the case of the exponential horn and assuming solutions of the form

$$\phi = e^{j\omega t} e^{j\beta z} \quad (2.62)$$

⁴Really it makes more sense to think of this as a cuton frequency since the waves can propagate as we increase the frequency. However, the literature refers to this as a cutoff so this convention has been chosen.

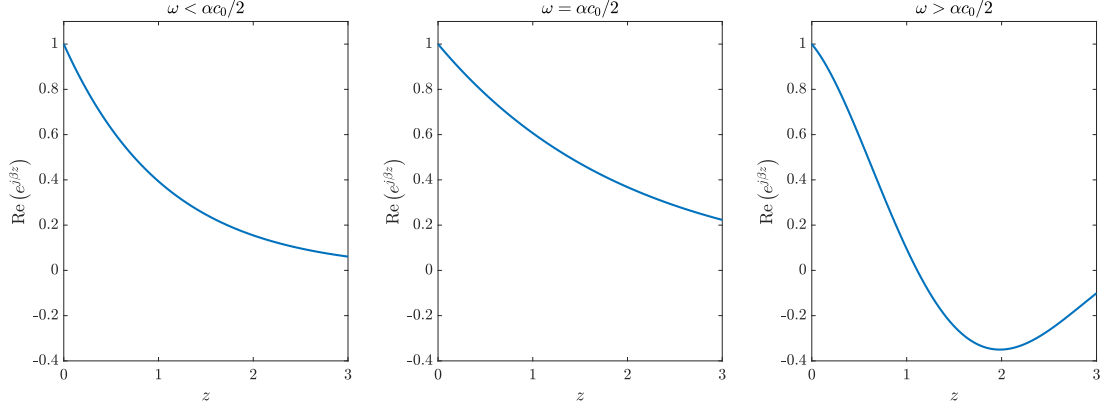


Figure 2.5: Plots of the real part of the spatial solution to the horn equation, $\text{Re}(e^{j\beta z})$ at different frequencies. Left: ω is less than the cutoff frequency goes to zero. Middle: ω is at the cutoff frequency and the solution still goes to zero but less severely. Right: ω is above cutoff frequency and waves can propagate.

the alternate form of the horn equation becomes

$$-\frac{\omega^2}{c_0^2} + \beta^2 + \frac{\alpha^2}{4} = 0 \quad (2.63)$$

Solving for the wavenumber gives

$$\beta = \pm \frac{1}{2} \sqrt{4 \frac{\omega^2}{c_0^2} - \alpha^2} \quad (2.64)$$

The wave number in this case is the same as that of the square root term in the untransformed system. The cutoff behaviour is still present but because the transformed variable has been scaled by the cross section, there is no frequency independent imaginary part. The behaviour is recovered when transforming back to the original variable, but the mathematics has been simplified somewhat in this case.

2.3.2 Energy analysis

Energy analysis can be performed on the horn equation, with a general bore profile, to show that it is well behaved. Considering first the infinite domain $z \in \mathbb{R}$ and taking the inner product of the first of (2.49) with p gives

$$\frac{1}{\rho_0 c_0^2} \langle p, S \partial_t p \rangle_{\mathbb{R}} + \langle p, \partial_z (S v) \rangle_{\mathbb{R}} = 0 \quad (2.65)$$

Following the same procedure as in Sec. 2.2.2 results in

$$\frac{d\mathcal{H}_{he}}{dt} = 0 \quad (2.66)$$

where \mathcal{H}_{he} is the energy in the acoustic tube given by

$$\mathcal{H}_{he} = \frac{1}{2\rho_0 c_0^2} \|\sqrt{S}p\|_{\mathbb{R}}^2 + \frac{\rho_0}{2} \|\sqrt{S}v\|_{\mathbb{R}}^2 \quad (2.67)$$

This describes a lossless system so that

$$\mathcal{H}_{he}(t) = \mathcal{H}_{he}(0) \geq 0, \quad t \in \mathbb{R}^+ \quad (2.68)$$

A similar expression can be found using the velocity potential and the scaled velocity potential

$$\mathcal{H}_{he} = \frac{\rho_0}{2c_0^2} \|\sqrt{S}\partial_t\psi\|_{\mathbb{R}}^2 + \frac{\rho_0}{2} \|\sqrt{S}\partial_z\psi\|_{\mathbb{R}}^2 \quad (2.69a)$$

$$\mathcal{H}_{he} = \frac{\rho_0}{2c_0^2} \|\partial_t\phi\|_{\mathbb{R}}^2 + \frac{\rho_0}{2} \|\partial_z\phi\|_{\mathbb{R}}^2 + \frac{\rho_0}{2} \left\| \sqrt{\frac{\partial_{zz}S}{2S} - \left(\frac{\partial_z S}{S}\right)^2} \phi \right\|_{\mathbb{R}}^2 \quad (2.69b)$$

Bounds on the solution

Once again, it is clear that the energy of the system is a non-negative, real constant and the solutions to the system are bounded by the equation

$$\|\sqrt{S}p\|_{\mathbb{R}}^2 + \rho_0^2 c_0^2 \|\sqrt{S}v\|_{\mathbb{R}}^2 = 2\rho_0 c_0^2 \mathcal{H}_{he}(0) \quad (2.70)$$

which, as in the case of the wave equation, describes an ellipse in the phase space. At any given time, the solution must lie on the level curve given by (2.70). This implies that

$$\|\sqrt{S}p\|_{\mathbb{R}} \leq c_0 \sqrt{2\rho_0 \mathcal{H}_{he}(0)}, \quad \|\sqrt{S}v\|_{\mathbb{R}} \leq \sqrt{\frac{2\mathcal{H}_{he}(0)}{\rho_0}} \quad (2.71)$$

Whereas dispersion analysis could only be performed for the case of an exponential horn (or a geometry that allows for constant coefficient) the energy analysis presented here shows that the system is bounded for a general class of bore profiles.

Energy over a finite domain

Now consider the Equations (2.49) over the finite domain $z \in \mathcal{D}$. The energy analysis over this domain changes (2.66) to

$$\frac{d\mathcal{H}_{he}}{dt} + \mathcal{B}_{he} = 0 \quad (2.72)$$

where \mathcal{H}_{he} is now defined over \mathcal{D} and the power gain or lost at the end of the horn is

$$\mathcal{B}_{he} = -pSv|_{z=0} + pSv|_{z=L} \quad (2.73)$$

2.3.3 Modes of the system

In general, it is not possible to give analytic expressions for the modes of system (2.49) except for special cases. Here, we present the modes of an exponential horn with boundary conditions relevant to brass musical instruments: Neumann at $z = 0$ and Dirichlet at $z = L$.

Solutions to (2.49) can be written in terms of the acoustic velocity potential as

$$\psi = e^{j\omega t} e^{-\frac{\alpha}{2}z} (A \sin(\beta_a z) + B \cos(\beta_a z)) \quad (2.74)$$

where the wavenumber has been split into $\beta = -\frac{j\alpha}{2} \pm \beta_a$. This solution is suitable providing the angular frequencies are above cutoff.

For a Neumann condition at $z = 0$, the solutions are of the form

$$\psi = B e^{j\omega t} e^{-\frac{\alpha}{2}z} \left(\frac{\alpha}{2\beta_a} \sin(\beta_a z) + \cos(\beta_a z) \right) \quad (2.75)$$

Setting boundary conditions at $z = L$ constrains the possible values of β_a , and therefore the possible modal frequencies. For a Dirichlet termination this is given by the implicit expression

$$\tan(\beta_a L) = -\frac{2\beta_a}{\alpha} \quad (2.76)$$

For $\alpha = 0$, the expression is the same as for the cylindrical tube⁵. As $\beta_a \rightarrow \infty$, the constraint is also similar to that of the cylinder

$$\beta_{am} L \rightarrow \frac{(2m-1)\pi}{2}, \quad m \in \mathbb{Z}^+, m \rightarrow \infty \quad (2.77)$$

or

$$\omega_m \rightarrow \frac{c_0}{2} \sqrt{\left(\frac{(2m-1)\pi}{L} \right)^2 + \alpha^2} \quad (2.78)$$

Tab. 2.2 shows the angular frequencies of the resonances of a cylindrical tube and exponential horn terminated with these boundary conditions.

Cylinder Resonances [rad · s ⁻¹]	Horn Resonances [rad · s ⁻¹]	Percentage Difference [%]
511	1122	119.77
1532	1864	21.74
2553	2771	8.56
3574	3734	4.50
4595	4721	2.76
5617	5720	1.86
6637	6725	1.34
7658	7735	1.001
8679	8747	0.78
9700	9761	0.63

Table 2.2: Resonance frequencies of 1 m horns of cylindrical and exponential profile, flaring constant being 5 m⁻¹, and percentage difference of horn resonances relative to cylinder resonances. $c_0 = 325 \text{ m} \cdot \text{s}^{-1}$.

Comparison of exponential horn to cylindrical tube

It is clear from the previous section that the exponential horn does behave similarly to a cylindrical tube with the same boundary conditions, producing a distinct sets of resonances. These resonance frequencies exhibit a shift as a function of the flaring parameter α . The shift is more apparent at lower frequencies. At high frequencies, the resonances approach that of a cylinder. This means that the effect of positively flaring the tube walls is to increase the frequency of the lower resonances relative to the higher frequencies and highlights the importance of the instrument bell in its overall tuning.

⁵A useful sanity check when looking at these systems is that they reduce to systems we already know.

2.3.4 Input impedance

As for the modes of the acoustic tube, it is not always possible to write an analytical expression for the input impedance. An analytical expression is available for the input impedance of an exponential horn, which shall be discussed here; other methods for calculating the input impedance will be discussed in the next subsection.

For an exponential horn open at the far end—but using a simple Dirichlet condition, not a radiation condition—the input impedance is

$$Z_{in} = -\frac{j\rho_0\omega}{S_0} \frac{\tan(\beta_a L)}{\beta_a + \frac{\alpha}{2}\tan(\beta_a L)} \quad (2.79)$$

See Fig. 2.6 for the impedance of an exponential horn open at the far end with comparisons to the resonances of a cylinder.

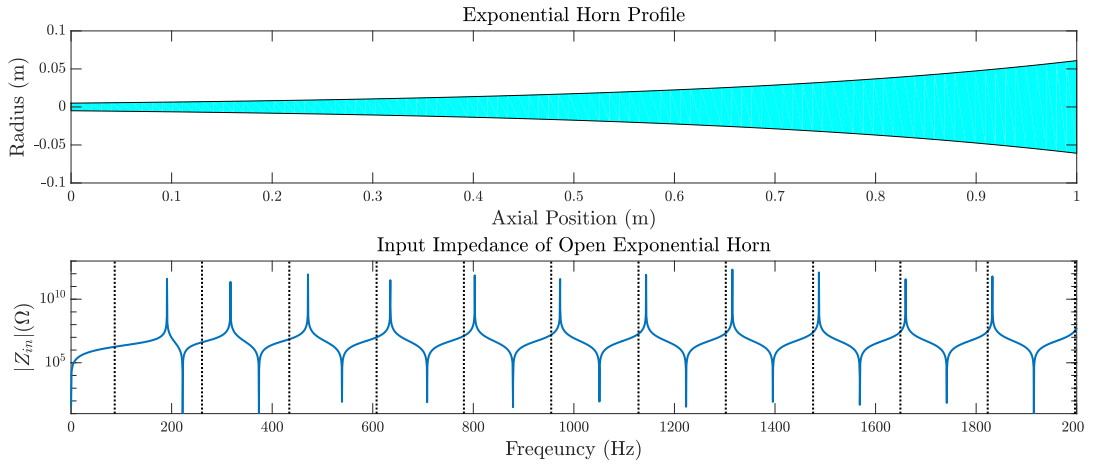


Figure 2.6: Top: Profile of an exponential horn of length 1 m, opening radius $r(0) = 0.005$ m and flare parameter $\alpha = 5 \text{ m}^{-1}$. Bottom: Input impedance for this horn with an open end. $c_0 = 347.23 \text{ m} \cdot \text{s}^{-1}$ and $\rho_0 = 1.1769 \text{ kg} \cdot \text{m}^{-3}$. Dashed vertical lines show the resonances of a cylindrical tube with corresponding boundary conditions.

2.3.5 The Transmission Matrix Method

The Transmission Matrix Method (TMM) can be used to determine a ‘ground truth’ for the calculation of input impedances when no analytical solution exists and is regularly used in predicting impedances of real musical instruments [37, 56]. The TMM is a frequency domain method that approximates the bore profile as a series of concatenated cylindrical or conical tubes. In this work, concatenated cylinders will be used; see Fig. 2.7 for a representation of this approximation.

Here, the TMM will be used as a reference point to test the numerical methods presented in the next chapter. To begin, the first derivative form of the horn equation can be expressed in the frequency domain as

$$SY\hat{p} + \partial_z(S\hat{v}) = 0, \quad Z\hat{v} + \partial_z\hat{p} = 0 \quad (2.80)$$

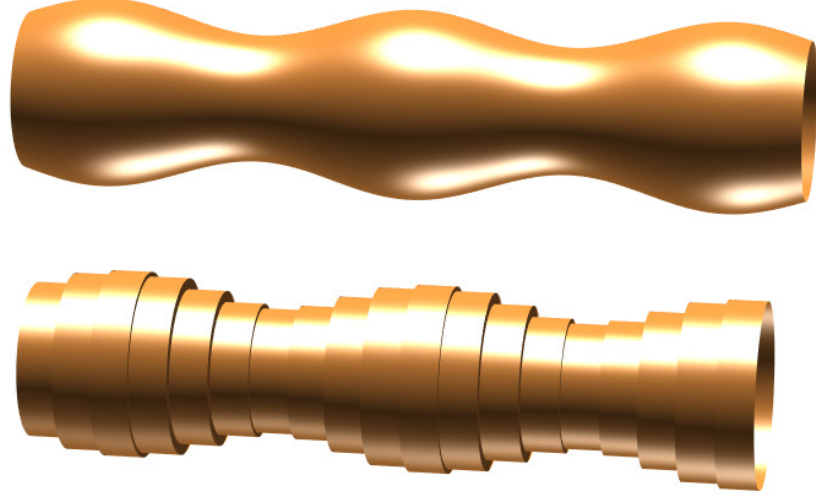


Figure 2.7: Top: A general acoustic tube. Bottom: An approximation of an acoustic tube using a series of concatenated cylinders.

where $\hat{p}(\omega, z)$ and $\hat{v}(\omega, z)$ are the Fourier transforms of the acoustic pressure and particle velocity. For a lossless acoustic tube

$$Y = Y_0(\omega) = \frac{j\omega}{\rho_0 c_0^2}, \quad Z = Z_0(\omega) = \rho_0 j\omega \quad (2.81)$$

are the lossless shunt admittance and series impedance⁶ of the system—these expressions will later be modified to include losses in Sec. 2.4.

The bore profile is then approximated by a series of cylinders of length ΔL . Each cylinder has a corresponding surface area S_l , where $l \in \mathbb{Z}^+$ is used to index the position of the cylinder, and pressure and velocity at the opening of the cylinder, \hat{p}_l and \hat{v}_l ; see Fig. 2.8. In general, the series impedance, Z_l , and shunt admittance, Y_l , will be different in each cylinder. The transmission matrix is then used to show the relationship between the pressure and velocity at both ends of the cylindrical section

$$\begin{bmatrix} \hat{p}_l \\ \hat{v}_l \end{bmatrix} = \underbrace{\begin{bmatrix} \cosh(\Gamma_l \Delta L) & Z_{cl} \sinh(\Gamma_l \Delta L) \\ \frac{1}{Z_{cl}} \sinh(\Gamma_l \Delta L) & \cosh(\Gamma_l \Delta L) \end{bmatrix}}_{\mathbf{T}_l} \begin{bmatrix} \hat{p}_{l+1} \\ \hat{v}_{l+1} \end{bmatrix} \quad (2.82)$$

where $\Gamma_l = (Z_l Y_l)^{0.5}$ is the propagation constant⁷, and $Z_{cl} = \frac{1}{S_l} (Z_l / Y_l)^{0.5}$ is the characteristic impedance.

The pressure and velocity at the input of the tube can then be related to those at the end of the tube by

$$\begin{bmatrix} \hat{p}_0 \\ \hat{v}_0 \end{bmatrix} = \mathbf{T} \begin{bmatrix} \hat{p}_N \\ \hat{v}_N \end{bmatrix} \quad (2.83)$$

⁶Not to be confused with the input impedance.

⁷Although not technically a constant as it depends on frequency and tube radius, both of which vary, this terminology has been left so as to fit with the literature. This is also the same as the spatial wavenumber β but again has been left in this form to match the literature in the TMM.

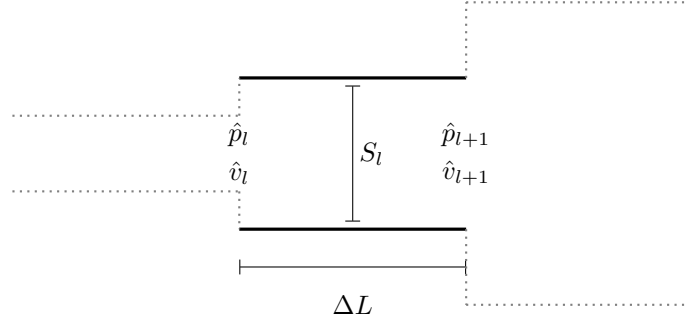


Figure 2.8: Schematic of an element in the TMM.

where

$$\mathbf{T} = \prod_{l=0}^N \mathbf{T}_l \quad (2.84)$$

is the transmission matrix of the system. For a given radiation impedance, $Z_r = \hat{p}_N / S_N \hat{v}_N$, the output pressure and velocity can be written as

$$\begin{bmatrix} \hat{p}_N \\ \hat{v}_N \end{bmatrix} = \begin{bmatrix} S_N Z_r \\ 1 \end{bmatrix} \hat{v}_N \quad \text{or} \quad \begin{bmatrix} 1 \\ 1/S_N Z_r \end{bmatrix} \hat{p}_N \quad (2.85)$$

so that the input variables are both proportional to either \hat{p}_N or \hat{v}_N . The following algorithm can then be implemented to calculate an input impedance for the system:

- Discretize the cross-sectional area into $N = L/\Delta L$ cylindrical elements
- For a given frequency calculate \mathbf{T}
- Take the product of \mathbf{T} with (2.85)⁸ to give

$$\begin{bmatrix} \hat{p}_0 \\ \hat{v}_0 \end{bmatrix} = \mathbf{T} \begin{bmatrix} S_N Z_r \\ 1 \end{bmatrix} \hat{v}_N \implies \begin{bmatrix} \hat{p}_0/\hat{v}_N \\ \hat{v}_0/\hat{v}_N \end{bmatrix} = \mathbf{T} \begin{bmatrix} Z_r \\ 1 \end{bmatrix} \quad (2.86)$$

- Calculate the input impedance at that frequency from

$$Z_{in} = \frac{\hat{p}_0/\hat{v}_N}{S_0 \hat{v}_0/\hat{v}_N} \quad (2.87)$$

- Repeat for other frequencies

Tab. 2.3 shows the resonances for an exponential horn open at one end calculated using the modal frequencies (2.76) and by finding the maxima of the absolute value of the input impedance peaks calculated using the TMM with two values of ΔL . It shows that for a sufficiently fine resolution, the TMM is a good method for solving the equations. However, this leads to long computation times that make the method unsuitable for synthesis purposes. It is also not possible to incorporate time varying gestures using the TMM as the results refer to the steady state solutions of the system, limiting its applicability as an interesting musical instrument.

⁸For the case of $Z_r = \infty$ then use the second of (2.85).

Exact [rad · s ⁻¹]	TMM $\Delta L = 0.1$ m	TMM $\Delta L = 0.01$ m
1122	1107	1122
1864	1834	1864
2771	2721	2771
3734	3661	3734
4721	4622	4720
5720	5588	5719
6725	6549	6724
7735	7489	7733
8747	8377	8745
9761	9103	9759

Table 2.3: Angular frequencies of resonances of 1 m long exponential horn with flaring constant being 5 m⁻¹ calculated using the exact expression (2.76) and the Transmission Matrix Method with element lengths of 0.1 m and 0.01 m. $c_0 = 325$ m · s⁻¹.

2.4 Viscous and thermal losses

So far, only lossless wave propagation has been considered in this work. In reality, wave propagation in acoustic tubes is far from lossless: effects due to viscosity and heat transfer need to be included in our model. Before extending our acoustic tube model, let us first re-examine the lossless shunt admittance and series impedance of the horn equation. Under transformation in the complex frequency domain, $j\omega \rightarrow s$ these become

$$Y_0(s) = \frac{s}{\rho_0 c_0^2}, \quad Z_0(s) = \rho_0 s \quad (2.88)$$

There are two important properties to note. The first is that when s is real, the admittance and impedance are both real. The second is that for when the real part of s is positive, the real parts of the admittance and impedance are positive. This property is known as *positive realness* and is useful as it is another way of classifying systems as passive; we shall define positive realness in Sec. 2.4.2. As we look to extend our models, we shall look for this property in the functions to ensure that the system is passive.

For musical applications the viscothermal losses are confined to a thin boundary layer along the tube walls rather than in the main volume of air in the tube [115].

Dimensionless viscous and thermal boundary layer thicknesses, respectively, are [63]

$$r_v = r \sqrt{\frac{\rho_0 \omega}{\eta}}, \quad r_t = \nu r \sqrt{\frac{\rho_0 \omega}{\eta}} \quad (2.89)$$

These quantities are given in terms of thermodynamic gas constants including the shear viscosity, η , and Prandtl number, $P_r = \nu^2$. See Tab. 2.4 for a list of thermodynamic constants and associated values. In this work, thermodynamic constants will be defined at a temperature $T = 26.85$ °C.

2.4.1 The Zwikker and Kosten model

A model that will be at the focus of this work is the one proposed by Zwikker and Kosten [182], although the form presented by Benade [13] will be used here. The Zwikker and Kosten model treats the viscous and thermal effects separately, putting the viscous effects into a

Name	Symbol	Definition
Speed of sound	c_0	$3.4723 \times 10^2 (1 + 0.00166\Delta T) \text{ m} \cdot \text{s}^{-1}$
Air density	ρ_0	$1.1769 (1 - 0.00335\Delta T) \text{ kg} \cdot \text{m}^{-3}$
Shear viscosity	η	$1.846 \times (1 + 0.0025\Delta T) \text{ kg} \cdot \text{s}^{-1} \cdot \text{m}^{-1}$
Root of Prandtl number	ν	$0.8410 (1 - 0.0002\Delta T)$
Ratio of specific heats	γ	$1.4017 (1 - 0.00002\Delta T)$

Table 2.4: List of thermodynamic constants and their calculation as a function of ΔT which is the temperature deviation from 26.85 °C. Originally presented by Benade [13] and reprinted by Keefe [94]

series impedance and the thermal effects into a shunt admittance. Recalling the first derivative form of the horn equation over the domain $z \in \mathcal{D}$ to give the frequency response of the pressure and particle velocity in a tube

$$SY\hat{p} + \partial_z(S\hat{v}) = 0, \quad Z\hat{v} + \partial_z\hat{p} = 0 \quad (2.90)$$

the viscous and thermal losses can be incorporated into the system by using

$$Y = \frac{j\omega}{\rho_0 c_0^2} (1 + (\gamma - 1) F_t), \quad Z = \frac{\rho_0 j\omega}{1 - F_v} \quad (2.91)$$

where γ is the ratio of specific heats and

$$F_t = \phi(\sqrt{-j}r_t), \quad F_v = \phi(\sqrt{-j}r_v), \quad \phi(\xi) = \frac{2}{\xi} \frac{J_1(\xi)}{J_0(\xi)} \quad (2.92)$$

The functions J_0 and J_1 are Bessel functions of zeroth and first order.

This model is suitable for cylindrical tubes; see the work of Stinson [154], Stinson and Champoux [155], and Christensen [46] for viscothermal models using different tube cross-section geometries.

2.4.2 Approximations of the model and positive real functions

Despite the Zwikker and Kosten model being a good match for experiments [53], this model is difficult to implement in the time domain due to the lack of representation of the ratio of Bessel functions in F_t and F_v . As a result, approximations must be made for time domain applications.

Approximations of the Zwikker and Kosten model

Multiple approximations in terms of a power series expansion in r_v and r_t exist for the Zwikker and Kosten model. Benade [13] and Keefe⁹ [94] give expansions for large and small values of the boundary layers. Benade approached this by evaluating the impedance and admittance as the frequencies approached zero and infinity, whereas Keefe used truncated power series and asymptotic expansions. Keefe also focused on matching the small and large expressions over a particular transition region, something missing in Benade's original work.

⁹In Keefe's original publication [94] there appears to be an error in the values of G and ωL for the small expansion for the powers of the tube radius. This has been corrected in this work.

Although it is not clear if Benade and Keefe used the same methods, Benade's expressions can be obtained through simplification of those presented by Keefe.

The large term expansions corresponds to a high frequency (or large tube radius) limit and are suitable for most applications in brass instruments. Caussé *et al.* [37] used this argument to come up with their own expression that goes up to the second power of $r_{v,t}$, which is also a truncation of Keefe's large frequency limit¹⁰. Bilbao and Chick [24] presented another form of Keefe and Caussé *et al.*'s models for use in the time domain. Kemp *et al.* [97] used simplified version that neglected the frequency independent loss term in the impedance.

An alternative to approximating impedances and admittances is to approximate the propagation constant Γ . This is how the Webster-Lokshin model [79] is presented, although Benade [13] attributes it to Rayleigh [157]. In this case, the loss is applied to the second derivative form of the wave equation in pressure, leaving the temporal behaviour of the velocity as the lossless momentum conservation equation. This is different to the treatment in the other approximations as the thermal and viscous effects are mixed. Tab. 2.5 shows the expansions of the Zwikker and Kosten impedance and admittance attributed to Benade, Keefe, Caussé *et al.*, and Bilbao and Chick, and Tab. 2.6 shows the propagation constants of these expressions along with the Webster-Lokshin model. From these tables it is clear that the all of the approximations presented can be deduced from Keefe's forms through simplifications—the expressions of Benade, Caussé *et al.*, and Bilbao and Chick are simplified impedances and admittances and Webster-Lokshin is a simplified propagation constant.

Model	$r_v, r_t \ll 1$	$r_v, r_t \gg 1$
Zwikker & Kosten	$Z = \frac{\rho_0 j \omega}{1 - F_v}$ $Y = \frac{j \omega}{\rho_0 c_0^2} (1 + (\gamma - 1) F_t)$	
Benade	$Z = \rho_0 j \omega \left(\frac{4}{3} - \frac{8j}{r_v^2} \right)$ $Y = \frac{j \omega}{\rho_0 c_0^2} \left(\gamma - (\gamma - 1) \frac{j r_t^2}{8} \right)$	$Z = \rho_0 j \omega \left(1 - \frac{2j^{3/2}}{r_v} \right)$ $Y = \frac{j \omega}{\rho_0 c_0^2} \left(1 - (\gamma - 1) \frac{2j^{3/2}}{r_t} \right)$
Keefe	$Z = \rho_0 j \omega \left(\frac{4}{3} - \frac{8j}{r_v^2} \right)$ $Y = \frac{j \omega}{\rho_0 c_0^2} \left[\gamma - (\gamma - 1) \frac{j r_t^2}{8} \left(1 - \frac{13 r_t^4}{384} \right) \right]$	$Z = \rho_0 j \omega \left(1 - \frac{2j^{3/2}}{r_v} - \frac{3j}{r_v^2} - (4 + 15j) \frac{\sqrt{2}}{8 r_v^3} \right)$ $Y = \frac{j \omega}{\rho_0 c_0^2} \left(1 - (\gamma - 1) \left(\frac{2j^{3/2}}{r_t} - \frac{j}{r_t^2} - \frac{j^{1/2}}{4 r_t^3} \right) \right)$
Caussé <i>et al.</i>	Not provided	$Z = \rho_0 j \omega \left(1 - \frac{2j^{3/2}}{r_v} - \frac{3j}{r_v^2} \right)$ $Y = \frac{j \omega}{\rho_0 c_0^2} \left(1 - (\gamma - 1) \left(\frac{2j^{3/2}}{r_t} - \frac{j}{r_t^2} \right) \right)$
Bilbao and Chick	Not provided	$Z = \rho_0 j \omega \left(1 - \frac{2j^{3/2}}{r_v} - \frac{3j}{r_v^2} \right)$ $Y = \frac{j \omega}{\rho_0 c_0^2} \left(1 - (\gamma - 1) \frac{2j^{3/2}}{r_t} \right)$

Table 2.5: Frequency domain impedance and admittances that include viscous and thermal losses in acoustic tubes

The exact form of $\Gamma = \sqrt{ZY}$ for the Zwikker and Kosten model is shown in Fig. 2.9 along with the associated errors of the expansions in Tab. 2.6. Note that the small and large expansions have been joined in these plots and that the Caussé *et al.*, Bilbao and Chick, and Webster-Lokshin models have been plotted in the small boundary layer region, despite being defined in the large limit. All models tend toward the Zwikker and Kosten model at high frequencies but only the expressions of Benade and Keefe match at low frequencies (since the

¹⁰There is also a typographical error in Caussé *et al.*'s original paper which has been corrected here: in the expression for Z , there should be a $\sqrt{2}$ not a 2.

Propagation Constant
Zwikker & Kosten $\forall r_v, r_t$ $\Gamma = \frac{j\omega}{c_0} \left(\frac{1 + (\gamma - 1)F_t}{1 - F_v} \right)^{1/2}$
Benade $r_v, r_t \ll 1$ $\Gamma = \frac{j\omega}{c_0} \left(\gamma \frac{4}{3} - (\gamma - 1)\nu^2 - j \left(\gamma \frac{8}{r_v^2} + (\gamma - 1) \frac{r_t^2}{6} \right) \right)^{1/2}$ $r_v, r_t \gg 1$ $\Gamma = \frac{j\omega}{c_0} \left(1 - 2j^{3/2} \left(\frac{1}{r_v} + \frac{\gamma - 1}{r_t} \right) - (\gamma - 1) \frac{4j}{r_v r_t} \right)^{1/2}$
Keefe $r_v, r_t \ll 1$ $\Gamma = \frac{j\omega}{c_0} \left(\gamma \frac{4}{3} - (\gamma - 1)\nu^2 \left(1 - \frac{13r_t^4}{48} \right) - j \left(\gamma \frac{8}{r_v^2} + (\gamma - 1) \frac{r_t^2}{6} - \frac{13r_t^6}{2304} \right) \right)^{1/2}$ $r_v, r_t \gg 1$ $\Gamma = \frac{j\omega}{c_0} \left(1 - 2j^{3/2} \left(\frac{1}{r_v} + \frac{\gamma - 1}{r_t} \right) - j \left(\frac{3}{r_v^2} - (\gamma - 1) \left(\frac{1}{r_t^2} - \frac{4}{r_v r_t} \right) \right) \right. \\ - \frac{\sqrt{2}(4 + 15j)}{8r_v^3} + (\gamma - 1)j^{1/2} \left(\frac{2}{r_v r_t^2} - \frac{6}{r_v^2 r_t} + \frac{1}{4r_t^3} \right) \\ + (\gamma - 1) \left(\frac{1}{2r_v r_t^3} + \frac{3}{r_v^2 r_t^2} + \frac{\sqrt{2}(4j^{3/2} - 15j^{1/2})}{4r_v^3 r_t} \right) \\ \left. - (\gamma - 1) \left(\frac{3j^{3/2}}{4r_v^2 r_t^3} + \frac{\sqrt{2}(4j - 15)}{8r_v^3 r_t^2} - \frac{\sqrt{2}(4j^{1/2} + 15j^{3/2})}{32r_v^3 r_t^3} \right) \right)^{1/2}$
Caussé <i>et al.</i> $r_v, r_t \gg 1$ $\Gamma = \frac{j\omega}{c_0} \left(1 - 2j^{3/2} \left(\frac{1}{r_v} + \frac{\gamma - 1}{r_t} \right) - j \left(\frac{3}{r_v^2} - (\gamma - 1) \left(\frac{1}{r_t^2} - \frac{4}{r_v r_t} \right) \right) \right. \\ \left. + (\gamma - 1)j^{1/2} \left(\frac{2}{r_v r_t^2} - \frac{6}{r_t r_v^2} \right) - (\gamma - 1) \frac{3}{r_v^2 r_t^2} \right)^{1/2}$
Bilbao and Chick $r_v, r_t \gg 1$ $\Gamma = \frac{j\omega}{c_0} \left(1 - 2j^{3/2} \left(\frac{1}{r_v} + \frac{\gamma - 1}{r_t} \right) - j \left(\frac{3}{r_v^2} + \frac{4(\gamma - 1)}{r_v r_t} \right) - \frac{j^{1/2} 6(\gamma - 1)}{r_v^2 r_t} \right)^{1/2}$
Webster-Lokshin $r_v, r_t \gg 1$ $\Gamma = \frac{j\omega}{c_0} \left(1 - 2j^{3/2} \left(\frac{1}{r_v} + \frac{\gamma - 1}{r_t} \right) \right)^{1/2}$

Table 2.6: Propagation constants that include viscous and thermal losses in acoustic tubes.

other three models do not have low frequency forms). The real part of Γ is best approximated by Keefe but this is not the case for the imaginary part, with the models of Benade, Caussé *et al.* and Bilbao and Chick having a smaller error around the transition region. However, the discontinuity at the transition is smaller for Keefe than for Benade which is a feature of Keefe's model.

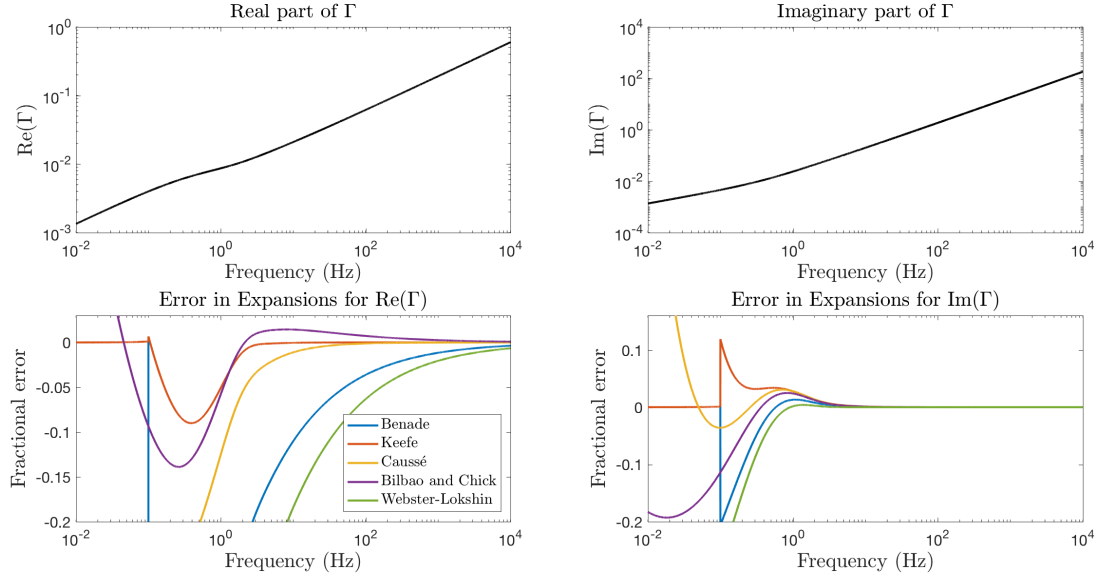


Figure 2.9: Top: Real (left) and imaginary (right) parts of Γ calculated using the Zwikker and Kosten Model for a tube of radius 0.005 m. Bottom: Fractional error of the real and imaginary parts of Γ from the expansions given by Benade (blue), Keefe (red), Caussé *et al.* (yellow), Bilbao and Chick (purple) and Webster-Lokshin (green). Note that the small and large expansions have been connected around $r_v = 1$ and $r_t = \nu$.

In all of the approximations above, fractional powers of $j\omega$ are present. This creates some nontrivial problems from a time domain modelling perspective; upon transforming from the frequency domain to the time domain, these operators become fractional derivatives with respect to time that require their own discrete approximation [41, 42, 171]. Hélié and Matignon [81], Mignot *et al.* [118] and Lombard and Mercier [106], to name a few, have presented methods to approximate fractional derivatives with applications to acoustic tubes; see Chap. 3 for a method applied in finite-difference schemes.

Positive real functions

So far, the loss model has only been discussed in the frequency domain yet we intend to construct a time domain system. The expansions provided can be transformed to the time domain but we cannot, at first, know if this will result in a passive system. It is therefore of use to introduce the concept of a positive real function.

A complex function $f(s)$ is defined as positive real if [165, 174]

$$\operatorname{Re}(f(s)) \geq 0 \quad \text{if} \quad \operatorname{Re}(s) \geq 0$$

$$f \text{ is real when } \operatorname{Im}(s) = 0$$

The importance of this classification is that if $f(s)$ is positive real, then it can be realised by a passive one-port structure meaning that, from a simulation perspective, the energy of the modelled system will not grow beyond the amount of energy that is supplied to it.

Some useful properties of positive real functions are:

1. The poles and zeros of the function lie in the left hand half of the complex plane.
2. If $f(s)$ is positive real then $(1/f(s))$ is positive real—this applies to admittance realisations.
3. The sum of two positive real functions is positive real—we can make a large positive real structure from smaller positive real elements.

In their current form, the large r models of Keefe and Caussé *et al.* are not positive real—at low frequencies the admittance approaches a negative value. The Benade, Bilbao and Chick, and the Webster-Lokshin models are positive real and can therefore be realised in the time-domain. We chose the model of Bilbao and Chick for this work as it offers the greatest accuracy to the original Zwikker and Kosten model of the suitable expansions. Transforming the Bilbao and Chick model to the time domain gives

$$\frac{S}{\rho_0 c_0^2} \partial_t p + \partial_z (Sv) + q \partial_t^{1/2} p = 0 \quad (2.94a)$$

$$\rho_0 \partial_t v + \partial_z p + fv + g \partial_t^{1/2} v = 0 \quad (2.94b)$$

where

$$f = 3 \frac{\eta \pi}{S}, \quad g = 2 \sqrt{\frac{\rho_0 \eta \pi}{S}}, \quad q = \frac{2(\gamma - 1)}{\nu c_0^2} \sqrt{\eta \pi \frac{S}{\rho_0^3}} \quad (2.95)$$

2.4.3 Circuit representation of the Zwikker and Kosten model

Although the power series expansions produce usable expressions to approximate the Zwikker and Kosten model, they are not guaranteed to be passive when modelled in the time domain. Instead, we can draw on work from electrical network theory to construct equivalent circuits; see App. A for an introduction to the concepts used here. We have already discussed that if an impedance or admittance can be classified as a positive real function, then the process it describes is passive. Network synthesis investigates how such a passive impedance can be described through connections of smaller, passive elements—the fundamental elements being the capacitor, inductor, and resistor.

Analysing the model of Zwikker and Kosten in the complex plane shows that the poles and zeros are interlaced on the negative real axis; see Fig. 2.10.

This particular arrangement of poles and zeros means that the function can be described by structures containing only two types of elements, either RC (resistor and capacitor) or RL (resistor and inductor) [165].

2.4.4 Cauer and Foster forms of RL and RC circuits

Two element structures are of particular use as they allow for simple canonical realisations of an impedance or admittance. Two particular types of circuit will be considered here: Cauer

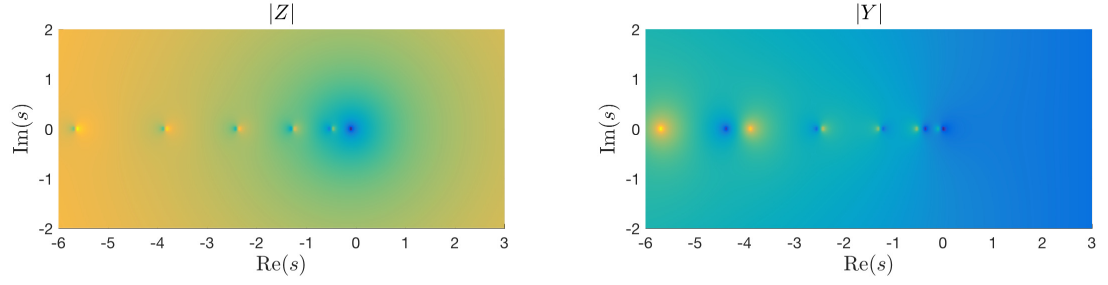


Figure 2.10: Left: Magnitude of Z in the complex plane. Right: Magnitude of Y in the complex plane. Poles are bright yellow and zeros are green/blue. Note that surfaces have been plotted using a logarithmic plot to accentuate the poles and zeros. A tube of radius 0.03 m has been used to highlight the poles and zeros in a reasonable range.

and Foster. Canonical realisations also exist for general impedances but the realisations are not simple, e.g., Brune synthesis[165, 174].

Cauer form

The Cauer forms are derived from a continued fraction expansion of the impedance or admittance that is to be approximated. If the expansion is around infinity, the first Cauer form is used; if the expansion is around zero, the second Cauer form is used. Fig. 2.11 shows the first form for an RL circuit and the second form for an RC circuit. Note that for admittances, the conductivity $G = 1/R$ is used to describe the behaviour of the resistor.

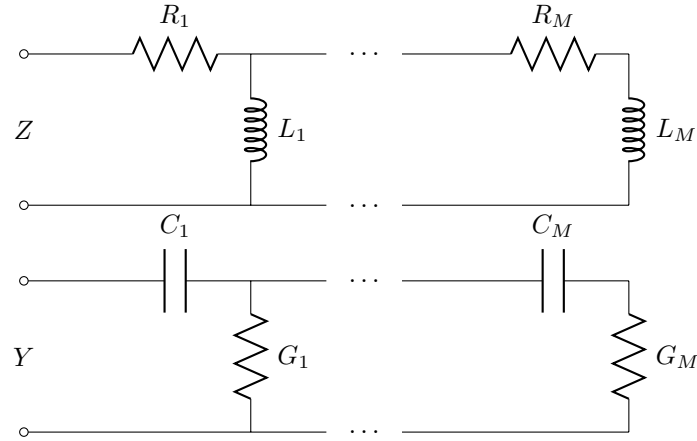


Figure 2.11: Top: First form of Cauer RL circuit. Bottom: Second form of Cauer RC circuit.

The impedance of the first form RL circuit is given by the continued fraction expansion

$$Z = R_1 + \frac{1}{\frac{1}{L_1 j\omega} + \dots \frac{1}{R_M + \frac{1}{L_M j\omega}}} \quad (2.96)$$

The admittance of the RC circuit is given by

$$Y = \frac{1}{\frac{1}{C_1 j\omega} + \frac{1}{G_1 + \frac{1}{\frac{1}{C_M j\omega} + \frac{1}{G_M}}}} \quad (2.97)$$

Foster form

Another type of RL and RC circuit are the first and second Foster forms. The first form consists of a series connection of parallel elements; the second form is the reverse, parallel connection of series elements. The first and second Foster forms are illustrated in Fig. 2.12.

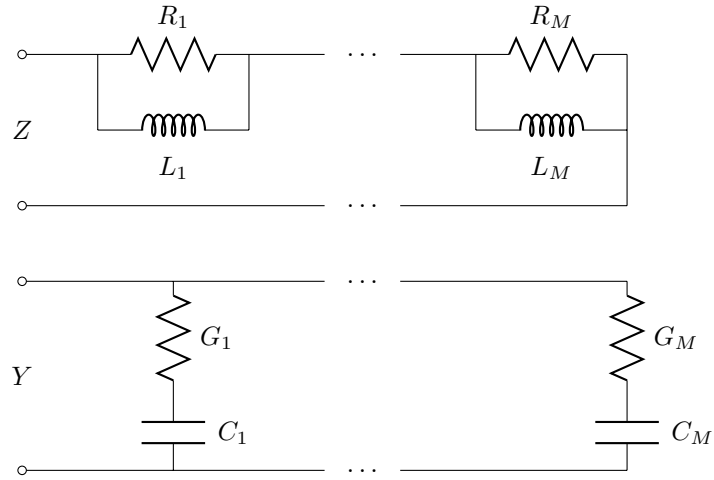


Figure 2.12: Top: First form of Foster RL structure. Bottom: Second form of Foster RC . Both structures have M branches.

The impedances of the q^{th} branches of the first form are

$$Z_q = \frac{R_q L_q j\omega}{R_q + L_q j\omega} \quad (2.98)$$

The admittances of the q^{th} branches in the second form are

$$Y_q = \frac{G_q C_q j\omega}{G_q + C_q j\omega} \quad (2.99)$$

For structures constructed entirely of either first or second Foster forms with M branches, it is easy to obtain the total impedance and admittance, respectively, as

$$Z = \sum_{q=1}^M \frac{R_q L_q j\omega}{R_q + L_q j\omega} \quad (2.100a)$$

$$Y = \sum_{q=1}^M \frac{G_q C_q j\omega}{G_q + C_q j\omega} \quad (2.100b)$$

This kind of structure is of particular use when using optimisation procedures to find appropriate element values in the final expression for the immittance, as each branch is independent of the others, minimising the amount of mathematics required.

Providing all of the circuit elements have positive values, the total impedance and admittance of these structures will be positive real. This means that these structures are suitable for modelling physical, passive mechanisms such as viscous and thermal losses in acoustic tubes.

2.4.5 Cauer structure representation of loss model

Thompson *et al.* [162] use Cauer structures to model viscous and thermal losses in acoustic tubes¹¹. First the impedance and admittance are written as

$$Z = \rho_0 j\omega - \rho_0 j\omega \frac{1}{1 - \left(\frac{2J_1(\sqrt{-j}r_v)}{\sqrt{-j}r_v J_0(\sqrt{-j}r_v)} \right)^{-1}} \quad (2.101a)$$

$$Y = \frac{j\omega}{\rho_0 c_0^2} + \frac{j\omega(\gamma - 1)}{\rho_0 c_0^2} \frac{2J_1(\sqrt{-j}r_t)}{\sqrt{-j}r_t J_0(\sqrt{-j}r_t)} \quad (2.101b)$$

and continued fraction expansions (CFE) are used on the second term in each expression to give

$$Z = L_0 j\omega + R_1 + \frac{1}{\frac{1}{L_1 j\omega} + \ddots \frac{1}{R_M + \frac{1}{\frac{1}{L_M j\omega}}}} \quad (2.102a)$$

$$Y = C_0 j\omega + \frac{1}{\frac{1}{C_1 j\omega} + \frac{1}{G_1 + \ddots \frac{1}{\frac{1}{C_M j\omega} + \frac{1}{G_M}}}} \quad (2.102b)$$

where

$$R_q = qR_\nu, \quad L_q = \frac{L_0}{2q+1}, \quad q = 1, \dots, M \quad (2.103a)$$

$$G_q = qG_t, \quad C_q = (\gamma - 1) \frac{C_0}{2q-1}, \quad q = 1, \dots, M \quad (2.103b)$$

and $L_0 = \rho_0$, $R_\nu = 8\rho_0\eta/r^2$, $C_0 = 1/\rho_0 c_0^2$, $G_t = 8\eta(\gamma - 1)C_0/(\rho_0 r^2 \nu^2)$. See Fig. 2.13 for the circuit structures.

In principle the model of Thompson *et al.* approximates the model of Zwikker and Kosten to arbitrary accuracy, see Figs. 2.14 and 2.15. However, it requires many branches for it to be useful over the musical frequency range for a given radius—at least 16 branches are required for a tube of radius 0.005 m to reach 1% accuracy over the 0 – 1 kHz band.

Looking forward to designing numerical schemes that include attenuation processes, it is

¹¹In Thompson *et al.*'s original paper, the surface area is included in the expressions. Here it has been factorised.

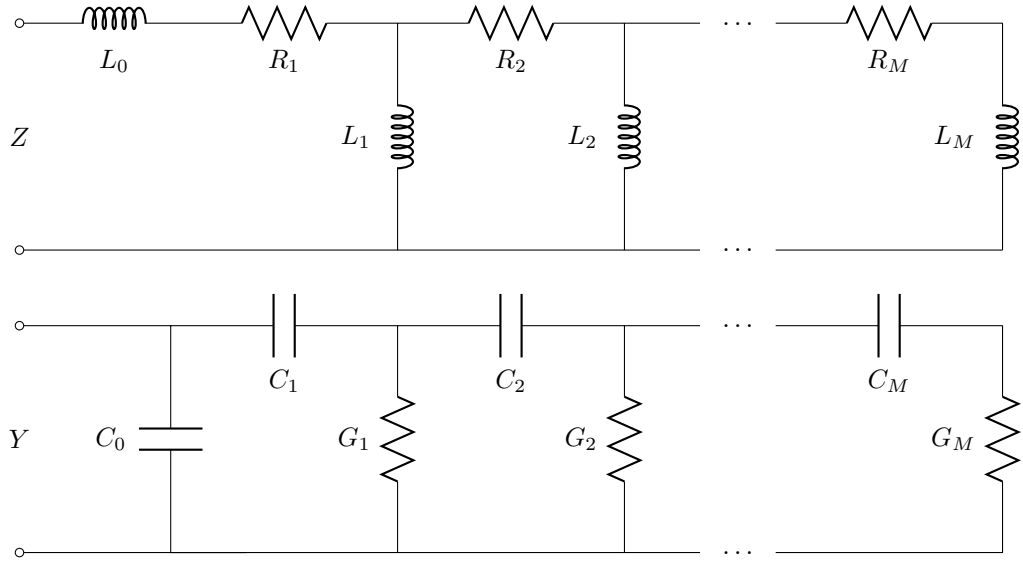


Figure 2.13: Cauer structures. Top: Impedance structure. Bottom: Admittance structure.

clear that the Cauer structure is not particularly suited for efficient implementation, see Chap. 3. Optimisation procedures could be applied for accuracy over a wide frequency range, however, the nature of the CFE makes it challenging to implement. Instead, the Foster structure, discussed in the next section, will be applied as it is amenable to this kind of application.

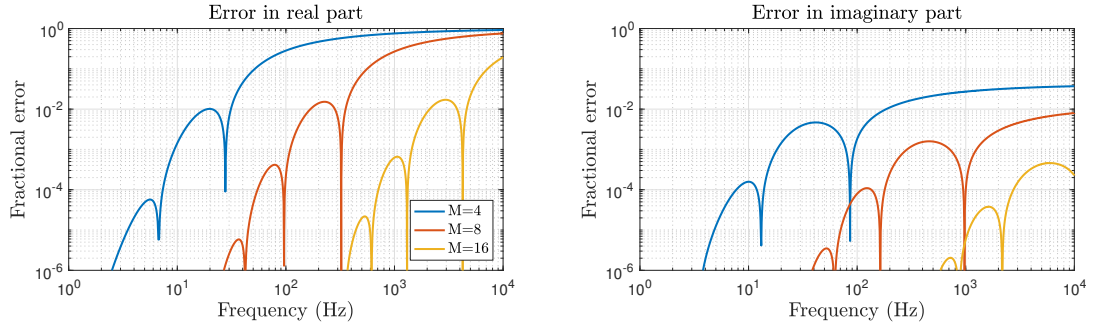


Figure 2.14: Fractional error of impedance calculated using the Cauer structure for a tube of radius 0.005 m. Left: Error in real part of impedance. Right: Error in imaginary part of impedance.

2.4.6 Foster structure representation of loss model

To use the Foster structure, see [26, 27], the functions Z and Y of the Zwikker and Kosten model can be separated into lossless and lossy parts

$$Z = Z_0 + Z_v, \quad Y = Y_0 + Y_t \quad (2.104)$$

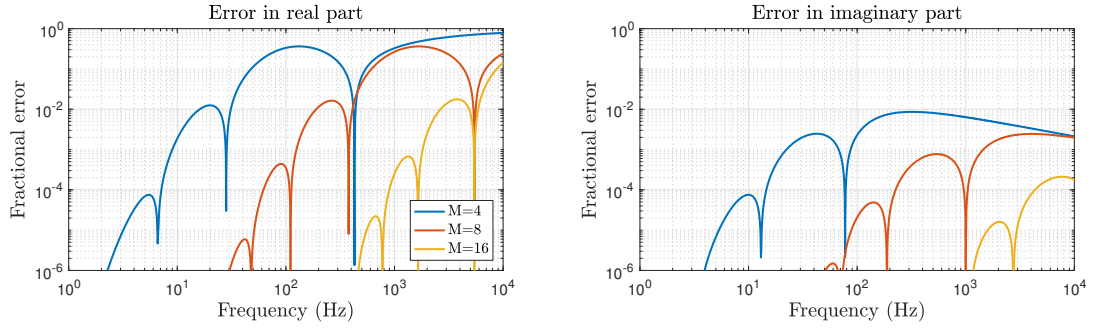


Figure 2.15: Fractional error of admittance calculated using the Cauer structure for a tube of radius 0.005 m. Left: Error in real part of admittance. Right: Error in imaginary part of admittance.

where the lossless propagation parts, Z_0 and Y_0 , are the same as (2.81) and the lossy parts are

$$Z_v = j\omega\rho_0 \frac{F_v}{1 - F_v}, \quad Y_t = \frac{j\omega}{\rho_0 c_0^2} (\gamma - 1) F_t \quad (2.105)$$

Fig. 2.16 shows the absolute value Z_v and Y_t in the complex plane. This again shows interlaced poles and zeros. For numerical reasons it is important to treat the lossless and lossy parts separately, this will become clear in the next chapter.

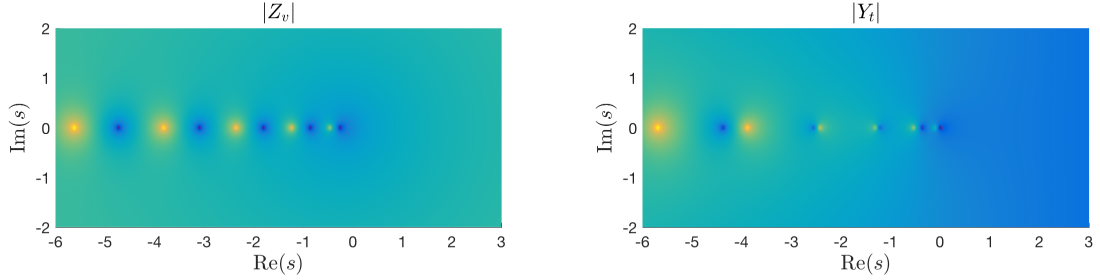


Figure 2.16: Left: Magnitude of Z_v in the complex plane. Right: Magnitude of Y_t in the complex plane. Poles are yellow and zeros are dark blue. Note that surfaces have been plotted using a logarithmic plot to accentuate the poles and zeros. The tube radius is 0.03 m

We can modify the admittance of this model by removing an equivalent capacitor of capacitance $\hat{C} = (\gamma - 1)/\rho_0 c_0^2$ leaving the modified admittance

$$\hat{Y}_t = j\omega\hat{C} \frac{F_t}{1 - F_t} \quad (2.106)$$

It is clear that Z_v and \hat{Y}_t are of the same form, and therefore element values for one of the immittances can be reused for the other after applying some scaling. Whereas the Cauer structure in the previous section is a direct expansion of the model of Zwikker and Kosten, a Foster structure can be used in an optimisation procedure to calculate element values that fit to the impedances of Zwikker and Kosten curves. The approximations to these immittances

are

$$Z_v^M = R_0 + \sum_{q=1}^M \frac{R_q L_q j\omega}{R_q + L_q j\omega} \quad (2.107a)$$

$$\hat{Y}_t^M = G_0 + \sum_{q=1}^M \frac{G_q C_q j\omega}{G_q + C_q j\omega} \quad (2.107b)$$

The structures representing Z_v and Y_t using the Foster form are presented in Fig. 2.17.

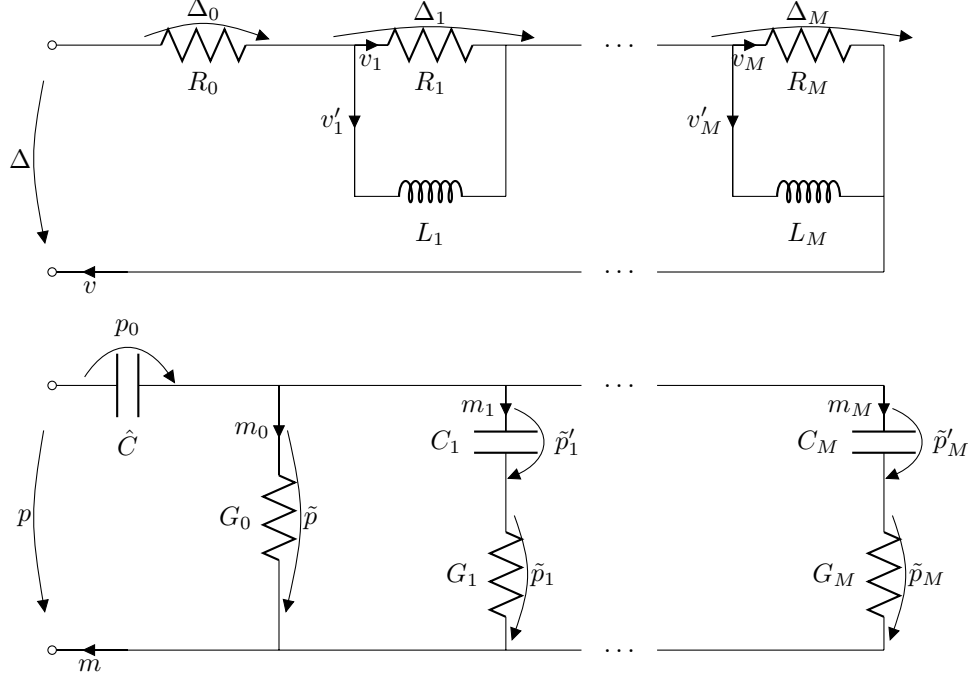


Figure 2.17: Top: Z_v Foster structure. Bottom: Y_t Foster structure.

2.4.7 Time domain system of the Foster structure

The Foster structure can be incorporated into the acoustic tube equations by using the following PDE system

$$\frac{S}{\rho_0 c_0^2} \partial_t p + \partial_z (Sv) + Sm = 0 \quad (2.108a)$$

$$\rho_0 \partial_t v + \partial_z p + \Delta = 0 \quad (2.108b)$$

where m is the current going into the RC circuit for Y_t and Δ is the voltage over the RL circuit. Using Kirchoff's current laws, the following relations for these values are

$$p = p_0 + \tilde{p}, \quad m = \sum_{q=0}^M m_q, \quad \tilde{p} = \tilde{p}_q + \tilde{p}'_q, \quad q = 1, \dots, M \quad (2.109a)$$

$$m = \hat{C} \partial_t p_0, \quad m_0 = G_0 \tilde{p}, \quad m_q = G_q \tilde{p}_q = C_q \partial_t \tilde{p}'_q, \quad q = 1, \dots, M \quad (2.109b)$$

$$\Delta = \sum_{q=0}^M \Delta_q, \quad v = v_q + v'_q, \quad q = 1, \dots, M \quad (2.110a)$$

$$\Delta_0 = R_0 v, \quad \Delta_q = R_q v_q = L_q \partial_t v'_q, \quad q = 1, \dots, M \quad (2.110b)$$

where $p_0, \tilde{p}, \tilde{p}_q, \tilde{p}'_q$ and Δ_q are interpreted as partial voltages over the circuit elements and m_q, v_q and v'_q are interpreted as partial currents from each node.

2.4.8 Energy analysis of Foster structure

Foster structures correspond to positive real impedances and admittances and are therefore passive systems. We can also show this in the time domain using energy methods.

Taking the inner product of the first of (2.108) with p over the domain \mathcal{D} then employing integration by parts and substituting the second of (2.108) gives

$$\frac{d\mathcal{H}_{he}}{dt} + \mathcal{B}_{he} + \langle Sv, \Delta \rangle_{\mathcal{D}} + \langle p, Sm \rangle_{\mathcal{D}} = 0 \quad (2.111)$$

The final two terms can be approached separately using (2.109) and (2.110). The velocity term becomes

$$\begin{aligned} \langle Sv, \Delta \rangle_{\mathcal{D}} &\stackrel{(2.110a)}{=} \sum_{q=0}^M \langle Sv, \Delta_q \rangle_{\mathcal{D}} \\ &\stackrel{(2.110a)}{=} \langle Sv, \Delta_0 \rangle_{\mathcal{D}} + \sum_{q=1}^M \langle S(v_q + v'_q), \Delta_q \rangle_{\mathcal{D}} \\ &\stackrel{(2.110b)}{=} \langle Sv, R_0 v \rangle_{\mathcal{D}} + \sum_{q=1}^M \langle Sv_q, R_q v_q \rangle_{\mathcal{D}} + \langle Sv'_q, L_q \partial_t v'_q \rangle_{\mathcal{D}} \\ &\stackrel{(2.4)}{=} \frac{d\mathcal{H}_v}{dt} + \mathcal{Q}_v \end{aligned} \quad (2.112)$$

where

$$\mathcal{H}_v = \sum_{q=1}^M \frac{1}{2} \|\sqrt{SL_q} v'_q\|_{\mathcal{D}}^2 \geq 0 \quad (2.113a)$$

$$\mathcal{Q}_v = \|\sqrt{SR_0} v\|_{\mathcal{D}}^2 + \sum_{q=1}^M \|\sqrt{SR_q} v_q\|_{\mathcal{D}}^2 \geq 0 \quad (2.113b)$$

Similarly, the pressure term of the energy analysis becomes

$$\begin{aligned}
\langle p, Sm \rangle_{\mathcal{D}} &\stackrel{(2.109a)}{=} \langle p_0 + \tilde{p}, Sm \rangle_{\mathcal{D}} \\
&\stackrel{(2.109a)}{=} \langle p_0, Sm \rangle_{\mathcal{D}} + \sum_{q=0}^M \langle \tilde{p}, Sm_q \rangle_{\mathcal{D}} \\
&\stackrel{(2.109a)}{=} \langle p_0, Sm \rangle_{\mathcal{D}} + \langle \tilde{p}, Sm_0 \rangle_{\mathcal{D}} + \sum_{q=1}^M \langle \tilde{p}_q + \tilde{p}'_q, Sm_q \rangle_{\mathcal{D}} \\
&\stackrel{(2.109b)}{=} \langle p_0, S\hat{C}\partial_t p_0 \rangle_{\mathcal{D}} + \langle \tilde{p}, SG_0 \tilde{p} \rangle_{\mathcal{D}} + \sum_{q=1}^M \langle \tilde{p}_q, SG_q \tilde{p}_q \rangle_{\mathcal{D}} + \langle \tilde{p}'_q, SC_q \partial_t \tilde{p}'_q \rangle_{\mathcal{D}} \\
&\stackrel{(2.4)}{=} \frac{d\mathcal{H}_t}{dt} + \mathcal{Q}_t
\end{aligned} \tag{2.114}$$

where

$$\mathcal{H}_t = \frac{1}{2} \|\sqrt{S\hat{C}}p_0\|_{\mathcal{D}}^2 + \frac{1}{2} \sum_{q=1}^M \|\sqrt{SC_q}\tilde{p}'_q\|_{\mathcal{D}}^2 \geq 0 \tag{2.115a}$$

$$\mathcal{Q}_t = \|\sqrt{SG_0}\tilde{p}\|_{\mathcal{D}}^2 + \sum_{q=1}^M \|\sqrt{SG_q}\tilde{p}_q\|_{\mathcal{D}}^2 \geq 0 \tag{2.115b}$$

Incorporating these terms into the energy balance gives

$$\frac{d}{dt} (\mathcal{H}_{he} + \mathcal{H}_v + \mathcal{H}_t) + \mathcal{B}_{he} + \mathcal{Q}_v + \mathcal{Q}_t = 0 \tag{2.116}$$

It is clear that the energy and dissipation terms are non-negative and the solutions of the system are therefore bounded.

2.4.9 Numerical optimisation procedures

One approach to setting the circuit elements for the Foster structure would be to determine the location of the poles of the Zwickler and Kosten model numerically and truncate the expression to the first M poles; this is how the Causer structure is applied [162]. However, this method does not provide the most optimal results in every application. Numerical optimisation procedures are then of use to find element values [25].

To guarantee a passive realisation of the structure, the impedance can be rewritten in terms of the free parameters $\mathbf{x} = [a_0, \dots, a_M, b_1, \dots, b_M]^T$

$$Z_v^M(\omega, \mathbf{x}) = e^{a_0} + \sum_{q=1}^M \frac{e^{a_q} j\omega}{e^{b_q} + j\omega}, \quad a_q, b_q \in \mathbb{R} \tag{2.117}$$

so that

$$R_0 = e^{a_0}, \quad R_q = e^{a_q}, \quad L_q = e^{a_q - b_q} \tag{2.118}$$

Use of the exponential function simplifies some of the mathematics used in optimisation procedures¹². It also removes limits on a_q and b_q as the exponential function produces positive real values for any real input.

¹²Online searches describe this reparametrisation as the ‘log trick’, see <https://justindomke.wordpress.com/log-gradient-descent/>, last accessed on 30th January 2017, for a brief description of this.

A cost function $E(\mathbf{x})$ is then defined which is used to determine how far our approximated function deviates from the exact function over a finite set of frequencies $\mathbf{w} = [\omega_0, \dots, \omega_R]^T$, where R is an integer. We shall use ω_r to denote the r^{th} element of \mathbf{w} . Here we investigate two such cost functions. One looks at the deviation over the real part of the impedance

$$E_R = \frac{1}{2} \sum_{r=0}^R \left(\frac{\text{Re}(Z_{vr}) - \text{Re}(Z_{vr}^M)}{\text{Re}(Z_{vr})} \right)^2 \quad (2.119)$$

where $Z_{vr}^M = Z_v^M(\omega_r, \mathbf{x})$ and $Z_{vr} = Z_v(\omega_r)$. The other looks over the magnitude of the impedance

$$E_M = \frac{1}{2} \sum_{r=0}^R \left(\frac{|Z_{vr} - Z_{vr}^M|}{|Z_{vr}|} \right)^2 \quad (2.120)$$

where $|\cdot|$ denotes the absolute value. Both E_R and E_M are always non-negative, real numbers, which are necessary conditions for this optimisation problem. We expect that using E_R should produce results that approximate the losses of the model, determined by the real part of the admittance/impedance, better than optimising over the magnitude of the impedances. However, as the real and imaginary parts are combined in the absolute operation, the results produced using E_M should approximate the overall behaviour of viscous and thermal effects in air better than optimising over only the real part.

To find the minimum of a function $F(\mathbf{x})$ of multiple variables contained in vector \mathbf{x} , we begin with an initial guess, \mathbf{x}^0 , and then use an iterative procedure to find a new point so that

$$\mathbf{x}^{i+1} = \mathbf{x}^i - \epsilon \mathbf{d}^i(F), \quad i = 0, 1, \dots \quad (2.121)$$

where $\mathbf{d}^i(F)$ is a descent direction at the i^{th} iteration, and ϵ is the step size, the distance that the direction is followed. We now look at two such ways to determine the descent direction.

Steepest descent

A simple optimisation procedure is the steepest descent algorithm [30, 153]. This is an iterative method that follows the negative gradient of the function we are trying to approximate towards a local minimum. The descent direction for the steepest descent algorithm is given by

$$\mathbf{d}^i = \frac{\nabla F(\mathbf{x}^i)}{|\nabla F(\mathbf{x}^i)|}, \quad i = 0, 1, \dots \quad (2.122)$$

where ∇ denotes the multidimensional gradient operator.

The step size is very important for the efficiency of this algorithm; too small and it will take a long time to reach a minimum, too large and it will overshoot the minimum and potentially position \mathbf{x}^{i+1} so that it increases the function F . Since this procedure only finds local minima, the algorithm must be run multiple times with different initial guesses that are randomly placed in the domain in an attempt to find a global minimum.

Newton's method

Steepest descent is useful in that it can approach a minimum with relatively little computational effort at each iteration. However, convergence is slow. It is therefore useful to use a method that approaches the minimum in a more efficient manner.

Newton's method [30, 153] is a second order method that locally approximates a function as a quadratic and moves towards the minimum faster than the steepest descent method. The descent direction for this algorithm is

$$\mathbf{d}^i = [\mathbf{H}(F(\mathbf{x}^i))]^{-1} \nabla F(\mathbf{x}^i) \quad (2.123)$$

where \mathbf{H} is the Hessian matrix of F given by

$$\mathbf{H}(F) = \begin{bmatrix} \frac{\partial^2 F}{\partial x_1^2} & \frac{\partial^2 F}{\partial x_1 \partial x_2} & \cdots & \frac{\partial^2 F}{\partial x_1 \partial x_m} \\ \frac{\partial^2 F}{\partial x_2 \partial x_1} & \frac{\partial^2 F}{\partial x_2^2} & \cdots & \frac{\partial^2 F}{\partial x_2 \partial x_m} \\ \vdots & \vdots & \ddots & \vdots \\ \frac{\partial^2 F}{\partial x_m \partial x_1} & \frac{\partial^2 F}{\partial x_m \partial x_2} & \cdots & \frac{\partial^2 F}{\partial x_m^2} \end{bmatrix} \quad (2.124)$$

In practice, Newton's method is used with a trust region set by ϵ_T so that the descent direction is modified to

$$\mathbf{d}^i = [\mathbf{H}(F(\mathbf{x}^i)) + \epsilon_T \mathbf{I}]^{-1} \nabla F(\mathbf{x}^i) \quad (2.125)$$

Optimisation procedure for the Foster structure

To optimise the Foster structure, we aim to minimise the functions $E_R(\mathbf{x})$ and $E_M(\mathbf{x})$. The elements of the gradient and Hessian of the cost functions¹³ are

$$\frac{\partial E_R}{\partial x_q} = - \sum_{r=0}^R \frac{\text{Re}(Z_{vr} - Z_{vr}^M)}{\text{Re}(Z_{vr})} \text{Re} \left(\frac{\partial Z_{vr}^M}{\partial x_q} \right) \quad (2.126a)$$

$$\frac{\partial^2 E_R}{\partial x_p \partial x_q} = \sum_{r=0}^R \left[\frac{1}{(\text{Re}(Z_{vr}))^2} \text{Re} \left(\frac{\partial Z_{vr}^M}{\partial x_p} \right) \left(\frac{\partial Z_{vr}^M}{\partial x_q} \right) - \frac{\text{Re}(Z_{vr} - Z_{vr}^M)}{(\text{Re}(Z_{vr}))^2} \text{Re} \left(\frac{\partial^2 Z_{vr}^M}{\partial x_p \partial x_q} \right) \right] \quad (2.126b)$$

$$\frac{\partial E_M}{\partial x_q} = - \sum_{r=0}^R \left(\frac{1}{|Z_{vr}|^2} \text{Re} \left((Z_{vr} - Z_{vr}^M)^* \frac{\partial Z_{vr}^M}{\partial x_q} \right) \right) \quad (2.127a)$$

$$\frac{\partial^2 E_M}{\partial x_p \partial x_q} = \sum_{r=0}^R \left[\frac{1}{|Z_{vr}|^2} \text{Re} \left(\frac{\partial Z_{vr}^{M*}}{\partial x_p} \frac{\partial Z_{vr}^M}{\partial x_q} \right) - \frac{1}{|Z_{vr}|^2} \text{Re} \left((Z_{vr} - Z_{vr}^M)^* \frac{\partial^2 Z_{vr}^M}{\partial x_p \partial x_q} \right) \right] \quad (2.127b)$$

where $*$ denotes complex conjugation and

$$\frac{\partial Z_v^M}{\partial a_0} = e^{a_0}, \quad \frac{\partial Z_v^M}{\partial a_q} = \frac{e^{a_q} j\omega}{e^{b_q} + j\omega}, \quad \frac{\partial Z_v^M}{\partial b_q} = - \frac{e^{a_q + b_q} j\omega}{(e^{b_q} + j\omega)^2}, \quad q = 1, \dots, M \quad (2.128)$$

$$\frac{\partial^2 Z_v^M}{\partial a_0^2} = e^{a_0}, \quad \frac{\partial^2 Z_v^M}{\partial a_0 \partial a_q} = 0, \quad \frac{\partial^2 Z_v^M}{\partial a_0 \partial b_q} = 0, \quad \frac{\partial^2 Z_v^M}{\partial a_q \partial b_p} = 0, \quad p \neq q \quad (2.129a)$$

¹³It is fine to take the gradient operator within the real function. First, define $f(\xi) = \text{Re}(z(\xi))$ and $z(\xi) = x(\xi) + jy(\xi) \implies f(\xi) = x(\xi)$. The derivatives are $df/d\xi = dx/d\xi$ and $dz/d\xi = dx/d\xi + jdy/d\xi$ so that $\text{Re}(dz/d\xi) = dx/d\xi = df/d\xi \implies d\text{Re}(z)/d\xi = \text{Re}(dz/d\xi)$

$$\frac{\partial^2 Z_v^M}{\partial a_q^2} = \frac{e^{a_q} j\omega}{e^{b_q} + j\omega}, \quad \frac{\partial^2 Z_v^M}{\partial a_q \partial b_q} = -\frac{e^{a_q+b_q} j\omega}{(e^{b_q} + j\omega)^2}, \quad \frac{\partial^2 Z_v^M}{\partial b_q^2} = \frac{2j\omega e^{a_q+2b_q}}{(e^{b_q} + j\omega)^3} - \frac{j\omega e^{a_q+b_q}}{(e^{b_q} + j\omega)^2} \quad (2.129b)$$

For this system we also have

$$\frac{\partial Z_{vr}^{M*}}{\partial x_q} = \left(\frac{\partial Z_{vr}^M}{\partial x_q} \right)^* \quad (2.130)$$

The Foster structure allows for reasonably straightforward calculations of the derivatives of the cost functions—for the Cauey structure the procedure is much more involved.

App. B presents tables of coefficient values for different filter orders using both E_R and E_M as the cost functions over the logarithmically spaced frequency range between 0.1 Hz and 10 kHz so that the elements of the frequency vector \mathbf{w} are

$$\omega_r = 2\pi \left(0.1 e^{\left(\frac{r}{R} \log\left(\frac{10^4}{0.1} \right) \right)} \right), \quad r = 0, 1, \dots, R \quad (2.131)$$

Figs. 2.18 and 2.19 show the accuracy of these approximations when they are optimised using E_R and E_M respectively.

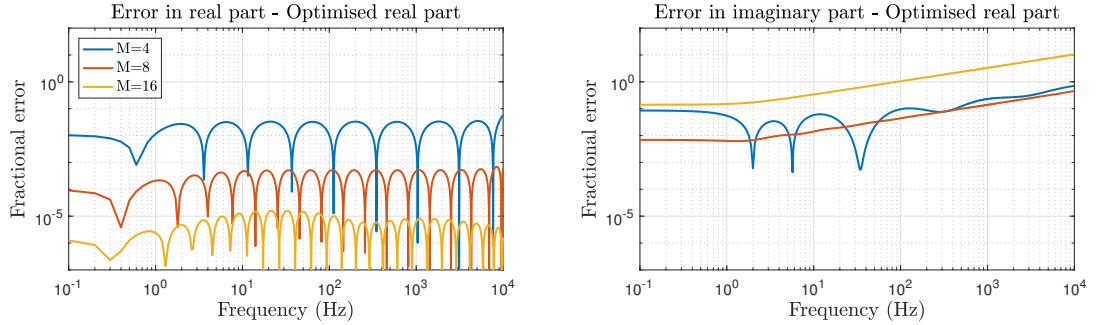


Figure 2.18: Fractional error of Foster model optimised to Z_v using E_R for a tube of 0.005 m over a frequency range 0 Hz to 10 kHz. Left: Error in real part. Right: Error in imaginary part.

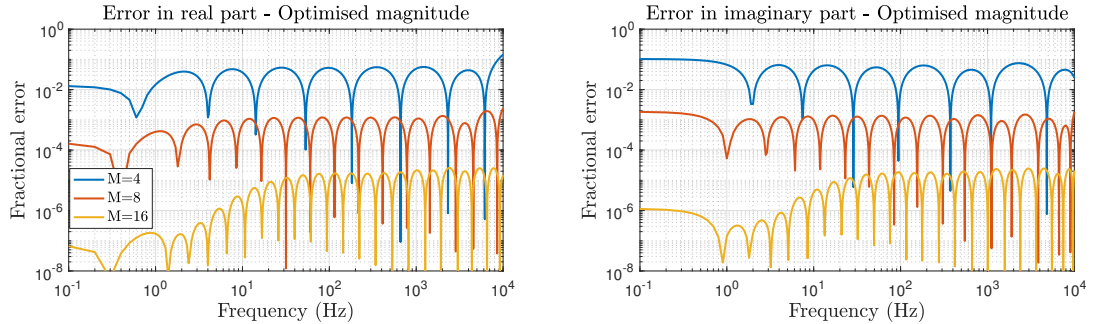


Figure 2.19: Fractional error of Foster model optimised to Z_v using E_M for a tube of 0.005 m over a frequency range 0 Hz to 10 kHz. Left: Error in real part. Right: Error in imaginary part.

Both cost functions allow for improved accuracy as the order of the structure is increased. Using E_R gives an error in the real part : less than 10 % for $M = 4$, less than 0.1 % for $M = 8$, and around 0.001 % for $M = 16$. However, since the cost function focuses on the real

part of the function, the imaginary part is not taken into account which allows for larger errors. Using E_M gives an error in the real part : less than 10 % for $M = 4$, around 0.1 % for $M = 8$, and around 0.001 % for $M = 16$. The accuracy is similar for the imaginary part.

It should be noted that the poles and zeros of this new impedance do not necessarily match those of the original function. This is to be expected as we are not directly expanding the function. Instead we are trying to find another function that matches the target over a particular frequency range.

It is also important to note that although we have performed an optimisation for one particular tube radius and temperature for the impedance, we can show in the following sections that small changes can be made so that these parameters can be reused for the admittance as well as for changes to the tube radius and air temperature.

2.4.10 Reusing Z_v coefficients for \hat{Y}_t

The coefficient values for Z_v can be reused for the filter \hat{Y}_t since they both have the same functional form. Recall that

$$Z_v = j\omega\rho_0 \frac{F_v}{1 - F_v}, \quad \hat{Y}_t = \frac{j\omega(\gamma - 1)}{\rho_0 c_0^2} \frac{F_t}{1 - F_t} \quad (2.132)$$

Substituting the angular frequencies in terms of the respective dimensionless characteristic parameters gives

$$Z_v = \left[\frac{j\eta r_v^2}{r^2} \frac{F_v(r_v)}{1 - F_v(r_v)} \right] \quad (2.133)$$

$$\begin{aligned} \hat{Y}_t &= \frac{\gamma - 1}{\rho_0^2 c_0^2 \nu^2} \left[\frac{j\eta r_t^2}{r^2} \frac{F_t(r_t)}{1 - F_t(r_t)} \right] \\ &= \frac{\gamma - 1}{\rho_0^2 c_0^2 \nu^2} Z_v(r_t) \\ &= \frac{\gamma - 1}{\rho_0^2 c_0^2 \nu^2} Z_v(\nu r_v) \end{aligned} \quad (2.134)$$

The function \hat{Y}_t is then the same as Z_v except for a multiplicative factor of $C_0/\rho_0\nu^2$ and a change of variables from $r_v \rightarrow \nu r_v$. The Foster structure can then be modified using a multiplicative factor and changing the angular frequency using $\omega \rightarrow \nu^2\omega$.

$$\hat{Y}_t \approx \frac{\gamma - 1}{\rho_0^2 c_0^2 \nu^2} e^{a_0} + \sum_{q=1}^M \frac{\gamma - 1}{\rho_0^2 c_0^2 \nu^2} \frac{e^{a_q} \nu^2 j\omega}{e^{b_q} + \nu^2 j\omega} \quad (2.135)$$

The same element values for Z_v^M can be used for \hat{Y}_t^M using

$$G_0 = \frac{\gamma - 1}{\rho_0^2 c_0^2 \nu^2} e^{a_0}, \quad G_q = \frac{\gamma - 1}{\rho_0^2 c_0^2 \nu^2} e^{a_q}, \quad C_q = \frac{\gamma - 1}{\rho_0^2 c_0^2} e^{a_q - b_q} \quad (2.136)$$

or

$$G_0 = \frac{\gamma - 1}{\rho_0^2 c_0^2 \nu^2} R_0, \quad G_q = \frac{\gamma - 1}{\rho_0^2 c_0^2 \nu^2} R_q, \quad C_q = \frac{\gamma - 1}{\rho_0^2 c_0^2} L_q \quad (2.137)$$

For typical room temperatures $\nu < 1$, so the domain of \hat{Y}_t falls within that of Z_v . Figs. 2.20 and 2.21 show the admittances calculated using the element values calculated by optimising

over the real part and the magnitude of Z_v . These show similar order errors to those of the original impedance.

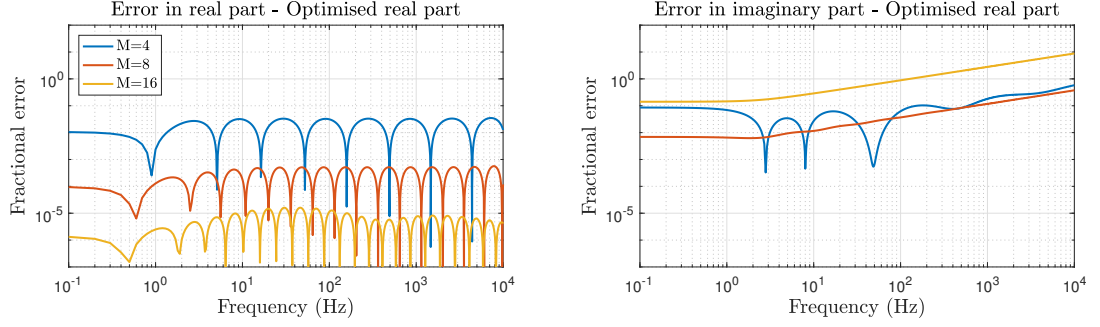


Figure 2.20: Fractional error of Foster model optimised to Z_v using E_R for a tube of 0.005 m over a frequency range 0 Hz to 10 kHz when it is applied to admittance \hat{Y}_t . Left: Error in real part. Right: Error in imaginary part.

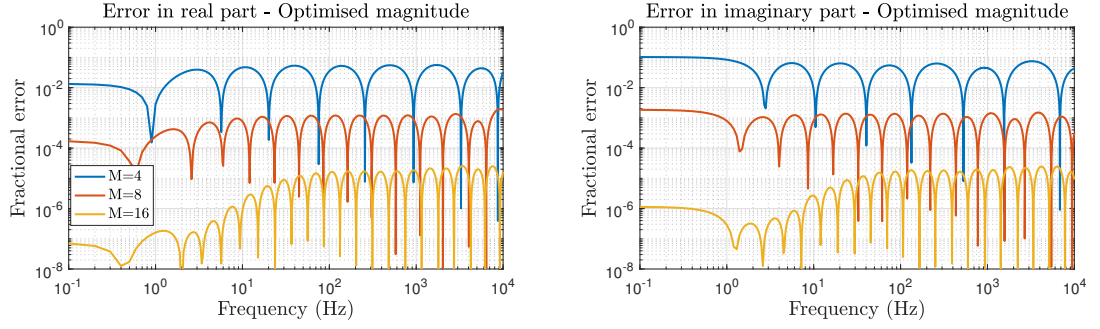


Figure 2.21: Fractional error of Foster model optimised to Z_v using E_M for a tube of 0.005 m over a frequency range 0 Hz to 10 kHz when it is applied to admittance \hat{Y}_t . Left: Error in real part. Right: Error in imaginary part.

2.4.11 Generalising for different tube radii and temperatures

The method of finding the coefficients so far is designed to be used on tubes of one particular radius—the accuracy of the results would decrease if we were to use the same coefficients for a tube of different radius. It is therefore useful to be able to transform these coefficients so that they can be applied to tubes of differing radius. Again returning to the expression for the impedance at one particular radius r_1 , with dimensionless parameter r_{v1} and impedance

$$Z_{v1} = \frac{j\eta r_{v1}^2}{r_1^2} \frac{F_v(r_{v1})}{1 - F_v(r_{v1})} \quad (2.138)$$

Another impedance for a tube of radius r_2 with dimensionless parameter r_{v2} is

$$Z_{v2} = \frac{j\eta r_{v2}^2}{r_2^2} \frac{F_v(r_{v2})}{1 - F_v(r_{v2})} \quad (2.139)$$

The variables r_{v1} and r_{v2} lie over different ranges because they correspond to different tube radii. They can be related as

$$r_{v2} = \frac{r_2}{r_1} r_{v1} \quad (2.140)$$

So the second impedance can be written as

$$\begin{aligned} Z_{v2} &= \left(\frac{r_1}{r_2} \right)^2 \left(\frac{\eta j}{r_1^2} \left(\frac{r_2}{r_1} r_{v1} \right)^2 \frac{F_v \left(\frac{r_2}{r_1} r_{v1} \right)}{1 - F_v \left(\frac{r_2}{r_1} r_{v1} \right)} \right) \\ &= \left(\frac{r_1}{r_2} \right)^2 Z_{v1} \left(\frac{r_2}{r_1} r_{v1} \right) \end{aligned} \quad (2.141)$$

We can therefore reuse the impedance calculated for a tube of radius \bar{r} for tubes of different radii r by scaling the impedance and using the transform $\omega \rightarrow \left(\frac{r}{\bar{r}} \right)^2 \omega$. The element values then become

$$R_0 = \left(\frac{\bar{r}}{r} \right)^2 e^{a_0}, \quad R_q = \left(\frac{\bar{r}}{r} \right)^2 e^{a_q}, \quad L_q = e^{a_q - b_q} \quad (2.142)$$

Note that the inductor values do not change in this case. Fig. 2.22 shows the error in the impedance when the element values are modified in this way for two different tube radii.

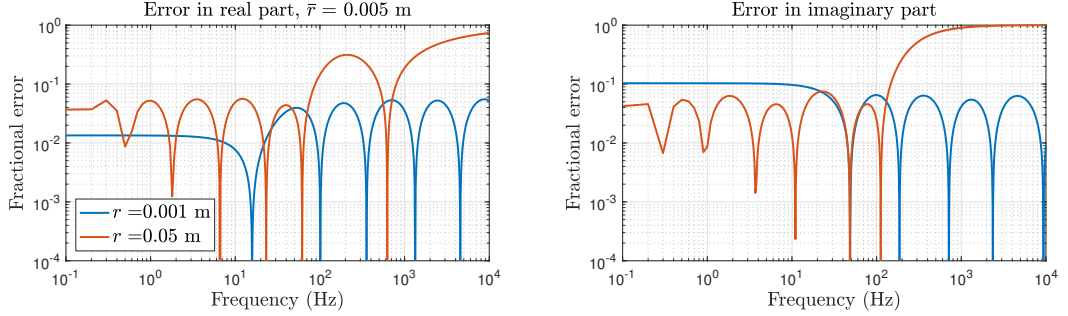


Figure 2.22: Fractional error of the impedance using the element values in (2.142) for a fourth order filter. The original impedance was optimised using E_M for a tube radius of 0.005 m and a temperature of 26.85°C. Left: Error in real part. Right: Error in imaginary part.

When the $r < \bar{r}$, the error remains at the same magnitude. When the $r > \bar{r}$, the error is larger at high frequencies. This is not surprising as the smaller magnitude will be included within the original range that was optimised over, whereas the larger magnitude will lie outside the original range. It is therefore useful to make sure that optimisation is performed for reasonably large tube radius. A typical range for the radii of a trumpet is between 0.004 m and 0.15 m. This is reasonably large so in practice it is worthwhile to optimise the parameter values for several radii which are used over different ranges.

A similar method can be used for different temperatures. In this case the element values become

$$R_0 = \frac{\eta}{\bar{\eta}} e^{a_0}, \quad R_q = \frac{\eta}{\bar{\eta}} e^{a_q}, \quad L_q = \frac{\rho_0}{\bar{\rho}_0} e^{a_q - b_q} \quad (2.143)$$

where $\bar{\eta}$ and $\bar{\rho}_0$ are the values of viscosity and density that are used in the original optimisation procedure. Fig. 2.23 shows the error in the impedance calculated at different temperatures using the values. The impedance is not as sensitive to changes in temperature as it is to changing the radii so the error remains roughly the same.

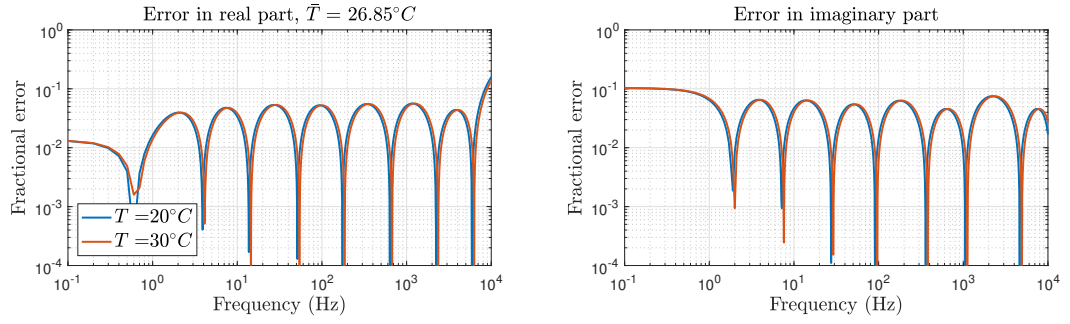


Figure 2.23: Fractional error of the impedance using the element values in (2.143) for a fourth order filter. The original impedance was optimised using E_M for a tube radius of 0.005 m and a temperature of 26.85°C. Left: Error in real part. Right: Error in imaginary part.

2.4.12 Restricting optimisation ranges

The accuracy of the Foster structure can be improved by limiting the frequency range over which they are optimised [25]. The previous results used a wide range from 0 Hz to 10 kHz. However, the dynamics of brass instruments are dominated by effects over a smaller range. Figs. 2.24 and 2.25 show the errors in the Foster approximations when optimised over the range 20 Hz to 3 kHz.

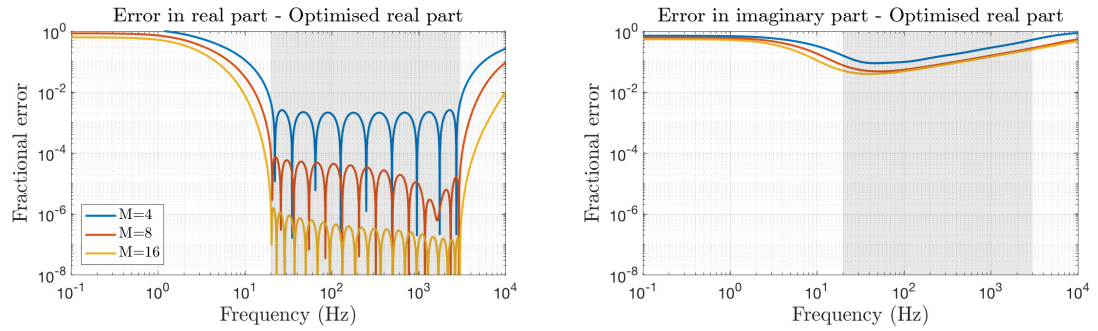


Figure 2.24: Fractional error of Foster model optimised to Z_v using E_R for a tube of 0.005 m over a frequency range 20 Hz to 3 kHz. Left: Error in real part. Right: Error in imaginary part. The shaded area shows the frequency range that optimisation was performed over.

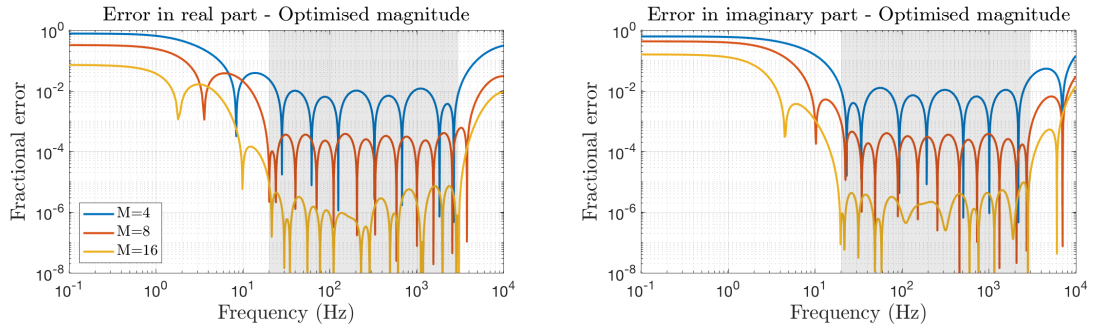


Figure 2.25: Fractional error of Foster model optimised to Z_v using E_M for a tube of 0.005 m over a frequency range 20 Hz to 3 kHz. Left: Error in real part. Right: Error in imaginary part. The shaded area shows the frequency range that optimisation was performed over.

It is clear that the error in the real part of the impedance is reduced by an order of magnitude when optimisation is performed over a smaller frequency range when using both E_R and E_M , and similarly for the error in the imaginary part when using E_M .

2.4.13 Comparisons of viscothermal models

The frequency domain models of Benade [13], Keefe [94], Caussé *et al.* [37], Webster-Lokshin [79], and Bilbao and Chick [24] are accurate approximations of the viscothermal model of Zwikker and Kosten. However, some of these expressions are not positive real and require truncation if they are to be used in the time domain. Also, due to the use of fractional derivatives when transformed to the time domain, further approximations are required, which can damage accuracy.

Due to the structure of the impedance and admittance in the complex domain, circuit representations can be derived that have passive time-domain representations. The Cauer structure presented by Thompson *et al.* [162] is a very accurate model for low frequencies as can be observed in Figs. 2.14 and 2.15. However, to use the Cauer structure in a musically useful way requires high order structures that will slow down the performance of time domain simulations. The Foster structure [25, 26, 27] leads to a very flexible optimisation framework that can be applied over different frequency ranges. Some off line computation is required, but only one set of coefficients need be stored for reasonable accuracy. Figs. 2.26 and 2.27 show a comparison of these two models. It is clear that the accuracy of the Cauer structure is greater at low frequencies than the Foster structure when optimised over both E_R and E_M . However, the Foster structure offers a more consistent error across the frequency range over which it is optimised; the error in the Cauer structure increases rapidly and becomes larger than that of the Foster structure. This cross-over happens within the normal operating range of brass instruments and would therefore require more elements for the Cauer structure to be useful given that, in a discrete setting, computational cost and memory usage will scale with the order of the approximation. The Foster structure therefore produces greater accuracy for a lower order structure.

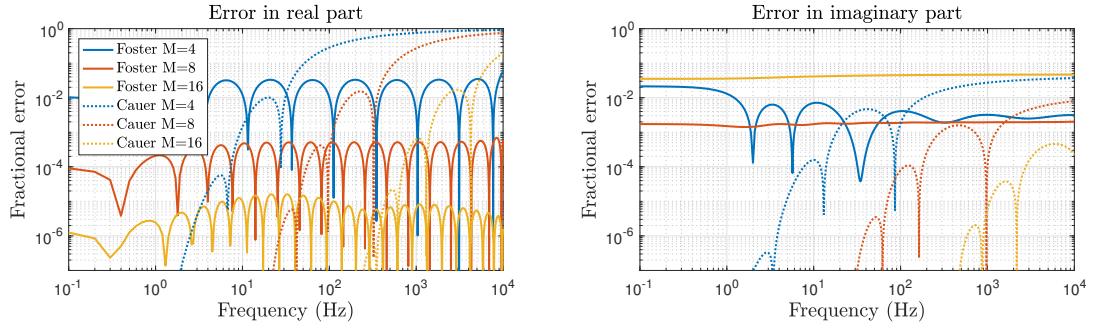


Figure 2.26: Fractional error of the impedance for the Foster model, optimised using E_R (solid lines) over a frequency range 0 Hz to 10 kHz, and for Cauer model (dashed lines) for a tube of 0.005. Left: Error in real part. Right: Error in imaginary part.

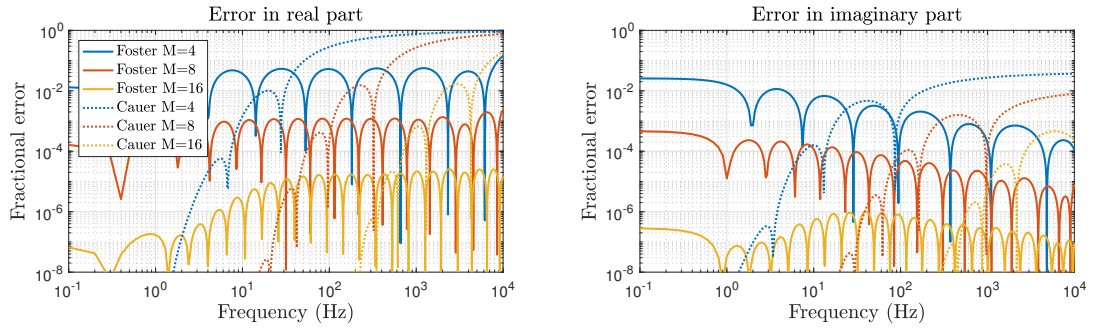


Figure 2.27: Fractional error of the impedance for the Foster model, optimised using E_M (solid lines) over a frequency range 0 Hz to 10 kHz, and for Cauer model (dashed lines) for a tube of 0.005. Left: Error in real part. Right: Error in imaginary part.

The Foster model can be optimised over a smaller frequency range, which improves accuracy. However, some care must be taken when reducing the range. For example, the mechanism for extreme high note playing is still unclear [105], so viscous and thermal effects may need to be included in the upper frequency ranges.

There are some extra complexities when using the Foster structure. Although using E_R as the cost function allows for better accuracy on the real part of the impedance, the error in the imaginary part is not taken into account. The cost function E_M does take into account errors in both the real and imaginary parts of the impedance, but, in general, the error in the real part is higher than that calculated using E_R .

Chapter 3

Finite-difference time-domain methods: Applications to acoustic tubes

“The worthwhile problems are the ones you can really solve or help solve, the ones you can really contribute something to... No problem is too small or too trivial if we can really do something about it.”

— Richard P. Feynman

The models described in the previous chapter yield a good description of the dynamics of acoustic tubes in the linear regime. Because of the spatially varying character of the bore, analytic solutions are not available in general. We must therefore look to numerical methods to solve the PDEs.

In the construction of numerical schemes, particularly for synthesis applications, we must consider the following:

1. Stability
2. Accuracy
3. Efficiency

Stability concerns how the solutions develop over time. The simulations should at most display bounded growth which does not interfere with the computation of the solutions. This is particularly important for combined systems where care must be taken at their interfaces, e.g., at the domain boundaries. The user should expect usable results for any configuration selected.

In a mathematical sense, accuracy relates to how well our numerical method approximates the original equations in terms of a deviation from the original result or how the scheme converges. Additional accuracy concerns arise in audio applications as numerical methods can impose frequency dependent errors such as numerical dispersion and bandwidth limitation. Care must be taken in this setting as such errors are audible and would make the method useless if too extreme.

Efficiency relates to how much time is required to process the algorithm. In a scientific setting, the user will sacrifice long run times on a computer processor if it produces very accurate results. In a creative setting, the user may wish for a faster application so as to quickly explore and refine the sounds being constructed. As such there is an intimate link between accuracy and efficiency.

This chapter is concerned with the numerical problem and finite-difference time-domain (FDTD) methods will be applied to the systems discussed in the previous chapter. To begin, a summary of previous numerical methods used for solving the spatially varying horn equation are presented, and justification for using FDTD methods is given. This is followed by an introduction to the FDTD method. The grids on which the domains are represented are introduced along with shifting operators that are used to make the discrete approximations to derivatives. Accuracy and convergence of the discrete operators are discussed. This section will also cover discrete identities and frequency transformations.

The remainder then follows parallel treatment to that of Chap. 2, splitting into lossless and lossy problems. In the lossless section there is an investigation into numerical schemes for the wave and horn equations. There are multiple choices of FDTD schemes for an individual problem so time is taken to explore two different schemes, one explicit and the other implicit. Numerical dispersion analysis is performed on the schemes and is followed by energy analysis which allows for a discussion on numerical boundary conditions. Although the implicit scheme, which utilises the bilinear transform, lends itself to simpler energy analysis than the explicit scheme, frequency warping effects are more prominent given equal grid spacings and there is a higher computational cost. However, the bilinear transform can be used to guarantee passivity in the lossy problem, whilst leaving the lossless part in explicit form; this is exploited in later sections.

The final section focusses on discrete modelling of viscous and thermal losses. Simulations are performed using the loss models from the previous chapter. A fractional derivative operator is derived for use in the Bilbao and Chick approximation of the Zwikker and Kosten model. Finally the discrete form of the Foster network is presented. The Foster network lends itself well to numerical simulation as the individual branches can be updated independently of each other. Frequency warping effects reduce the accuracy of the higher order structures but can be taken into account when searching for element values. All of the models are then compared in the final discussion.

3.1 Numerical methods for solving PDEs

Here we cover the previous methods used to solve the spatially varying horn equation and give justification for using the finite-difference time-domain method.

3.1.1 Previous numerical methods applied to the horn equation

The transmission matrix method (TMM) described in Sec. 2.3.5 is commonly used in musical acoustics research as it offers a high degree of accuracy to the user [37, 56]. However, this technique is constrained to steady state solutions, which limits its applications in constructing a flexible virtual musical instrument.

Modal methods have been applied to the time domain case of an acoustic tube in the

MoReeSC framework [148] but these methods are difficult to apply if the resonances of the system vary with time, as in the case of time varying valves we wish to study in Chap. 5.

Wave based methods have seen much success in physical modelling. The earliest application of travelling wave solutions was to voice synthesis using the Kelly-Lochbaum (KL) framework [96]. This time domain synthesis method is similar to the frequency domain TMM as the cross-sectional area of a tube is approximated by a series concatenated cylinders, and scattering of waves is performed at the junction between each cylinder. As with the TMM, the bore profile can be approximated using concatenated cones with spherical wavefronts, but convex profiles can lead to non-causal and unstable behaviour due to a pole positioned in the right hand side of the complex plane [18]. To avoid this, a frequency domain mapping that cuts around this unstable pole must be applied [117].

Digital waveguides (DWG) [151] operate in a similar fashion to the KL framework and have been applied to acoustic tube systems for brass [18, 47, 82, 92, 116] and woodwind [146, 152] instrument modelling. Discrete spatial samples of the forwards and backwards wave solutions are stored in delay lines. The solutions are then propagated by ‘shifting’ the elements of the delay lines. For finite domains, boundary conditions are derived that reflect one delay line into the other. In addition, the scattering behaviour present over the interior of the domain can be consolidated into one digital filter that is applied at a termination. This consolidation can aid in the stability of the framework; Scavone [146] showed that the instabilities present in the modelling of convex tube profiles using a spherical wave KL framework were effectively cancelled out as they were lumped together in the DWG framework.

The shifting of delay line elements produces efficient simulations. However, as the order of the terminating filter increases, for example, by requiring more scattering elements to describe a complex bore profile, the computational advantage of DWGs decreases. In addition, including time-varying phenomena, such as moving valves, makes implementation difficult. Digital waveguide filters are an extension to DWG and have been applied to simulations of acoustic tubes [7, 166, 167].

3.1.2 Passive numerical methods

As with the continuous time domain problems, numerical methods can also display issues with growth, even if the original system is bounded. For the wave based methods, passivity is ensured through examination of the reflection and transmission properties of the scattering junctions [19]. An alternative method is to extend the energy methods described in Chap. 2 to the discrete domain.

One such extension is used in the Port-Hamiltonian (PH) framework [59, 164] which has been applied to systems such as analogue circuits [57, 60], lossy wave systems [111], an electro-mechanical piano [58], vocal folds [54] and a simplified brass instrument system [108, 109]. This method focuses on the conserved energy of the system, including the energy stored and dissipated within the system, along with the energy injected into the system through driving terms. Discretisation of the problem is then applied using guaranteed stable methods, such as the bilinear transform which is discussed later in Sec. 3.2.6. This, however, results in implicit schemes that display a high level of numerical dispersion and require solutions to systems of linear equations.

3.1.3 The finite-difference time-domain method

Finite-difference time-domain (FDTD) methods offer a flexible means of modelling physical systems. The derivative of a function is defined to be the limit of

$$\frac{df}{dz} = \lim_{h \rightarrow 0} \frac{f(z+h) - f(z)}{h} \quad (3.1)$$

Instead of taking the limit of the step size h to approach zero, we can fix it to be a small, but non-zero, value. Substituting this into differential equations changes a calculus problem into an algebraic problem that can be solved in a loop over the dimensions of interest. The analysis of these schemes, however, requires some higher level mathematical skill. See the texts of Gustafsson *et al.* [71] and Strikwerda [156] for overviews of FDTD methods and that of Bilbao for applications to musical acoustics [21]. Finite-volume methods are an extension of finite-difference methods, see the text of Leveque [103], and have been applied in, e.g., room acoustics simulations by Botteldooren [31, 32] and more recently by Hamilton [74]. These methods are of use when boundaries have complex geometries—since the boundaries of the one-dimensional brass system are relatively simple we will stick to FDTD methods.

Although the computational load is higher for FDTD methods than that of DWGs, the compute time is more than reasonable on modern home computers (at least for the case of one-dimensional systems). In addition, modifications to the internal geometry of the system modelled with a FDTD scheme does not significantly change the computation time, as opposed to the DWG framework.

The passivity of FDTD methods can be shown through the extension of the energy methods previously described in this work. The form of these discrete energies bear resemblance to their continuous counterparts, so analysis in the continuous case is beneficial before applying the numerical method.

3.2 Basics of FDTD methods: Étude II

This section introduces the fundamental concepts of FDTD scheme design.

3.2.1 Grids

The first step in using FDTD methods is to discretise the domain of interest. All of the independent variables of interest, which in this work are space and time, are approximated on grids that are equally spaced in each dimension—although the spacings for each dimension are generally different.

For time domain problems, it is sensible to set the temporal grid size, k , by the sample rate, F_s , so that $k = 1/F_s$. This is useful as we immediately know the maximum frequency bandwidth of the simulation given by the Nyquist limit [151]. For sound synthesis purposes, we are primarily concerned with the range of human hearing, namely between 20 Hz and 20 kHz [63]. However, discrete numerical methods can introduce unwanted audible dispersion. This can be rectified through the use of oversampling, which extends the frequency bandwidth of the simulations and improves the dispersion characteristics over the audible frequency range, but with the cost of increased computation times. The balance between accuracy and performance is an important theme in synthesis methods.

The spatial domain is sampled on a grid of step size h . Some FDTD schemes allow for independent control over the spatial and temporal grid spacings but others place some limit on these sizes if the scheme is to be stable, this will be discussed later for specific FDTD schemes.

The temporal grid will be labelled by integers n and the spatial grid by l ; see Fig. 3.1. These labels correspond to actual times $t_n = nk$ and positions $z_l = lh$, where h is the spatial grid size. The temporal index will lie over the non-negative integers $n \in \mathbb{Z}^+ = \{0, 1, \dots, \infty\}$ and the spatial index will lie over all of the integers $l \in \mathbb{Z} = \{-\infty, \dots, -1, 0, 1, \dots, \infty\}$. A discrete domain corresponding to \mathcal{D} in the previous chapter is given by $d = \{l \in \mathbb{Z} \mid 0 \leq l \leq N\}$, where $N = \text{floor}(L/h)$ is the number of discrete points in the spatial domain.

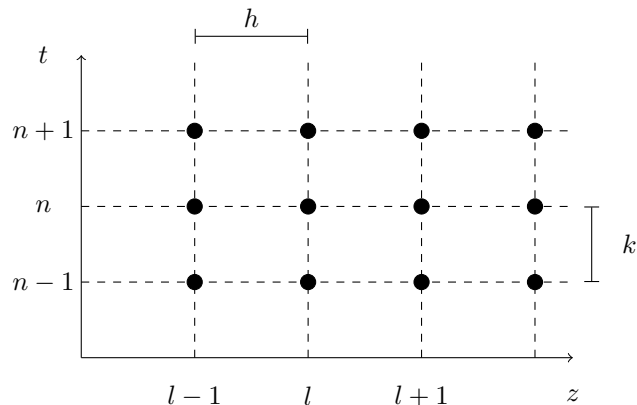


Figure 3.1: Discretised domain for a finite-difference scheme. The temporal domain is sampled at intervals of time k s and labelled using integers n . The spatial domain is sampled at intervals of length h m and labelled using integers l . Black circles denote the grid function f at each temporal and spatial point.

The variables of interest in simulations will be approximated on these grids. A compact notation of subscripts and superscripts will be used to define a grid function

$$f_l^n \approx f(t_n = nk, z_l = lh) \quad (3.2)$$

where the superscript denotes the temporal index and the subscript the spatial index. The grid function, f_l^n , is not a sample of the original function, $f(t, z)$, but is an approximation; it is worth highlighting this subtlety.

Interleaved grids

For first derivative PDE systems, we will employ interleaved grids as presented by Yee in electromagnetism [179]. In this case, one of the dependent variables will be approximated on the integer grid mentioned above, and the other on the in-between grids in either space, see Fig. 3.2 at left, or space/time, see Fig. 3.2 at right.

A function $g(t, z)$ approximated on a spatially interleaved grid is denoted by

$$g_{l+1/2}^n \approx g(nk, (l + 1/2)h) \quad (3.3)$$

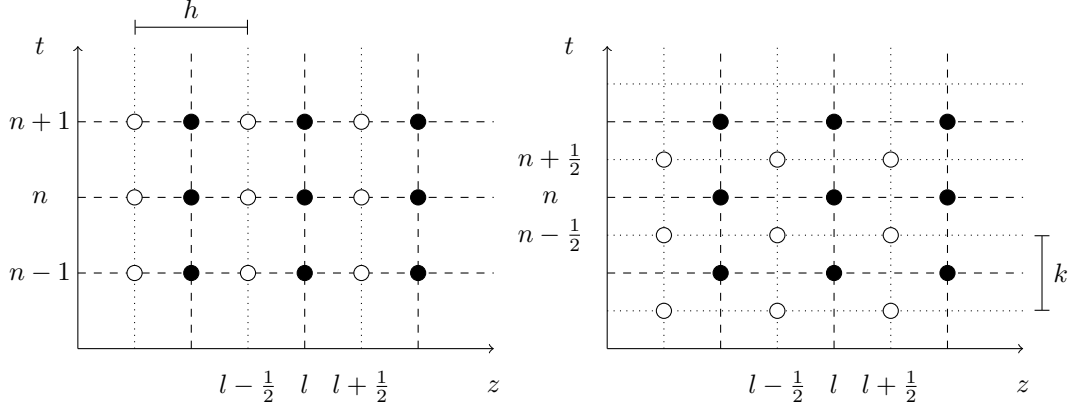


Figure 3.2: Left: Grids that are interleaved only in space. Right: Grids that are interleaved in time and space. Dashed lines show the original grid labelled by the integers n and l . Dotted lines show the interleaved grid. Black circles denote the locations of the grid function, f , on the integer field. White circles denote the locations grid function, g , on the interleaved grids.

If it is approximated on a spatially and temporally interleaved grid then it is denoted by

$$g_{l+1/2}^{n+1/2} \approx g((n+1/2)k, (l+1/2)h) \quad (3.4)$$

For spatially interleaved grids another domain is defined $\bar{d} \in \{l \in \mathbb{Z} \mid 0 \leq l \leq N-1\}$ which lies between the points represented by d .

The discrete domains mentioned above label sampled points of the continuous domains. For example, the finite discrete domains d and \bar{d} correspond to points that lie within the continuous domain \mathcal{D} . However, because \bar{d} is used for functions that are indexed using half integers, this domain represents the points between those of d .

3.2.2 Finite-difference operators

In this section we consider the infinite temporal and spatial domains. To construct approximations to derivatives we must first define temporal and spatial shifting operators, $w_{t\pm}$ and $w_{z\pm}$, whose action is to advance the function by one grid point forwards or backwards in the chosen dimension so that

$$w_{t+}f_l^n = f_l^{n+1}, \quad w_{t-}f_l^n = f_l^{n-1} \quad (3.5a)$$

$$w_{z+}f_l^n = f_{l+1}^n, \quad w_{z-}f_l^n = f_{l-1}^n \quad (3.5b)$$

A selection of discrete approximations to the first time derivative, ∂_t , is as follows

$$\delta_{t+} = \frac{w_{t+} - 1}{k}, \quad \delta_t = \frac{w_{t+} - w_{t-}}{2k}, \quad \delta_{t-} = \frac{1 - w_{t-}}{k} \quad (3.6)$$

In this work, the lower case delta symbol, δ , will be used for discrete approximations to differential operators. The three operators above are called, respectively, the ‘forwards’, ‘centred’ and ‘backwards’ difference operators due to which time steps they utilise.

An approximation to the second time derivative can be constructed from the forwards and

backwards difference operators

$$\delta_{tt} = \delta_{t+}\delta_{t-} = \frac{w_{t+} - 2 + w_{t-}}{k^2} \approx \partial_{tt} \quad (3.7)$$

Note that the second difference operator is no longer a square of one operator but a product of two different ones.

Our operators are, in general, acting on functions of two variables. If these operators are applied to a time series then they reduce to approximating ordinary differentiation. Fig. 3.3 shows the stencils of the temporal difference operators.

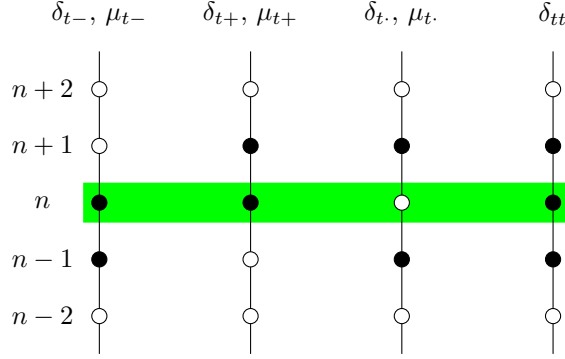


Figure 3.3: Stencils of temporal difference operators, labelled at top, when applied to a grid function at time step n (highlighted in green). Black circle denotes the grid functions that are used, white circles are unused by the operator.

Similarly, the discrete first operators for the spatial derivative, ∂_z , are

$$\delta_{z+} = \frac{w_{z+} - 1}{h}, \quad \delta_{z\cdot} = \frac{w_{z+} - w_{z-}}{2h}, \quad \delta_{z-} = \frac{1 - w_{z-}}{h} \quad (3.8)$$

and the discrete second spatial derivative

$$\delta_{zz} = \delta_{z+}\delta_{z-} = \frac{w_{z+} - 2 + w_{z-}}{h^2} \approx \partial_{zz} \quad (3.9)$$

The stencils of the spatial difference operators are presented in Fig. 3.4.

Averaging operators are used to centre schemes. Temporal averaging operators are

$$\mu_{t+} = \frac{w_{t+} + 1}{2}, \quad \mu_{t\cdot} = \frac{w_{t+} + w_{t-}}{2}, \quad \mu_{t-} = \frac{1 + w_{t-}}{2} \quad (3.10)$$

Spatial averaging operators are

$$\mu_{z+} = \frac{w_{z+} + 1}{2}, \quad \mu_{z\cdot} = \frac{w_{z+} + w_{z-}}{2}, \quad \mu_{z-} = \frac{1 + w_{z-}}{2} \quad (3.11)$$

The centred difference operators can be constructed using difference and averaging operators

$$\delta_{t\cdot} = \delta_{t+}\mu_{t-} = \mu_{t+}\delta_{t-} \quad (3.12a)$$

$$\delta_{z\cdot} = \delta_{z+}\mu_{z-} = \mu_{z+}\delta_{z-} \quad (3.12b)$$

All of the operators mentioned in this section can be applied to functions that are

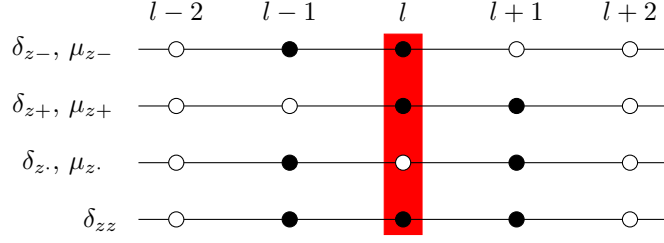


Figure 3.4: Stencils of temporal difference operators, labelled at left, when applied to a grid function at spatial step l (highlighted in red). Black circle denotes the grid functions that are used, white circles are unused by the operator.

approximated on the interleaved grids, e.g.,

$$w_{t+g_{l+1/2}}^{n+1/2} = g_{l+1/2}^{n+3/2}, \quad w_{z-g_{l+1/2}}^{n+1/2} = g_{l-1/2}^{n+1/2} \quad (3.13)$$

3.2.3 Accuracy of discrete operators

Let us now look at the behaviour of the difference operators on continuous functions of one variable. Accuracy of individual operators can be determined by performing a suitable Taylor expansion [156]. Examining the centred time difference operator on the continuous time dependent function $f(t)$ and performing a Taylor expansion around $t = nk$ gives

$$\begin{aligned} \delta_t f(nk) &= \frac{f((n+1)k) - f((n-1)k)}{2k} \\ &= \frac{1}{2k} \left(f(nk) + k \left. \frac{df}{dt} \right|_{t=nk} + \frac{k^2}{2} \left. \frac{d^2f}{dt^2} \right|_{t=nk} + \frac{k^3}{6} \left. \frac{d^3f}{dt^3} \right|_{t=nk} + \dots \right. \\ &\quad \left. - f(nk) + k \left. \frac{df}{dt} \right|_{t=nk} - \frac{k^2}{2} \left. \frac{d^2f}{dt^2} \right|_{t=nk} + \frac{k^3}{6} \left. \frac{d^3f}{dt^3} \right|_{t=nk} - \dots \right) \end{aligned} \quad (3.14)$$

$$= \left. \frac{df}{dt} \right|_{t=nk} + \mathcal{O}(k^2) \quad (3.15)$$

where $\mathcal{O}(\cdot)$ denotes the truncation error; in this case the operator is second order accurate. This tells us that the centred difference operator is a reasonable approximation to the first time derivative at $t = nk$ and deviates from the exact value on the order of the square of the time step.

Performing the same expansion on the forwards difference operator gives

$$\delta_{t+} f(nk) = \frac{1}{k} (f((n+1)k) - f(nk)) \quad (3.16)$$

$$= \frac{1}{k} \left(f(nk) + k \left. \frac{df}{dt} \right|_{t=nk} + \frac{k^2}{2} \left. \frac{d^2f}{dt^2} \right|_{t=nk} + \dots - f(nk) \right) \quad (3.17)$$

$$= \left. \frac{df}{dt} \right|_{t=nk} + \mathcal{O}(k) \quad (3.18)$$

At first glance, it would appear that the forwards difference operator is less accurate than the centred one, since the forwards operator deviates from the exact solution by the order of the time step rather than the square of the time step. However, if we instead take the Taylor

expansion around $t = (n + \frac{1}{2})k$ this results in

$$\delta_{t+} f(nk) = \left. \frac{df}{dt} \right|_{t=(n+\frac{1}{2})k} + \mathcal{O}(k^2) \quad (3.19)$$

In this case the forwards difference operator is second order accurate when expanded in-between the two grid points it uses—this is why interleaved grids are useful for PDE systems using first derivatives (see Section 3.4). Improved accuracy can also be found by using different operators in the scheme—this is not a trivial task and requires effort and intuition to develop the most accurate schemes. Tab. 3.1 shows the expansion points that give second order accuracy for different discrete operators.

Temporal		Spatial	
Operators	Expansion point	Operators	Expansion point
$\delta_{tt}, \delta_{t\cdot}, \mu_{t\cdot}$	$t = nk$	$\delta_{zz}, \delta_{z\cdot}, \mu_{z\cdot}$	$z = lh$
δ_{t+}, μ_{t+}	$t = (n + \frac{1}{2})k$	δ_{z+}, μ_{z+}	$z = (l + \frac{1}{2})h$
δ_{t-}, μ_{t-}	$t = (n - \frac{1}{2})k$	δ_{z-}, μ_{z-}	$z = (l - \frac{1}{2})h$

Table 3.1: Differential operators and the expansion point that gives second order accuracy in time or space.

The type of analysis discussed in this section can be extended to combinations of operators used to approximate a PDE system. In this case, the accuracy is given by the *truncation error* [156] that determines how well the overall scheme approximates the original PDE. Additional forms of determining the accuracy of schemes will be discussed in this work with regards to numerical dispersion.

In general the FDTD operators will be applied to grid functions in the rest of this work.

3.2.4 Inner products and useful identities

To determine the passivity of a numerical scheme, we look to extending the energy methods used throughout Chap. 2 in the discrete setting. As such we require discrete forms of the identities presented in Sec. 2.1.2.

The discrete counterpart to the inner product (2.1) is the discrete inner product. The discrete inner product [71] of two functions, f_l and g_l , that lie over the same spatial domain d is given by

$$\langle f, g \rangle_d = \sum_{l=0}^N h f_l g_l \quad (3.20)$$

The inner product in the discrete domain is therefore the Reimann sum and taking the limit of $h \rightarrow 0$ would produce an integral (as in the continuous case). Other inner products can also be defined such as the weighted inner product

$$\langle f, g \rangle_d^\chi = \sum_{l=0}^N h \chi_l f_l g_l \quad (3.21)$$

where

$$\chi_l = \begin{cases} \frac{1}{2}, & l = 0, N \\ 1, & 0 < l < N \end{cases} \quad (3.22)$$

For the most part, the weighted inner product is the same as the inner product except that the values at the boundary are weighted in a different manner. We can think of these two inner products as different ways of setting the Riemann sums; see Fig. 3.5 for a geometric visualisation of this. The weighted inner product uses the values at the ends of the domain and therefore uses only half rectangles for these points. The inner product has the end points defined part way into the domain and therefore uses full rectangles.

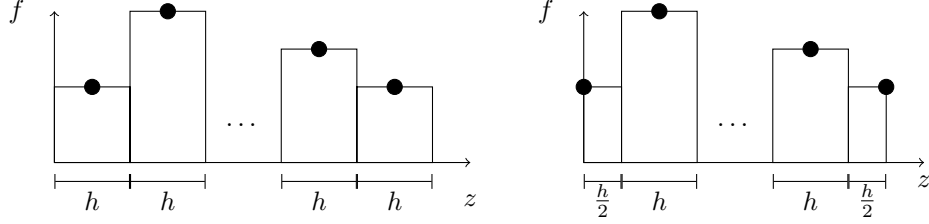


Figure 3.5: Left: Geometric visualisation of inner product. Right: Geometric visualisation of weighted inner product. At the boundaries of the domain, the weighted inner product uses only half a spatial step. Black circles denote the values of f on the spatial grid.

As in the continuous case, the discrete l_2 norm is defined as

$$\|f\|_d = \sqrt{\langle f, f \rangle_d}, \quad \|f\|_d^\chi = \sqrt{\langle f, f \rangle_d^\chi} \quad (3.23)$$

Similarly, the inner product of two functions $f_{l+1/2}$ and $g_{l+1/2}$ that lie on the interleaved grids on the domain \bar{d} is

$$\langle f, g \rangle_{\bar{d}} = \sum_{l=0}^{N-1} h f_{l+1/2} g_{l+1/2} \quad (3.24)$$

$$\|f\|_{\bar{d}} = \sqrt{\langle f, f \rangle_{\bar{d}}} \quad (3.25)$$

The weighted inner product will not be used on this domain.

The following identities (point-wise and summed over the domain since this is independent of time) will be utilised in this work

$$(\delta_t \cdot f)(\delta_{tt} f) = \delta_{t+} \left(\frac{1}{2} (\delta_{t-} f)^2 \right) \implies \langle \delta_t \cdot f, \delta_{tt} f \rangle_d = \delta_{t+} \left(\frac{1}{2} \|\delta_{t-} f\|_d^2 \right) \quad (3.26a)$$

$$(\delta_t \cdot f) f = \delta_{t+} \left(\frac{1}{2} f w_{t-} f \right) \implies \langle \delta_t \cdot f, f \rangle_d = \delta_{t+} \left(\frac{1}{2} \langle f, w_{t-} f \rangle_d^2 \right) \quad (3.26b)$$

$$(\delta_{t+} f) \mu_{t+} f = \delta_{t+} \left(\frac{1}{2} f^2 \right) \implies \langle \delta_{t+} f, \mu_{t+} f \rangle_d = \delta_{t+} \left(\frac{1}{2} \|f\|_d^2 \right) \quad (3.26c)$$

$$(\mu_t \cdot f) f = \mu_{t+} (f w_{t-} f) \implies \langle \mu_t \cdot f, f \rangle_d = \mu_{t+} (\langle f, w_{t-} f \rangle_d) \quad (3.26d)$$

$$(\mu_t \cdot f)(\delta_t \cdot f) = \delta_t \cdot \left(\frac{1}{2} f^2 \right) \implies \langle \mu_t \cdot f, \delta_t \cdot f \rangle_d = \delta_t \cdot \left(\frac{1}{2} \|f\|_d^2 \right) \quad (3.26e)$$

$$f w_{t-} f = (\mu_{t-} f)^2 - \frac{k^2}{4} (\delta_{t-} f)^2 \implies \langle f, w_{t-} f \rangle_d = \|\mu_{t-} f\|_d^2 - \frac{k^2}{4} \|\delta_{t-} f\|_d^2 \quad (3.26f)$$

$$\begin{aligned}\delta_{t+}(fg) &= (\delta_{t+}f)(\mu_{t+}g) + (\mu_{t+}f)(\delta_{t+}g) \\ \implies \delta_{t+}(\langle f, g \rangle_d) &= \langle \delta_{t+}f, \mu_{t+}g \rangle_d + \langle \mu_{t+}f, \delta_{t+}g \rangle_d\end{aligned}\tag{3.26g}$$

$$\begin{aligned}f(\mu_{t+}\mu_{t-}f) &= \mu_{t-}((\mu_{t+}f)^2) - \frac{k^2}{8}\delta_{tt}(f^2) \\ \implies \langle f, \mu_{t+}\mu_{t-}f \rangle_d &= \mu_{t-}(\|\mu_{t+}f\|_d^2) - \frac{k^2}{8}\delta_{tt}(\|f\|_d^2)\end{aligned}\tag{3.26h}$$

These identities hold for all inner products regardless of the domain they are taken over.

The discrete form of integration by parts is summation by parts and in this work we will use forms for the inner product and weighted inner product. Consider two functions f_l and $g_{l+1/2}$ defined over d and \bar{d} respectively. Define another function g'_l over d that is the backwards derivative of $g_{l+1/2}$ so that $g'_l = \delta_{z-}g_{l+1/2}$. Taking the inner product of f_l with g'_l over d gives

$$\begin{aligned}\langle f, g' \rangle_d &= \langle f, \delta_{z-}g \rangle_d = \sum_{l=0}^N h f_l \left(\frac{g_{l+1/2} - g_{l-1/2}}{h} \right) \\ &= - \sum_{l=0}^{N-1} h \left(\frac{f_{l+1} - f_l}{h} \right) g_{l+1/2} - f_0 g_{-1/2} + f_N g_{N+1/2} \\ &= -\langle \delta_{z+}f, g \rangle_{\bar{d}} - f_0 g_{-1/2} + f_N g_{N+1/2}\end{aligned}\tag{3.27}$$

Using summation by parts over interleaved grids, it is natural to change the domains over which the inner product is taken. We can think of this as moving from the normal spatial grid, d , to the interleaved one, \bar{d} . This process also introduces terms that lie outside of the domain—these additional terms must be set through the application of boundary conditions.

A similar process results in the summation by parts identity for the weighted inner product

$$\langle f, \delta_{z-}g \rangle_d^\chi = -\langle \delta_{z+}f, g \rangle_{\bar{d}} - f_0 \mu_{z-}g_{1/2} + f_N \mu_{z-}g_{N+1/2}\tag{3.28}$$

Again, the domain of summation is changed from d to \bar{d} but in this case, the type of inner product changes and the terms at the extremes of the domain are centred at the boundary. The identities (3.27) and (3.28) bear resemblance to those used in the Summation-by-Parts Finite Difference Methods, see, e.g., [158, 172].

The following inequalities will also be used

$$\|\delta_{z+}f\|_{\bar{d}} \leq \frac{2}{h}\|f\|_d^\chi \leq \frac{2}{h}\|f\|_d\tag{3.29a}$$

$$\|\sqrt{g}\delta_{z+}f\|_{\bar{d}} \leq \frac{2}{h}\|\sqrt{\mu_{z-}g}f\|_d\tag{3.29b}$$

which come from summation by parts.

3.2.5 Discrete frequency transforms

The discrete form of the Laplace transform is the Z transform which allows us to analyse discrete time functions in the frequency domain. This should not be confused with the use of z as the axial coordinate; the choice of transform name has been left so as to match with the rest of the literature. In this section we apply them to the infinite domain. The Z transform

of a discrete time series f^n is defined as

$$\hat{f}(e^{sk}) = \sum_{n=-\infty}^{\infty} e^{-skn} f^n \quad (3.30)$$

where it is recalled that s is the complex frequency. If s is restricted to $s = j\omega$ then the Z transform becomes the Discrete time Fourier Transform (DFT)

$$\hat{f}(e^{j\omega k}) = \mathfrak{F}(f) = \sum_{n=-\infty}^{\infty} e^{-j\omega kn} f^n \quad (3.31)$$

For both the discrete Laplace and Fourier transforms the angular frequency is limited so that $-\pi/k \leq \omega \leq \pi/k$.

Under discrete Laplace transformation, the time shifting operators can be interpreted as a multiplication

$$w_{t\pm} f^n \rightarrow (e^{sk})^{\pm 1} \hat{f} \implies w_{t\pm} \rightarrow (e^{sk})^{\pm 1} \quad (3.32)$$

From this, we can write the discrete difference operators in the frequency domain as

$$\delta_{t+} \rightarrow \frac{e^{sk} - 1}{k}, \quad \delta_{t-} \rightarrow \frac{1 - e^{-sk}}{k}, \quad \delta_{t\cdot} \rightarrow \frac{e^{sk} - e^{-sk}}{2k} \quad (3.33a)$$

$$\delta_{tt} \rightarrow \frac{e^{sk} - 2 + e^{-sk}}{k^2} \quad (3.33b)$$

$$\mu_{t+} \rightarrow \frac{e^{sk} + 1}{2}, \quad \mu_{t-} \rightarrow \frac{1 + e^{-sk}}{2} \quad (3.33c)$$

Similarly a discrete spatial Fourier transform can be defined as

$$\hat{g}(e^{j\beta h}) = \sum_{l=-\infty}^{\infty} e^{-j\beta hl} g_l \quad (3.34)$$

where the wavenumber is limited between $-\pi/h \leq \beta \leq \pi/h$. The spatial shifting operators can also be interpreted as a multiplication in the discrete spatial frequency domain

$$w_{z\pm} g_l \rightarrow (e^{j\beta h})^{\pm 1} \hat{g} \implies w_{z\pm} \rightarrow (e^{j\beta h})^{\pm 1} \quad (3.35)$$

This leads to spatial difference operators being represented in the spatial frequency domain as

$$\delta_{z+} \rightarrow \frac{e^{j\beta h} - 1}{h}, \quad \delta_{z-} \rightarrow \frac{1 - e^{-j\beta h}}{h}, \quad \delta_{z\cdot} \rightarrow \frac{e^{j\beta h} - e^{-j\beta h}}{2h} \quad (3.36a)$$

$$\delta_{zz} \rightarrow \frac{e^{j\beta h} - 2 + e^{-j\beta h}}{h^2} \quad (3.36b)$$

$$\mu_{z+} \rightarrow \frac{e^{j\beta h} + 1}{2}, \quad \mu_{z-} \rightarrow \frac{1 + e^{-j\beta h}}{2} \quad (3.36c)$$

Over the infinite domain the discrete wavenumber must be real, which results in the following expressions

$$\delta_{z+} \rightarrow \frac{2je^{\frac{j\beta h}{2}}}{h} \sin\left(\frac{\beta h}{2}\right), \quad \delta_{z-} \rightarrow \frac{2je^{-\frac{j\beta h}{2}}}{h} \sin\left(\frac{\beta h}{2}\right), \quad \delta_{z\cdot} \rightarrow \frac{j}{h} \sin(\beta h) \quad (3.37a)$$

$$\delta_{zz} \rightarrow -\frac{4 \sin^2(\frac{\beta h}{2})}{h^2} \quad (3.37b)$$

$$\mu_{z+} \rightarrow e^{j\frac{\beta h}{2}} \cos\left(\frac{\beta h}{2}\right), \quad \mu_{z-} \rightarrow e^{-j\frac{\beta h}{2}} \cos\left(\frac{\beta h}{2}\right) \quad (3.37c)$$

3.2.6 The bilinear transform

The bilinear transform, also known as the Tustin transform or the trapezoid rule, [180] is a discrete frequency mapping

$$j\omega \rightarrow \frac{2}{k} \frac{1 - e^{-j\tilde{\omega}k}}{1 + e^{-j\tilde{\omega}k}} \quad (3.38)$$

This maps the continuous frequency ω to the discrete frequency $\tilde{\omega}$ and is used, for example, in the wave digital filter [62] and port-Hamiltonian frameworks [60]. This transform is useful as it preserves the passivity of the continuous system. It does, however, introduce frequency warping effects which are highlighted in Fig. 3.6, and will be further investigated in later sections. At low frequencies, the bilinear transform behaves the same way as ordinary frequencies but exhibits increasing deviation with increasing frequency. This is important for synthesis purposes as audible dispersion is produced that requires oversampling to rectify. An additional problem with the use of the bilinear transform is that it can result in implicit numerical schemes for distributed systems that require additional computations to solve.

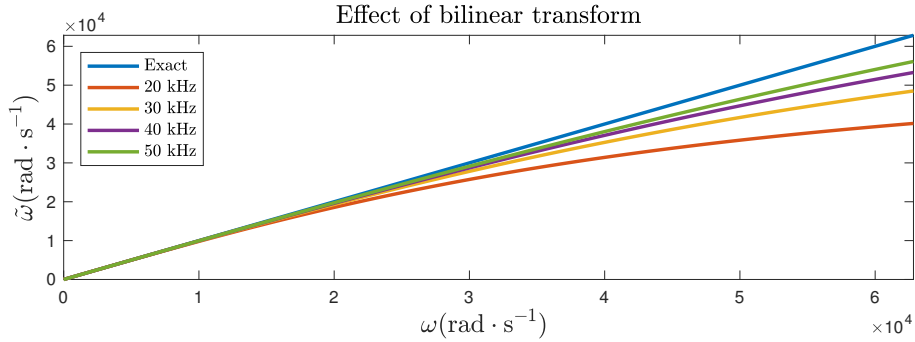


Figure 3.6: Effect of bilinear transform on frequency mapping at different sample rates. At high frequencies, the bilinear transform warps the frequency away from where it is supposed to be represented. This is improved with a higher sample rate but never truly goes away.

The time domain interpretation is

$$\partial_t \rightarrow \mu_{t+}^{-1} \delta_{t+} \quad \text{or} \quad \mu_{t-}^{-1} \delta_{t-} \quad (3.39)$$

where the -1 denotes the inverse of the averaging function.

The bilinear transform can be seen as a specific application of a Möbius transformation that maps the complex plane onto a circle [91]. A similar process, known as the Cayley transform, maps the upper half of the complex domain onto the unit circle [29].

3.3 Scheme design: The wave equation

Now we look at two FDTD schemes that solve the wave equation. This gives an example of how different schemes can be selected, along with highlighting the advantages, and

disadvantages, of using such schemes.

3.3.1 An explicit scheme

First we look at the following scheme that produces an explicit update to model the wave equation (2.17)

$$\frac{\rho_0}{c_0^2} \delta_{tt} \psi_l^n - \rho_0 \delta_{zz} \psi_l^n = 0 \quad (3.40)$$

Here the variables ψ_l^n are grid functions. We can check the accuracy of scheme (3.40) by applying this combination of operators onto the continuous functions $\psi(t, z)$ and performing a Taylor expansion around $t = nk$ and $z = lh$. This gives

$$\frac{\rho_0}{c_0^2} \delta_{tt} \psi - \rho_0 \delta_{zz} \psi = \frac{\rho_0}{c_0^2} \partial_{tt} \psi - \rho_0 \partial_{zz} \psi + \mathcal{O}(k^2, h^2) \quad (3.41)$$

The truncation error is $\mathcal{O}(k^2, h^2)$, so scheme (3.40) is therefore nominally second order accurate in time and space. When $c_0 k/h = 1$, this scheme gives an exact solution to the wave equation and is therefore of infinite accuracy. This exact accuracy at $c_0 k/h = 1$ is also exploited in the DWG framework.

Expanding (3.40) and rearranging for time step $n + 1$, which is assumed to be unknown, gives

$$\psi_l^{n+1} = 2 \left(1 - \left(\frac{c_0 k}{h} \right)^2 \right) \psi_l^n + \left(\frac{c_0 k}{h} \right)^2 (\psi_{l+1}^n + \psi_{l-1}^n) - \psi_l^{n-1} \quad (3.42)$$

3.3.2 Numerical dispersion

Numerical dispersion analysis can be performed on (3.40). Using the frequency domain ansatz

$$\psi_l^n = e^{j\omega nk} e^{j\beta lh} \quad (3.43)$$

and substituting into (3.40) gives the numerical characteristic equation

$$\sin^2 \left(\frac{\omega k}{2} \right) = \left(\frac{c_0 k}{h} \right)^2 \sin^2 \left(\frac{\beta h}{2} \right) \quad (3.44)$$

Rearranging for ω gives the numerical dispersion relation

$$\omega = \pm \frac{2}{k} \sin^{-1} \left(\frac{c_0 k}{h} \sin \left(\frac{\beta h}{2} \right) \right) \quad (3.45)$$

which is to be compared to the frequency independent dispersion relation for the continuous case (2.23).

The numerical dispersion relation gives information on how the discrete scheme affects the propagation behaviour of the system. In general, discretisation leads to dispersion—wave speed is frequency (or wavenumber) dependent. This is evident in the phase and group velocities

$$v_p = \pm \frac{2 \sin^{-1} \left(\frac{c_0 k}{h} \sin \left(\frac{\beta h}{2} \right) \right)}{\beta}, \quad v_g = \pm c_0 \frac{\cos \left(\frac{\beta h}{2} \right)}{\sqrt{1 - \left(\frac{c_0 k}{h} \sin \left(\frac{\beta h}{2} \right) \right)^2}} \quad (3.46)$$

3.3.3 Stability and von Neumann analysis

Although the solutions to the wave equation are bounded in the continuous domain, this is not guaranteed for the discrete case. A method of checking whether the scheme will be stable is von Neumann analysis [156]. The steps in this method are similar to those in the previous section on numerical dispersion but extended to complex frequencies, in order to examine conditions under which exponential growth, or instability can occur. The utility of this technique is limited to the case of constant coefficient PDE systems defined over infinite domains, with some extensions to the analysis of simple boundary conditions available under so-called GKS analysis [71]. In this work we will focus on energy methods to prove stability. However, it is worth briefly covering von Neumann analysis for completeness.

The discrete frequency domain ansatz, this time with complex temporal frequency, is

$$\psi_l^n = e^{snk} e^{j\beta lh} \quad (3.47)$$

where we recall that $s = \sigma + j\omega$. Substituting into scheme (3.40) gives the characteristic equation

$$e^{sk} + 2 \left(2 \left(\frac{c_0 k}{h} \right)^2 \sin^2 \left(\frac{\beta h}{2} \right) - 1 \right) + e^{-sk} = 0 \quad (3.48)$$

Solving for e^{sk} gives

$$e^{sk} = 1 - 2 \left(\frac{c_0 k}{h} \right)^2 \sin^2 \left(\frac{\beta h}{2} \right) \pm 2 \sqrt{\left(1 - 2 \left(\frac{c_0 k}{h} \right)^2 \sin^2 \left(\frac{\beta h}{2} \right) \right)^2 - 1} \quad (3.49)$$

For stable solutions—that is solutions with no exponential growth—then $|e^{sk}| \leq 1$ which means that

$$\left| 1 - 2\lambda^2 \sin^2 \left(\frac{\beta h}{2} \right) \right| \leq 1 \quad (3.50)$$

where $\lambda = c_0 k/h$ is the Courant number [103]. The inequality holds if $\lambda \leq 1$, known as the Courant-Friedrichs-Lewy (CFL) condition [48]. This means there is a bound on the relationship between the temporal grid size and spatial grid size. This can also be determined from inspection of the numerical dispersion relation (3.45); the argument of the arcsine function must lie between -1 and $+1$ which can only be satisfied if the CFL condition is satisfied.

3.3.4 Bandwidth of scheme

Returning to the dispersion relation, we can see that (3.45) can be rewritten as

$$\omega = \pm \frac{2}{k} \sin^{-1} \left(\lambda \sin \left(\frac{\beta h}{2} \right) \right) \quad (3.51)$$

The Courant number therefore gives us information about how much bandwidth is available in the scheme; see Fig. 3.7.

It is clear that the maximum angular frequency is given by

$$\omega_{max} = \frac{2}{k} \sin^{-1}(\lambda) \quad (3.52)$$

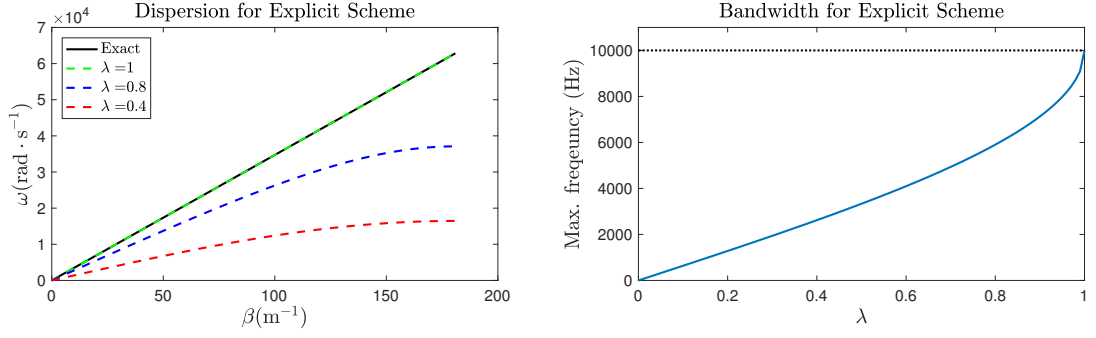


Figure 3.7: Left: Dispersion for scheme (3.40) for different values of λ at a sample rate of 20 kHz. As λ moves away from the CFL condition, frequencies are warped. Right: Bandwidth as a function of λ for the explicit scheme. The dashed line shows the Nyquist frequency.

For the case of $\lambda = 1$, the Nyquist frequency is the highest possible frequency that can be represented by the scheme and the numerical dispersion relation and phase and group velocities are the same as for the continuous case

$$\omega = \pm\beta c_0, \quad v_p = v_g = \pm c_0 \quad (3.53)$$

and the scheme is thus exact. When $\lambda < 1$, so that the h is increased for fixed k , the bandwidth is reduced and frequency warping occurs. The latter is highlighted in Fig. 3.7 as the dispersion relation deviates from the exact form.

3.3.5 Energy analysis

As in the continuous case, we can define a numerical energy for our finite-difference schemes [71]. Henceforth, the time and spatial indices of ψ are suppressed and assumed to be n and l unless otherwise stated. Taking the inner product of $\delta_t \psi$ with scheme (3.40) over d gives

$$\frac{\rho_0}{c_0^2} \langle \delta_t \psi, \delta_{tt} \psi \rangle_d - \rho_0 \langle \delta_t \psi, \delta_{zz} \psi \rangle_d = 0 \quad (3.54)$$

Using summation by parts, (3.27), gives

$$\frac{\rho_0}{c_0^2} \langle \delta_t \psi, \delta_{tt} \psi \rangle_d + \rho_0 \langle \delta_t \delta_{z+} \psi, \delta_{z+} \psi \rangle_{\bar{d}} - \rho_0 \delta_t \psi_0 \delta_{z+} \psi_{-1} + \rho_0 \delta_t \psi_N \delta_{z+} \psi_N = 0 \quad (3.55)$$

Employing (3.26a) and (3.26b) gives

$$\delta_{t+} \mathbf{h}_{we} + \mathbf{b}_{we} = 0 \quad (3.56)$$

where

$$\mathbf{h}_{we} = \frac{\rho_0}{2c_0^2} \|\delta_t \psi\|_d^2 + \frac{\rho_0}{2} \langle \delta_{z+} \psi, w_t - \delta_{z+} \psi \rangle_{\bar{d}} \quad (3.57)$$

is the discrete energy of the system and

$$\mathbf{b}_{we} = -\rho_0 \delta_t \psi_0 \delta_{z+} \psi_{-1} + \rho_0 \delta_t \psi_N \delta_{z+} \psi_N \quad (3.58)$$

is the power gain or loss at the tube boundaries. The power loss term is useful as it suggests strategies for setting numerical boundary conditions.

Unlike in the continuous case, we cannot immediately say that the energy of the system is always non-negative—and therefore cannot say that the solutions are bounded; some further mathematical legwork is required. Using (3.26f), the second term in the discrete energy becomes

$$\begin{aligned} \frac{\rho_0}{2} \langle \delta_{z+}\psi, w_{t-}\delta_{z+}\psi \rangle_{\bar{d}} &= \frac{\rho_0}{2} \left(\|\mu_{t-}\delta_{z+}\psi\|_{\bar{d}}^2 - \frac{k^2}{4} \|\delta_{t-}\delta_{z+}\psi\|_{\bar{d}}^2 \right) \\ &\geq -\frac{\rho_0 k^2}{8} \|\delta_{t-}\delta_{z+}\psi\|_{\bar{d}}^2 \end{aligned} \quad (3.59)$$

From inequality (3.29a) we can then say that

$$\frac{\rho_0 k^2}{8} \|\delta_{t-}\delta_{z+}\psi\|_{\bar{d}}^2 \leq \frac{\rho_0 k^2}{2h^2} \|\delta_{t-}\psi\|_d^2 \quad (3.60)$$

which means that the total discrete energy satisfies

$$\mathfrak{h}_{we} \geq \frac{\rho_0}{2c_0^2} \|\delta_{t-}\psi\|_d^2 - \frac{\rho_0 k^2}{2h^2} \|\delta_{t-}\psi\|_d^2 = (1 - \lambda^2) \frac{\rho_0}{2c_0^2} \|\delta_{t-}\psi\|_d^2 \quad (3.61)$$

The discrete energy is always non-negative provided that

$$1 - \lambda^2 \geq 0 \quad (3.62)$$

which is the same result we get from von Neumann analysis.

The power in using energy analysis rather than von Neumann analysis is that energy methods can be extended to handle variable coefficient PDE systems as well as boundary conditions. This will be demonstrated in Sec. 3.4. On the other hand, von Neumann analysis, when it applies, yields additional useful information regarding numerical dispersion.

3.3.6 Boundary conditions

The boundary terms generated from the energy analysis gives some guidance as to the choice of appropriate difference operators that terminate the system at the boundaries. In this case an obvious choice is

$$\delta_{t-}\psi_0 = 0, \quad \delta_{t-}\psi_N = 0 \quad (\text{Dirichlet}) \quad (3.63a)$$

$$\delta_{z+}\psi_{-1} = 0, \quad \delta_{z+}\psi_N = 0 \quad (\text{Neumann}) \quad (3.63b)$$

However, from Sec. 3.2.3 we can see that the Neumann boundary conditions are not centred about the domain boundary, and thus some degradation in accuracy is to be expected.

The expression for the discrete energy given in (3.57) is consistent with the expression for the continuous energy in the limit as grid spacing becomes small. It is not, however, unique; other choices of inner product are available that result in different choices of boundary conditions, giving more power to this type of approach. If we use the weighted inner product

in the energy analysis we end up with

$$\mathfrak{h}_{we} = \frac{1}{2} (\|\delta_t \psi\|_d^x)^2 + \frac{c_0^2}{2} \langle \delta_z \psi, w_t - \delta_z \psi \rangle_{\bar{d}}, \quad \mathfrak{b}_{we} = c_0^2 (\delta_t \psi_0 \delta_z \psi_0 - \delta_t \psi_N \delta_z \psi_N) \quad (3.64)$$

In this case the Neumann boundary conditions would be

$$\delta_z \psi_0 = 0, \quad \delta_z \psi_N = 0 \quad (3.65)$$

which do offer second order accuracy at $l = 0$ and $l = N$. These Neumann conditions will be called centred.

DWG interpretation of boundary conditions

For the case of $\lambda = 1$, these boundary conditions reduce to DWG terminations [21]. The uncentred FDTD Neumann boundary condition at $l = 0$ is the same as feeding a leftward going wave, $\psi^-(nk, lh)$, into the rightward going wave, $\psi^+(nk, lh)$, with a single time step delay so that

$$\delta_z \psi_0^n = 0 \quad \equiv \quad \psi^+(nk, 0) = \psi^-((n-1)k, 0) \quad (3.66)$$

The centred FDTD Neumann boundary condition is the same application but without the delay

$$\delta_z \psi_0^n = 0 \quad \equiv \quad \psi^+(nk, 0) = \psi^-(nk, 0) \quad (3.67)$$

3.3.7 Modes of the system

We can investigate the effect of these two boundary conditions on the modes of the system in a similar fashion to the continuous case. For simplicity we will operate at the stability limit $\lambda = 1$ so that $\beta = \omega/c_0$, giving a best case scenario. From the dispersion analysis we can write the solutions as

$$\psi_l^n = e^{j\omega kn} \left(A \sin \left(\frac{\omega h l}{c_0} \right) + B \cos \left(\frac{\omega h l}{c_0} \right) \right) \quad (3.68)$$

where A and B are constants determined by boundary conditions. Tab. 3.2 shows the modal solutions and frequencies for the two types of Neumann boundary conditions applied at both ends of the tube.

Boundary condition	Solution	Mode frequencies
Uncentred Neumann	$\psi_{l(m)}^n = B_m e^{j\omega_m n k} \left(\frac{\sin \left(\frac{\omega_m h (l+1)}{c_0} \right) - \sin \left(\frac{\omega_m h l}{c_0} \right)}{\sin \left(\frac{\omega_m h}{c_0} \right)} \right)$	$\omega_m = \frac{m\pi c_0}{h(N+1)},$ $m = 1, 2, \dots$
Centred Neumann	$\psi_{l(m)}^n = B_m e^{j\omega_m n k} \cos \left(\frac{\omega_m h l}{c_0} \right)$	$\omega_m = \frac{m\pi c_0}{hN},$ $m = 1, 2, \dots$

Table 3.2: Modal solutions and modal frequencies for the wave equation solved with the explicit scheme (3.40) using the uncentred and centred Neumann boundary conditions at $l = 0$ and $l = N$.

The centred boundary conditions yield the modal frequencies that are derived from the exact case shown in Tab. 2.1. The uncentred boundary conditions, when used in the same way, have modal frequencies lower than they should be—the tube appears to be of length $L + h$ rather than L . This, however, corresponds to boundaries of the domain set at $l = 0$ and

$l = N$ with l lying over the integers. If, instead, we set l to lie over a half integer domain and use the uncentered boundary conditions, then this will correspond to the correct length¹. If we were to use the centred boundary conditions, the tube will appear to be shorter. This highlights how important it is to think about how we set up our FDTD schemes and how the boundary conditions are selected.

3.3.8 Implementation

Scheme (3.40) can be implemented by either looping over the spatial domain at each time step or, alternatively, using a matrix formulation [21]. As the code generated in this thesis is primarily produced using MATLAB, which is well suited for problems involving matrices, we discuss this implementation here. In addition, explicit schemes have sparse representations, operations which have been optimised in MATLAB.

To implement the matrix formulation, we first define the vector

$$\Psi^n = [\psi_0^n, \dots, \psi_N^n]^T \quad (3.69)$$

then (3.40) can be represented as

$$\Psi^{n+1} = \mathbf{B}\Psi^n - \Psi^{n-1} \quad (3.70)$$

where \mathbf{B} is a sparse square matrix of size $N + 1$. The elements of this matrix, $B_{q,r}$, are defined for the q^{th} row and r^{th} column, where q and r run from 0 to N

$$B_{l,l} = 2(1 - \lambda^2), \quad l = 0, \dots, N \quad (3.71a)$$

$$B_{l,l+1} = \lambda^2, \quad l = 0, \dots, N - 1 \quad (3.71b)$$

$$B_{l,l-1} = \lambda^2, \quad l = 1, \dots, N \quad (3.71c)$$

It should be noted that this indexing makes references to zeroth columns and vectors; this has been done so as to match with the original labelling of the scheme. Pseudocode for such an implementation is shown in Alg. 1.

Algorithm 1 Pseudocode for implementation of explicit FDTD scheme for the wave equation.

```

Define simulation parameters
Construct  $\mathbf{B}$ 
Initialise  $\Psi^{n+1}$ ,  $\Psi^n$ , and  $\Psi^{n-1}$ 
for  $n = 1 \rightarrow$  no. timesteps do
     $\Psi^{n+1} \leftarrow \mathbf{B}\Psi^n - \Psi^{n-1}$ 
     $\Psi^{n-1} \leftarrow \Psi^n$ 
     $\Psi^n \leftarrow \Psi^{n+1}$ 
end for

```

Fig. 3.8 shows solutions to the wave equation calculated using scheme (3.42) after initialising with a Hann pulse.

¹We can use a finite-volume interpretation [103] to understand why different energy analysis allows for different position of the boundaries. For the weighted inner product, we can think of the boundary cells as being half the size of the interior cells which is linked to the factors of a half in the weighted inner product definition. As a result, the flux over the exterior wall of that cell is aligned with the cell centre. In the other case of the inner product, the cell at the boundary is a full cell, hence the extra length. This is linked to Fig. 3.5.

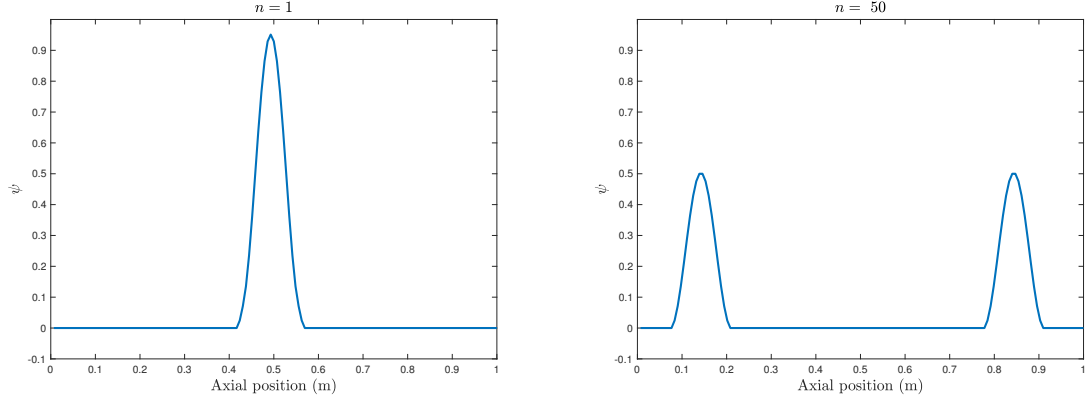


Figure 3.8: Solutions calculated using scheme (3.42) at two time instants. The sample rate is 20 kHz and $\lambda = 1$. The acoustic velocity potential has been initialised with an Hann pulse of width 21 steps.

Boundary conditions can be implemented by modifying the elements of \mathbf{B} . For the uncentred Neumann conditions

$$B_{0,0} = 2 - \lambda^2, \quad B_{N,N} = 2 - \lambda^2 \quad (3.72)$$

For the centred Neumann conditions

$$B_{0,1} = 2\lambda^2, \quad B_{N,N-1} = 2\lambda^2 \quad (3.73)$$

Dirichlet boundary conditions can be implemented by only updating the interior points so that $\Psi = [\psi_1, \dots, \psi_{N-1}]^T$ and \mathbf{B} being a square matrix of size $N - 1$.

$$B_{l,l} = 2(1 - \lambda^2), \quad l = 0, \dots, N - 2 \quad (3.74a)$$

$$B_{l,l+1} = \lambda^2, \quad l = 0, \dots, N - 3 \quad (3.74b)$$

$$B_{l,l-1} = \lambda^2, \quad l = 1, \dots, N - 1 \quad (3.74c)$$

Calculating energy

The energy of the system can be monitored using the summed form [163]

$$\mathfrak{h}_{sum}^{n+1} = \frac{\mathfrak{h}_{we}^{n+1} - \mathfrak{h}_{we}^0 + k \sum_{q=0}^n \mathfrak{b}_{we}^{n+1/2}}{\lfloor \mathfrak{h}_{we}^0 \rfloor_2} = 0 \quad (3.75)$$

which is the discrete form of the integrated energy² (2.41). The operator $\lfloor \cdot \rfloor_2$ denotes rounding to the nearest power of two towards zero so that

$$\lfloor \mathfrak{h}_{we}^0 \rfloor_2 = 2^{\text{fix}(\log_2(\mathfrak{h}_{we}^0))} \quad (3.76)$$

where $\text{fix}(\cdot)$ denotes rounding towards zero.

²Note that in this chapter we shall be considering lossless boundary conditions so $\mathfrak{b}_{we} = 0$.

In practice, the value of \mathfrak{h}_{sum} is never exactly zero due to finite machine precision. We can, however, see bit wise deviations of size 2.2204×10^{-16} which corresponds to machine epsilon in double precision floating point arithmetic; see Fig. 3.9.

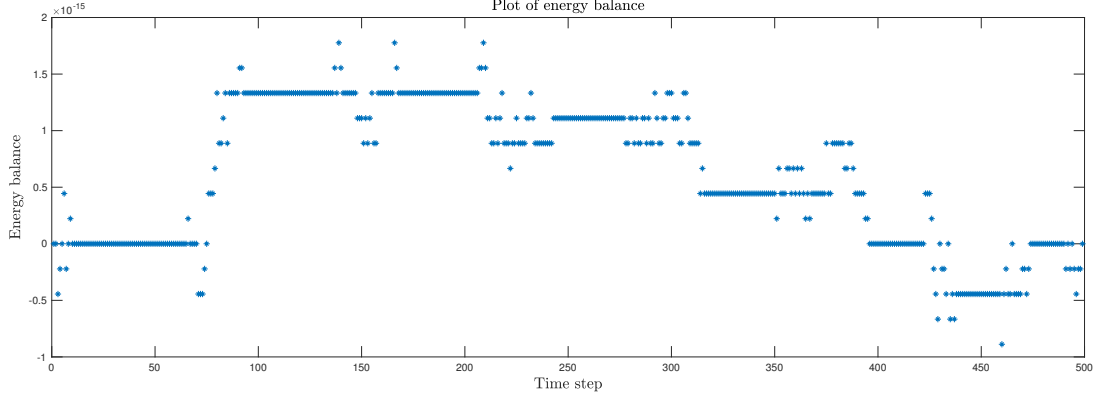


Figure 3.9: Plot of \mathfrak{h}_{sum} for the system in Fig. 3.8. The energy is calculated using the weighted inner product form (3.64).

Monitoring the energy is useful as a debugging tool when creating discrete schemes. Any unexplained deviations beyond machine precision would suggest that there are problems with implementation.

3.3.9 An implicit scheme: Variation on a scheme

An alternative finite-difference scheme can be constructed using the bilinear transform

$$\frac{\rho_0}{c_0^2} (\mu_{t+}^{-1} \delta_{t+}) (\mu_{t-}^{-1} \delta_{t-}) \psi_l^n - \rho_0 \delta_{zz} \psi_l^n = 0 \quad (3.77)$$

or

$$\frac{\rho_0}{c_0^2} \delta_{tt} \psi_l^n - \rho_0 \mu_{t+} \mu_{t-} \delta_{zz} \psi_l^n = 0 \quad (3.78)$$

The method of construction of scheme (3.78) is also known as the Crank-Nicolson method [160]. A similar approach can be applied in the PH framework [60].

The truncation error for the implicit scheme (3.78) is the same as the truncation error of the explicit scheme (3.40): $\mathcal{O}(k^2, h^2)$.

The update for this scheme is given by

$$\begin{aligned} \left(1 + \frac{\lambda^2}{2}\right) \psi_l^{n+1} - \frac{\lambda^2}{4} (\psi_{l+1}^{n+1} + \psi_{l-1}^{n+1}) &= (2 - \lambda^2) \psi_l^n - \left(1 + \frac{\lambda^2}{2}\right) \psi_l^{n-1} \\ &\quad + \frac{\lambda^2}{2} (\psi_{l+1}^n + \psi_{l-1}^n) + \frac{\lambda^2}{4} (\psi_{l+1}^{n-1} + \psi_{l-1}^{n-1}) \end{aligned} \quad (3.79)$$

It is clear that this scheme is implicit, as there are three unknowns at time step $n + 1$.

3.3.10 Numerical dispersion analysis

Using the discrete frequency domain ansatz, (3.43), the numerical dispersion of scheme (3.78) is given by

$$\tan^2\left(\frac{\omega k}{2}\right) = \lambda^2 \sin^2\left(\frac{\beta h}{2}\right) \quad (3.80)$$

or

$$\omega = \pm \frac{2}{k} \tan^{-1}\left(\lambda \sin\left(\frac{\beta h}{2}\right)\right) \quad (3.81)$$

Fig. 3.10 at left shows the dispersion of the implicit scheme for different values of λ . The maximum frequency of this scheme is given by

$$\omega_{max} = \frac{2}{k} \tan^{-1}(\lambda) \quad (3.82)$$

When $\lambda = 1$, $\omega_{max} = \pi/(2k)$ which is half of the total possible frequency bandwidth allowed by the Nyquist theorem for a given time step k , see Fig. 3.10 at right. In fact, it is only in the limit of $\lambda \rightarrow \infty$ that the maximum frequency of the scheme coincides with the Nyquist frequency. As a result, the sample rate must be set sufficiently high, either temporally or spatially, to correctly represent the frequency range of interest.

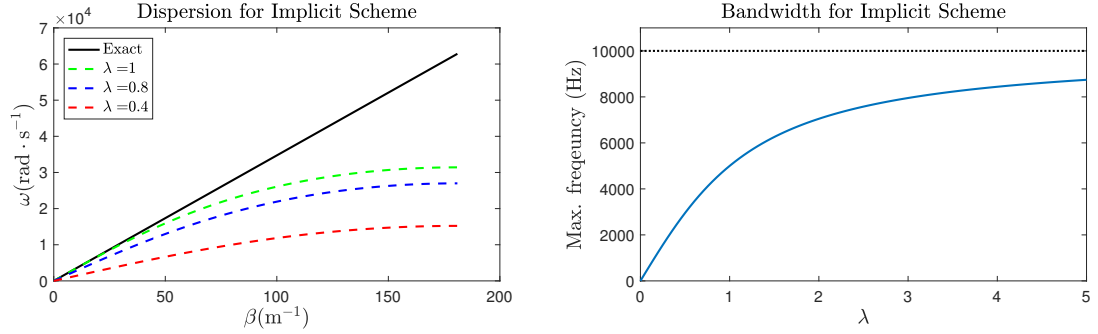


Figure 3.10: Left: Dispersion for scheme (3.78) for different values of λ at a sample rate of 20 kHz. Even for $\lambda = 1$, the dispersion deviates from the exact dispersion relation. Right: Bandwidth of implicit scheme as a function of λ . The dashed line shows the Nyquist frequency which this scheme can never fully achieve.

3.3.11 Energy analysis

Energy analysis for scheme (3.78) can be performed in the same way as in the explicit case by taking the inner product with $\delta_t \psi$ over d

$$\frac{\rho_0}{c_0^2} \langle \delta_t \psi, \delta_{tt} \psi \rangle_d - \rho_0 \langle \delta_t \psi, \mu_{t+} \mu_{t-} \delta_{zz} \psi \rangle_d = 0 \quad (3.83)$$

Using summation by parts and identities (3.26a) and (3.26c)³ gives

$$\delta_{t+} \mathbf{h}_{we}^{(imp)} + \mathbf{b}_{we}^{(imp)} = 0 \quad (3.84)$$

³Recall that $\delta_t = \delta_{t+} \mu_{t-} = \delta_{t-} \mu_{t+}$

where

$$\mathfrak{h}_{we}^{(imp)} = \frac{\rho_0}{2c_0^2} \|\delta_t \psi\|_d^2 + \frac{\rho_0}{2} \|\mu_t - \delta_z \psi\|_d^2 \geq 0 \quad (3.85)$$

and

$$\mathfrak{b}_{we}^{(imp)} = \rho_0 (-\delta_t \psi_0 \mu_t + \mu_t - \delta_z \psi_{-1} + \delta_t \psi_N \mu_t + \mu_t - \delta_z \psi_N) \quad (3.86)$$

It is clear in this case that the discrete energy, $\mathfrak{h}^{(imp)}$, is always non-negative and thus there are no constraints on the grid spacing h or time step k —this scheme is said to be unconditionally stable.

The same procedure can be performed using the weighted inner product to yield centred boundary conditions

$$\mathfrak{h}_{we}^{(imp)} = \frac{\rho_0}{2c_0^2} (\|\delta_t \psi\|_d^2) + \frac{\rho_0}{2} \|\mu_t - \delta_z \psi\|_d^2 \geq 0 \quad (3.87)$$

and

$$\mathfrak{b}_{we}^{(imp)} = \rho_0 (-\delta_t \psi_0 \mu_t + \mu_t - \delta_z \psi_0 + \delta_t \psi_N \mu_t + \mu_t - \delta_z \psi_N) \quad (3.88)$$

3.3.12 Implementation

The implicit scheme is implemented using the matrix-vector form as follows

$$\mathbf{A}\Psi^{n+1} = \mathbf{B}\Psi^n - \mathbf{A}\Psi^{n-1} \implies \Psi^{n+1} = \mathbf{A}^{-1}\mathbf{B}\Psi^n - \Psi^{n-1} \quad (3.89)$$

where \mathbf{A} and \mathbf{B} are sparse $N \times N$ matrices with elements

$$A_{l,l} = 1 + \frac{\lambda^2}{2}, \quad B_{l,l} = 2 - \lambda^2, \quad l = 0, \dots, N \quad (3.90a)$$

$$A_{l,l+1} = -\frac{\lambda^2}{4}, \quad B_{l,l+1} = \frac{\lambda^2}{2}, \quad l = 0, \dots, N-1 \quad (3.90b)$$

$$A_{l,l-1} = -\frac{\lambda^2}{4}, \quad B_{l,l-1} = \frac{\lambda^2}{2}, \quad l = 1, \dots, N \quad (3.90c)$$

Noncentred Neumann conditions can be applied using

$$A_{0,0} = 1 + \frac{\lambda^2}{4}, \quad B_{0,0} = 2 - \frac{\lambda^2}{2} \quad (3.91a)$$

$$A_{N,N} = -\frac{\lambda^2}{4}, \quad B_{N,N} = 2 - \frac{\lambda^2}{2} \quad (3.91b)$$

Centred Neumann conditions can be applied using

$$A_{0,1} = -\frac{\lambda^2}{2}, \quad B_{0,1} = \lambda^2 \quad (3.92a)$$

$$A_{N,N-1} = -\frac{\lambda^2}{2}, \quad B_{N,N-1} = \lambda^2 \quad (3.92b)$$

Fig. 3.11 shows solutions to the wave equation initialised with a Hann pulse solved using the implicit scheme, as was done previously for the explicit scheme. It is clear that dispersion is present in this scheme as there are ripples that lie behind each of the wave fronts—compare to Fig. 3.8 where there are no ripples and the solutions are exact. Fig. 3.12 shows the energy for this system.

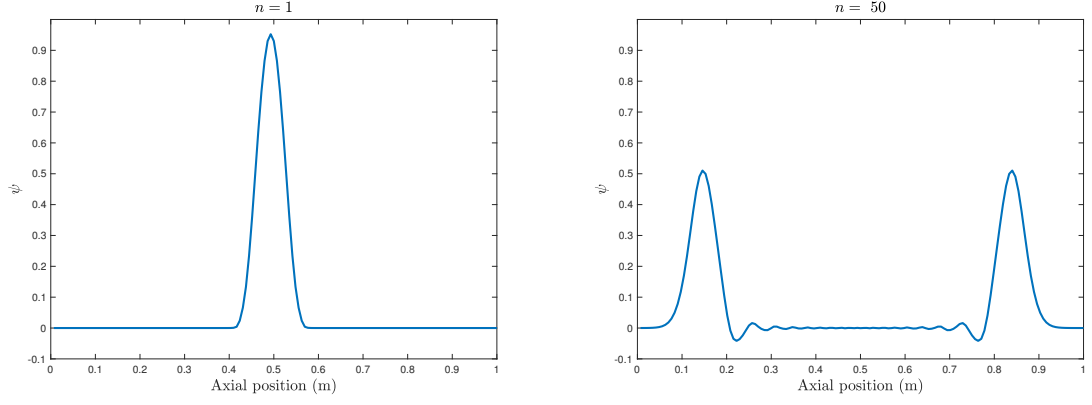


Figure 3.11: Solutions calculated using scheme (3.89) at two time instances. The sample rate is 20 kHz and $\lambda = 1$. The acoustic velocity potential has been initialised with an Hann pulse of width 21 steps. Both sides of the domain are terminated using the centred Neumann conditions.

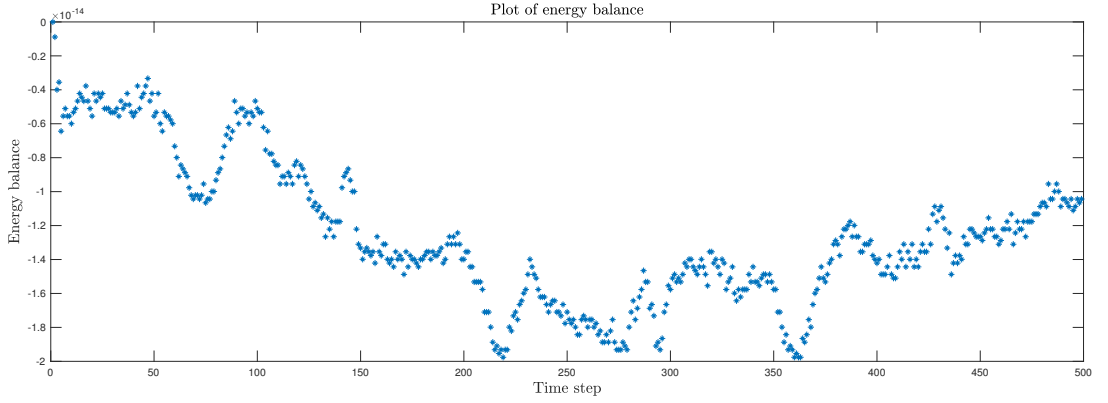


Figure 3.12: Plot of \mathfrak{h}_{sum} for the system in Fig. 3.11. The energy is calculated using the weighted inner product form (3.87).

3.3.13 Explicit vs implicit schemes

As in the continuous time case, a numerical input impedance may be derived using frequency domain analysis. An input impedance for the explicit and implicit schemes can be defined as

$$Z_{in} = \frac{\rho_0}{S_0} \frac{\mathfrak{F}(\delta_t \psi_0^n)}{\mathfrak{F}(\delta_z \psi_0^n)} \quad (3.93)$$

where \mathfrak{F} denotes the discrete Fourier transform.

It is clear from the numerical dispersion analysis that the solutions to both (3.40) and (3.78) are of the form

$$\psi_l^n = e^{j\omega kn} (Ae^{j\beta hl} + Be^{-j\beta hl}) \quad (3.94)$$

where A and B are constants. Assuming a Dirichlet boundary condition at $l = N$, this can be written as

$$\psi_l^n = Ae^{j\omega kn} (e^{j\beta hl} - e^{2j\beta hN} e^{-j\beta hl}) \quad (3.95)$$

so that Z_{in} becomes

$$Z_{in} = -\frac{\rho_0}{S_0} \frac{h}{k} \frac{j \sin(\omega k)}{\sin(\beta h)} \tan(\beta h N) \quad (3.96)$$

We can then substitute the suitable numerical dispersion relations between β and ω for the explicit and implicit schemes to calculate an input impedance. In this case the dispersion relation is given by specifying a velocity at $l = 0$ as an impulse. In practice, $\delta_z \cdot \psi_0^n$ is impulsive in the time domain leading to a unity frequency response with zero phase meaning that the input impedance is related to the Fourier transform of the pressure signal.

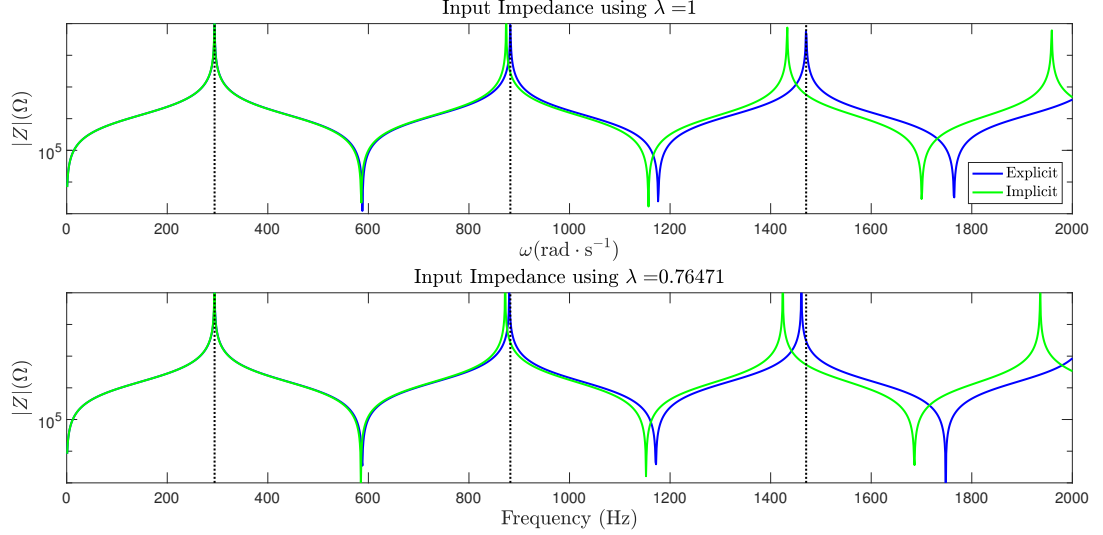


Figure 3.13: Input impedances calculated for a cylinder of length 0.3 m and radius 0.01 m using the explicit (blue) and implicit (green) schemes. Top: Input impedance calculated using $\lambda = 1$. Bottom: Input impedance calculated using $\lambda = 0.7972$. Dashed vertical line show the exact resonances. Sample rate is 20 kHz.

Fig. 3.13 shows the input impedance calculated from the two schemes with reference to the exact calculation. For $\lambda = 1$, the explicit scheme gives the same result as the exact expression whereas the implicit scheme starts to deviate at higher frequencies. For lower values of λ , frequency warping is present in both schemes but is more severe for the implicit scheme.

It is worthwhile to take a moment to compare these explicit and implicit schemes in the context of the desirable properties of a numerical method, outlined at the beginning of this chapter.

Stability

The implicit scheme (3.78) is shown to be unconditionally stable and therefore there are no limits set on the temporal and spatial step sizes. The explicit scheme can also be shown to be stable, but this is conditional on the ratio of the spatial step size to the temporal step size⁴. A lower bound is placed on the spatial step size, therefore, investigations that require a fine spatial resolution require a high temporal sample rate.

⁴This is stated in Theorem 1.6.2 in the text of Strikwerda [156]: *There are no explicit, unconditionally stable, consistent finite-difference schemes for hyperbolic systems of partial differential equations.*

Accuracy

Use of the implicit scheme introduces severe numerical dispersion which, in practice, cannot be fully removed. As a result, frequency warping is present accompanied by reduction of bandwidth. The explicit scheme, on the other hand, displays no numerical dispersion when operating at the stability limit, $\lambda = 1$, allowing for bandwidth up to the Nyquist frequency. When operating away from the stability limit ($\lambda < 1$), some numerical dispersion is introduced but it is not as severe as in the implicit scheme for the same temporal and spatial step sizes. These effects of numerical dispersion are highlighted in the input impedances shown in Fig. 3.13.

Efficiency

Matrix implementation of the implicit scheme uses dense matrices, whereas sparse matrices define the update for the explicit scheme. As such, the computational time differs between the two methods. Using the same relation between temporal and spatial step size ($\lambda = 1$, $T = 26.85^\circ\text{C}$), the temporal loop for a 1 s duration simulation at a temporal sample rate of 20 kHz of a 1 m long tube takes around 0.02 s using the explicit scheme and 0.06 s using the implicit scheme. Simulations were performed in MATLAB R2016b on a 2013 MacBook Pro with 2.8 GHz Intel Core i7 processor. The schemes were implemented in their most optimal manner: the implicit scheme used a full matrix representation⁵, the explicit used a sparse matrix implementation.

Numerical energy and passive numerical methods

In both the explicit and implicit FDTD schemes for the wave equation presented in this chapter, a numerical energy can be defined that is similar in form to that derived from the continuous system. However, the energies for each scheme are distinct from each other and the amount of analysis required to show non-negativity varies—the energy of the implicit scheme is shown to be non-negative immediately, whereas the explicit scheme requires several steps to determine passivity. In addition, the choice of inner product used to define the numerical energy determines how passive boundary conditions are implemented, which, in turn, can have implications on the size of the domain.

Such implicit schemes are employed to guarantee stability for schemes used in the modelling nonlinear wave propagation or collisions [40]. However, implementation of these methods results in longer simulation times. In addition, to achieve a high level of accuracy using these implicit schemes requires using either a finer spatial resolution or a higher temporal sample rate to overcome numerical dispersion, further increasing computational requirements.

Energy balance methods, such as the PH framework, typically employ temporal discretisations that preserve the passivity of the system [57, 109]. An N element PH system is presented in terms of a state vector $\mathbf{x} = [x_0, x_1, \dots, x_N]^T$ and the associated Hamiltonian $H = \sum_{i=0}^N H_i(x_i)$, where H_i gives the energy corresponding to the i^{th} state variable. The temporal behaviour is given by

$$\partial_t \mathbf{x} = \mathbf{J} \nabla_{\mathbf{x}} H \quad (3.97)$$

⁵Use of sparse representation increases the computational time of the implicit scheme to 0.12 s

where \mathbf{J} is a state matrix that describes the interactions between individual elements of the system and $\nabla_{\mathbf{x}}$ is the multi-dimensional gradient with respect to the state variable. For linear storage elements $H_i \propto \frac{1}{2} (x_i)^2$, therefore (3.97) becomes

$$\partial_t \mathbf{x} = \mathbf{J}' \mathbf{x} \quad (3.98)$$

where $\mathbf{J}' \propto \mathbf{J}$ takes into account any constants of proportionality in the definition H_i .

A guaranteed stable discretisation of (3.97) involves using the forwards time difference operator to approximate ∂_t and the following approximation for each element of the multi-dimensional gradient

$$[\nabla_{\mathbf{x}} H]_i \approx \frac{H_i(x_i^{n+1}) - H_i(x_i^n)}{x_i^{n+1} - x_i^n} \quad (3.99)$$

which for linear storage elements becomes

$$[\nabla_{\mathbf{x}} H]_i \approx \frac{1}{2} \frac{(x_i^{n+1})^2 - (x_i^n)^2}{x_i^{n+1} - x_i^n} \quad (3.100)$$

$$\approx \frac{1}{2} (x_i^{n+1} + x_i^n) \quad (3.101)$$

$$\approx \mu_{t+} x_i^n \quad (3.102)$$

The discrete form of (3.97) is therefore

$$\delta_{t+} \mathbf{x} = \mathbf{J}' \mu_{t+} \mathbf{x} \quad (3.103)$$

which is clearly an application of the bilinear transform to (3.98) and will therefore suffer from frequency warping effects.

3.3.14 Schemes for PDEs using first vs. second derivatives

The wave equation does not have to be solved in the form using second derivatives. An equivalent description of the system can be given using differential equations for the acoustic pressure and particle velocity variables. In Torin's thesis [163], a small investigation was made into the differences in results between first and second derivative forms of FDTD schemes for the simple harmonic oscillator. In that study, it was shown that the first derivative forms showed a smaller deviation in the numerical energy calculations than the second derivative forms; the latter was shown to be more sensitive to rounding effects caused by implementation of the scheme.

In the previous chapter, it was shown that the second derivative equation solutions were bounded by their first derivatives of the solutions, whereas the actual solutions were bounded to the first derivative system equations. In this case, the explicit scheme for the wave equation, (3.40) can be recast using pressure, p_l^n , and velocity, $v_{l+1/2}^{n+1/2}$, as

$$\rho_0 \delta_{t-} v - \partial_{z+} p = 0, \quad l \in \bar{d} \quad (3.104a)$$

$$\frac{1}{\rho_0 c_0^2} \partial_t p + \partial_{z-} v = 0, \quad l \in d \quad (3.104b)$$

with corresponding energy balance

$$\mathfrak{h}_{we} + \mathfrak{b}_{we} = 0 \quad (3.105)$$

$$\mathfrak{h}_{we} = \frac{1}{2\rho_0 c_0^2} (\|p\|_d^\chi)^2 + \frac{\rho_0}{2} \langle v, w_{t-} v \rangle_{\bar{d}} \geq 0, \quad \lambda \leq 1 \quad (3.106)$$

$$\mathfrak{b}_{we} = -\mu_{t+} p_0^n \mu_{z-} v_{1/2} + \mu_{5+} p_N^n \mu_{z-} v_{N+1/2} \quad (3.107)$$

In general, in this thesis, we will consider the first derivative PDE system equations for the horn equation although will use the second derivative form for simple discussion of boundary conditions. We shall use the acoustic velocity potential when modelling wave propagation in three-dimensions later in Chap. 4.

3.4 Scheme design: the horn equation

Now, we look at ways of discretising the horn equation. In this case, we are trying to discretise PDE systems with spatially varying coefficients, so the typical frequency domain analysis tools are no longer available for use.

3.4.1 An explicit scheme

An explicit scheme for the transmission line form of the horn equation (2.49) is given by

$$\frac{\bar{S}_l}{\rho_0 c_0^2} \delta_{t+} p_l^n + \delta_{z-} \left(S_{l+1/2} v_{l+1/2}^{n+1/2} \right) = 0, \quad \rho_0 \delta_{t-} v_{l+1/2}^{n+1/2} + \delta_{z+} p_l^n = 0 \quad (3.108)$$

In this case an interleaved scheme has been used, where the spatial and temporal grid points for the velocity field lie between those of the pressure field, see Fig. 3.2. Of course, this could be presented with the grids for pressure and velocity interchanged; (3.108) is just one way to create an explicit scheme. The values \bar{S}_l and $S_{l+1/2}$ are approximations to the surface area on the different grids; see Fig. 3.14.

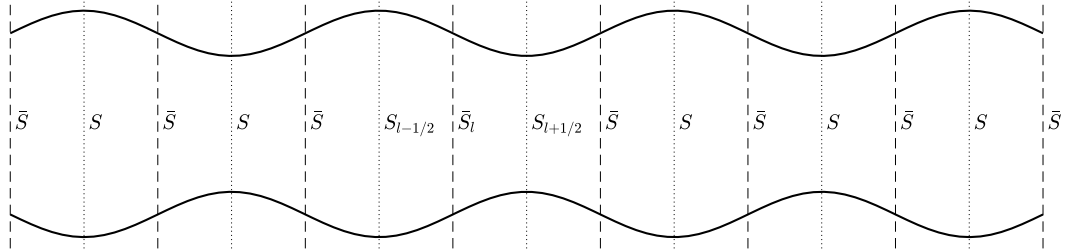


Figure 3.14: Bore profile and surface areas on different grids. Solid line shows the bore profile. Dashed line shows the spatial grid that \bar{S} is calculated on and dotted line shows the grid that S is sampled on.

The update for scheme (3.108) is given by

$$p_l^{n+1} = p_l^n - \frac{\rho_0 c_0 \lambda}{\bar{S}_l} \left(S_{l+1/2} v_{l+1/2}^{n+1/2} - S_{l-1/2} v_{l-1/2}^{n+1/2} \right), \quad l \in d \quad (3.109a)$$

$$v_{l+1/2}^{n+1/2} = v_{l+1/2}^{n-1/2} - \frac{\lambda}{\rho_0 c_0} (p_{l+1}^n - p_l^n), \quad l \in \bar{d} \quad (3.109b)$$

The update for the pressure will require boundary conditions to be chosen at $l = 0$ and $l = N$ —the scheme will require values for $v_{-1/2}$ and $v_{N+1/2}$, respectively, which lie outside the domain. This is not the case for the velocity update, which is entirely determined by values internal to the domain.

Energy analysis

As in the case of dispersion analysis for the continuous horn equation, the spatial inhomogeneity in the system due to the change in cross sectional area means that it is not, in general, possible to perform von Neumann analysis on the scheme for the horn equation. As standard frequency domain analysis cannot be used to determine stability of (3.108) we look for a discrete energy to find bounds on the solutions. Temporal and spatial indices are suppressed and assumed to be n and l for p , and $n + 1/2$ and $l + 1/2$ for v , unless otherwise stated. Spatial indices are also suppressed for the surface areas and assumed to be l for \bar{S} , and $l + 1/2$ for S . Taking the weighted inner product of μ_{t+p} with the first of (3.108) over d gives

$$\frac{1}{\rho_0 c_0^2} \langle \mu_{t+p}, \bar{S} \delta_{t+p} \rangle_d^x + \langle \mu_{t+p}, \delta_{z-} (Sv) \rangle_d^x = 0 \quad (3.110)$$

Summation by parts, (3.28), results in

$$\frac{1}{\rho_0 c_0^2} \langle \mu_{t+p}, \bar{S} \delta_{t+p} \rangle_d^x + \langle \mu_{t+p}, \delta_{z+p} (Sv) \rangle_{\bar{d}} + \mathfrak{b}_{he} = 0 \quad (3.111)$$

where

$$\mathfrak{b}_{he} = -\mu_{t+p} \mu_{z-} (S_{1/2} v_{1/2}) + \mu_{t+p} \mu_{z-} (S_{N+1/2} v_{N+1/2}) \quad (3.112)$$

Substituting the second of (3.108) gives

$$\frac{1}{\rho_0 c_0^2} \langle \mu_{t+p}, \bar{S} \delta_{t+p} \rangle_d^x + \rho_0 \langle \delta_t v, (Sv) \rangle_{\bar{d}} + \mathfrak{b}_{he} = 0 \quad (3.113)$$

Using (3.26b) and (3.26c) results in

$$\delta_{t+} \mathfrak{h}_{he} + \mathfrak{b}_{he} = 0 \quad (3.114)$$

where

$$\mathfrak{h}_{he} = \frac{1}{2\rho_0 c_0^2} \left(\|\sqrt{\bar{S}} p\|_d^x \right)^2 + \frac{\rho_0}{2} \langle Sv, w_{t-} v \rangle_{\bar{d}} \quad (3.115)$$

As for the explicit scheme for the wave equation, it is not immediately obvious that the energy analysis of (3.108) results in a non-negative energy; further work must be done to prove that the solutions are bounded and the scheme is therefore stable.

Using (3.26f) and the second of (3.108), the second term of the numerical energy can be

rewritten as

$$\begin{aligned}
\frac{\rho_0}{2} \langle Sv, w_{t-} v \rangle_{\bar{d}} &\stackrel{(3.26f)}{=} \frac{\rho_0}{2} \left(\|\sqrt{S} \mu_{t-} v\|_{\bar{d}}^2 - \frac{k^2}{4} \|\sqrt{S} \delta_{t-} v\|_{\bar{d}}^2 \right) \\
&\geq -\frac{\rho_0 k^2}{8} \|\sqrt{S} \delta_{t-} v\|_{\bar{d}}^2 \\
&\stackrel{(3.108)}{\geq} -\frac{k^2}{8\rho_0} \|\sqrt{S} \delta_{z+p}\|_{\bar{d}}^2
\end{aligned} \tag{3.116}$$

Using (3.29b) and (3.29a), this can be reinserted into the numerical energy expression so that

$$\begin{aligned}
\mathfrak{h}_{he} &\stackrel{(3.29b)}{\geq} \frac{1}{2\rho_0 c_0^2} \left(\|\sqrt{S} p\|_d^\chi \right)^2 - \frac{k^2}{2\rho_0 h^2} \|\sqrt{\mu_{z-} S} p\|_d^2 \\
&\stackrel{(3.29a)}{\geq} \frac{1}{2\rho_0 c_0^2} \left(\|\sqrt{S} p\|_d^\chi \right)^2 - \frac{k^2}{2\rho_0 h^2} \left(\|\sqrt{\mu_{z-} S} p\|_d^\chi \right)^2 \\
&\geq \frac{1}{2\rho_0 c_0^2} \langle (\bar{S} - \lambda^2 \mu_{z-} S) p, p \rangle_d^\chi
\end{aligned} \tag{3.117}$$

If

$$\bar{S}_l = \mu_{z-} S_{l+1/2} \tag{3.118}$$

then the CFL bound

$$\lambda \leq 1 \tag{3.119}$$

is satisfactory for the energy to be non-negative and therefore the scheme produces bounded solutions. Note in particular that this condition is convenient to use as it is independent of the continuous bore profile.

3.4.2 Boundary conditions

We can see from the definition of \mathfrak{h}_{he} that we can define our boundary conditions from $\mu_{t+} p_0$, $\mu_{t+} p_N$, $\mu_{z-}(S_{1/2} v_{1/2})$ and $\mu_{z-}(S_{N+1/2} v_{N+1/2})$. Since the weighted inner product has been used in calculating an energy these boundary conditions are centred. Lossless boundary conditions are therefore defined by

$$p_0 = 0, \quad p_N = 0, \quad (\text{Dirichlet}) \tag{3.120a}$$

$$\mu_{z-}(S_{1/2} v_{1/2}) = 0, \quad \mu_{z-}(S_{N+1/2} v_{N+1/2}) = 0, \quad (\text{Neumann}) \tag{3.120b}$$

3.4.3 Implementation

Scheme (3.109) can be implemented in matrix form. Defining the vectors for pressure and velocity as $\mathbf{p} = [p_0, \dots, p_N]^T$ and $\mathbf{v} = [v_{1/2}, \dots, v_{N-1/2}]^T$, the scheme can be written as

$$\mathbf{v}^{n+1/2} = \mathbf{v}^{n-1/2} + \mathbf{B} \mathbf{p}^n, \quad \mathbf{p}^{n+1} = \mathbf{p}^n + \mathbf{D} \mathbf{v}^{n+1/2} \tag{3.121}$$

where \mathbf{B} and \mathbf{D} are sparse matrices of size $N \times (N + 1)$ and $(N + 1) \times N$ respectively. The elements of these matrices are given by

$$B_{l,l} = \frac{\lambda}{\rho_0 c_0}, \quad B_{l,l+1} = -\frac{\lambda}{\rho_0 c_0}, \quad l = 0, \dots, N-1 \quad (3.122a)$$

$$D_{l,l} = -\rho_0 c_0 \lambda \frac{S_{l+1/2}}{\bar{S}_l}, \quad l = 0, \dots, N \quad (3.122b)$$

$$D_{l,l-1} = \rho_0 c_0 \lambda \frac{S_{l-1/2}}{\bar{S}_l}, \quad l = 1, \dots, N \quad (3.122c)$$

At the boundaries of the domain, it is sufficient to set the values of \bar{S}_0 and \bar{S}_N to be those given by the continuous case at $z = 0$ and $z = L$, rather than trying to assign a value to $S_{-1/2}$ and $S_{N+1/2}$ outside of the domain for averaging purposes.

For Neumann boundary conditions, elements of \mathbf{D} are modified to

$$D_{0,0} = -2\rho_0 c_0 \lambda \frac{S_{1/2}}{\bar{S}_0}, \quad D_{N,N-1} = 2\rho_0 c_0 \lambda \frac{S_{N-1/2}}{\bar{S}_N} \quad (3.123)$$

Rather than redefining our matrix notation to correctly index surface areas, Dirichlet boundary conditions can be implemented by assigning the boundary entries of \mathbf{B} and \mathbf{D} to zero

$$B_{0,0} = 0, \quad B_{N-1,N} = 0 \quad (3.124a)$$

$$D_{0,0} = 0, \quad D_{N,N-1} = 0 \quad (3.124b)$$

This is equivalent to $p_0^n, p_N^n = 0$.

3.4.4 An implicit scheme

An implicit scheme to model the horn equation is given by

$$\frac{\bar{S}_l}{\rho_0 c_0^2} \delta_{t+} p_l^n = -\delta_{z-} \mu_{t+} \left(S_{l+1/2} v_{l+1/2}^n \right), \quad \rho_0 \delta_{t+} v_{l+1/2}^n = -\delta_{z+} \mu_{t+} p_l^n \quad (3.125)$$

where the pressure and velocity fields are temporally aligned but interleaved with respect to space. Scheme (3.125) results in the update

$$p_l^{n+1} + \frac{\rho_0 c_0 \lambda}{2\bar{S}_l} \left(S_{l+1/2} v_{l+1/2}^{n+1} - S_{l-1/2} v_{l-1/2}^{n+1} \right) = p_l^n - \frac{\rho_0 c_0 \lambda}{2\bar{S}_l} \left(S_{l+1/2} v_{l+1/2}^n - S_{l-1/2} v_{l-1/2}^n \right) \quad (3.126a)$$

$$l \in d$$

$$v_{l+1/2}^{n+1} + \frac{\lambda}{2\rho_0 c_0} (p_{l+1}^{n+1} - p_l^{n+1}) = v_{l+1/2}^n - \frac{\lambda}{2\rho_0 c_0} (p_{l+1}^n - p_l^n), \quad l \in \bar{d} \quad (3.126b)$$

Energy analysis

We again look to produce a discrete energy for (3.125). In this case, the temporal index for v is assumed to be n . Taking the weighted inner product of $\mu_{t+} p$ with the first of (3.125) over d

results in

$$\frac{1}{\rho_0 c_0^2} \langle \mu_{t+p}, \bar{S} \delta_{t+p} \rangle_d^\chi + \langle \mu_{t+p}, \delta_{z-\mu_{t+}}(Sv) \rangle_d^\chi = 0 \quad (3.127)$$

Employing summation by parts, (3.28), results in

$$\frac{1}{\rho_0 c_0^2} \langle \mu_{t+p}, \bar{S} \delta_{t+p} \rangle_d^\chi - \langle \delta_{z+\mu_{t+p}}, \mu_{t+}(Sv) \rangle_{\bar{d}} + \mathfrak{h}_{he}^{(imp)} = 0 \quad (3.128)$$

where

$$\mathfrak{h}_{he}^{(imp)} = -\mu_{t+p_0} \mu_{t+\mu_{z-}}(S_{1/2} v_{1/2}) + \mu_{t+p_N} \mu_{t+\mu_{z-}}(S_{1/2} v_{N+1/2}) \quad (3.129)$$

Then substituting the second of (3.125) and using (3.26c) gives

$$\delta_{t+} \mathfrak{h}_{he}^{(imp)} + \mathfrak{h}_{he}^{(imp)} = 0 \quad (3.130)$$

where

$$\mathfrak{h}_{he}^{(imp)} = \frac{1}{2\rho_0 c_0^2} \left(\|\sqrt{\bar{S}} p\|_d^\chi \right)^2 + \frac{\rho_0}{2} \|\sqrt{S} v\|_{\bar{d}}^2 \geq 0 \quad (3.131)$$

It is clear that the numerical energy for scheme (3.125) is always non-negative, regardless of how the cross sectional area is defined or the choice of spatial step size.

3.4.5 Implementation

Scheme (3.126) can be represented in matrix vector form

$$\mathbf{A} \begin{bmatrix} \mathbf{p}^{n+1} \\ \mathbf{v}^{n+1} \end{bmatrix} = \mathbf{B} \begin{bmatrix} \mathbf{p}^n \\ \mathbf{v}^n \end{bmatrix} \implies \begin{bmatrix} \mathbf{p}^{n+1} \\ \mathbf{v}^{n+1} \end{bmatrix} = \mathbf{A}^{-1} \mathbf{B} \begin{bmatrix} \mathbf{p}^n \\ \mathbf{v}^n \end{bmatrix} \quad (3.132)$$

where \mathbf{A} and \mathbf{B} are square matrices of size $2N + 1$. These matrices can be decomposed in block form as

$$\mathbf{A} = \begin{bmatrix} \mathbf{I}^{(N+1)} & \mathbf{C} \\ \mathbf{D} & \mathbf{I}^{(N)} \end{bmatrix}, \quad \mathbf{B} = \begin{bmatrix} \mathbf{I}^{(N+1)} & -\mathbf{C} \\ -\mathbf{D} & \mathbf{I}^{(N)} \end{bmatrix} \quad (3.133)$$

where $\mathbf{I}^{(N+1)}$ and $\mathbf{I}^{(N)}$ are identity matrices of size $N + 1$ and N , and \mathbf{C} and \mathbf{D} are sparse matrices of size $N + 1 \times N$ and $N \times N + 1$ respectively with element values

$$C_{l,l} = \frac{\rho_0 c_0 \lambda}{2} \frac{S_{l+1/2}}{\bar{S}_l}, \quad l = 0, \dots, N \quad (3.134a)$$

$$C_{l,l-1} = -\frac{\rho_0 c_0 \lambda}{2} \frac{S_{l-1/2}}{\bar{S}_l}, \quad l = 1, \dots, N \quad (3.134b)$$

$$D_{l,l} = -\frac{\lambda}{2\rho_0 c_0}, \quad D_{l,l+1} = \frac{\lambda}{2\rho_0 c_0}, \quad l = 0, \dots, N - 1 \quad (3.134c)$$

Neumann boundary conditions can be applied by modifying the elements of \mathbf{C} to

$$C_{0,0} = \rho_0 c_0 \lambda \frac{S_{1/2}}{\bar{S}_0}, \quad C_{N,N-1} = -\rho_0 c_0 \lambda \frac{S_{N-1/2}}{\bar{S}_N} \quad (3.135)$$

Dirichlet boundary conditions can be implemented in a similar fashion to the explicit

scheme by assigning elements of the system matrices to zero

$$A_{0,0} = 0, \quad A_{N,N} = 0 \quad (3.136a)$$

$$C_{0,0} = 0, \quad C_{N,N-1} = 0 \quad (3.136b)$$

$$D_{0,0} = 0, \quad D_{N-1,N} = 0 \quad (3.136c)$$

3.4.6 Explicit vs. implicit scheme

Unlike the schemes for the wave equation, it is not possible to derive a closed form expression that describes the behaviour of schemes (3.108) and (3.125). This is because they cannot be written in a spatially homogenous way for a changing bore profile. Instead, the simulations must be run for a significant period of time to offer a suitable resolution or a state space solution can be found in the frequency domain.

To calculate an input impedance, a volume velocity is imposed at the input. This leads to system matrices that include a Neumann boundary condition at $l = 0$. The volume velocity injected into the acoustic tube is

$$U^{n+1/2} = \mu_{z-} \left(S_{1/2} v_{1/2}^{n+1/2} \right) \quad (3.137)$$

We can then rewrite the spatial difference operator in terms of the averaging operator

$$\delta_{z-} = \frac{2}{h} (1 - \mu_{z-}) \implies \delta_{z-} \left(S_{1/2} v_{1/2}^{n+1/2} \right) = \frac{2}{h} \left(S_{1/2} v_{1/2}^{n+1/2} - U^{n+1/2} \right) \quad (3.138)$$

which adds a driving term to the update scheme. For the explicit scheme, this become

$$\mathbf{p}^{n+1} = \mathbf{p}^n + \mathbf{D} \mathbf{v}^{n+1/2} + \mathbf{U}^{n+1/2} \quad (3.139)$$

where $\mathbf{U}^{n+1/2} = [2\rho_0 c_0 \lambda U^{n+1/2} / \bar{S}_0, 0, \dots, 0]^T$ is the input volume velocity which is the same size as the pressure vector. A similar approach can be taken for the implicit scheme, where the volume velocity is now centred at integer time steps

$$U^n = \mu_{z-} \left(S_{1/2} v_{1/2}^n \right) \quad (3.140)$$

The update for the implicit scheme is now

$$\begin{bmatrix} \mathbf{p}^{n+1} \\ \mathbf{v}^{n+1} \end{bmatrix} = \mathbf{A}^{-1} \mathbf{B} \begin{bmatrix} \mathbf{p}^n \\ \mathbf{v}^n \end{bmatrix} + \mathbf{U}^{n+1/2} \quad (3.141)$$

where the volume velocity vector is now $\mathbf{U}^{n+1/2} = \mathbf{A}^{-1} [2\rho_0 c_0 \lambda \mu_{t+} U^n / \bar{S}_0, 0, \dots, 0]^T$.

Fig. 3.15 shows the impedances for an exponential horn with a Dirichlet boundary condition at $l = N$, calculated using the explicit and implicit horn equation schemes. These are compared to the exact solution for the horn's input impedance. The simulations were performed at 20 kHz and were run for a duration of 10 s. A value of $\lambda = 0.9838$ was used for both the explicit and implicit simulations. The volume velocities $U^{n+1/2}$ and $\mu_{t+} U^n$ were initialised with a value of unity at $n = 0$ and zero for all other n . The output of the simulations was the pressure at $l = 0$ and these values were temporally averaged with their

previous value to centre the results with the volume velocity⁶. The Discrete Fourier Transform of the output was then taken to give the input impedance⁷. For lossless systems, simulations of the input impedance do not exactly match those of the exact case as we would require extremely long simulation times. We can, however, make comparisons with the position of the maxima of the impedances. The peaks calculated with the explicit scheme show good agreement with the exact case up to 2000 Hz. The implicit scheme begins to display some frequency warping at the second peak. The performance of the implicit scheme could be improved by using a finer grid resolution, which is not possible for the explicit scheme for a fixed sample rate, but this would increase computation time. As stated in the Sec. 3.3.13 for the wave equation, the implicit scheme already takes a longer time to run relative to the explicit scheme (for the same grid spacing); to get the same accuracy as that provided by the explicit scheme would require significantly more computation time.

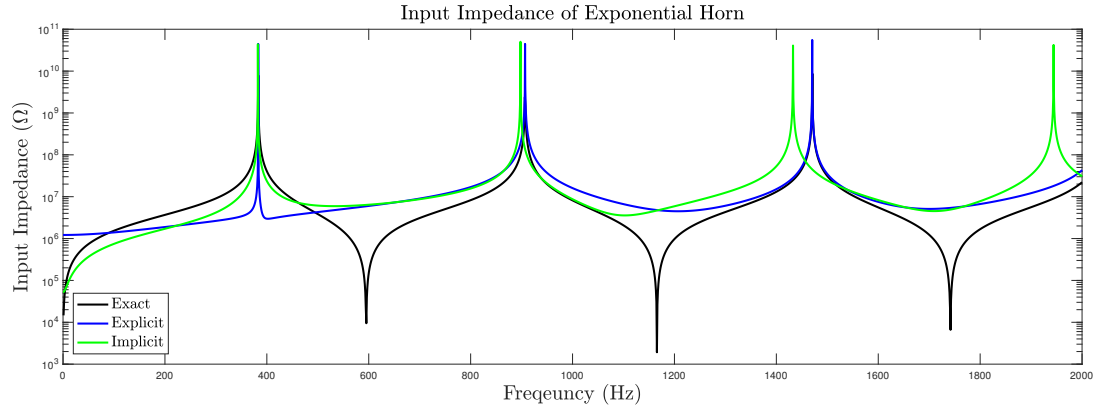


Figure 3.15: Input impedances for an exponential horn of length $L = 0.3$ m, flaring parameter $\alpha = 5 \text{ m}^{-1}$, and opening radius $r_0 = 0.005$ m calculated using the exact expression (black), and explicit finite-difference scheme (blue), and an implicit finite-difference scheme (green). Sample rate is 20 kHz and simulations were run for 10 s.

3.4.7 A note in defence of the bilinear transform

So far it would seem that the bilinear transform is not an appropriate tool for any application in physical modelling, due to its severe frequency warping effects and increased computational load due to implicit solving of equations. However, suitable applications can be found in the next section where its stability preserving property can be taken advantage of. It is even possible to counteract the frequency warping effects when designing numerical filters.

When blindly applied the problems of the bilinear transform outweigh its benefit, but with subtle use its strengths can truly be realised. In the remainder of this work, the explicit scheme will be applied to the lossless part of the problem, the implicit scheme has only been shown to highlight the issues with a blanket application of the bilinear transform [90].

⁶We can treat the injected volume velocity of the implicit scheme, $\mu_{t+}U^n$ as its own individual time series $U^{n+1/2}$ for simplicity. This means, however, that the pressure must be averaged.

⁷The DFT of the volume velocity, in this case, has a magnitude of unity and a phase of zero, hence the DFT of the output gives the input impedance.

3.5 Scheme design: the horn equation with losses

We now consider schemes that model the viscous and thermal effects in acoustic tubes using the approximations presented in the previous chapter. These new schemes will be slight modifications to the explicit scheme used to model the horn equation, with the bilinear transform used to preserve passivity of the models. Unless otherwise stated, the temporal and spatial indices of the pressure variable, p , are n and l , and the indices for the velocity variable, v , are $n + 1/2$ and $l + 1/2$. The spatial indices for the surface areas \bar{S} and S are assumed to be l and $l + 1/2$ respectively.

3.5.1 Model with fractional derivatives

In this section, we consider the Bilbao and Chick model [24] given by (2.94). Immediately it is obvious that something is missing from our current library of FDTD operators—an operator must be created that approximates fractional temporal derivatives.

Approximation to fractional derivatives

Approximations to fractional derivatives have seen much work in the field of control theory. Vinagre *et al.* [171] present a collection of approximations that can be used in both the continuous and discrete time domains. The approximations are generated in the frequency domain and then transformed to the time domain to become either differential equations (in the continuous case) or difference equations (in the discrete case). These approximations include rational functions derived from polynomial series expansions (PSE), continued fractions expansions (CFE), or numerical fitting procedures. One can interpret these approximations as Finite Impulse Response (FIR) or Infinite Impulse Response (IIR) filters, where a PSE will usually generate an FIR filter and a CFE an IIR filter.

For discrete approximations, a generating function, $\tilde{\Omega}$, is chosen to map the continuous frequencies, ω , to the discrete frequencies, $\tilde{\omega}$ so that

$$j\omega \rightarrow \tilde{\Omega}(e^{-j\tilde{\omega}k}) \quad (3.142)$$

Expansion methods are then used to arrive at a discrete approximation. We are already familiar with one such generating function: the bilinear transform

$$\tilde{\Omega}_{bt} = \frac{2}{k} \frac{1 - e^{-j\tilde{\omega}k}}{1 + e^{-j\tilde{\omega}k}} \quad (3.143)$$

Another mapping we have encountered, although not explicitly as a mapping, corresponds to the backwards temporal difference operator

$$\tilde{\Omega}_{\delta_{t-}} = \frac{1}{k} (1 - e^{-j\tilde{\omega}k}) \quad (3.144)$$

Vinagre *et al.* constructed a fractional derivative operator using a CFE on the bilinear transform and CFE and PSE on the backwards time difference operator. Using the PSE on the backwards time difference operator produces the Grünwald-Leitnikov operator, an instance of an FIR filter. Step responses showed that the approximation using the CFE on the bilinear transform best matched the exact response for the discrete case.

Chen and Moore [41] also used the bilinear transform as a generating function but used the Muir-recursion to generate the rational function. They also presented another approximation from the Al-Alaoui operator [3], a weighted mix of backwards time difference operator and bilinear transform, using a CFE.

$$\tilde{\Omega}_{AA} = \frac{8}{7k} \frac{1 - e^{-j\tilde{\omega}k}}{1 + e^{-j\tilde{\omega}k}/7} \quad (3.145)$$

The Al-Alaoui operator was a better fit but this study used a low sample rate relative to that used in musical acoustics. A later review by Chen *et al.* [42] used the CFE on the bilinear transform along with other mixed generating functions.

These methods have been applied in time-domain brass instrument modelling: fitting procedures were used by Bilbao [22, 23] to construct FIR filters, the Grünwald-Leitnikov operator was used by Kemp *et al.* [97], and the CFE of the bilinear transform was used by Bilbao and Chick [24]. For these works, FIR type approximations required more terms than IIR type for a given accuracy, although, in general, FIR types have preferable stability properties.

Haddar *et al.* [72] provide an alternative to direct expansions of fractional order derivatives by replacing them with a diffusive system of differential equations. A quadrature rule must be applied to find appropriate weights for the states of the system, either from expansions or numerical fitting procedures. This method has been applied in works on acoustic tubes by, for example, Lombard *et al.* [107], Lombard and Mercier [106] and Benjamin *et al.* [17].

In this work we follow that of Bilbao and Chick [24] to arrive at a fractional order differentiator by using a CFE on the bilinear transform. In the frequency domain we have

$$(j\omega)^{1/2} \approx \left(\tilde{\Omega}_{bt}\right)^{1/2} = \sqrt{\frac{2}{k} \left(\frac{1 - e^{-j\tilde{\omega}k}}{1 + e^{-j\tilde{\omega}k}}\right)} \quad (3.146)$$

Setting aside the factor $\sqrt{2/k}$ for the moment, a general power series form of the expansion is

$$\sqrt{\left(\frac{1 - e^{-j\tilde{\omega}k}}{1 + e^{-j\tilde{\omega}k}}\right)} \approx \frac{f^{(0)}}{g^{(0)}} \quad (3.147)$$

where $f^{(0)}(e^{-j\tilde{\omega}k})$ and $g^{(0)}(e^{-j\tilde{\omega}k})$ are infinite power series of $e^{-j\tilde{\omega}k}$. We denote the r^{th} term of these functions using subscripts $f_r^{(0)}$ and $g_r^{(0)}$. The CFE is then constructed by using Viscovatov's algorithm [49]. This algorithm proceeds as follows:

$$\begin{aligned} \sqrt{\left(\frac{1 - e^{-j\tilde{\omega}k}}{1 + e^{-j\tilde{\omega}k}}\right)} &\approx \underbrace{\frac{f^{(0)}}{g^{(0)}}}_{\text{Expression}} + \underbrace{\frac{f_0^{(0)}}{g_0^{(0)}} - \frac{f_0^{(0)}}{g_0^{(0)}}}_{+0} \\ &= \frac{f_0^{(0)}}{g_0^{(0)}} + \frac{f^{(0)} - \frac{f_0^{(0)}}{g_0^{(0)}}g^{(0)}}{g^{(0)}} \end{aligned}$$

The constant term in the numerator of the second term cancels out meaning that the

expression can be written

$$\begin{aligned}\sqrt{\left(\frac{1 - e^{-j\tilde{\omega}k}}{1 + e^{-j\tilde{\omega}k}}\right)} &\approx \frac{f_0^{(0)}}{g_0^{(0)}} + \frac{e^{-j\tilde{\omega}k}g^{(1)}}{g^{(0)}} \\ &= \xi^{(0)} + \frac{e^{-j\tilde{\omega}k}}{\frac{f^{(1)}}{g^{(1)}}}\end{aligned}$$

where $\xi^{(0)} = f_0^{(0)}/g_0^{(0)}$, $f^{(1)} = g^{(0)}$ and $g^{(1)} = \frac{f^{(0)} - f_0^{(0)}g^{(0)}/g_0^{(0)}}{e^{-j\tilde{\omega}k}}$. This process can then be repeated on the lowest fraction term. For the i^{th} iteration, the new functions are given as

$$\xi^{(i)} = \frac{f_0^{(i)}}{g_0^{(i)}}, \quad f^{(i)} = g^{(i-1)}, \quad g^{(i)} = \frac{f^{(i-1)} - f_0^{(i-1)}g^{(i-1)}/g_0^{(i-1)}}{e^{-j\tilde{\omega}k}} \quad (3.148)$$

A CFE for the original expression is then of the form

$$\sqrt{\left(\frac{1 - e^{-j\tilde{\omega}k}}{1 + e^{-j\tilde{\omega}k}}\right)} \approx \xi^{(0)} + \frac{e^{-j\tilde{\omega}k}}{\xi^{(1)} + \frac{e^{-j\tilde{\omega}k}}{\ddots}} \quad (3.149)$$

At this point, the expansion is still infinite and therefore must be truncated for it to be used in a numerical scheme. Truncating after $2M$ terms, where M is the final order of the filter, gives

$$\sqrt{\left(\frac{1 - e^{-j\tilde{\omega}k}}{1 + e^{-j\tilde{\omega}k}}\right)} \approx \xi^{(0)} + \frac{e^{-j\tilde{\omega}k}}{\xi^{(1)} + \frac{e^{-j\tilde{\omega}k}}{\ddots + \frac{e^{-j\tilde{\omega}k}}{\xi^{(2M-1)} + \frac{e^{-j\tilde{\omega}k}}{\xi^{(2M)}}}}} \quad (3.150)$$

$$\approx \xi^{(0)} + \frac{e^{-j\tilde{\omega}k}}{\xi^{(1)} + \frac{\xi^{(2M-1)}\xi^{(2M)} + e^{-j\tilde{\omega}k}}{\xi^{(2M)}}} \quad (3.151)$$

The lowest level of the truncated CFE can be rewritten as

$$\frac{b_0^{(1)} + b_1^{(1)}e^{-j\tilde{\omega}k}}{a_0^{(1)}} \quad (3.152)$$

where

$$b_0^{(1)} = \xi^{(2M-1)}\xi^{(2M)}, \quad b_1^{(1)} = 1, \quad a_0^{(1)} = \xi^{(2M)} \quad (3.153)$$

We can then rewrite the entire CFE as a series expansion using the coefficients $b_r^{(i)}$ and $a_r^{(i)}$.

For each iteration, the lowest level can be rewritten in a similar form to (3.153) using

$$b_0^{(i)} = \xi^{(2M-i)}b_0^{(i-1)}, \quad b_r^{(i)} = a_{r-1}^{(i-1)} + \xi^{(2M-i)}b_r^{(i-1)}, \quad r = 1, \dots, i \quad (3.154a)$$

$$a_r^{(i)} = b_r^{(i-1)}, \quad r = 0, \dots, i \quad (3.154b)$$

This leads to a discrete frequency domain approximation to the square root of the imaginary part of the Laplace variable

$$(j\omega)^{1/2} \approx \sqrt{\frac{2}{k}} \frac{\sum_{r=0}^M b_r (e^{-j\tilde{\omega}k})^{-r}}{\sum_{r=0}^M a_r (e^{-j\tilde{\omega}k})^{-r}} \quad (3.155)$$

where b_r and a_r are given by the final iteration of the CFE inversion and they have been normalised so that $a_0 = 1$. This leads to a discrete operator that approximates the fractional derivative

$$\delta_{t^{1/2}} \approx \sqrt{\frac{2}{k}} \left(\sum_{r=0}^M a_r w_{t^-}^{-r} \right)^{-1} \left(\sum_{r=0}^M b_r w_{t^-}^{-r} \right) \quad (3.156)$$

To summarise, the procedure that arrives at an M^{th} order IIR filter that models fractional derivatives is as follows:

1. Construct two infinite power series expansions to the numerator and denominator of the bilinear transform, neglecting the factor $\sqrt{2/k}$
2. Use (3.148) to find the coefficients, ξ , of the CFE up to the $2M^{\text{th}}$ term
3. Rearrange the truncated CFE to create a rational expansion using (3.153) and (3.154) to acquire coefficients a_r and b_r
4. Normalise these coefficients so that $a_0 = 1$

Fig. 3.16 shows the real and imaginary parts of $(j\omega)^{1/2}$, and the approximations constructed from this algorithm for different filter orders. In this case, the power series expansions are arrived at through Taylor's method. For a sample rate of 50 kHz, a filter order

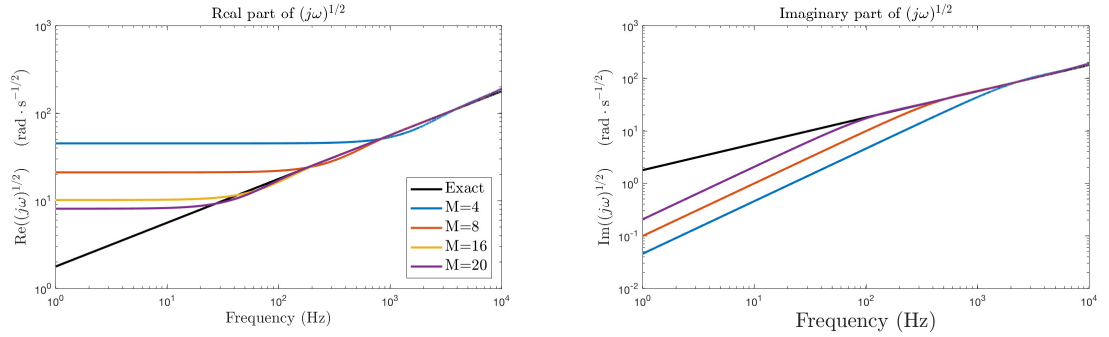


Figure 3.16: Left: Real part of $(j\omega)^{1/2}$. Right: Imaginary part of $(j\omega)^{1/2}$. Black line shows the exact value. Coloured lines show approximations to the fractional derivative using the IIR filter of differing orders constructed from the CFE of the bilinear transform at 50 kHz.

of $M = 20$ is suitable for the frequency range of 20 Hz to 10 kHz. This increases the number of points that need to be stored per update—over the interior of the domain, the lossless scheme requires only the previous values to be stored for both the pressure and velocity updates. A scheme using the fractional derivative would therefore require 40 points per pressure and velocity update when $M = 20$.

The accuracy at lower frequencies would improve if we were to use a higher order filter. However, as the order M of the approximation grows, effects of numerical precision begin to

amount. Fig. 3.17 shows two pole-zero plots. For $M = 20$, all the poles lie within the unit circle. For $M = 33$, we see that a spurious pole has appeared outside of the unit circle, meaning that exponential growth will occur if such a design is used in a simulation routine.

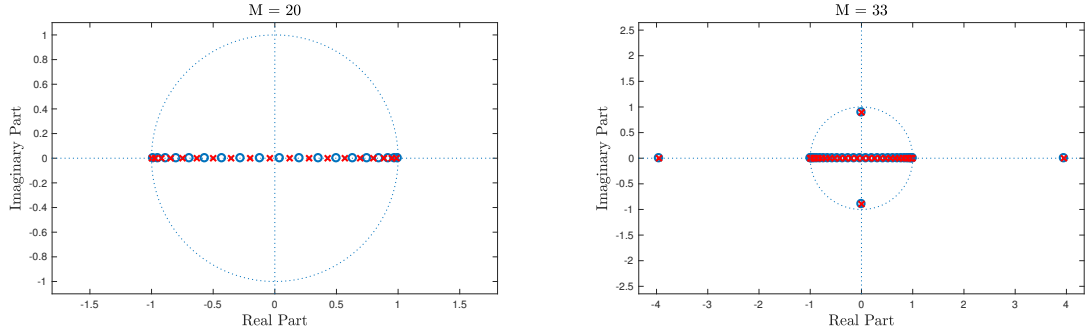


Figure 3.17: Pole-zero plots for fractional derivative filter at 50 kHz. Left: Filter order of 20. Right: Filter order of 33. Poles are marked as red crosses and zeros as blue circles. Dashed vertical and horizontal lines show where the real and imaginary axes lie. Dashed circle is the unit circle.

When the same algorithm is performed with single precision, poles outside of the unit circle are produced at $M = 16$, suggesting that rounding error during the construction of the CFE is the cause of the spurious poles.

Fig. 3.18 shows the frequency response of the CFE applied to the Al-Alaoui operator at 50 kHz. Although the $M = 20$ order filter is better at low frequencies than the one constructed using the bilinear transform, in general the Al-Alaoui operator is worse at higher frequencies. This contradicts what Chen *et al.* [41, 42] said about this operator but they were interested in a lower frequency range than here. We will therefore use the filter constructed using the bilinear transform for the approximation to the fractional derivative.

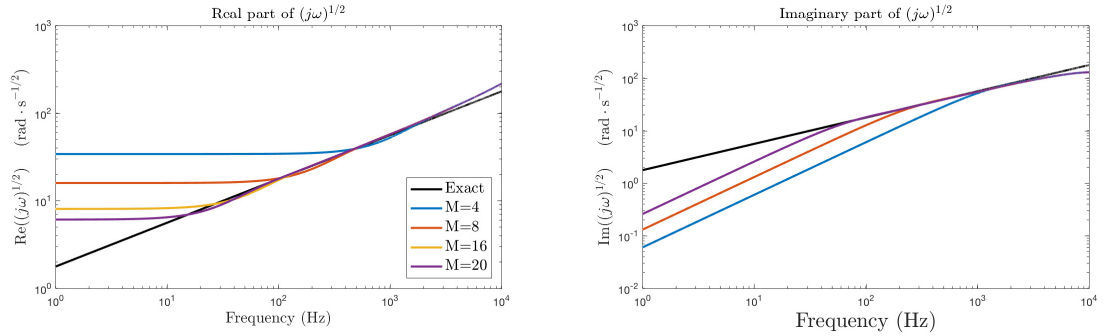


Figure 3.18: Left: Real part of $(j\omega)^{1/2}$. Right: Imaginary part of $(j\omega)^{1/2}$. Black line shows the exact value. Blue, red and orange lines show approximations to the fractional derivative using the IIR filter of order 4 (blue), 8 (red), 16 (orange), and 20 (purple) constructed from the CFE of the bilinear transform at 50 kHz.

Scheme with fractional derivative

A suitable scheme that uses the approximation to the fractional derivative in Eq. (2.94) is

$$\frac{\bar{S}}{\rho_0 c_0^2} \delta_{t+} p + \delta_{z-} (Sv) + q \delta_{t^{1/2}} \mu_{t+} p = 0 \quad (3.157a)$$

$$\rho_0 \delta_{t-} v + \delta_{z+} p + f \mu_{t-} v + g \delta_{t^{1/2}} \mu_{t-} v = 0 \quad (3.157b)$$

where

$$f_{l+1/2} = 3 \frac{\eta \pi}{S_{l+1/2}}, \quad g_{l+1/2} = 2 \sqrt{\frac{\rho_0 \eta \pi}{S_{l+1/2}}}, \quad q_l = \frac{2(\gamma - 1)}{\nu c_0^2} \sqrt{\frac{\eta \pi \bar{S}_l}{\rho_0^3}} \quad (3.158)$$

In constructing this scheme, we hope to preserve some of the properties of the explicit lossless model, namely the good dispersion characteristics, whilst preserving the passivity of the system by applying the bilinear transform to the lossy part of the model. However, passivity via energy analysis has not been shown for this scheme.

Multiplying (3.157) by $\sum_{r=0}^M a_r w_{t-}^r$ and rearranging gives the following update

$$p_l^{n+1} = \sum_{r=0}^M Q_{pp}^{(r)} w_{t-}^r p_l^n - Q_{pv}^{(r)} w_{t-}^r \delta_{z-} (S_{l+1/2} v_{l+1/2}^{n+1/2}), \quad l = 0, \dots, N \quad (3.159a)$$

$$v_{l+1/2}^{n+1/2} = \sum_{t=0}^M Q_{vv}^{(r)} w_{t-}^r v_{l+1/2}^{n-1/2} - Q_{vp}^{(r)} w_{t-}^r (\delta_{z+} p_l^n), \quad l = 0, \dots, N-1 \quad (3.159b)$$

where, for $r = 0, \dots, M$,

$$Q_{pp}^{(r)} = \frac{2\bar{S}_l (a_r - a_{r+1}) - \rho_0 c_0^2 k q_l (b_r + b_{r+1})}{2\bar{S}_l a_0 + \rho_0 c_0^2 k q_l b_0} \quad (3.160a)$$

$$Q_{pv}^{(r)} = \frac{2\rho_0 c_0^2 k a_r}{2\bar{S}_l a_0 + \rho_0 c_0^2 k q_l b_0} \quad (3.160b)$$

$$Q_{vv}^{(r)} = \frac{2\rho_0 (a_r - a_{r+1}) - k (f_{l+1/2} (a_r + a_{r+1}) + g_{l+1/2} (b_r + b_{r+1}))}{(2\rho_0 + k f_{l+1/2}) a_0 + k g_{l+1/2} b_0} \quad (3.160c)$$

$$Q_{vp}^{(r)} = \frac{2k a_r}{(2\rho_0 + k f_{l+1/2}) a_0 + k g_{l+1/2} b_0} \quad (3.160d)$$

The values of a_{M+1} and b_{M+1} are set to zero. Simulation results produced using scheme (3.160) are presented later in Sec. 3.5.4.

Increase in computational load

Introducing the approximation to the fractional derivative to the scheme increases the number of time instances which must be stored: whilst the lossless, explicit horn equation, (3.108), required only the previous values for the pressure and particle velocity, the scheme with the fractional derivative approximation now requires the previous M values to be stored. Ideally, we would choose a value of $M = 20$, increasing the number of previous values tenfold. This in turn increases the amount of calculations required at each spatial sample: the lossless scheme only required three multiplications to update the pressure and velocity; the lossy scheme now requires $3 \times 20 = 60$ multiplications for each sample.

3.5.2 Complete models for Zwicker and Kosten: Foster structure

A discrete form of the Foster network representation, (2.108) - (2.110), is

$$\frac{\bar{S}}{\rho_0 c_0^2} \delta_{t+} p + \delta_{z-} (Sv) + \bar{S}m = 0 \quad (3.161a)$$

$$\rho_0 \delta_{t-} v + \delta_{z+} p + \Delta = 0 \quad (3.161b)$$

$$p = p_0 + \tilde{p}, \quad m = \sum_{q=0}^M m_q, \quad \tilde{p} = \tilde{p}_q + \tilde{p}'_q, \quad q = 1, \dots, M \quad (3.162a)$$

$$m = \hat{C} \delta_{t+} p_0, \quad m_0 = G_0 \mu_{t+} \tilde{p}, \quad m_q = G_q \mu_{t+} \tilde{p}_q = C_q \delta_{t+} \tilde{p}'_q, \quad q = 1, \dots, M \quad (3.162b)$$

$$\Delta = \sum_{q=0}^M \Delta_q, \quad v = v_q + v'_q, \quad q = 1, \dots, M \quad (3.163a)$$

$$\Delta_0 = R_0 \mu_{t-} v, \quad \Delta_q = R_q \mu_{t-} v_q = L_q \delta_{t-} v'_q, \quad q = 1, \dots, M \quad (3.163b)$$

Again this scheme uses the explicit form for the propagation part and the bilinear transform for the losses. The updates for pressure equations are given by

$$p_l^{n+1} = \alpha_l^{(p)} p_l^n + \beta_l^{(p)} \left(S_{l+1/2} v_{l+1/2}^{n+1/2} - S_{l-1/2} v_{l-1/2}^{n+1/2} \right) + \alpha_{0,l}^{(p)} p_{0,l}^n + \sum_{q=1}^M \alpha_{q,l}^{(p)} \tilde{p}_{q,l}^n \quad (3.164a)$$

$$l \in d$$

$$p_{0,l}^{n+1} = \epsilon_l^{(p)} p_{0,l}^n + \nu_l^{(p)} (p_l^{n+1} + p_l^n) + \sum_{q=1}^M v_{q,l}^{(p)} \tilde{p}_{q,l}^n, \quad l \in d \quad (3.164b)$$

$$\tilde{p}_{q,l}^{n+1} = \tau_{q,l}^{(p)} \tilde{p}_{q,l}^n + \xi_{q,l}^{(p)} \left(p_l^{n+1} + p_l^n - p_{0,l}^{n+1} - p_{0,l}^n \right), \quad l \in d \quad (3.164c)$$

where

$$\alpha_l^{(p)} = \frac{1 - E_l \bar{G}_l}{1 + E_l \bar{G}_l}, \quad \beta_l^{(p)} = -\frac{\rho_0 c_0^2 k}{\bar{S}_l h (1 + E_l \bar{G}_l)}, \quad \alpha_{0,l}^{(p)} = \frac{2E_l \bar{G}_l}{1 + E_l \bar{G}_l}, \quad \alpha_{q,l}^{(p)} = \frac{2E_l \bar{G}_{q,l}}{1 + E_l \bar{G}_l} \quad (3.165a)$$

$$\epsilon_l^{(p)} = \frac{2\hat{C}_l - \bar{G}_l k}{2\hat{C}_l + \bar{G}_l k}, \quad \nu_l^{(p)} = \frac{\bar{G}_l k}{2\hat{C}_l + \bar{G}_l k}, \quad v_{q,l}^{(p)} = -\frac{2\bar{G}_{q,l} k}{2\hat{C}_l + \bar{G}_l k} \quad (3.165b)$$

$$\tau_{q,l}^{(p)} = \frac{2C_{q,l} - G_{q,l} k}{2C_{q,l} + G_{q,l} k}, \quad \xi_{q,l}^{(p)} = \frac{G_{q,l} k}{2C_{q,l} + G_{q,l} k} \quad (3.165c)$$

$$\bar{G}_{q,l} = \frac{2C_{q,l} G_{q,l}}{2C_{q,l} + k G_{q,l}}, \quad \bar{G}_l = G_{0,l} + \sum_{q=1}^M \bar{G}_{q,l}, \quad E_l = \frac{\rho_0 c_0^2 k \hat{C}_l}{2\hat{C}_l + \bar{G}_l k} \quad (3.165d)$$

The velocity update is

$$v_{l+1/2}^{n+1/2} = \alpha_{l+1/2}^{(v)} v_{l+1/2}^{n+1/2} + \beta_{l+1/2}^{(v)} (p_{l+1}^n - p_l^n) + \sum_{q=1}^M \alpha_{q,l+1/2}^{(v)} v_{q,l+1/2}^{n-1/2}, \quad l \in \bar{d} \quad (3.166a)$$

$$v_{q,l+1/2}^{n+1/2} = \tau_{q,l+1/2}^{(v)} v_{q,l+1/2}^{n-1/2} + \xi_{q,l+1/2}^{(v)} \left(v_{l+1/2}^{n+1/2} + v_{l+1/2}^{n-1/2} \right), \quad l \in \bar{d} \quad (3.166b)$$

where

$$\alpha_{l+1/2}^{(v)} = \frac{2\rho_0 - k\bar{R}_{l+1/2}}{2\rho_0 + k\bar{R}_{l+1/2}}, \quad \beta_{l+1/2}^{(v)} = -\frac{2k/h}{2\rho_0 + k\bar{R}_{l+1/2}}, \quad \alpha_{q,l+1/2}^{(v)} = \frac{2k\bar{R}_{q,l+1/2}}{2\rho_0 + k\bar{R}_{l+1/2}} \quad (3.167a)$$

$$\tau_{q,l+1/2}^{(v)} = \frac{2L_{q,l+1/2} - kR_{q,l+1/2}}{2L_{q,l+1/2} + kR_{q,l+1/2}}, \quad \xi_{q,l+1/2}^{(v)} = \frac{kR_{q,l+1/2}}{2L_{q,l+1/2} + kR_{q,l+1/2}} \quad (3.167b)$$

$$\bar{R}_{q,l+1/2} = \frac{2L_{q,l+1/2}R_{q,l+1/2}}{2L_{q,l+1/2} + kR_{q,l+1/2}}, \quad \bar{R}_{l+1/2} = R_{0,l+1/2} + \sum_{q=1}^M \bar{R}_{q,l+1/2} \quad (3.167c)$$

Discrete energy analysis

Energy analysis of system (3.161)-(3.163) is as follows. Taking the weighted inner product of (3.161) with $\mu_{t+}p$ over d and using summation by parts gives

$$\delta_{t+} \mathfrak{h}_{he} + \mathfrak{b}_{he} + \langle Sv, \mu_{t+} \Delta \rangle_{\bar{d}} + \langle \mu_{t+} p, \bar{S}m \rangle_d^x = 0 \quad (3.168)$$

It is not clear whether at this point the system is stable, further work must be done to show this.

$$\begin{aligned} \langle Sv, \mu_{t+} \Delta \rangle_{\bar{d}} &\stackrel{(3.163a)}{=} \sum_{q=0}^M \langle Sv, \mu_{t+} \Delta_q \rangle_{\bar{d}} \\ &\stackrel{(3.163a)}{=} \langle Sv, \mu_{t+} \Delta_0 \rangle_{\bar{d}} + \sum_{q=1}^M \langle S(v_q + v'_q), \mu_{t+} \Delta_q \rangle_{\bar{d}} \\ &\stackrel{(3.163b)}{=} \langle Sv, R_0 \mu_{t+} v \rangle_{\bar{d}} + \sum_{q=1}^M \langle Sv_q, R_q \mu_{t+} \mu_{t-} v_q \rangle_{\bar{d}} + \langle Sv'_q, L_q \delta_t \cdot v'_q \rangle_{\bar{d}} \\ &\stackrel{(3.26b)}{=} \delta_{t+} \mathfrak{h}_v + \mathfrak{q}_v \end{aligned} \quad (3.169)$$

where

$$\mathfrak{h}_v = \frac{1}{2} \sum_{q=1}^M \langle v'_q, SL_q w_{t-} v'_q \rangle_{\bar{d}} \quad (3.170a)$$

$$\mathfrak{q}_v = \langle v, SR_0 \mu_{t+} \mu_{t-} v \rangle_{\bar{d}} + \sum_{q=1}^M \langle v_q, SR_q \mu_{t+} \mu_{t-} v_q \rangle_{\bar{d}} \quad (3.170b)$$

$$\begin{aligned}
\langle \mu_{t+p}, \bar{S}m \rangle_d^\chi &\stackrel{(3.162a)}{=} \langle \mu_{t+}(p_0 + \tilde{p}), \bar{S}m \rangle_d^\chi \\
&\stackrel{(3.162a)}{=} \langle \mu_{t+p_0}, \bar{S}m \rangle_d^\chi + \sum_{q=0}^M \langle \mu_{t+\tilde{p}}, \bar{S}m_q \rangle_d^\chi \\
&\stackrel{(3.162b)}{=} \langle \mu_{t+p_0}, \bar{S}m \rangle_d^\chi + \langle \mu_{t+\tilde{p}}, \bar{S}m_0 \rangle_d^\chi + \sum_{q=1}^M \langle \mu_{t+}(\tilde{p}_q + \tilde{p}'_q), \bar{S}m_q \rangle_d^\chi \\
&\stackrel{(3.162b)}{=} \langle \mu_{t+p_0}, \bar{S}\hat{C}\delta_{t+p_0} \rangle_d^\chi + \langle \mu_{t+\tilde{p}}, \bar{S}G_0\mu_{t+\tilde{p}} \rangle_d^\chi \\
&\quad + \sum_{q=1}^M \langle \mu_{t+\tilde{p}_q}, \bar{S}G_q\mu_{t+\tilde{p}_q} \rangle_d^\chi + \langle \mu_{t+\tilde{p}'_q}, \bar{S}C_q\delta_{t+\tilde{p}'_q} \rangle_d^\chi \\
&\stackrel{(3.26c)}{=} \delta_{t+} \mathfrak{h}_t + \mathfrak{q}_t
\end{aligned} \tag{3.171}$$

where

$$\mathfrak{h}_t = \frac{1}{2} \left(\|\sqrt{\bar{S}\hat{C}}p_0\|_d^\chi \right)^2 + \frac{1}{2} \sum_{q=1}^M \left(\|\sqrt{\bar{S}C_q}\tilde{p}'_q\|_d^\chi \right)^2 \geq 0 \tag{3.172a}$$

$$\mathfrak{q}_t = \left(\|\sqrt{\bar{S}G_0}\mu_{t+\tilde{p}}\|_d^\chi \right)^2 + \sum_{q=1}^M \left(\|\sqrt{\bar{S}G_q}\mu_{t+\tilde{p}_q}\|_d^\chi \right)^2 \geq 0 \tag{3.172b}$$

So that the total energy balance of the system is

$$\delta_{t+} (\mathfrak{h}_{he} + \mathfrak{h}_v + \mathfrak{h}_t) + \mathfrak{b}_{he} + \mathfrak{q}_v + \mathfrak{q}_t = 0 \tag{3.173}$$

In this form, it is not clear that the energy of the system is non-negative and we cannot yet say that the solutions are bounded. To prove this, the energy balance must be modified to prove stability.

Modified energy balance

We can rewrite \mathfrak{q}_v using (3.26h) to give

$$\begin{aligned}
\mathfrak{q}_v &= \mu_{t-} \left(\|\sqrt{SR_0}\mu_{t+}v\|_d^2 + \sum_{q=1}^M \|\sqrt{SR_q}\mu_{t+}v_q\|_d^2 \right) - \frac{k^2}{8} \delta_{tt} \left(\|\sqrt{SR_0}v\|_d^2 + \sum_{q=1}^M \|\sqrt{SR_q}v_q\|_d^2 \right) \\
&= \delta_{t+} \mathfrak{h}_{mod} + \mathfrak{q}_{mod}
\end{aligned} \tag{3.174}$$

where

$$\mathfrak{h}_{mod} = -\frac{k^2}{8} \delta_{t-} \left(\|\sqrt{SR_0}v\|_d^2 + \sum_{q=1}^M \|\sqrt{SR_q}v_q\|_d^2 \right) \tag{3.175a}$$

$$\mathfrak{q}_{mod} = \mu_{t-} \left(\|\sqrt{SR_0}\mu_{t+}v\|_d^2 + \sum_{q=1}^M \|\sqrt{SR_q}\mu_{t+}v_q\|_d^2 \right) \geq 0 \tag{3.175b}$$

The change in energy of the system is now given by

$$\delta_{t+} (\mathfrak{h}_{we} + \mathfrak{h}_v + \mathfrak{h}_{mod} + \mathfrak{h}_t) + \mathfrak{q}_{mod} + \mathfrak{q}_t = 0 \tag{3.176}$$

Rewriting \mathfrak{h}_{he} using (3.26f) gives

$$\mathfrak{h}_{he} = \frac{1}{2\rho_0 c_0^2} \left(\|\sqrt{\bar{S}}p\|_d^\chi \right)^2 + \frac{\rho_0}{2} \|\sqrt{S}v\|_d^2 - \frac{\rho_0 k^2}{8} \|\sqrt{S}\delta_{t-v}\|_{\bar{d}} \quad (3.177)$$

Substituting (3.161b) gives

$$\mathfrak{h}_{he} = \frac{1}{2\rho_0 c_0^2} \left(\|\sqrt{\bar{S}}p\|_d^\chi \right)^2 + \frac{\rho_0}{2} \|\sqrt{S}v\|_d^2 - \frac{k^2}{8\rho_0} \|\sqrt{S}\delta_{z+p}\|_{\bar{d}}^2 - \frac{k^2}{8\rho_0} \|\sqrt{S}\Delta\|_{\bar{d}}^2 - \frac{k^2}{4\rho_0} \langle S\delta_{z+p}, \Delta \rangle_{\bar{d}} \quad (3.178)$$

Similarly, \mathfrak{h}_v can be rewritten using (3.26f)

$$\mathfrak{h}_v = \frac{1}{2} \sum_{q=1}^M \|\sqrt{SL_q}\mu_{t-v'_q}\|_{\bar{d}}^2 - \frac{k^2}{4} \|\sqrt{SL_q}\delta_{t-v'_q}\|_{\bar{d}}^2 \quad (3.179)$$

Using (3.26g) on the expression for \mathfrak{h}_{mod} gives

$$\mathfrak{h}_{mod} = -\frac{k^2}{4} \left(\langle SR_0\mu_{t-v}, \delta_{t-v} \rangle_{\bar{d}} + \sum_{q=1}^M \langle SR_q\mu_{t-v_q}, \delta_{t-v_q} \rangle_{\bar{d}} \right) \quad (3.180)$$

Using (3.163) and (3.161b) gives

$$\begin{aligned} \mathfrak{h}_{mod} &= -\frac{k^2}{4} \left(-\frac{1}{\rho_0} \langle S\Delta_0, \delta_{z+p} + \Delta \rangle_{\bar{d}} + \sum_{q=1}^M \langle S\Delta_q, \delta_{t-v} - \delta_{t-v'_q} \rangle_{\bar{d}} \right) \\ &= \frac{k^2}{4} \left(\frac{1}{\rho_0} \langle S\Delta, \delta_{z+p} + \Delta \rangle_{\bar{d}} + \sum_{q=1}^M \|\sqrt{SL_q}\delta_{t-v'_q}\|_{\bar{d}}^2 \right) \end{aligned} \quad (3.181)$$

Combining the new expressions for \mathfrak{h}_{we} , \mathfrak{h}_v and \mathfrak{h}_{mod} gives

$$\begin{aligned} \mathfrak{h}_{we} + \mathfrak{h}_v + \mathfrak{h}_{mod} &= \frac{1}{2\rho_0 c_0^2} \left(\|\sqrt{\bar{S}}p\|_d^\chi \right)^2 + \frac{\rho_0}{2} \|\sqrt{S}v\|_d^2 - \frac{k^2}{8\rho_0} \|\sqrt{\bar{S}}\delta_{z+p}\|_{\bar{d}}^2 \\ &\quad + \frac{k^2}{8\rho_0} \|\sqrt{S}\Delta\|_{\bar{d}}^2 + \frac{1}{2} \sum_{q=1}^M \|\sqrt{SL_q}\mu_{t-v'_q}\|_{\bar{d}}^2 \end{aligned} \quad (3.182)$$

The same reasoning can be applied as for the lossless horn equation to show that

$$\mathfrak{h}_{we} + \mathfrak{h}_v + \mathfrak{h}_{mod} \geq 0, \quad \text{when } \lambda \leq 1, \quad \bar{S}_l = \mu_{z-S_{l+1/2}} \quad (3.183)$$

which is the same condition as for the lossless horn equation. Summarising, this means that

$$\mathfrak{h}_{we} + \mathfrak{h}_v + \mathfrak{h}_{mod} + \mathfrak{h}_t \geq 0 \quad \text{when } \lambda \leq 1, \quad \bar{S}_l = \mu_{z-S_{l+1/2}} \quad (3.184a)$$

$$\mathfrak{q}_{mod} + \mathfrak{q}_t \geq 0 \quad (3.184b)$$

The solutions are therefore bounded.

3.5.3 Frequency warping in Foster structure

We can show that the chosen discretisation of the Foster network is the same as applying the bilinear transform to the lossy part of the impedance. As such, it is a hybrid discretisation rule: the wave-like behaviour of the system is approximated using a low-dispersion explicit method, and losses using the bilinear transform, thus maintaining an explicit algorithm and avoiding the dispersive effects of a globally applied trapezoid rule.

Recall that the total impedance of the system, Z , can be split into lossless, Z_0 , and lossy, Z_v , parts

$$Z = Z_0 + Z_v \quad (3.185)$$

For the scheme using the Foster network, the lossless part is given in the discrete frequency domain by

$$Z_0 = \rho_0 \frac{1 - e^{-j\tilde{\omega}k}}{k} \quad (3.186)$$

Transforming to the discrete frequency domain, and noting that the velocity variable is indexed at $n + 1/2$, gives

$$Z_0(\tilde{\omega}) = \frac{2j}{k} \sin\left(\frac{\tilde{\omega}k}{2}\right) \quad (3.187)$$

In this case the frequency mapping of the lossless part of propagation is given by $\omega \rightarrow \frac{2}{k} \sin\left(\frac{\tilde{\omega}k}{2}\right)$.

The q^{th} branch of the lossy part is given in the continuous frequency domain by

$$Z_{vq}^M(\omega) = \frac{R_q L_q j\omega}{R_q + L_q j\omega} \quad (3.188)$$

Using the bilinear transform so that $\omega \rightarrow \frac{2}{k} \tan\left(\frac{\tilde{\omega}k}{2}\right)$ produces

$$Z_{vq}^M(\tilde{\omega}) = \frac{R_q L_q \frac{2j}{k} \tan\left(\frac{\tilde{\omega}k}{2}\right)}{R_q + L_q \frac{2j}{k} \tan\left(\frac{\tilde{\omega}k}{2}\right)} \quad (3.189)$$

for the discrete lossy impedance.

Returning to the time domain network and transforming (3.163a) and (3.163b) of the velocity update scheme to the discrete frequency domain gives

$$\hat{v} = \hat{v}_q + \hat{v}'_q, \quad \hat{\Delta}_q = \cos\left(\frac{\tilde{\omega}k}{2}\right) R_q \hat{v}_q = \frac{2j}{k} \sin\left(\frac{\tilde{\omega}k}{2}\right) L_q \hat{v}'_q \quad (3.190)$$

where \hat{v} , \hat{v}_q , \hat{v}'_q , and $\hat{\Delta}_q$ are the discrete Fourier transforms of the particle velocity and q^{th} branch currents and voltages of the Foster network. The factor $e^{j\frac{\tilde{\omega}k}{2}}$, resulting in the cos and sin terms, occurs because the time series Δ^n is aligned with the integer labelled time series but the currents are aligned at the half integer time series. Combining these equations gives

$$\begin{aligned} \hat{v} &= \left(\frac{1}{\cos\left(\frac{\tilde{\omega}k}{2}\right) R_q} + \frac{k}{2j \sin\left(\frac{\tilde{\omega}k}{2}\right) L_q} \right) \hat{\Delta}_q \\ &= \left(\frac{2j \sin\left(\frac{\tilde{\omega}k}{2}\right) L_q + k \cos\left(\frac{\tilde{\omega}k}{2}\right) R_q}{2j \cos\left(\frac{\tilde{\omega}k}{2}\right) \sin\left(\frac{\tilde{\omega}k}{2}\right) L_q R_q} \right) \hat{\Delta}_q \\ \implies \hat{\Delta}_q &= \frac{R_q L_q \frac{2j}{k} \tan\left(\frac{\tilde{\omega}k}{2}\right)}{R_q + L_q \frac{2j}{k} \tan\left(\frac{\tilde{\omega}k}{2}\right)} \hat{v} = Z_{vq}^M(\tilde{\omega}) \hat{v} \end{aligned} \quad (3.191)$$

From this we can see that the voltage, Δ_q , is given by the q^{th} branch of the impedance Z_v^M where the angular frequency has been mapped to the discrete frequency domain using the bilinear transform. However, the lossless part of the scheme uses a different frequency mapping that results in the explicit scheme. The same process can be shown for the pressure scheme.

The use of the bilinear transform in the discretisation of the Foster network results in frequency warping that reduces the accuracy of the optimised network at high frequencies. This effect is shown in Figs. 3.19 and 3.20 where the errors for the networks calculated in the previous chapter using E_M are calculated using the warped frequency $\tilde{\omega}$ and compared to the exact.

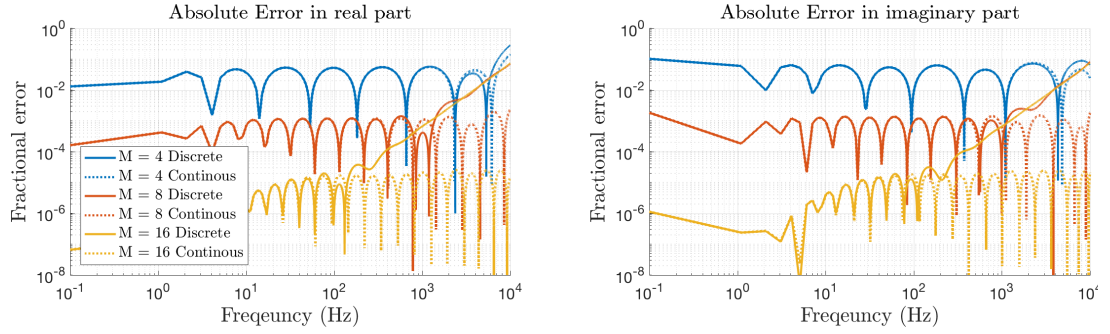


Figure 3.19: Errors in impedance when calculated using the bilinear transform at a sample rate of 50 kHz (solid lines) and the exact frequency (dashed) for the Foster network optimised using E_M over 0 Hz to 10 kHz. Left: Error in real part. Right: Error in imaginary part.

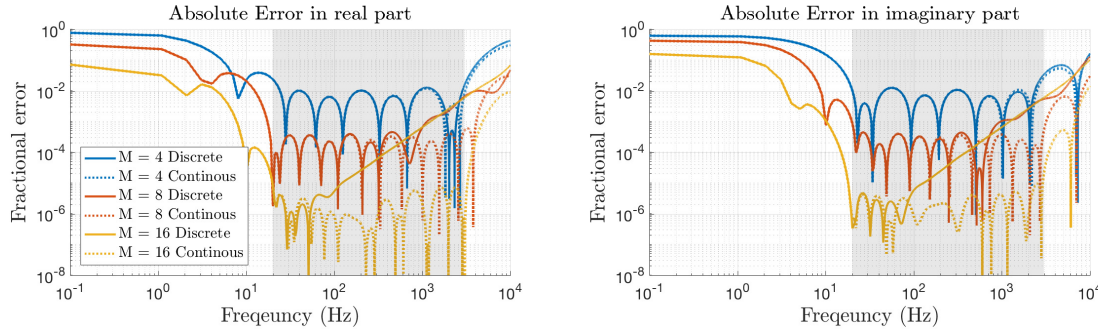


Figure 3.20: Errors in impedance when calculated using the bilinear transform at a sample rate of 50 kHz (solid lines) and the exact frequency (dashed) for the Foster network optimised using E_M over 20 Hz to 3 kHz. Left: Error in real part. Right: Error in imaginary part. Grey box shows optimisation range.

For $M = 4$, there is little impact on the accuracy of the networks when the bilinear transform is applied. However, for $M = 8$ and $M = 16$, there is a clear reduction in accuracy at higher frequencies.

To rectify this, the frequencies can be ‘pre-warped’ [25] in the optimisation procedure by using

$$\tilde{\omega}' = \frac{2}{k} \tan^{-1} \left(\frac{\omega k}{2} \right) \quad (3.192)$$

The network impedances are then given as functions of these pre-warped frequencies $Z_v^M(\tilde{\omega}')$,

whilst the original impedance we are approximating is left as a function of the continuous frequency. The cost function to optimise over the magnitude function becomes

$$E'_M = \frac{1}{2} \sum_{r=0}^R \left(\frac{|Z_v(\omega_r) - Z_v^M(\tilde{\omega}'_r)|}{|Z_v(\omega_r)|} \right)^2 \quad (3.193)$$

Using the new cost function will maintain the accuracy when applied in the discrete domain as shown in Figs. 3.21 and 3.22. Here the error remains relatively flat over the optimisation range.

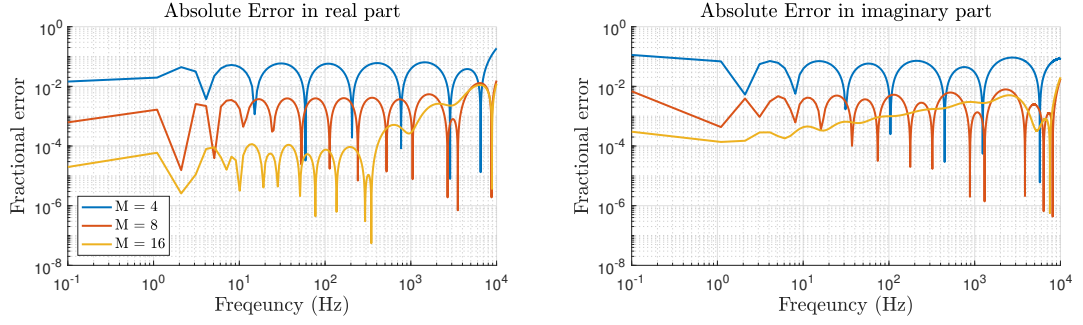


Figure 3.21: Errors in impedance calculated using the bilinear transform at 50 kHz for the Foster network optimised using E'_M over 0 Hz to 10 kHz with pre-warped frequencies. Left: Error in real part. Right: Error in imaginary part.

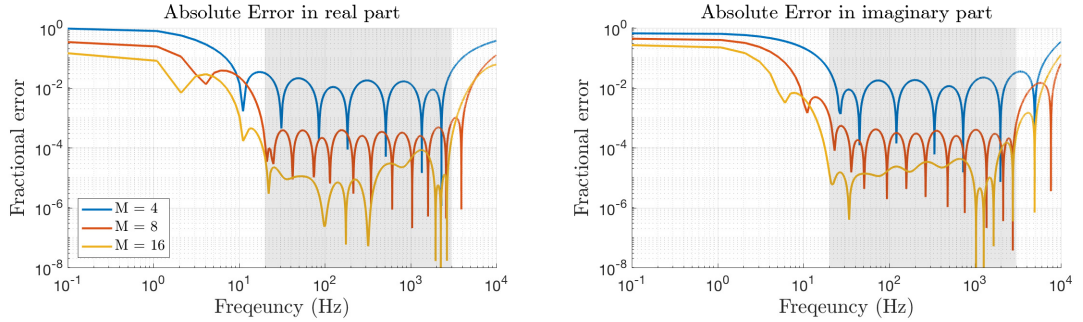


Figure 3.22: Errors in impedance calculated using the bilinear transform at 50 kHz for the Foster network optimised using E'_M over 20 Hz to 3 kHz with pre-warped frequencies. Left: Error in real part. Right: Error in imaginary part. Grey box shows optimisation range.

Increase in computational load

For each pressure update for the Foster structure there are:

- $4 + M$ multiplications to update the pressure p_l
- $3 + M$ multiplications to update the equivalent voltage p_0
- $M \times 5$ to update all of the equivalent voltages \tilde{p}'_q

To update the pressure therefore requires $7 + 7M$ multiplications. For $M = 16$, a total of 116 multiplications are required, more than twice the amount required for the scheme using the

approximation to the fractional derivative. However, for $M = 4$, we require 35 multiplications, which is less than half required for the scheme using the fractional derivative.

3.5.4 Comparison of loss models

Here we compare input impedances simulated using the FDTD schemes presented in this chapter that include viscous and thermal losses and compare with results using the TMM. Two cases are considered: a cylinder of length 1 m and radius 0.005 m, and an exponential horn of length 0.5 m with radii of 0.005 m and 0.05 m at the entrance and exit of the horn. The cylinder is representative of the cylindrical portion of a trumpet, the exponential horn is similar to the flaring portion of a trumpet. All FDTD simulations were performed at 50 kHz with a simulation duration of 10 s. Volume velocities were injected using (3.138) and the tubes were terminated with a Dirichlet boundary condition at the end so that $p_N^n = 0$ for all n . The first 8 peak positions and corresponding magnitudes of the input impedance were calculated using a quadratic fitting procedure.

Cylinder results

Here we present input impedances calculated for a cylindrical acoustic tube. Fig. 3.23 shows the results using the loss model of Bilbao and Chick, scheme (3.160). The input impedance magnitudes and angle do not match the TMM computation at low frequencies; this is where the fractional derivative approximation varies greatly from the exact response. There is a better match at higher frequencies where peaks emerge. The peak positions have an error less than 3% when $M = 4$ and between $10^{-4}\%$ and $10^{-2}\%$ when $M = 20$. The accuracy of the peak position tends to improve at higher frequencies. Peak magnitude error is high for low order filters but improves to be on the order of 1% and below for high order filters.

Figs. 3.24-3.25 show impedances calculated using scheme (3.164) and (3.166) that simulate the Foster network using network values acquired from E'_M using the frequency ranges 0.1 Hz to 10 kHz and 20 Hz to 3 kHz respectively. The impedance calculated using values from the wider frequency range fits the TMM computation well over the full frequency range presented; since filters were fit at 0.1 Hz there isn't the deviation at low frequencies seen in Fig. 3.23. Peak position errors are all less than 0.1% for all structures except for the first peak when $M = 4$, which has an error less than 1%. Peak position error is less than 3% for the $M = 8$ and $M = 16$ structures and less than 7% for the $M = 4$ structure.

The input impedance calculated using the network values optimised over the reduced range differs from the TMM calculation at low frequencies for all filter structures and at high frequencies for $M = 4$. However, there is good agreement over the optimised frequency range, which is where the first 8 peaks lie. Peak position errors are less than 0.1% and peak magnitude errors are less than 3% for all filter structures.

Run times over the temporal loop for the simulations using different filters were:

- 21.77 s for Bilbao and chick model ($M = 20$)
- 27.65 s for the Foster structure ($M = 16$)
- 18.49 s for the Foster structure ($M = 8$)
- 14.03 s for the Foster structure ($M = 4$)

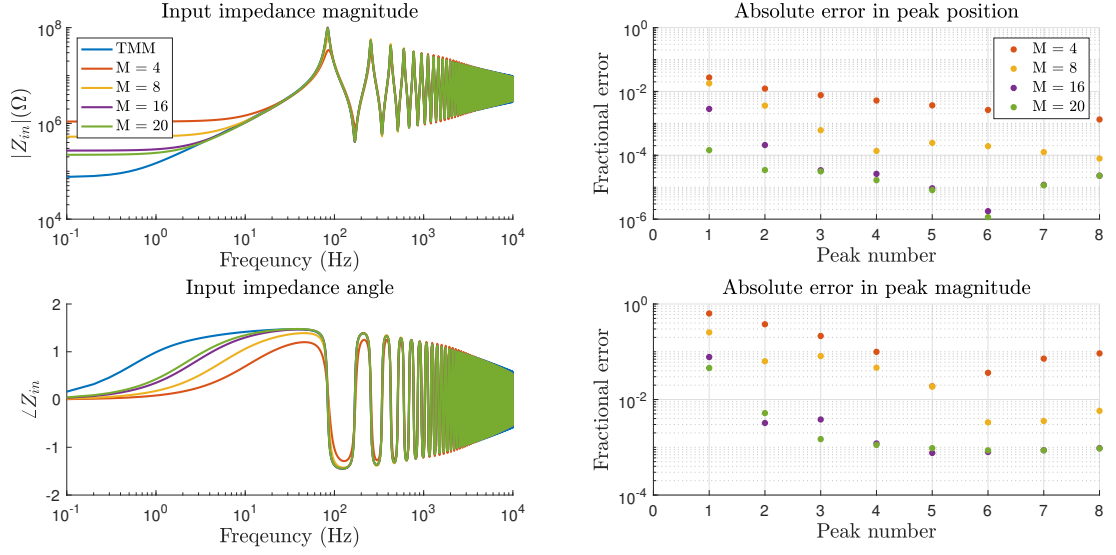


Figure 3.23: Input impedance calculated using the loss model of Bilbao and Chick for different filter orders. Top left: Input impedance magnitude. Bottom left: Input impedance phase. Top right: Absolute percentage error in input impedance peak position relative to TMM. Bottom right: Absolute percentage error in input impedance peak magnitude.

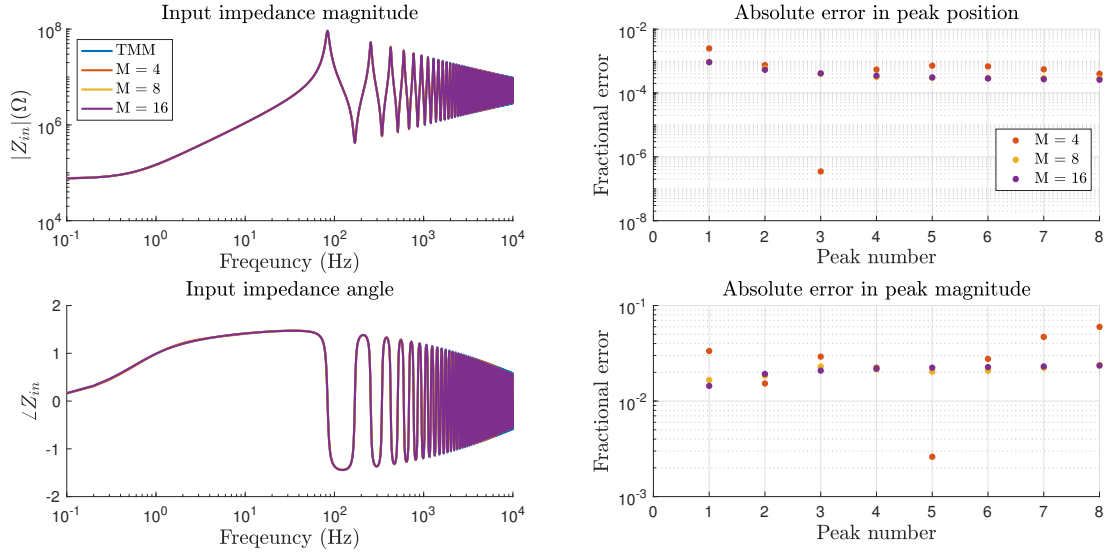


Figure 3.24: Input impedance calculated using the Foster network with coefficients acquired by optimising of E'_M from 0 Hz to 10 kHz. Top left: Input impedance magnitude. Bottom left: Input impedance phase. Top right: Absolute percentage error in input impedance peak position relative to TMM. Bottom right: Absolute percentage error in input impedance peak magnitude.

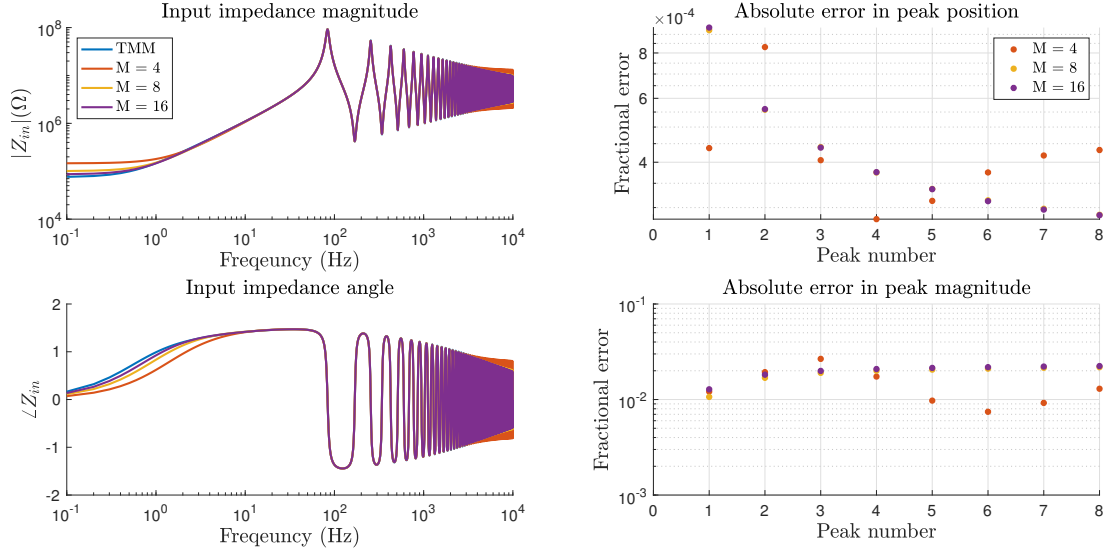


Figure 3.25: Input impedance calculated using the Foster network with coefficients acquired by optimising of E'_M from 20 Hz to 3 kHz. Top left: Input impedance magnitude. Bottom left: Input impedance phase. Top right: Absolute percentage error in input impedance peak position relative to TMM. Bottom right: Absolute percentage error in input impedance peak magnitude.

Exponential horn results

Here we present input impedances calculated for an exponential horn. Fig. 3.26 shows the input impedance calculated using the scheme with the Bilbao and Chick loss model. The absolute errors in the positions of the input impedance peaks are less than 3 % for $M = 4$ and less than 0.02% for $M = 20$. The error in the peak magnitude is less than 3% for $M = 4$ and less than 1% for $M = 20$. The error in the first peak magnitude is better for the exponential horn than for the cylinder since this first peak has a higher frequency (the fractional derivative approximation deviates from the exact result at low frequencies).

Figs. 3.27 and 3.28 show the input impedances of an exponential horn simulated using the Foster network. Element values were calculated by optimising for a tube radius of 0.05 m, the maximum radius of this horn, using E'_M . Fig. 3.27 shows the input impedance using values optimised over 0.1 Hz to 10 kHz. Peak position error is less than 0.1% for $M = 4$ and less than 0.02% for $M = 16$. Peak magnitude error is less than 11% for $M = 4$ and less than 4% for $M = 16$.

Fig. 3.28 uses element values optimised over the frequency range 20 Hz to 3 kHz. Peak position error is less than 0.1% for $M = 4$ and less than 0.02% for $M = 16$. Peak magnitude error is less than 20% for $M = 4$ and less than 4% for $M = 16$.

Run times over the temporal loop for the simulations using different filters were:

- 12.19 s for Bilbao and chick model ($M = 20$)
- 16.64 s for the Foster structure ($M = 16$)
- 12.27 s for the Foster structure ($M = 8$)
- 9.99 s for the Foster structure ($M = 4$)

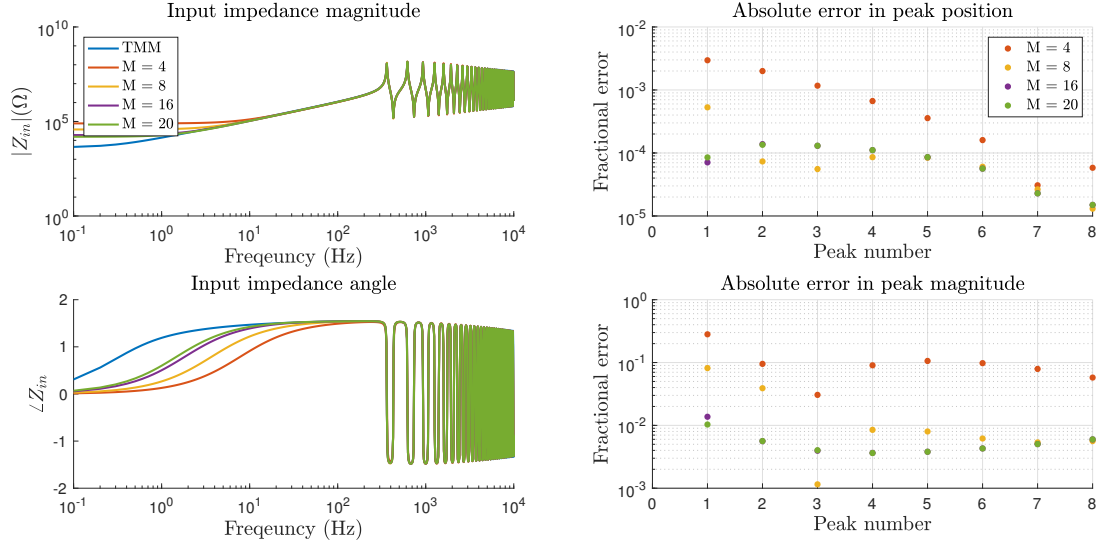


Figure 3.26: Input impedance of an exponential horn calculated using the Bilbao and Chick loss model using different filter orders. Top left: Input impedance magnitude. Bottom left: Input impedance phase. Top right: Absolute percentage error in input impedance peak position relative to TMM. Bottom right: Absolute percentage error in input impedance peak magnitude.

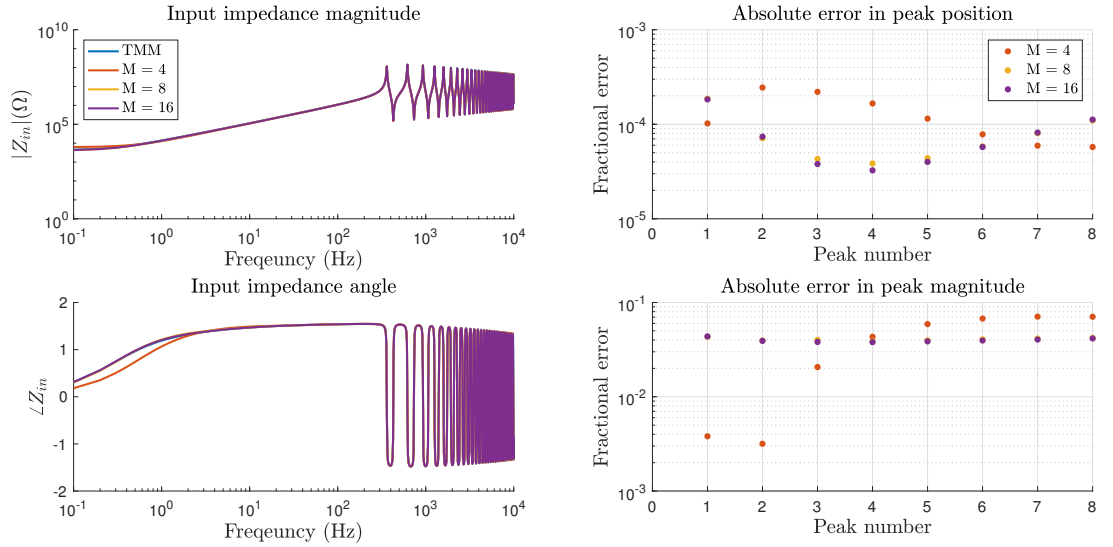


Figure 3.27: Input impedance of an exponential horn calculated using the Foster network with coefficients acquired by optimising of E'_M from 0 Hz to 10 kHz. Top left: Input impedance magnitude. Bottom left: Input impedance phase. Top right: Absolute percentage error in input impedance peak position relative to TMM. Bottom right: Absolute percentage error in input impedance peak magnitude.

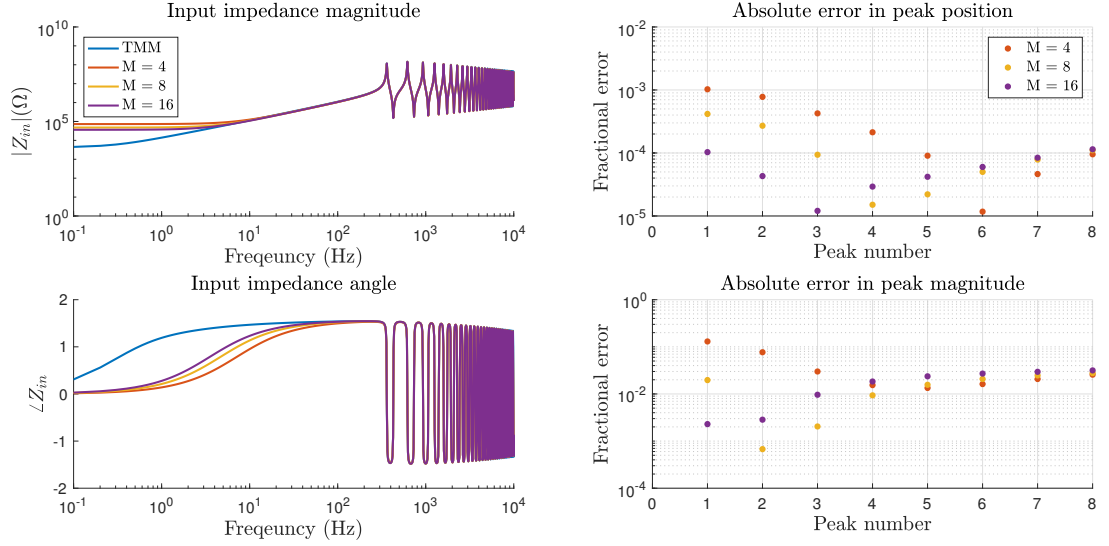


Figure 3.28: Input impedance of an exponential horn calculated using the Foster network with coefficients acquired by optimising of E'_M from 20 Hz to 3 kHz. Top left: Input impedance magnitude. Bottom left: Input impedance phase. Top right: Absolute percentage error in input impedance peak position relative to TMM. Bottom right: Absolute percentage error in input impedance peak magnitude.

3.6 Conclusions

This chapter has focussed on how FDTD methods can be used in problems relating to acoustic tubes. Simple boundary conditions have been chosen so as to focus on the properties of various schemes over the domain interior.

We began with the simplest system, a lossless cylindrical tube, and the effect of FDTD scheme on the simulations. This was then extended to an acoustic tube of variable cross-sectional area. For a cylindrical tube, the explicit scheme on an interleaved time and space grid was able to produce exact results whereas the implicit scheme, where only the spatial grids are interleaved, produced frequency warping and was never able to match the exact solutions. The frequency warping is due to the application of the bilinear transform in these schemes. Similar performance occurs in a tube of varying cross-sectional area, although the explicit scheme cannot give exact solutions due to discretisation of the bore. Of course, in practice, the explicit scheme is not infallible as the spatial domain requires truncation—resulting in either an incorrect domain size if the spatial step is not modified or some small degree of frequency warping if it is. However, this is a very small effect relative to the frequency warping present in the implicit scheme.

The bilinear transform does have its uses, namely the guaranteed passivity of the discrete schemes if the continuous system is known to be passive; this is motivation behind its use in the Port-Hamiltonian framework [164] and in nonlinear schemes [40]. This makes it an ideal partner to use in tandem with the explicit scheme as the foundation of our system solver. The effects of viscous and thermal losses are relatively small compared to the main propagation elements of the system but are important enough to modify resonances and increase the complexity of the simulations. As a result, the mathematical simplicity of the bilinear

transform is a useful property in the analysis of these systems but its frequency warping nature is less apparent when used in the lossy part.

Modelling of the lossy part has been tackled using two approaches: using a truncated model of the immittances that require an extra approximation to fractional derivatives, and by constructing equivalent electrical networks that directly approximate the immittances. Before considering the numerics applied to the simulation of these models, it is worth pointing out that the models themselves are different approaches to approximating the Zwikker and Kosten loss model (as shown in Chap. 2). The truncated model is described for a high frequency/large tube radius limit, whereas the Foster network can be optimised over different ranges.

The truncated expansion model is useful as it does not require any offline computation for changes in cross-sectional area. However, approximating the fractional order derivatives requires high order recursions to be of use and even then the approximation fails for low frequencies. It is also affected by numerical rounding errors meaning that the stability of the system is compromised when trying to improve accuracy. Although the development of the fractional order derivative approximation starts from the bilinear transform, the final operator deviates due to truncation of the CFE.

The use of numerical fitting procedures in the Foster network allows for great accuracy with a relatively low computational cost. One can even modify the optimised parameters so that they can be applied to systems of different radii and temperatures, although with a slight loss of accuracy. Simulating this model in the time domain requires some care since the current formulation is equivalent to applying the bilinear transform to the continuous model. This reduces the accuracy of the filter structures when the element values are applied straight to the discrete system. The frequency warping can be taken into account by ‘pre-warping’ the frequency vector in the optimisation procedure. When this is performed, the filters maintain their accuracy over the optimised frequency range.

Chapter 4

Modelling radiation of sound from an acoustic tube

“Life is like a trumpet—if you don’t put anything into it, you don’t get anything out of it.”

— William Christopher Handy

So far, we have considered the brass instrument as a confined system; waves have been fully reflected by the lossless boundary conditions of an ideally open or closed tube. Although these models are useful for a preliminary treatment of the brass instrument system, the reality is more complicated (and interesting). For a listener to hear a sound produced by the instrument, the instrument system must transfer energy into the listening space and therefore lose energy. This energy loss is frequency dependent in a non-trivial way. It also turns out that there are length correction effects present that modify the position of the instrument’s resonances [63]. In this chapter we begin to refine our brass instrument model to include a more realistic open tube condition.

Two methods of modelling sound radiation are considered and treatment of both will follow in a parallel manner. The first model treats the behaviour of sound radiation through a lumped radiation impedance. As with the case of the tube wall losses, this model is not immediately useable in the time domain but can be approximated by an equivalent electrical network leading, ultimately, to a recursive algorithm. The second model directly models the transfer of energy from the one-dimensional tube system to the three-dimensional air system. Although this system is more computationally expensive, it does allow for extensions that include realistic acoustic environment and hearing models (something which is beyond the scope of this work).

For both models the problem is stated in the continuous domain first and then discretised. Energy conservation shows that these systems are passive. Results produced using the algorithms developed in this chapter are presented.

4.1 Radiation impedance models

Rayleigh [157] and Morse [121] consider radiation from a cylindrical tube with an infinite flange; this system being modelled as a tube within a large wall. In this case, the interface

between the cylinder and the free space was considered as a vibrating piston. Whereas Rayleigh only considered a rigid piston, Morse considered the effect of nonuniform motion on the piston but did not apply it to the case of an open cylinder. Zorumski [181] extended the rigid piston model in an infinite flange to include an admittance at the tube walls and the effect this has on conversion between the planar and higher modes. Amir *et al.* [5] also investigated mode conversion in the lossless cylinder with an infinite flange and used ‘edge functions’ that converged faster than normal mode solutions.

The radiating portion of a brass instrument, however, is far from an infinite flange. A treatment for plane waves exiting an unflanged cylindrical pipe was given by Levine and Schwinger [104]. This model is arrived at by matching the plane waves from a cylindrical tube to the spherical waves of the free field through manipulation of Green’s theorem. Caussé *et. al* [37] modified the planar radiation model to better represent spherical waves by using a ratio of the area of the spherical wavefront to that of the planar wavefront at the end of the horn.

Hélie and Rodet [83] provide a spherical model of radiation from a horn. Instead of using a vibrating piston, the radiating part of the horn is considered to be an area of a sphere that vibrates. Averaging over the surface allowed for the model to be incorporated into one-dimensional models. However, averaging introduces errors that are significant at small flaring angles.

As planar wave propagation is considered in the interior of the acoustic tube, the Levine and Schwinger model was chosen as a radiation condition for this work. The model is given in terms of a complex reflection function

$$R = -|R|e^{2j\frac{\omega\Delta l}{c_0}} \quad (4.1)$$

where the reflection magnitude and length correction are, respectively,

$$|R| = \exp \left(-\frac{2r_L\omega}{\pi c_0} \int_0^{r_L\frac{\omega}{c_0}} \frac{\tan^{-1}(-J_1(x)/N_1(x))}{x \left[\left(r_L\frac{\omega}{c_0} \right)^2 - x^2 \right]^{1/2}} dx \right) \quad (4.2a)$$

$$\Delta l = \frac{r_L}{\pi} \left(\int_0^{r_L\frac{\omega}{c_0}} \frac{\log \left(\pi J_1(x) [J_1(x)^2 + N_1(x)^2]^{1/2} \right)}{x \left[\left(r_L\frac{\omega}{c_0} \right)^2 - x^2 \right]^{1/2}} dx + \int_0^\infty \frac{\log [1/(2I_1(x)K_1(x))]}{x \left[x^2 + \left(r_L\frac{\omega}{c_0} \right)^2 \right]^{1/2}} dx \right) \quad (4.2b)$$

where r_L is the radius at the end of the tube, J_1 and N_1 are Bessel functions of first and second kind, I_1 and K_1 are the modified Bessel functions of first and second kind¹. The $\exp(\cdot)$ notation, rather than e^{\cdot} , has been used in the reflection magnitude for clarity.

¹In Levine and Schwinger’s original manuscript, these functions are described as the cylindrical functions.

The radiation impedance is given by

$$Z_R = \rho_0 c_0 \frac{1 + R}{1 - R} \quad (4.3)$$

4.1.1 Network representation of radiation model

The form of (4.1) is expressed in the frequency domain. To be used in a time domain model, some further approximations must be made.

Caussé *et al.* [37] provide some approximations that could be used in the time domain, but they are only valid over a limited frequency range. Silva *et al.* [147] used fitting procedures to match Padé approximations to the Levine and Schwinger model. These approximations can be applied over a wider frequency range than that presented by Caussé *et al.*, and were later used by Bilbao and Chick [24] in the form of a passive network, see Fig. 4.1, for modelling acoustic tubes, and by Harrison *et al.* [75, 76] for a full brass instrument synthesis environment. A similar method was presented by Hélié and Rodet [83] to model the spherical radiation model in the time domain.

The radiation impedance is associated with a one-port circuit element, with pressure, \bar{p} , associated with a voltage and particle velocity, \bar{v} , associated with a current. Additional state variables of the circuit are associated currents $v_{(1)}$, $v_{(2)}$, $v_{(3)}$, and $v_{(4)}$, and voltage $p_{(1)}$. The internal state variables are distinguished from those used for the pressure and velocity inside an acoustic tube through the use of brackets in the subscripts.

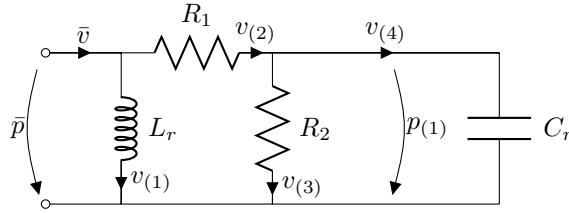


Figure 4.1: Circuit representation of approximation to the Levine and Schwinger radiation model.

The radiation impedance given by this network is

$$Z_{rad} = \frac{L_r(R_1 + R_2)j\omega + L_r R_1 R_2 C_r (j\omega)^2}{R_1 + R_2 + (L_r + R_1 R_2 C_r)j\omega + L_r R_2 C_r (j\omega)^2} \quad (4.4)$$

with element values

$$R_1 = \rho_0 c_0, \quad L_r = 0.613 \rho_0 r_L, \quad R_2 = 0.505 \rho_0 c_0, \quad C_r = 1.111 \frac{r_L}{\rho_0 c_0^2} \quad (4.5)$$

The voltage and current at the open terminal are related to the pressure and velocity at the end of the acoustic tube by

$$\bar{p} = p(t, L), \quad \bar{v} = v(t, L) \quad (4.6)$$

and the internal state variables are given by

$$\bar{v} = v_{(1)} + v_{(2)}, \quad \bar{p} = L_r \frac{dv_{(1)}}{dt}, \quad \bar{p} = R_1 v_{(2)} + p_{(1)} \quad (4.7a)$$

$$v_{(2)} = v_{(3)} + v_{(4)}, \quad p_{(1)} = R_2 v_{(3)}, \quad v_{(4)} = C_r \frac{dp_{(1)}}{dt} \quad (4.7b)$$

We do not need to solve for all of these state variables; (4.7) can be reduced to

$$\bar{v} = v_{(1)} + \left(\frac{1}{R_2} + C_r \frac{d}{dt} \right) p_{(1)} \quad (4.8a)$$

$$\bar{p} = L_r \frac{dv_{(1)}}{dt} \quad (4.8b)$$

$$\bar{p} = \left(1 + \frac{R_1}{R_2} + R_1 C_r \frac{d}{dt} \right) p_{(1)} \quad (4.8c)$$

Fig. 4.2 shows the radiation reflection magnitude and length correction calculated using the Levine and Schwinger expression (4.2) and the network approximation (4.4) for a tube radius of 0.05 m, typical of the end of a trumpet. The Levine and Schwinger model is defined only for planar propagation; in this case the upper frequency limit is 2661 Hz at a temperature of 26.85° C and was calculated using the `integral` function in MATLAB.

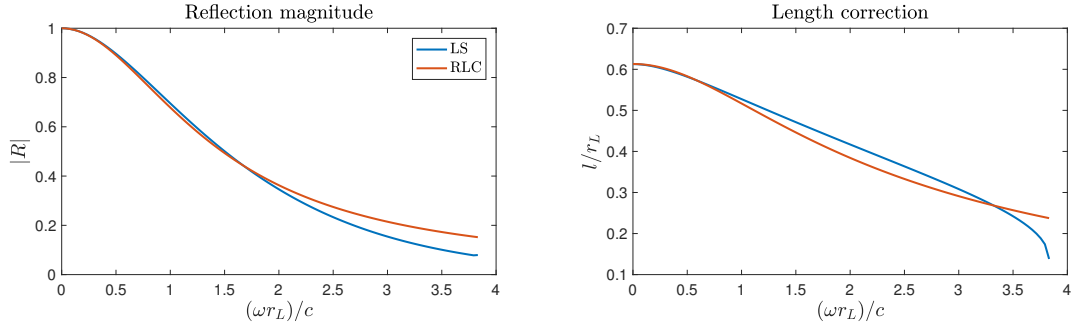


Figure 4.2: Left: Radiation reflection magnitude for a tube of radius 0.05 m calculated using the Levine and Schwinger model (blue) and the network approximation. Right: Radiation length correction.

The network approximation is a good match at low frequencies but deviates at high frequencies.

4.1.2 Energy analysis

Although it is known that this network is passive, it is useful to derive an energy for the system when it is used in tandem with the horn equation. Recalling the power transfer at the boundary from the energy analysis of the horn equation (2.49) over the domain \mathcal{D} is

$$\mathcal{B}_{he} = -pSv|_{z=0} + pSv|_{z=L} \quad (4.9)$$

Replacing the boundary term at $z = L$ with the associated voltage and current in our radiation network allows for the following manipulation

$$\begin{aligned}
pSv|_{z=L} &\stackrel{(4.6)}{=} S(L)\bar{p}\bar{v} \\
&\stackrel{(4.7a)}{=} S(L)\bar{p}(v_{(1)} + v_{(2)}) \\
&\stackrel{(4.7a)}{=} S(L)\left(L_r v_{(1)} \frac{dv_{(1)}}{dt} + \bar{p}v_{(2)}\right) \\
&\stackrel{(4.7a)}{=} S(L)\left(L_r v_{(1)} \frac{dv_{(1)}}{dt} + (R_1 v_{(2)} + p_{(1)})v_{(2)}\right) \\
&\stackrel{(4.7b)}{=} S(L)\left(L_r v_{(1)} \frac{dv_{(1)}}{dt} + R_1 v_{(2)}^2 + p_{(1)}(v_{(3)} + v_{(4)})\right) \\
&\stackrel{(4.7b)}{=} S(L)\left(L_r v_{(1)} \frac{dv_{(1)}}{dt} + R_1 v_{(2)}^2 + R_2 v_{(3)}^2 + C_r p_{(1)} \frac{dp_{(1)}}{dt}\right) \\
&\stackrel{(2.4)}{=} \frac{d\mathcal{H}_{rad}}{dt} + \mathcal{Q}_{rad}
\end{aligned} \tag{4.10}$$

where

$$\mathcal{H}_{rad} = \frac{S(L)}{2} \left(L_r v_{(1)}^2 + C_r p_{(1)}^2 \right) \geq 0 \tag{4.11a}$$

$$\mathcal{Q}_{rad} = S(L) \left(R_1 v_{(2)}^2 + R_2 v_{(3)}^2 \right) \geq 0 \tag{4.11b}$$

In this case, the boundary condition contains a storage component, along with dissipation as discussed in Sec. 2.2.3. Combining this with the energy for the whole system gives

$$\frac{d}{dt} (\mathcal{H}_{he} + \mathcal{H}_{rad}) + \mathcal{Q}_{rad} + \mathcal{B}'_{he} = 0 \tag{4.12}$$

where $\mathcal{B}'_{he} = -pSv|_{z=0}$. The total energy of the system and the power loss from the radiation model are non-negative values and the solutions to the system are therefore bounded.

4.1.3 Numerical scheme

We now look to discretising the network structure approximating the Levine and Schwinger radiation impedance presented in Sec. 4.1.1. The pressure and velocity at the end of the horn are related to the voltage and current of the network by

$$\bar{p} = \mu_{t+} p_N, \quad \bar{S}_N \bar{v} = \mu_{z-} (S_{N+1/2} v_{N+1/2}) \tag{4.13}$$

where $\bar{p}^{n+1/2}$ and $\bar{v}^{n+1/2}$ lie on the interleaved temporal grid. The internal state variables are given by

$$\bar{v} = \mu_{t+} v_{(1)} + \mu_{t+} v_{(2)}, \quad \bar{p} = L_r \delta_{t+} v_{(1)}, \quad \bar{p} = R_1 \mu_{t+} v_{(2)} + \mu_{t+} p_{(1)} \tag{4.14a}$$

$$v_{(2)} = v_{(3)} + v_{(4)}, \quad p_{(1)} = R_2 v_{(3)}, \quad \mu_{t+} v_{(4)} = C_r \delta_{t+} p_{(1)} \tag{4.14b}$$

where currents $v_{(1)}^n$, $v_{(2)}^n$, $v_{(3)}^n$, and $v_{(4)}^n$, and voltage $p_{(1)}^n$ are aligned on the integer temporal grid. We can reduce system (4.14) to

$$\bar{v} = \mu_{t+} v_{(1)} + \frac{1}{R_2} \mu_{t+} p_{(1)} + C_r \delta_{t+} p_{(1)} \quad (4.15a)$$

$$\bar{p} = L_r \delta_{t+} v_{(1)} \quad (4.15b)$$

$$\bar{p} = \left(1 + \frac{R_1}{R_2}\right) \mu_{t+} p_{(1)} + R_1 C_r \delta_{t+} p_{(1)} \quad (4.15c)$$

This choice of discretisation is equivalent to applying the bilinear transform in (4.4). Fig. 4.3 shows the effect of using the bilinear transform on this system compared to the continuous case. For this system, the discretisation has little effect over the frequency domain of interest.

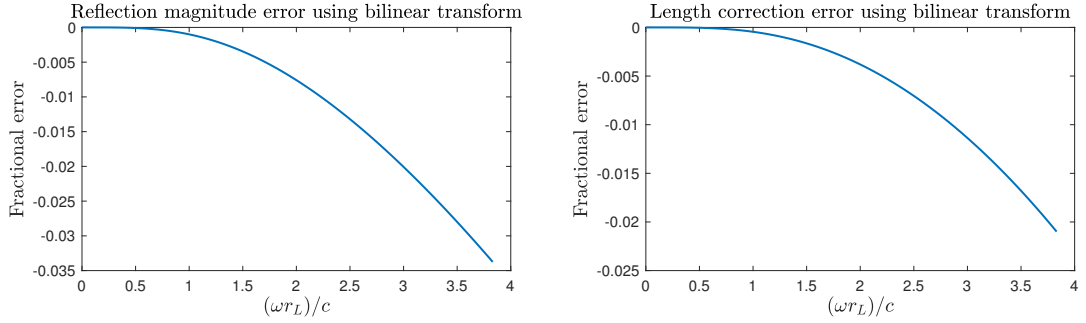


Figure 4.3: Left: Error in reflection magnitude of network when using the bilinear transform (dashed red) at 50 kHz. Right: Error in length correction.

To couple this model to the horn equation, we look at the pressure equations of (3.108) at $l = N$

$$\frac{\bar{S}_N}{\rho_0 c_0^2} \delta_{t+} p_N = -\delta_{z-} (S_{N+1/2} v_{N+1/2}) \quad (4.16)$$

Using the identity $\delta_{z-} = \frac{2}{h} (\mu_{z-} - w_{z-})$ results in

$$\begin{aligned} \frac{\bar{S}_N}{\rho_0 c_0^2} \delta_{t+} p_N &= -\frac{2}{h} (\mu_{z-} (S_{N+1/2} v_{N+1/2}) - S_{N-1/2} v_{N-1/2}) \\ &= -\frac{2}{h} (\bar{S}_N \bar{v} - S_{N-1/2} v_{N-1/2}) \end{aligned} \quad (4.17)$$

We then look to writing \bar{v} in terms of known values of $v_{(1)}$, $p_{(1)}$ and p_N^n as well as the unknown p_N^{n+1} . We do this by first expressing the current and voltage in terms of their previous values and the unknown pressure, and then substitute these into our expression for \bar{v} . This results in

$$p_N^{n+1} = \alpha^{(R)} p_N^n + \beta^{(R)} S_{N-1/2} v_{N-1/2} + \epsilon^{(R)} v_{(1)}^n + \nu^{(R)} p_{(1)}^n \quad (4.18a)$$

$$v_{(1)}^{n+1} = v_{(1)}^n + \frac{k}{L_r} \mu_{t+} p_N \quad (4.18b)$$

$$p_{(1)}^{n+1} = \tau^{(R)} p_{(1)}^n + \chi^{(R)} \mu_{t+} p_N \quad (4.18c)$$

where

$$\alpha^{(R)} = \frac{1 - E^{(R)}}{1 + E^{(R)}} \quad (4.18d)$$

$$\beta^{(R)} = \frac{2\rho_0 c_0^2 k}{\bar{S}_N h (1 + E^{(R)})} \quad (4.18e)$$

$$\epsilon^{(R)} = -\frac{2\rho_0 c_0^2 k}{h (1 + E^{(R)})} \quad (4.18f)$$

$$\nu^{(R)} = \epsilon^{(R)} \left(\frac{1}{2R_2} (\tau^{(R)} + 1) + \frac{C_r}{k} (\tau^{(R)} - 1) \right) \quad (4.18g)$$

$$\tau^{(R)} = \frac{R_1 C_r - H^{(R)}}{R_1 C_r + H^{(R)}} \quad (4.18h)$$

$$\chi^{(R)} = \frac{k}{R_1 C_r + H^{(R)}} \quad (4.18i)$$

$$E^{(R)} = \frac{\rho_0 c_0^2 k}{h} \left(\frac{k}{2L_r} + \left(\frac{1}{2R_2} + \frac{C_r}{k} \right) \chi^{(R)} \right) \quad (4.18j)$$

$$H^{(R)} = \frac{k}{2} \left(1 + \frac{R_1}{R_2} \right) \quad (4.18k)$$

4.1.4 Discrete energy analysis

Recalling that the discrete power transfer at the boundaries for the explicit scheme for the horn equation (3.108) is

$$\mathfrak{b}_{he} = -\mu_{t+} p_0 \mu_{z-} (S_{1/2} v_{1/2}) + \mu_{t+} p_N \mu_{z-} (S_{N+1/2} v_{N+1/2}) \quad (4.19)$$

we can find a discrete energy for our coupled system. We can rewrite the term at $l = N$ using (4.13) as $\mu_{t+} p_N \mu_{z-} (S_{N+1/2} v_{N+1/2}) = \bar{S}_N \bar{p} \bar{v}$ which can then be manipulated as follows

$$\begin{aligned} \bar{S}_N \bar{p} \bar{v} &\stackrel{(4.15a)}{=} \bar{S}_N \bar{p} \left(\mu_{t+} v_{(1)} + \frac{1}{R_2} \mu_{t+p(1)} + C_r \delta_{t+p(1)} \right) \\ &\stackrel{(4.14a)}{=} \bar{S}_N (L_r \mu_{t+} v_{(1)} \delta_{t+} v_{(1)} + \bar{p} \mu_{t+} v_{(2)}) \\ &\stackrel{(4.14a)}{=} \bar{S}_N (L_r \mu_{t+} v_{(1)} \delta_{t+} v_{(1)} + (R_1 \mu_{t+} v_{(2)} + \mu_{t+p(1)}) \mu_{t+} v_{(2)}) \\ &\stackrel{(4.14b)}{=} \bar{S}_N (L_r \mu_{t+} v_{(1)} \delta_{t+} v_{(1)} + R_1 (\mu_{t+} v_{(2)})^2 + \mu_{t+p(1)} (\mu_{t+} v_{(3)} + \mu_{t+} v_{(4)})) \\ &\stackrel{(4.14b)}{=} \bar{S}_N (L_r \mu_{t+} v_{(1)} \delta_{t+} v_{(1)} + R_1 (\mu_{t+} v_{(2)})^2 + R_1 (\mu_{t+} v_{(3)})^2 + C_r \mu_{t+p(1)} \delta_{t+p(1)}) \\ &\stackrel{(3.26c)}{=} \delta_{t+} \mathfrak{h}_{rad} + \mathfrak{q}_{rad} \end{aligned} \quad (4.20)$$

where

$$\mathfrak{h}_{rad} = \frac{\bar{S}_N}{2} (L_r v_{(1)}^2 + C_r p_{(1)}^2) \geq 0 \quad (4.21a)$$

$$\mathfrak{q}_{rad} = \bar{S}_N (R_1 (\mu_{t+} v_{(2)})^2 + R_2 (\mu_{t+} v_{(3)})^2) \geq 0 \quad (4.21b)$$

Combining this with the total energy of the system gives

$$\delta_{t+} (\mathfrak{h}_{he} + \mathfrak{h}_{rad}) + \mathfrak{q}_{rad} + \mathfrak{b}'_{he} = 0 \quad (4.22)$$

where $b'_{he} = -\mu_t + p_0 \mu_{z-} (S_{1/2} v_{1/2})$. It is clear that the combined energy and the losses due to radiation are non-negative and therefore the solutions to the system are bounded.

4.1.5 Simulation results

Simulations were performed for a cylindrical tube of length 1 m and radius of 0.05 m at a temperature of 26.85° C. The sample rate was 50 kHz, simulation duration 10 s, and Courant number $\lambda = 0.9861$. Losses were neglected over the interior of the acoustic tube.

Fig. 4.4 shows the energy evolution of the FDTD simulation and its total energy balance (3.75). At the 142nd time step, corresponding to the time taken for a disturbance to travel the length of the tube, energy is transferred from the end of tube to the radiation model; there is a reduction in the energy stored in the cylinder and an increase in the energy stored in the radiation model. The subsequent variations in energy of the tube and radiation model are not monotonically decreasing and increasing—oscillations in stored energy of the tube and the radiation model are observed. This is because there is additional exchange of energy between the two models after the pulse has initially interacted at the boundary. The energy of the overall system decreases over time due to the lossy processes in the radiation model. The total energy balance shows bit-wise deviations in the energy on the order of the machine precision.

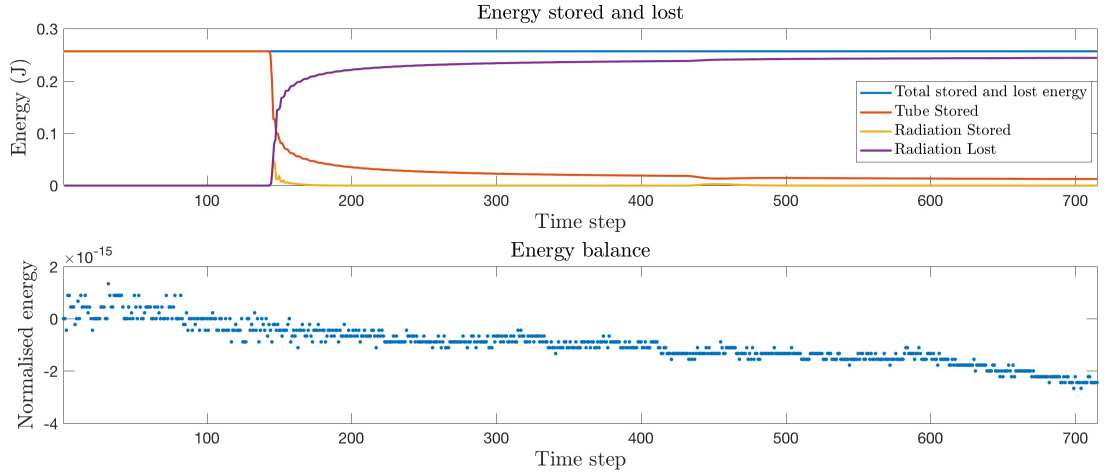


Figure 4.4: Top: Total stored energy (blue), stored energy in the tube (red), stored energy in the radiation model (yellow), and energy lost by the radiation model (purple). Bottom: Energy balance showing numerical precision of machine.

Input impedances were calculated from simulations using the procedure described in Sec. 3.4.3. Simulation results were compared to the exact expression [63] for the input impedance of a cylinder terminated with the Levine and Schwinger radiation impedance

$$Z_{(exact)} = \frac{j\rho_0 c_0}{S_0} \left(\frac{j\rho_0 c_0 \sin\left(\frac{\omega L}{c_0}\right) + Z_R \cos\left(\frac{\omega L}{c_0}\right)}{j\rho_0 c_0 \cos\left(\frac{\omega L}{c_0}\right) - Z_R \sin\left(\frac{\omega L}{c_0}\right)} \right) \quad (4.23)$$

Fig. 4.5 shows the input impedance calculated from simulations and $Z_{(exact)}$ along with the error in the frequency of the first ten peaks produced by the FDTD model. The error in

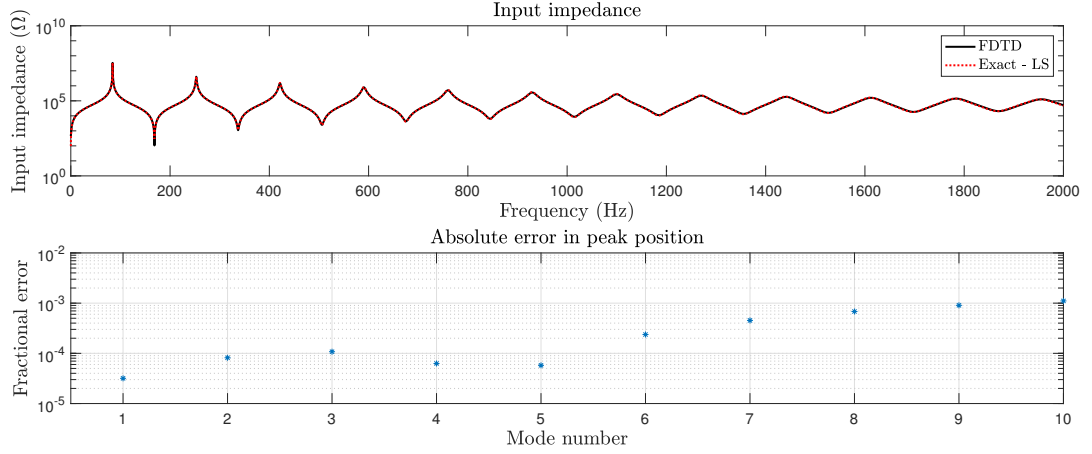


Figure 4.5: Top: Input impedance of a lossless cylinder of radius 0.05 m and length 1 m calculated using an FDTD simulation with lossy radiating end (solid black) and a frequency domain calculation terminated with the Levine and Schwinger radiation impedance (dashed red). Bottom: Absolute error in peak position of FDTD simulation relative to frequency domain calculation.

the position for the first five peaks is less than 0.02 % and increases to 0.1 % over the sixth to tenth peaks.

Fig. 4.6 shows the input impedance calculated for a cylinder of radius 0.1 m. The error in the peak position given by the FDTD model is slightly larger than for the smaller tube, but still lies under 0.4 % for the first ten peaks.

These results extend the comparison of the network approximation and the Levine and Schwinger radiation model. The errors in the FDTD simulation can be described in terms of the errors of the network model as opposed to numerical errors. We are therefore justified in our use of the bilinear transform to model the network radiation model, taking advantage of its passive behaviour. This is the same procedure employed for incorporating viscous and thermal losses in Chap. 3—using an explicit scheme for efficient and accurate modelling of wave propagation and the bilinear transform to preserve passivity of connected processes.

4.2 Coupling to a 3D acoustic field

An alternative to modelling a radiation impedance is to directly model the interaction of the tube with the three-dimensional space it occupies. There are multiple publications presenting simulations of the three-dimensional field in an acoustic tube; see [68, 69, 70] for three-dimensional modelling of woodwind instruments and [4, 137, 138] for two and three-dimensional modelling of brass instruments². However, there are several disadvantages to this approach. The most obvious in terms of developing a synthesis tool is computational cost—if we increase the size of the domain of interest, more computations are required at each time step, resulting in longer computation times. In addition, incorporation of the viscous and thermal boundary layer losses in higher dimensions requires an extremely high spatial resolution for accurate modelling. In contrast, the one-dimensional model presented in this

²Note that these works used a nonlinear propagation model.

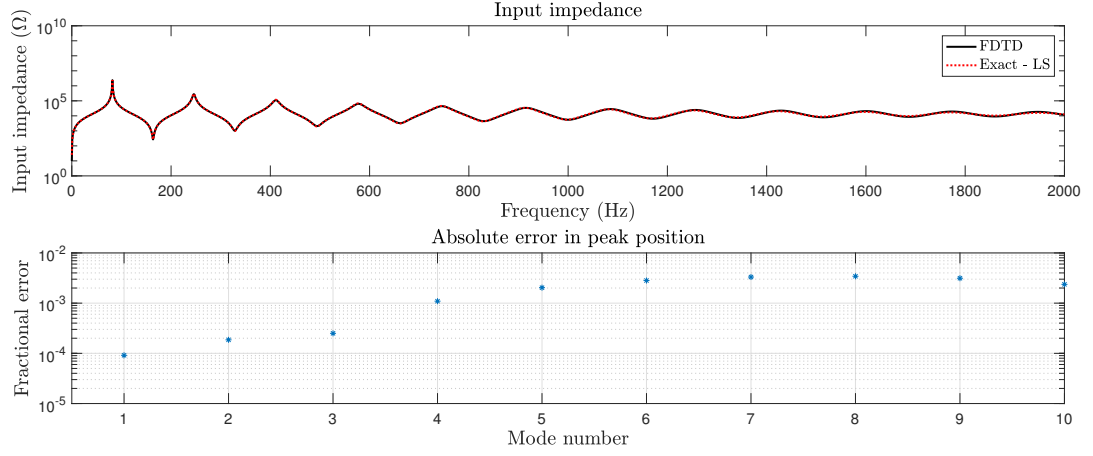


Figure 4.6: Top: Input impedance of a lossless cylinder of radius 0.1 m and length 1 m calculated using an FDTD simulation with lossy radiating end (solid black) and a frequency domain calculation terminated with the Levine and Schwinger radiation impedance (dashed red). Bottom: Absolute error in peak position of FDTD simulation relative to frequency domain calculation.

thesis requires little in terms of computing power and accurately models boundary layer losses. However, it does not allow for non-planar modes to be excited in the flaring portions of the instrument.

We can exploit the strengths of the one- and three- dimensional approaches: a one-dimensional acoustic tube model that incorporates the viscous and thermal losses in an efficient manner, and a model of the three-dimensional acoustic field that includes effects due to the flaring of the instrument bell and the radiation of sound away from the instrument. These two models are then coupled at a chosen point along the length of the instrument; we name this an embedded instrument system, see Fig. 4.7.

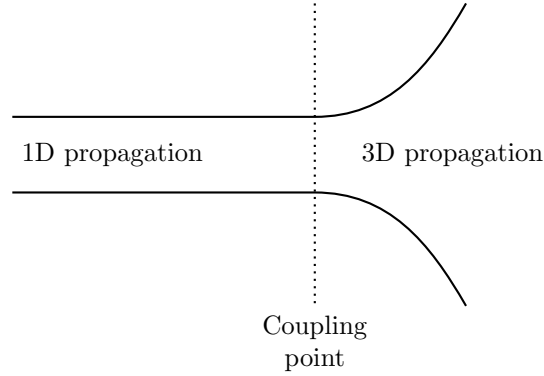


Figure 4.7: Schematic of an embedded system. The cylindrical, or slowly varying, portion of the instrument bore is modelled using a one-dimensional wave propagation model. In the flaring portions of the instrument, a three-dimensional wave propagation model is used. The dashed line shows the boundary between the two sections of the instrument.

This is somewhat similar to the method approached by Noreland [127], albeit in the time domain rather than the frequency domain. In Noreland's paper, a radiation impedance was calculated using a FDTD scheme in the flaring portion of the instrument. This radiation

impedance was used to terminate a TMM calculation over the remainder of the instrument where the bore profile was considered to be slowly varying. In a later paper by Noreland *et al.* [129], radiation behaviour was calculated using the Finite Element method and used in a bore optimisation procedure.

In [127] a two-dimensional curvilinear coordinate system was chosen to best represent the geometry of the walls of the instrument. However, as an observer moves further away from the instrument the grid spacing increases, which drastically reduces the available bandwidth of the simulated sounds. To avoid this, we instead use a scheme on a regular Cartesian grid.

4.2.1 Partial differential equations and integrals in higher dimensions: Étude IIIa

In this section, we retain the dimension of time $t \in \mathbb{R}$ but must extend our spatial domain to the Euclidean space \mathbb{R}^3 . Vectors will be identified using bold typeface. Coordinates are defined using the triple $(x', y', z') \in \mathbb{R}^3$. We will consider a cubic region of side length $L^{(3)}$ centred at the origin defined by $\mathcal{D}^{(3)} = \{(x', y', z') \in \mathbb{R}^3 \mid -L^{(3)}/2 \leq x', y', z' \leq L^{(3)}/2\}$. This region encloses a volume defined by $\mathcal{V} = \{(x', y', z') \in \mathbb{R}^3 \mid -L^{(3)}/2 < x', y', z' < L^{(3)}/2\}$ and is enclosed by a surface given by $\partial\mathcal{V} = \mathcal{D}^{(3)} \setminus \mathcal{V}$.

For a multidimensional scalar function, $f(t, x', y', z')$, the gradient of the function is

$$\nabla f = [\partial_{x'} f, \partial_{y'} f, \partial_{z'} f]^T \quad (4.24)$$

For a vector function $\mathbf{g}(t, x', y', z') = [g_{x'}(t, x', y', z'), g_{y'}(t, x', y', z'), g_{z'}(t, x', y', z')]^T$, the divergence is given by

$$\nabla \cdot \mathbf{g} = \partial_{x'} g_{x'} + \partial_{y'} g_{y'} + \partial_{z'} g_{z'} \quad (4.25)$$

The extension to higher dimensions of the second spatial derivative of a scalar function is the Laplacian operator given by

$$\nabla^2 f = \nabla \cdot \nabla f = \partial_{x'x'} f + \partial_{y'y'} f + \partial_{z'z'} f \quad (4.26)$$

We define the inner product of two scalar functions, f and g , over a three-dimensional cubic region $\mathcal{D}^{(3)}$ as

$$\langle f, g \rangle_{\mathcal{D}^{(3)}} = \int_{\mathcal{D}^{(3)}} f g dV = \int_{-L^{(3)}/2}^{L^{(3)}/2} \int_{-L^{(3)}/2}^{L^{(3)}/2} \int_{-L^{(3)}/2}^{L^{(3)}/2} f g dx' dy' dz' \quad (4.27)$$

Similarly the inner product of two vector functions, \mathbf{f} and \mathbf{g} , over the region $\mathcal{D}^{(3)}$ is

$$\langle \mathbf{f}, \mathbf{g} \rangle_{\mathcal{D}^{(3)}} = \int_{\mathcal{D}^{(3)}} \mathbf{f} \cdot \mathbf{g} dV \quad (4.28)$$

The three-dimensional L_2 norm is given by

$$\|f\|_{\mathcal{D}^{(3)}} = \sqrt{\langle f, f \rangle_{\mathcal{D}^{(3)}}}, \quad \|\mathbf{g}\|_{\mathcal{D}^{(3)}} = \sqrt{\langle \mathbf{g}, \mathbf{g} \rangle} \quad (4.29)$$

The continuous temporal identity (2.4) in the one-dimensional case extends to the three-dimensional case.

We shall also use the inner product and norm over the closed surface of a domain

$$\{f, g\}_{\partial\mathcal{V}} = \oint_{\partial\mathcal{V}} fg \, dA, \quad \|\{f\}\|_{\partial\mathcal{V}} = \sqrt{\{f, f\}_{\partial\mathcal{V}}} \quad (4.30)$$

here dA denotes integration over the surface of the domain.

Integration by parts extends to the three-dimensional case. An example using the derivative in the z' dimension over the cubic domain is

$$\int_{\mathcal{D}^{(3)}} f \partial_{z'} g dV = - \int_{\mathcal{D}^{(3)}} (\partial_{z'} f) g dV + \int_{-L^{(3)}/2}^{L^{(3)}/2} \int_{-L^{(3)}/2}^{L^{(3)}/2} f g|_{z'=\frac{L^{(3)}}{2}} - f g|_{z'=-\frac{L^{(3)}}{2}} dx' dy' \quad (4.31)$$

Notice that the boundary terms are integrations over surfaces of the domain. For this work, we use integration by parts in three-dimensions solely for problems concerning the Laplacian operator

$$\int_{\mathcal{D}^{(3)}} f \nabla^2 g dV = - \int_{\mathcal{D}^{(3)}} (\nabla f) \cdot (\nabla g) dV + \oint_{\partial\mathcal{V}} f \mathbf{n} \cdot \nabla g \, dA \quad (4.32)$$

where \mathbf{n} denotes the outward normal of the surface $\partial\mathcal{V}$. This is a specific application of the Divergence theorem [140]. Using the norm notation, Eq. (4.32) is given as

$$\langle f, \nabla^2 g \rangle_{\mathcal{D}^{(3)}} = -\langle \nabla f, \nabla g \rangle_{\mathcal{D}^{(3)}} + \{f, \mathbf{n} \cdot \nabla g\}_{\partial\mathcal{V}} \quad (4.33)$$

4.2.2 The 3D wave equation

The three-dimensional wave equation is given by [122]

$$\frac{\rho_0}{c_0^2} \partial_{tt} \psi - \rho_0 \nabla^2 \psi = 0 \quad (4.34)$$

where $\psi(t, x', y', z')$ is the acoustic velocity potential in three dimensions. The scalar pressure, $p_{3D}(t, x', y', z')$, and vector particle velocity, $\mathbf{v}_{3D}(t, x', y', z')$, fields are given by

$$p_{3D} = \rho_0 \partial_t \psi, \quad \mathbf{v}_{3D} = -\nabla \psi \quad (4.35)$$

4.2.3 Energy analysis

Taking the inner product of (4.34) with $\partial_t \psi$ over the cubic domain $\mathcal{D}^{(3)}$ results in

$$\frac{\rho_0}{c_0^2} \langle \partial_t \psi, \partial_{tt} \psi \rangle_{\mathcal{D}^{(3)}} - \rho_0 \langle \partial_t \psi, \nabla^2 \psi \rangle_{\mathcal{D}^{(3)}} = 0 \quad (4.36)$$

Applying integration by parts, (4.33), results in

$$\frac{\rho_0}{c_0^2} \langle \partial_t \psi, \partial_{tt} \psi \rangle_{\mathcal{D}^3} + \rho_0 \langle \partial_t \nabla \psi, \nabla \psi \rangle_{\mathcal{D}^3} + \mathcal{B}_{3we} = 0 \quad (4.37)$$

where

$$\mathcal{B}_{3we} = \rho_0 \{ \partial_t \psi, \mathbf{n} \cdot \nabla \psi \}_{\partial\mathcal{V}} \quad (4.38)$$

is the power transferred at the boundaries of the domain.

Using (2.4) results in the energy balance

$$\frac{d\mathcal{H}_{3we}}{dt} + \mathcal{B}_{3we} = 0 \quad (4.39)$$

where

$$\mathcal{H}_{3we}(t) = \frac{\rho_0}{2c_0^2} \|\partial_t \psi\|_{\mathcal{D}^{(3)}}^2 + \frac{\rho_0}{2} \|\nabla \psi\|_{\mathcal{D}^{(3)}}^2 \geq 0 \quad (4.40)$$

is the energy stored in the three-dimensional wave equation. This quantity is non-negative, therefore solutions are bounded.

4.2.4 Boundary conditions

A lossless Neumann condition at a boundary is given by

$$\mathbf{n} \cdot \nabla \psi = 0 \quad (4.41)$$

This boundary condition is used to model rigid walls in the acoustic field, such as the walls of a brass instrument.

Ideally, we wish to perform simulations in an infinite domain, so as not to have any resonances from the three-dimensional space interfering with the response of the instrument; the case of performing in a reverberant space is beyond the scope of this work. In practice, this is not possible, so we wish to define a smaller computational domain that absorbs waves at the domain boundaries, thus behaving as if in an infinite domain.

One such manner of achieving this is the application of Perfectly Matched Layers [16], where gradually increasing damping is introduced at the computational domain boundaries. This requires additional points on the domain boundaries, we would wish to minimise this.

An alternative is to use the absorbing boundary conditions of Engquist and Majda [55]. On the surfaces perpendicular to the z' axis, perfectly absorbing boundary conditions are given by

$$\square^- \psi \Big|_{z' = -\frac{L^{(3)}}{2}} = 0, \quad \square^+ \psi \Big|_{z' = \frac{L^{(3)}}{2}} = 0 \quad \square^\pm = \partial_{z'} \pm \frac{\partial_t}{c_0} \sqrt{1 - \left(\frac{\partial_{x'}}{\partial_t/c_0}\right)^2 - \left(\frac{\partial_{y'}}{\partial_t/c_0}\right)^2} \quad (4.42)$$

By symmetry, this can be extended to other boundary surfaces. However, the square root term in the \square operators prevents implementation. This is resolved by using a low order Taylor expansion, resulting in the first order approximation [55]

$$\frac{1}{c_0} \partial_t \psi + \mathbf{n} \cdot \nabla \psi = 0, \quad (x', y', z') \in \partial\mathcal{V} \quad (4.43)$$

Examples at the boundaries in the z' direction in $\mathcal{D}^{(3)}$ are

$$\frac{1}{c_0} \partial_t \psi - \partial_{z'} \psi = 0, \quad z' = -\frac{L^{(3)}}{2} \quad (4.44a)$$

$$\frac{1}{c_0} \partial_t \psi + \partial_{z'} \psi = 0, \quad z' = \frac{L^{(3)}}{2} \quad (4.44b)$$

By symmetry, similar conditions hold at the domain boundaries in the x' and y' dimensions. These boundary conditions were successfully applied by Torin [163] for embedding of percussion instruments.

For boundary conditions of the first-order Enquist-Majda type, the power transfer at the domain boundaries, (4.38), becomes

$$\mathcal{B}_{3we} = \frac{\rho_0}{c_0} \|\{\partial_t \psi\}\|_{\partial\mathcal{V}}^2 \geq 0 \quad (4.45)$$

This is non-negative and therefore the absorbing boundary conditions are passive. Additional work was performed by Higdon [84, 85] on developing discrete absorbing boundary conditions that are equivalent to those presented by Engquist and Majda; we use the first order approximation (4.43) in this work due to their simple application and determination of passivity.

4.2.5 Coupling the systems: Continuous case

To begin this study of embedding instruments, let us first consider a lossless cylinder placed in an enclosed volume of air. Propagation within the cylinder will be modelled using the one-dimensional horn equation (2.49). Propagation of sound in the enclosed volume of air will be described using the three-dimensional wave equation (4.34). These two models will be coupled so that energy can be transferred from the end point on the one-dimensional model at $z = L$, and one side of a disc Ω in the three-dimensional model; see Fig. 4.8. The disc has a radius r_L (the same as the radius the end of the acoustic tube), centred at the origin, and is orientated perpendicular to the z' axis. The surface of the disc is given by $\Omega = \{(x', y', z') \in \mathbb{R}^3 \mid \sqrt{x'^2 + y'^2} \leq r_L, z' = 0\}$. We label the sides of the disc directly in front, $z' = 0^+$, and behind, $z' = 0^-$, as Ω^+ and Ω^- respectively.

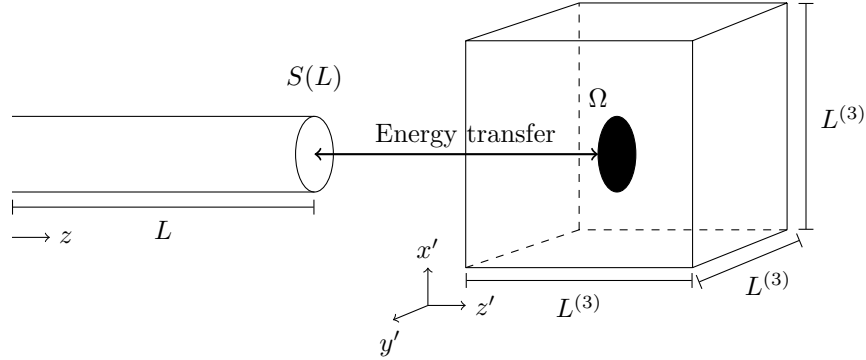


Figure 4.8: Schematic of embedded system. Energy is transferred between the cylinder, at left, and the enclosed volume of air, at right, via the point at the end of the tube and the surface Ω .

The energy balance for the three-dimensional system now becomes

$$\frac{d\mathcal{H}_{3we}}{dt} + \mathcal{B}_{3we} = \underbrace{-\rho_0 \int_{\Omega^+} \partial_t \psi \partial_{z'} \psi dA}_{\text{Power transfer on } \Omega^+} + \underbrace{\rho_0 \int_{\Omega^-} \partial_t \psi \partial_{z'} \psi dA}_{\text{Power transfer on } \Omega^-} \quad (4.46)$$

The energy balance shows power transfer on the two surfaces Ω^+ and Ω^- . However, we wish for sound to only be radiated from one side of Ω , and must set a suitable boundary condition on the other. In this case, we assume energy transfer only occurs on Ω^+ and a Neumann

boundary condition is considered on Ω^- . The energy balance becomes

$$\frac{d\mathcal{H}_{3we}}{dt} + \mathcal{B}_{3we} = -\rho_0 \int_{\Omega^+} \partial_t \psi \partial_{z'} \psi dA \quad (4.47)$$

Recall the energy balance (2.72) for the horn equation

$$\frac{d\mathcal{H}_{he}}{dt} + \mathcal{B}'_{he} = -pSv|_{z=L} \quad (4.48)$$

This allows us to couple the two systems using power conservation across the interface. A disturbance leaving the acoustic tube will inject energy into the acoustic space; likewise, any energy within the acoustic space that is incident on the surface Ω^+ will (partially) transfer into the tube. This means that the power transferred out of the end of the tube is equal to power transferred into the air box on the surface Ω^+ so that

$$pSv|_{z=L} = -\rho_0 \int_{\Omega^+} \partial_t \psi \partial_{z'} \psi dA \quad (4.49)$$

For the one-dimensional model, we assume that our variables lie on a planar cross-section of the tube, which, for practical purposes, is considered as an isophase surface. It is therefore suitable to assign the pressure on the surface Ω^+ to the value given at the end of the tube

$$\rho_0 \partial_t \psi = p(t, L), \quad (x', y', z') \in \Omega^+ \quad (4.50)$$

which, when substituted into (4.49), leads to

$$S(L)v(t, L) = - \int_{\Omega^+} \partial_{z'} \psi dA \quad (4.51)$$

4.2.6 Finite-difference operators and inner products in higher dimensions: Étude IIIb

We now discuss the discretisation of the three dimensional domain using finite-difference methods. A point on the grid is indexed using $\mathbf{l} = (l_{x'}, l_{y'}, l_{z'}) \in \mathbb{Z}^3$ so that a grid function is defined by

$$f_{\mathbf{l}}^n = f_{l_{x'}, l_{y'}, l_{z'}}^n \approx f(nk, l_{x'}h_3, l_{y'}h_3, l_{z'}h_3) \quad (4.52)$$

where h_3 is the three-dimensional grid spacing that, in general, is not equal to the grid spacing for the one-dimensional model, h . The spatial indices lie in the domain $d^{(3)} = \{\mathbf{l} \in \mathbb{Z}^3 \mid -\frac{N_3}{2} \leq l_{x'}, l_{y'}, l_{z'} \leq \frac{N_3}{2}\}$ where $N_3 = \text{floor}(L^{(3)}/h_3)$ is the number of points in each dimension on the spatial grid. For simplicity, let us assume that N_3 is an even number. The discrete domain $d^{(3)}$ corresponds to points in the continuous cubic domain $\mathcal{D}^{(3)}$. We must also consider points that lie on the surfaces of the domain. For example, the surfaces of the domain perpendicular to the x' axis are

$$b^{(x'-)} = \left\{ \mathbf{l} \in \mathbb{Z}^3 \mid l_{x'} = -\frac{N_3}{2}, -\frac{N_3}{2} \leq l_{y'}, l_{z'} \leq \frac{N_3}{2} \right\} \quad (4.53)$$

$$b^{(x'+)} = \left\{ \mathbf{l} \in \mathbb{Z}^3 \mid l_{x'} = \frac{N_3}{2}, -\frac{N_3}{2} \leq l_{y'}, l_{z'} \leq \frac{N_3}{2} \right\} \quad (4.54)$$

The notation used above can be extended to the other surfaces.

The spatial shifting operators for higher dimensions are

$$w_{x' \pm} f_1^n = f_{l_{x'} \pm 1, l_{y'}, l_{z'}}^n, \quad w_{y' \pm} f_1^n = f_{l_{x'}, l_{y'} \pm 1, l_{z'}}^n, \quad w_{z' \pm} f_1^n = f_{l_{x'}, l_{y'}, l_{z'} \pm 1}^n \quad (4.55)$$

Discrete approximations to the first spatial derivatives $\partial_{x'}$, $\partial_{y'}$, and $\partial_{z'}$ are, respectively,

$$\delta_{x'+} = \frac{w_{x'+} - 1}{h_3}, \quad \delta_{x'-} = \frac{1 - w_{x'-}}{h_3} \quad (4.56a)$$

$$\delta_{y'+} = \frac{w_{y'+} - 1}{h_3}, \quad \delta_{y'-} = \frac{1 - w_{y'-}}{h_3} \quad (4.56b)$$

$$\delta_{z'+} = \frac{w_{z'+} - 1}{h_3}, \quad \delta_{z'-} = \frac{1 - w_{z'-}}{h_3} \quad (4.56c)$$

Approximations to the second derivatives, $\partial_{x'x'}$, $\partial_{y'y'}$, and $\partial_{z'z'}$, are given by

$$\delta_{x'x'} = \delta_{x'+} \delta_{x'-} = \frac{w_{x'+} - 2 + w_{x'-}}{h_3^2} \quad (4.57a)$$

$$\delta_{y'y'} = \delta_{y'+} \delta_{y'-} = \frac{w_{y'+} - 2 + w_{y'-}}{h_3^2} \quad (4.57b)$$

$$\delta_{z'z'} = \delta_{z'+} \delta_{z'-} = \frac{w_{z'+} - 2 + w_{z'-}}{h_3^2} \quad (4.57c)$$

so that a simple approximation to the Laplacian is

$$\delta_{\nabla^2} = \delta_{x'x'} + \delta_{y'y'} + \delta_{z'z'} \quad (4.58)$$

The discrete three-dimensional inner product between functions f_1 and g_1 over $d^{(3)}$ is given by

$$\langle f, g \rangle_{d^{(3)}} = \sum_{1 \in d^{(3)}} h_3^3 f_1 g_1 \quad (4.59)$$

The weighted inner product is given by

$$\langle f, g \rangle_{d^{(3)}}^\chi = \sum_{1 \in d^{(3)}} h_3^3 \chi_1 f_1 g_1 \quad (4.60)$$

where χ_1 is a weighting function so that

$$\chi_1 = \begin{cases} 1, & \text{over the interior of the domain} \\ \frac{1}{2}, & \text{on the surfaces of the domain} \\ \frac{1}{4}, & \text{on the edges of the domain} \\ \frac{1}{8}, & \text{on the corners of the domain} \end{cases} \quad (4.61)$$

The discrete three-dimensional weighted inner product is similar to the one-dimensional weighted inner product in that boundary points are scaled.

Norms are again denoted by

$$\|f\|_{d^{(3)}} = \sqrt{\langle f, f \rangle_{d^{(3)}}}, \quad \|f\|_{d^{(3)}}^\chi = \sqrt{\langle f, f \rangle_{d^{(3)}}^\chi} \quad (4.62)$$

We will use the $\{\}$ bracket notation to signify the inner products over smaller domains.

We will only consider the weighted inner product and norm over a surface

$$\{f, g\}_{b(x'+)}^X = \sum_{\mathbf{l} \in b(x'+)} h_3^2 \chi_{\mathbf{l}} f_{\mathbf{l}} g_{\mathbf{l}}, \quad \|\{f\}\|_{b(x'+)}^X = \sqrt{\{f, f\}_{b(x'+)}^X} \quad (4.63)$$

Summation by parts is extended to three dimensions. For example, using the weighted inner product, summation by parts for discrete difference operator in the z' direction is

$$\langle f, \delta_{z'+} g \rangle_{d^{(3)}}^X = -\langle \delta_{z'-} f, g \rangle_{\bar{d}^{(3)}}^X - \{f, \mu_{z'-} g\}_{b(z'-)}^X + \{f, \mu_{z'+} g\}_{b(z'+)}^X \quad (4.64)$$

where $\bar{d}_{z'}^{(3)} = \{(l_{x'}, l_{y'}, l_{z'}) \in \mathbb{Z}^3 \mid -\frac{N_3}{2} \leq l_{x'}, l_{y'} \leq \frac{N_3}{2}, -\frac{N_3}{2} \leq l_{z'} \leq \frac{N_3}{2} - 1\}$. By symmetry (4.64) applies to other dimensions.

As in the one-dimensional case, the domain of the inner product changes when summation by parts is performed. This occurs only in the direction of the difference operator—the domain dimensions perpendicular to this remain unchanged and the weightings of the weighted inner product are not affected. For example, the weighted inner product over the domain $\bar{d}_{x'}^{(3)}$ is weighted at $l_{y'}, l_{z'} = \pm \frac{N_3}{2}$, but not for $l_{x'} = -\frac{N_3}{2}, \frac{N_3}{2} - 1$.

4.2.7 The simple scheme for the 3D wave equation

A discrete approximation to the three-dimensional wave equation (4.34) is

$$\frac{\rho_0}{c_0^2} \delta_{tt} \psi_{l_{x'}, l_{y'}, l_{z'}}^n - \rho_0 \delta_{\nabla^2} \psi_{l_{x'}, l_{y'}, l_{z'}}^n = 0 \quad (4.65)$$

which, over the domain interior, has the update

$$\begin{aligned} \psi_1^{n+1} = & 2(1 - 3\lambda^2) \psi_{l_{x'}, l_{y'}, l_{z'}}^n - \psi_{l_{x'}, l_{y'}, l_{z'}}^{n-1} \\ & + \lambda^2 \left(\psi_{l_{x'}+1, l_{y'}, l_{z'}}^n + \psi_{l_{x'}-1, l_{y'}, l_{z'}}^n + \psi_{l_{x'}, l_{y'}+1, l_{z'}}^n \right. \\ & \left. + \psi_{l_{x'}, l_{y'}-1, l_{z'}}^n + \psi_{l_{x'}, l_{y'}, l_{z'}+1}^n + \psi_{l_{x'}, l_{y'}, l_{z'}-1}^n \right) \end{aligned} \quad (4.66)$$

This particular scheme, and its generalisations, has been used in [31, 32]. Taking the weighted inner product of (4.65) with $\delta_t \psi_1^n$ over $d^{(3)}$ gives

$$\frac{\rho_0}{c_0^2} \langle \delta_t \psi, \delta_{tt} \psi \rangle_{d^{(3)}}^X - \rho_0 \langle \delta_t \psi, \delta_{\nabla^2} \psi \rangle_{d^{(3)}}^X = 0 \quad (4.67)$$

Using summation by parts, (4.64), gives

$$\begin{aligned} & \frac{\rho_0}{c_0^2} \langle \delta_t \psi, \delta_{tt} \psi \rangle_{d^{(3)}}^X + \rho_0 \left(\langle \delta_t \delta_{x'-} \psi, \delta_{x'-} \psi \rangle_{\bar{d}_{x'}^{(3)}}^X \right. \\ & \left. + \langle \delta_t \delta_{y'-} \psi, \delta_{y'-} \psi \rangle_{\bar{d}_{y'}^{(3)}}^X + \langle \delta_t \delta_{z'-} \psi, \delta_{z'-} \psi \rangle_{\bar{d}_{z'}^{(3)}}^X \right) + \mathfrak{b}_{3we} = 0 \end{aligned} \quad (4.68)$$

where

$$\begin{aligned} \mathfrak{b}_{3we} = & \frac{\rho_0}{c_0^2} \left(-\{\delta_t \psi, \delta_{x'-} \psi\}_{b(x'-)}^X + \{\delta_t \psi, \delta_{x'+} \psi\}_{b(x'+)}^X - \{\delta_t \psi, \delta_{y'-} \psi\}_{b(y'-)}^X \right. \\ & \left. + \{\delta_t \psi, \delta_{y'+} \psi\}_{b(y'+)}^X - \{\delta_t \psi, \delta_{z'-} \psi\}_{b(z'-)}^X + \{\delta_t \psi, \delta_{z'+} \psi\}_{b(z'+)}^X \right) \end{aligned} \quad (4.69)$$

is the power transfer at the domain boundaries. Using (3.26a) and (3.26b) gives

$$\delta_{t+} \mathfrak{h}_{3we} + \mathfrak{b}_{3we} = 0 \quad (4.70)$$

where

$$\begin{aligned} \mathfrak{h}_{3we} = & \frac{\rho_0}{2c_0^2} (\|\delta_{t-}\psi\|_{d^{(3)}}^x)^2 + \frac{\rho_0}{2} \left(\langle \delta_{x'}-\psi, w_{t-}\delta_{x'}-\psi \rangle_{\tilde{d}_{x'}^{(3)}}^x + \langle \delta_{y'}-\psi, w_{t-}\delta_{y'}-\psi \rangle_{\tilde{d}_{y'}^{(3)}}^x \right. \\ & \left. + \langle \delta_{z'}-\psi, w_{t-}\delta_{z'}-\psi \rangle_{\tilde{d}_{z'}^{(3)}}^x \right) \end{aligned} \quad (4.71)$$

is the discrete energy in the domain. As in the discussion of the explicit scheme (3.40) for the one-dimensional wave equation in Chap. 3, we wish to find conditions for which \mathfrak{h}_{3we} is non-negative, so that the solutions are bounded. Using (3.26f) and (3.29a) produces

$$\begin{aligned} \frac{\rho_0}{2} \langle \delta_{x'}-\psi, w_{t-}\psi \rangle_{\tilde{d}_{x'}^{(3)}}^x & \stackrel{(3.26f)}{\geq} -\frac{\rho_0 k^2}{8} \left(\|\delta_{t-}\delta_{x'}-\psi\|_{\tilde{d}_{x'}^{(3)}}^x \right)^2 \\ & \stackrel{(3.29a)}{\geq} -\frac{\rho_0 k^2}{2h_3^2} (\|\delta_{t-}\psi\|_{d^{(3)}}^x)^2 \end{aligned} \quad (4.72)$$

and likewise for the $\delta_{y'-}$ and $\delta_{z'-}$ terms. This leads to

$$\mathfrak{h}_{3we} \geq \frac{\rho_0}{2} \left(\frac{1}{c_0^2} - \frac{3k^2}{h_3^2} \right) (\|\delta_{t-}\psi\|_{d^{(3)}}^x)^2 \quad (4.73)$$

The discrete energy, \mathfrak{h}_{3we} , is non-negative provided that the three-dimensional Courant number satisfies

$$\lambda_3 = \frac{c_0 k}{h_3} \leq \frac{1}{\sqrt{3}} \quad (4.74)$$

For this case, solutions will be bounded. Note that the bound on the Courant number in three dimensions is different to that in one dimension. As a result, different spacings are used for the two systems. It is clear that for the three-dimensional case, the spatial grid spacing is larger than that used for the one-dimensional case, thus the bandwidth of the three-dimensional system is less than that of the one-dimensional system. The one-dimensional spatial step size could be set to be equal to the three-dimensional spatial step size, however, this would result in poor dispersion behaviour in the one-dimensional part of the problem. This extends from the discussion of numerical dispersion in Sec. 3.3.2.

In addition, scheme (4.65) suffers from direction-dependent numerical dispersion, which is not present in the one-dimensional models. On axis, that is in directions parallel to the x' , y' , and z' axes, the effects of numerical dispersion are strongest. However, on cube diagonals, there is no numerical dispersion. It is much simpler, mathematically, to align a horn with the z' axis so this is the chosen orientation. This may seem contradictory to the criticism regarding numerical dispersion in the scheme used by Noreland [127]. However, scheme (4.65) displays anisotropic numerical dispersion whereas the numerical dispersion of the scheme used by Noreland is inhomogenous—the dispersion characteristics change with distance from the horn. The work presented here could be extended to use other three-dimensional FDTD schemes with better on-axis dispersion properties, such as those studied in [74].

4.2.8 Boundary conditions

Discrete Neumann conditions at the boundaries perpendicular to the x' coordinate are given by

$$\delta_{x'}.\psi = 0, \quad (l_{x'}, l_{y'}, l_{z'}) \in b^{(x'-)}, b^{(x'+)} \quad (4.75)$$

Absorbing boundary conditions are given by

$$\frac{1}{c_0} \delta_t.\psi - \delta_{x'}.\psi = 0, \quad (l_{x'}, l_{y'}, l_{z'}) \in b^{(x'-)} \quad (4.76)$$

$$\frac{1}{c_0} \delta_t.\psi + \delta_{x'}.\psi = 0, \quad (l_{x'}, l_{y'}, l_{z'}) \in b^{(x'+)} \quad (4.77)$$

Both the Neumann and absorbing boundary conditions can be applied to the boundaries perpendicular to the y' and z' coordinates by symmetry.

Using the absorbing boundary conditions results in a non-negative power transfer term

$$\mathfrak{b}_{3we} = \frac{\rho_0}{c_0^2} \sum_{i \in \{x' \pm, y' \pm, z' \pm\}} \|\delta_t.\psi\|_{b(i)}^2 \geq 0 \quad (4.78)$$

The discrete absorbing boundary conditions modify the scheme at the boundaries. First, consider a point on the interior on the surface $b^{(x'-)}$ so that $l_{x'} = -\frac{N_3}{2}, -\frac{N_3}{2} < l_{y'}, l_{z'} < \frac{N_3}{2}$. The update (4.66) becomes

$$\begin{aligned} (1 + \lambda) \psi_{-\frac{N_3}{2}, l_{y'}, l_{z'}}^{n+1} = & 2(1 - 3\lambda^2) \psi_{-\frac{N_3}{2}, l_{y'}, l_{z'}}^n + (\lambda - 1) \psi_{-\frac{N_3}{2}, l_{y'}, l_{z'}}^{n-1} \\ & + \lambda^2 \left(2\psi_{-\frac{N_3}{2}+1, l_{y'}, l_{z'}}^n + \psi_{-\frac{N_3}{2}, l_{y'}+1, l_{z'}}^n + \psi_{-\frac{N_3}{2}, l_{y'}-1, l_{z'}}^n \right. \\ & \left. + \psi_{-\frac{N_3}{2}, l_{y'}, l_{z'}+1}^n + \psi_{-\frac{N_3}{2}, l_{y'}, l_{z'}-1}^n \right) \end{aligned} \quad (4.79)$$

On the edge $l_{x'}, l_{y'} = -\frac{N_3}{2}, -\frac{N_3}{2} < l_{z'} < \frac{N_3}{2}$

$$\begin{aligned} (1 + 2\lambda) \psi_{-\frac{N_3}{2}, -\frac{N_3}{2}, l_{z'}}^{n+1} = & 2(1 - 3\lambda^2) \psi_{-\frac{N_3}{2}, -\frac{N_3}{2}, l_{z'}}^n + (2\lambda - 1) \psi_{-\frac{N_3}{2}, -\frac{N_3}{2}, l_{z'}}^{n-1} \\ & + \lambda^2 \left(2\psi_{-\frac{N_3}{2}+1, -\frac{N_3}{2}, l_{z'}}^n + 2\psi_{-\frac{N_3}{2}, -\frac{N_3}{2}+1, l_{z'}}^n \right. \\ & \left. + \psi_{-\frac{N_3}{2}, -\frac{N_3}{2}, l_{z'}+1}^n + \psi_{-\frac{N_3}{2}, -\frac{N_3}{2}, l_{z'}-1}^n \right) \end{aligned} \quad (4.80)$$

On the corner $l_{x'}, l_{y'}, l_{z'} = -\frac{N_3}{2}$

$$\begin{aligned} (1 + 3\lambda) \psi_{-\frac{N_3}{2}, -\frac{N_3}{2}, -\frac{N_3}{2}}^{n+1} = & 2(1 - 3\lambda^2) \psi_{-\frac{N_3}{2}, -\frac{N_3}{2}, -\frac{N_3}{2}}^n + (3\lambda - 1) \psi_{-\frac{N_3}{2}, -\frac{N_3}{2}, -\frac{N_3}{2}}^{n-1} \\ & + 2\lambda^2 \left(\psi_{-\frac{N_3}{2}+1, -\frac{N_3}{2}, -\frac{N_3}{2}}^n + \psi_{-\frac{N_3}{2}, -\frac{N_3}{2}+1, -\frac{N_3}{2}}^n \right. \\ & \left. + \psi_{-\frac{N_3}{2}, -\frac{N_3}{2}, -\frac{N_3}{2}+1}^n \right) \end{aligned} \quad (4.81)$$

These boundary conditions can be extended to other surfaces, edges, and corners.

4.2.9 Matrix implementation

We look to extend the matrix implementation presented in Sec. 3.3.8 for the one-dimensional wave equation to three-dimensions for scheme (4.65), so as to take advantage of the performance of sparse matrix procedures in MATLAB. The values of the acoustic velocity potential, $\psi_{l_{x'}, l_{y'}, l_{z'}}^{n+1/2}$ are stored in the vector, $\Psi^{n+1/2}$, by concatenating all of the values in the domain into a single vector, as in [20, 163]; see Fig. 4.9 for an illustration of this.

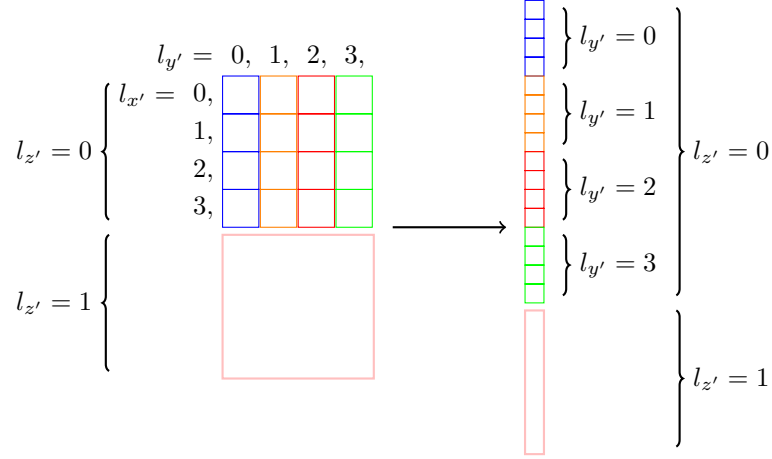


Figure 4.9: Illustration of the vectorisation of the three-dimensional grid function.

We can then construct matrices that represent the discrete spatial operators. Consider the general second difference matrix \mathbf{D} of size $(N_3 + 1) \times (N_3 + 1)$ whose elements are given by

$$D_{l,l} = -\frac{2}{h_3^2}, \quad 0 \leq l \leq N_3 \quad (4.82a)$$

$$D_{l,l+1} = \frac{1}{h_3^2}, \quad 0 \leq l \leq N_3 - 1 \quad (4.82b)$$

$$D_{l+1,l} = \frac{1}{h_3^2}, \quad 1 \leq l \leq N_3 \quad (4.82c)$$

The matrices for the difference operators in each direction are then given as

$$\mathbf{D}_{x'x'}^{(3)} = \mathbf{D} \otimes (\mathbf{I}^{(N_3+1)} \otimes \mathbf{I}^{(N_3+1)}) \quad (4.83a)$$

$$\mathbf{D}_{y'y'}^{(3)} = \mathbf{I}^{(N_3+1)} \otimes (\mathbf{D} \otimes \mathbf{I}^{(N_3+1)}) \quad (4.83b)$$

$$\mathbf{D}_{z'z'}^{(3)} = \mathbf{I}^{(N_3+1)} \otimes (\mathbf{I}^{(N_3+1)} \otimes \mathbf{D}) \quad (4.83c)$$

where $\mathbf{I}^{(N_3+1)}$ is the identity matrix of size $(N_3 + 1) \times (N_3 + 1)$ and \otimes denotes the Kronecker product [89]. The update (4.66) can be written in matrix form as

$$\Psi^{n+3/2} = \left(2\mathbf{I}^{(N_3+1)^3} + k^2 c_0^2 \left(\mathbf{D}_{x'x'}^{(3)} + \mathbf{D}_{y'y'}^{(3)} + \mathbf{D}_{z'z'}^{(3)} \right) \right) \Psi^{n+1/2} - \Psi^{n-1/2} \quad (4.84)$$

where $\mathbf{I}^{(N_3+1)^3}$ is the identity matrix of size $(N_3 + 1)^3$.

Boundary conditions are incorporated into this formulation through modification of the elements of the system matrices.

4.2.10 Coupling the systems: Discrete case

We now look to couple the discrete one-dimensional horn equation (3.108) (described using the pressure and particle velocity variables, p_l^n and $v_{l+1/2}^{n+1/2}$) with the three-dimensional wave equation (4.65) (described using the acoustic velocity potential $\psi_{l_{x'}, l_{y'}, l_{z'}}^{n+1/2}$). Recall that different grid spacings are being used: h for the one-dimensional system, and h_3 for the three-dimensional system. The time step, k , is the same for both systems.

To begin, we must first define the surface Ω_d that is a discrete representation of the surface Ω . One such case is to use a so-called ‘staircased’ approximation [21, 74, 163] given by

$$\Omega_d = \{(l_{x'}, l_{y'}, l_{z'}) \in \mathbb{Z}^3 \mid \sqrt{l_{x'}^2 + l_{y'}^2} \leq \frac{r_N}{h_3}, l_{z'} = 0\}$$

where the surface is centred at the origin and r_N is the radius at the end of the acoustic tube. The number of grid points that lie on Ω_d is N_Ω . Fig. 4.10 illustrates such a staircased approximation in the case of a circular region over a Cartesian grid.

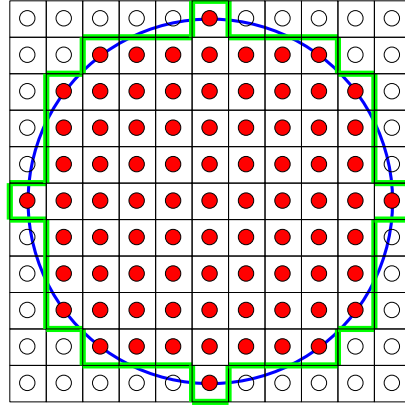


Figure 4.10: Staircased fitting applied to the interior of a circle, indicated by a blue line. Dots indicate grid points and black lines denote the area they approximate. Red centres denote grid points that lie within the circle, empty centres are those that lie without. The perimeter of the staircased approximation to the circle is indicated by a green line.

Considering Ω_d as a boundary results in the following energy balance

$$\begin{aligned} \delta_{t+} \mathfrak{h}_{3we} + \mathfrak{b}_{3we} &= -\rho_0 \sum_{\mathbf{l} \in \Omega_d} h_3^2 \delta_t \psi_1 \delta_{z'} - \psi_1 \\ &\quad + \rho_0 \sum_{\mathbf{l} \in \Omega_d^-} h_3^2 \delta_t \psi_1 \delta_{z'} + \psi_1 \end{aligned} \quad (4.85)$$

where the surface Ω_d^- is defined by

$$\Omega_d^- = \{(l_{x'}, l_{y'}, l_{z'}) \in \mathbb{Z}^3 \mid \sqrt{l_{x'}^2 + l_{y'}^2} \leq \frac{r_N}{h_3}, l_{z'} = -1\} \quad (4.86)$$

The numerical energy is now defined using

$$\begin{aligned} \mathfrak{h}_{3we} = \frac{\rho_0}{2c_0^2} (\|\delta_t - \psi\|_{d^{(3)}}^x)^2 + \frac{\rho_0}{2} \left(\langle \delta_{x'} - \psi, w_t - \delta_{x'} - \psi \rangle_{\bar{d}_{x'}^{(3)}}^x + \langle \delta_{y'} - \psi, w_t - \delta_{y'} - \psi \rangle_{\bar{d}_{y'}^{(3)}}^x \right. \\ \left. + \langle \delta_{z'} - \psi, w_t - \delta_{z'} - \psi \rangle_{\bar{d}_{z'}^{(3)} \setminus \Omega_d}^x \right) \end{aligned} \quad (4.87)$$

which is again non-negative provided $\lambda_3 \leq 1/\sqrt{3}$. The domain $\bar{d}_{z'}^{(3)} \setminus \Omega_d$ denotes the three-dimensional discrete domain that does not include Ω_d .

The terms in the right hand side of (4.85) appear to cancel out if left untreated. However, we wish to treat each surface, Ω_d and Ω_d^- , in a different manner, as in the continuous case: energy is transferred between the acoustic tube and the three-dimensional space over Ω_d and a Neumann boundary condition is applied on Ω_d^- using

$$\delta_{z'+} \psi_1 = 0, \quad \mathbf{l} \in \Omega_d^- \quad (4.88)$$

so that (4.85) becomes

$$\delta_{t+} \mathfrak{h}_{3we} + \mathfrak{b}_{3we} = -\rho_0 \sum_{\mathbf{l} \in \Omega_d} h_3^2 \delta_t \cdot \psi_1 \delta_{z'-} \psi_1 \quad (4.89)$$

The summation over Ω_d on the right hand side of (4.89) can be written in a vector form so that

$$\delta_{t+} \mathfrak{h}_{3we} + \mathfrak{b}_{3we} = -\rho_0 h_3^2 (\delta_t \cdot \Psi_{\Omega_d})^T (\delta_{z'-} \Psi_{\Omega_d}) \quad (4.90)$$

where $\Psi_{\Omega_d}^{n+1/2}$ is a column vector of length N_Ω whose elements are the values of the acoustic velocity potential grid function that lie on Ω_d .

We now look to coupling the energy of the acoustic tube to the three-dimensional field. Recalling from (3.114) that the discrete power transfer at the end of the acoustic tube is given by $\mu_{t+} p_N \mu_{z-} (S_{N+1/2} v_{N+1/2})$ we have

$$\mu_{t+} p_N \mu_{z-} (S_{N+1/2} v_{N+1/2}) = -\rho_0 h_3^2 (\delta_t \cdot \Psi_{\Omega_d})^T (\delta_{z'-} \Psi_{\Omega_d}) \quad (4.91)$$

Using this expression to combine the energies gives

$$\delta_{t+} (\mathfrak{h}_{he} + \mathfrak{h}_{3we}) + \mathfrak{b}'_{he} + \mathfrak{b}_{3we} = 0 \quad (4.92)$$

We have shown, separately, that solutions to each system are bounded and combining them in the way presented here does not affect this.

Returning to the power balance (4.91), we can set

$$\rho_0 \delta_t \cdot \Psi_{\Omega_d} = \mu_{t+} p_N \mathbf{q} \quad (4.93)$$

where $\mathbf{q} = [1, \dots, 1]^T$ is a column vector of length N_Ω that assigns the pressure at the end of the acoustic tube to a point on the surface Ω_d . Substituting back into our power balance gives

$$\begin{aligned} \mu_{t+} p_N \mu_{z-} (S_{N+1/2} v_{N+1/2}) &= -h_3^2 \mu_{t+} p_N \mathbf{q}^T \delta_{z'-} \Psi_{\Omega_d} \\ \implies \mu_{z-} (S_{N+1/2} v_{N+1/2}) &= -h_3^2 \mathbf{q}^T \delta_{z'-} \Psi_{\Omega_d} \end{aligned} \quad (4.94)$$

These conditions are discrete forms of the continuous coupling conditions (4.50) and (4.51).

4.2.11 Numerical scheme

We now determine the discrete implementation of the coupling between the one-dimensional horn equation and three-dimensional wave equation. First, we rewrite the horn equation at $l = N$ as

$$\frac{2\bar{S}_N}{\rho_0 c_0^2 k} (\mu_{t+} - 1) p_N + \frac{2}{h} (\mu_{z-} - w_{z-}) S_{N+1/2} v_{N+1/2} = 0 \quad (4.95)$$

and the wave equation on Ω_d to give

$$\frac{2\rho_0}{c_0^2 k} (\delta_{t-} - \delta_{t-}) \Psi_{\Omega_d} - \rho_0 \left(\delta_{x'x'} + \delta_{y'y'} + \left(\frac{\delta_{z'+} - \delta_{z'-}}{h_3} \right) \right) \Psi_{\Omega_d} = 0 \quad (4.96)$$

where we have used $\delta_{z'z'} = (\delta_{z'+} - \delta_{z'-})/h_3$. Multiplying by \mathbf{q}^T and rearranging gives

$$\mathbf{q}^T \left(\left(\frac{2\rho_0}{c_0^2 k} \delta_{t-} + \frac{\rho_0}{h_3} \delta_{z'-} \right) \Psi_{\Omega_d} \right) = \mathbf{q}^T \left(\left(\frac{2\rho_0}{c_0^2 k} \delta_{t-} + \rho_0 \left(\delta_{x'x'} + \delta_{y'y'} + \frac{1}{h_3} \delta_{z'+} \right) \right) \Psi_{\Omega_d} \right) \quad (4.97)$$

Using (4.93) and (4.94) yields

$$\frac{2N_{\Omega_d}}{c_0^2 k} \bar{p} - \frac{\rho_0}{h_3^3} \bar{S}_N \bar{v} = \rho_0 \mathbf{q}^T \left(\left(\frac{2}{c_0^2 k} \delta_{t-} + \delta_{x'x'} + \delta_{y'y'} + \frac{1}{h_3} \delta_{z'+} \right) \Psi_{\Omega_d} \right) \quad (4.98)$$

where $\bar{p}^{n+1/2} = \mu_{t+} p_N^n$ and $\bar{S}_N \bar{v}^{n+1/2} = \mu_{z'-} (S_{N+1/2} v_{N+1/2}^{n+1/2})$.

Combining this equation with that of the altered form of the horn equation (4.95) results in the system of equations

$$\mathbf{A} \begin{bmatrix} \bar{p} \\ \bar{S}_N \bar{v} \end{bmatrix} = \mathbf{b} \quad (4.99)$$

where

$$\mathbf{A} = \begin{bmatrix} \frac{2\bar{S}_N}{\rho_0 c_0^2 k} & \frac{2}{h} \\ \frac{2N_{\Omega_d}}{c_0^2 k} & -\frac{\rho_0}{h_3^3} \end{bmatrix}, \quad \mathbf{b} = \begin{bmatrix} \frac{2\bar{S}_N}{\rho_0 c_0^2 k} p_N^n + \frac{2}{h} S_{N-1/2} v_{N-1/2}^{n+1/2} \\ \rho_0 \mathbf{q}^T \left(\frac{2}{c_0^2 k} \delta_{t-} + \delta_{x'x'} + \delta_{y'y'} + \frac{1}{h_3} \delta_{z'+} \right) \Psi_{\Omega_d}^{n+1/2} \end{bmatrix} \quad (4.100)$$

Note that the update (4.99) requires the calculation of the inverse of the 2×2 matrix \mathbf{A} , which, for typical playing conditions, remains constant over time and can be computed outside of the temporal loop.

4.2.12 Simulation results

Simulations were performed at 50 kHz over a duration of 10 s. Two cylinders, both with a length of 1 m, were considered with radii 0.05 m and 0.1 m. In each case, the interior was modelled using the one dimensional horn equation (3.108). The enclosed volume of air representing the radiation field had a side length of 0.5 m and was terminated with first-order Enquist-Majda absorbing boundary conditions. The one-dimensional model was connected to the volume of air through the surface Ω_d which was aligned perpendicularly to the z' axis. The centre point of Ω_d coincided with the centre of the enclosed volume.

This simulation framework allows us to consider some non-physical configurations. Two scenarios were considered for each tube radius. In one case only the radiating surface is considered, and in the other a cylinder is connected to Ω_d ; see Fig. 4.11. In both cases, propagation within the cylinder is modelled in the one-dimensional parts. The difference

between the two is whether enclosed volume of air is affected by the cylinder. The bounding surface of the cylinder is an extension of the perimeter of Ω_d on the z' axis and defined using Neumann boundary conditions.

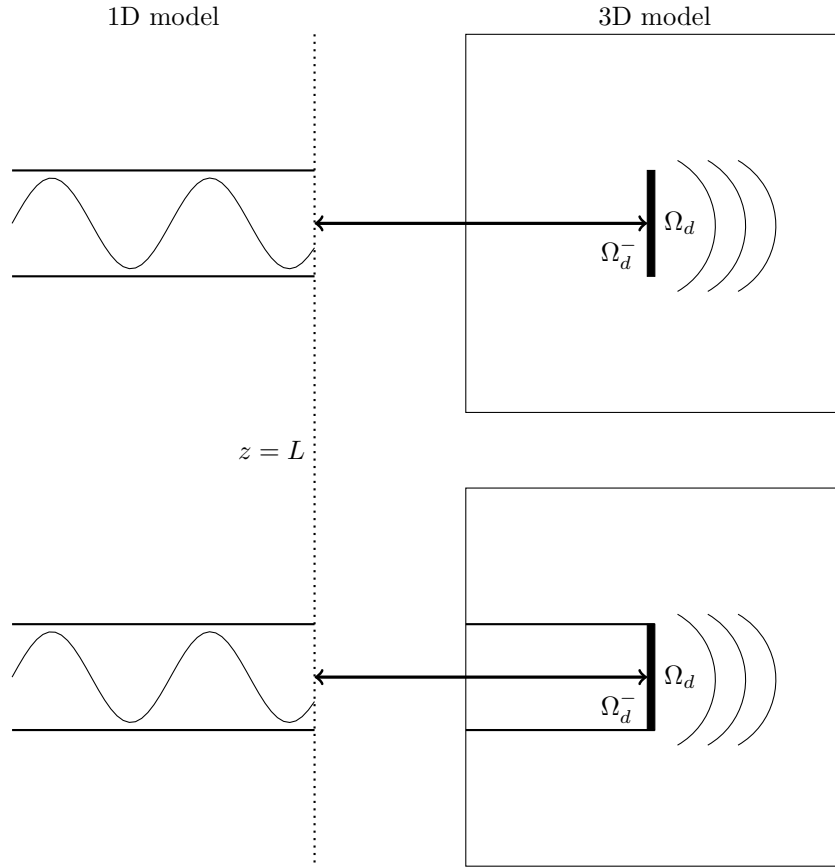


Figure 4.11: Layout of simulations. Left: Wave propagation in one-dimensional model of cylinder. Right: Cross-section of volume of air for the two simulation scenarios. Top: Only the surface Ω_d is positioned in the air box. Bottom: A cylindrical profile is positioned behind the surface Ω_d . Curved lines are a representation of sound leaving Ω_d .

Input impedances were calculated from the simulations and compared to the frequency domain expression terminated with the Levine and Schwinger radiation impedance, (4.23), for cylinders of two different radii; see Fig. 4.12. It is clear from the input impedance magnitude plots that the embedded systems behave differently from the model terminated with the Levine and Schwinger radiation impedance. These frequency shifts are shown in Fig. 4.13. When only the plane Ω_d is present in the enclosed volume of air, the frequencies of the impedance peaks are, in general, higher than the Levine and Schwinger model. Introducing the cylinder adjoining Ω_d shifts the peak frequencies down relative to those of the Levine and Schwinger model. In general, the peak positions for the plane only simulation display a smaller magnitude deviation than when the cylinder is included in the three-dimensional part of the problem.

Fig. 4.14 shows the energy evolution of the embedded FDTD system of radius 0.1 m with only the plane Ω_d in the box. It is clear that energy is exchanged between the acoustic tube and the air box and vice versa—this model also displays energy storing behaviour as seen in

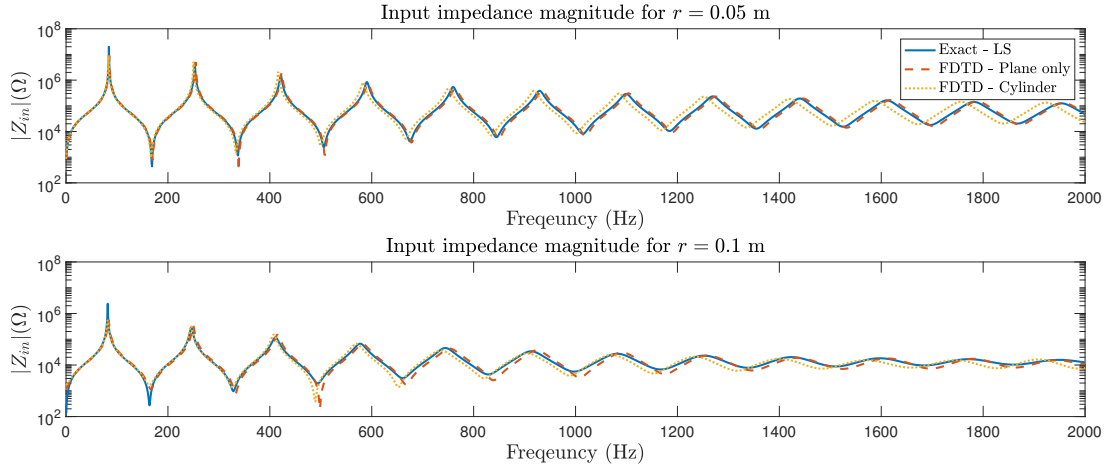


Figure 4.12: Input impedance magnitudes of two cylinders calculated using the frequency domain expression terminated with the Levine and Schwinger radiation impedance (solid blue) and using the embedded FDTD system with only the plane in the air box (dashed red) and the cylinder in the air box (dotted yellow). Top: Tube radius of 0.05 m. Bottom: Tube radius of 0.1 m.

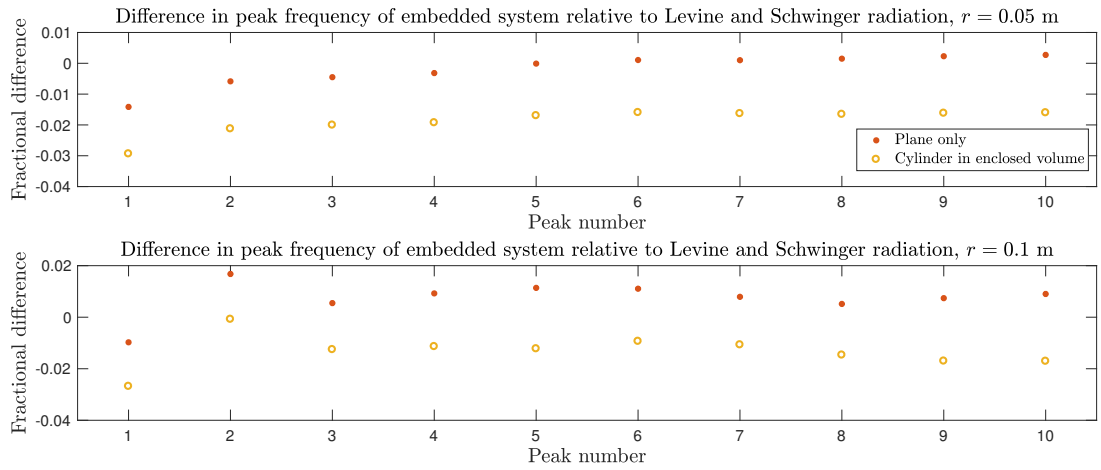


Figure 4.13: Fractional differences in peak frequency of embedded system using just a plane (red) and with a cylinder in the enclosed volume (yellow) relative to the exact solution terminated with the Levine and Schwinger radiation impedance. Top: Results for a tube of radius 0.05 m. Bottom: Results for a tube of radius 0.1 m.

the network approximation to the Levine and Schwinger model (see Sec. 4.1.2). Energy is also shown to be conserved to numerical precision of the machine. The energy transfer between

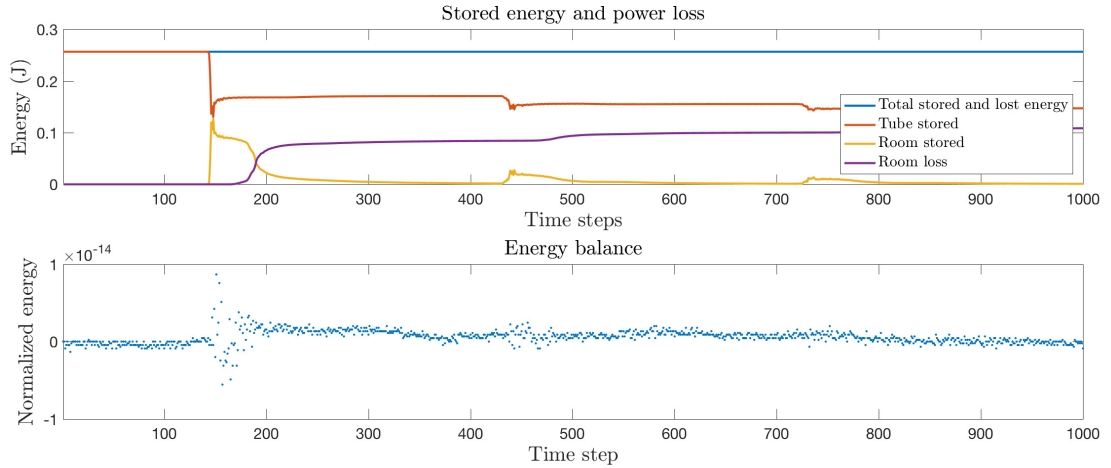


Figure 4.14: Top: Energy evolution of the embedded FDTD system with only the plane Ω_d in the enclosed volume of air. Bottom: Deviation in the total stored and lost energy over time.

the acoustic tube and the three-dimensional acoustic field is less than that seen in the network approximation to the Levine and Schwinger model. This is due to the smaller frequency bandwidth available to the three-dimensional Cartesian grid relative to the one-dimensional spatial grid. Since the acoustic tube is excited with a broadband impulse, higher frequencies that cannot travel in the three-dimensional scheme are reflected at the interface, causing a high frequency ringing in the system's impulse response. These high frequencies should be removed by including the viscous and thermal loss model over the interior of the acoustic tube.

4.3 Modelling a full instrument

We now have the ability to model a full instrument, neglecting the player, that can be compared to experimental measurements. The profile of a Smith Watkins trumpet with Kelly Screamer mouthpiece is shown in Fig. 4.15.

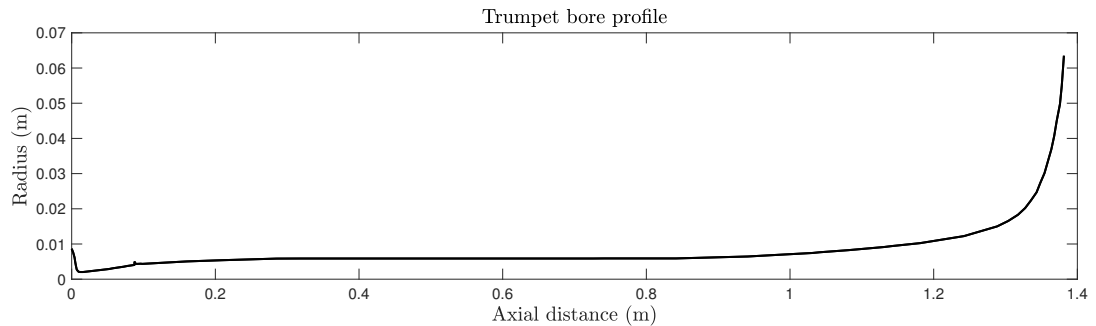


Figure 4.15: Bore profile of Smith Watkins trumpet.

Input impedance measurements were made by John Chick of the School of Engineering at

the University of Edinburgh, and compared against simulations. The one-dimensional part of the acoustic tube was simulated using (3.164) and (3.166), with a fourth order Foster structure. Two cases were simulated. The first used the approximation to the Levine and Schwinger radiation impedance presented in Sec. 4.1.3 to terminate the acoustic tube. The second case used the embedded system from Sec. 4.2.11. The final 0.08 m of the instrument bore, where $\partial_z S$ is reasonably large, was modelled using the three-dimensional wave equation, with the majority of the instrument modelled using the same one-dimensional model [78]. In the three-dimensional system, the walls of the instrument were described using a staircased approximation and were modelled as rigid boundaries using discrete Neumann boundary conditions. It should be noted, in general, that at typical audio rates, the staircased approximation does not reasonably approximate a cylinder if the radius is too small, so care must be taken when selecting the position at which the embedded system is connected.

Simulations³ were performed at 100 kHz for a duration of 1 s. Input impedances are presented in Fig. 4.16, with corresponding peak position and magnitude errors of the simulations shown in Fig. 4.17. Both models produce similar results at low frequencies. Above the fifth resonance peak the response of the models changes, with the approximation to the Levine and Schwinger radiation model producing peaks that are higher in frequency than those measured. The position of the higher peaks of the embedded system remain close to those measured experimentally, with an error less than 1 %, whereas the network radiation model gives a larger error of around 2 %. This matches with the comparison between the Levine and Schwinger model and the embedded system when applied to a cylinder; the embedded system always produces peaks of a lower frequency.

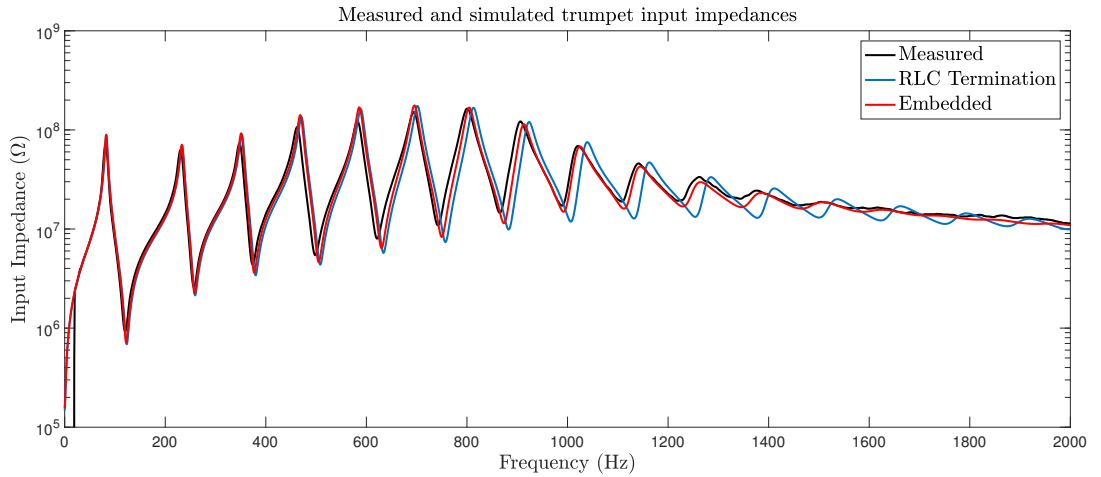


Figure 4.16: Input impedances of the Smith Watkins trumpet with Kelly Screamer mouthpiece; measured (black), simulation terminated with network approximation to Levine and Schwinger radiation impedance (blue), simulation of embedded system (red).

At high frequencies, above the twelfth resonance, the sharpness of the peaks seen in the experimental measurements reduces. This is also displayed in the embedded system but less so in the network radiation impedance model. This is most likely due to the plane wave approximation in the one-dimensional propagation model. In the embedded system, curved

³The mouthpiece for this instrument was particularly shallow, so a high spatial, and therefore temporal, resolution was required.

wavefronts are permitted in the three-dimensional part of the simulation. As the peaks of the experimental input impedance and that calculated from the embedded system become less defined at high frequencies, the network radiation model still displays sharp peaks. Although the error in magnitude of the embedded system appears to be greater than that produced by the network model, the overall behaviour of the system seems to match experiment better.

The run times over the temporal update loop for each simulation are:

- 5.70 s for the RLC termination model
- 1271.56 s for the embedded model

The embedded simulation takes over 200 times longer to perform the temporal update compared to the lumped RLC model. Note that these times do not take in the additional time required to construct the matrices that are used in the temporal update loop.

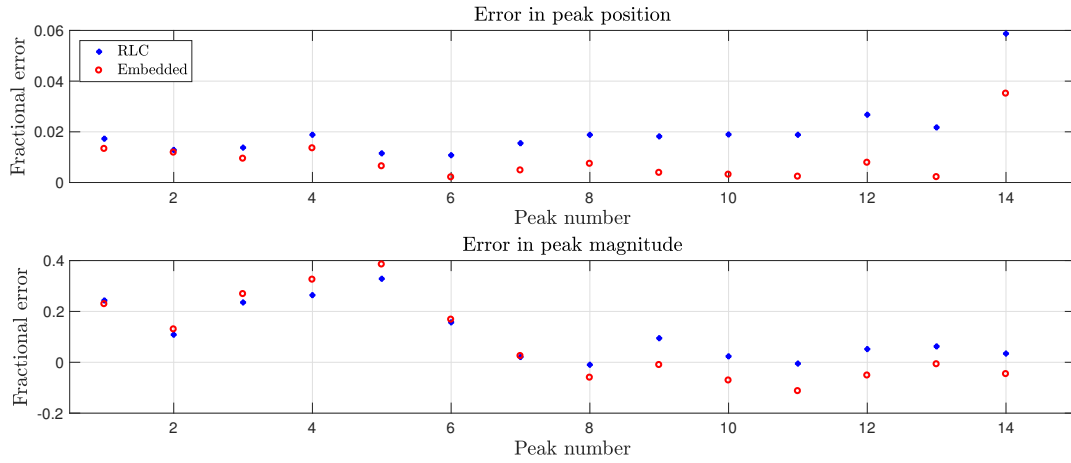


Figure 4.17: Top: Fractional error in peak position of input impedance of simulations relative to experimental measurement. Bottom: Fractional error in peak magnitude of impedance of simulations relative to experiments. Error in simulation terminated with network approximation shown in blue, error in embedded system shown in red.

4.4 Conclusions

This chapter has focussed on the boundary condition at the far end of the acoustic tube that radiates sound into the instrument's environment. Two approaches to modelling this problem have been presented. One uses a passive network approximation to the classic Levine and Schwinger radiation model, the other directly simulates the three-dimensional acoustic field in the flaring portion of the instrument, whilst the slowly varying part of the system is modelled in one-dimension.

Both models have stable implementations, as shown through energy analysis of the numerical schemes. The network model has the advantage of computational speed, requiring little in terms of storage and computation. The high frequency behaviour of this model, however, begins to diverge from experiments. It also does not give information about how

disturbances behave outside the instrument, requiring additional modelling to determine how the performance space interacts with the instrument.

The embedded system is of a different character. The high frequency resonance behaviour is more similar to that seen in experiments and it is possible to observe the sound field outside of the instrument. The disadvantage is significantly longer computation times.

Higher order structures could be used to improve the accuracy of the network approximation to the Levine and Schwinger radiation model. Alternatively, multiple simulations of propagation in cylinders could be performed using the embedded system and the radiation impedance can be extracted. The parameters of the network model could then be optimised to best fit these radiation impedance models, combining the accuracy of the embedded model with the efficiency of the network model.

Act II

Virtual Instrument

Chapter 5

Towards a complete instrument

“When scientists are asked what they are working on, their response is seldom ‘Finding the origin of the universe’ or ‘Seeking to cure cancer.’ Usually, they will claim to be tackling a very specific problem - a small piece of the jigsaw that builds up the big picture.”

— Martin Rees

The previous chapters of this work have focussed on the fundamental acoustics of the resonator of a brass instrument. We now move on from a static resonator to an instrument that a) is driven by a pressure source supplied by the user and b) whose resonances can be manipulated over time by the user.

The excitation mechanism of an acoustic tube can be described as a reed, regardless of the material it is constructed from. The instruments of the flute family, and certain organ pipes, are excited by an air reed, whilst the rest of the wind instruments use a mechanical reed. There are three main types of mechanical reed exciter [34, 63]: the single reed present in clarinets and saxophones; the double reed present in oboes and bassoons; and the lip reed employed by brass instruments. The lip reed shall be the focus of this work. The reed mechanism excites the air column within the instrument, producing a note near one of the instrument’s resonances. However, for a static bore profile this means there are several gaps in the instrument’s range.

Woodwind instruments (and also some early brass instruments such as the Serpent) have tone holes that modify the effective length of the instrument, thus allowing for additional pitches to be produced by the instrument. As metal working techniques improved, alternative methods to widen the pitch range of brass instruments were developed. Slides, seen in the modern trombone, allowed the player to lengthen the instrument by extending a section of cylindrical tubing. Another technique, which will be investigated in this work, uses valves to divert air flow into a different piece of tubing on the instrument which either lengthens or shortens the air column [35]. This is the most common feature in modern day brass instruments, seen in trumpets, French horns and tubas, to name a few. As well as introducing new notes to the instrument, partial depressing of the valves allows for multiple paths to be present in the instrument that creates some new timbral possibilities.

In this chapter, we introduce the remaining components required for a playable instrument which are used in the environment described in [75, 76]; the next chapter will introduce how

the instrument code is structured as well as how the user designs and controls the instrument.

The first section will introduce the lip model used to excite the instrument. This is an active area of research, so many models of varying complexity are available. Here, we discuss a simple outward striking reed model that creates suitable results. The model is presented in the continuous time domain first and then discretised using FDTD methods, followed by a discussion on energy analysis. The subsequent section describes how the instrument's resonances can be modified using a valve. This model, previously described in [22, 77], is developed from continuity of pressure and volume velocity between three connecting pieces of tubing and is shown to be passive in both the continuous and discrete time domains. The lossless, static system is first discussed followed by the inclusion of boundary layer losses as well as time-varying valve openings.

5.1 The lip reed model

The literature of wind instrument excitation mechanisms refers to the exciter as a pressure controlled valve [63]. Since we shall later be discussing the valves that modify the length of the air column, we shall not use this conflicting description, instead calling the exciter a reed.

Reed excitation mechanisms are primarily based on lumped masses. The simplest model involves a single mass that is constrained to movement in one-dimension—a damped, simple harmonic oscillator driven by the pressure difference over the lip. In some cases, such as the clarinet reed, the mass of the oscillator can be neglected [149, 151], but work using the full simple harmonic oscillator model can be seen, for example, in [20, 61, 86] in relation to single reed instruments and [1, 17, 47, 142] for applications to brass instruments. Extensions to the reed models include increasing the number of degrees of freedom of the individual mass [2] and modelling the reed as a series of connected masses [139]. Distributed models have been proposed where the reed is modelled as a one-dimensional bar [8]. Changes in the dynamics of the reed upon closure can be included through increasing the reed stiffness [168] or developing more complex models using penalty methods [28]. Many of these extensions have been applied to the clarinet reed; here we shall focus on the lip reed.

As well as the dynamics of the independent reed, the interaction between the reed and the instrument affects the overall output. Three classifications of reed exist, each with their own oscillatory behaviour [63]. An inward striking reed closes as the pressure difference increases slowly and plays below both the reed and instrument resonances. An outward striking reed opens as the pressure increases and plays above the instrument and reed resonances. The sliding door reed closes as the pressure difference is increased and plays below the instrument and reed resonances. The single reed exciter of the clarinet can be classified as an inward striking reed. The lip reed, when modelled using a single degree of freedom, varies between the outward striking and sliding door models depending on the pitch of the note.

Although features of a lip reed, such as the transition between outward striking and sliding door behaviour, require extra degrees of freedom for a full description, they also require additional control parameters that the user must select. As we look towards creating a usable musical instrument, we select the simplest model as our excitation mechanism.

5.1.1 A simple model

Here, we use the outward striking door model of the lip reed; see Fig. 5.1. This model is similar to the clarinet reed model in [20] without the collisions.

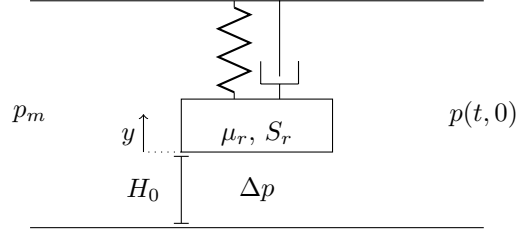


Figure 5.1: Schematic of lip reed.

The dynamics of a reed exciter are described by

$$\mu_r \frac{d^2 y}{dt^2} + \mu_r \sigma \frac{dy}{dt} + \mu_r \omega_0^2 y = S_r \Delta p \quad (5.1)$$

where $y(t)$ is the displacement of the reed from equilibrium, σ is a damping parameter, ω_0 is the natural angular frequency of the reed, S_r and μ_r are the effective surface area and mass of the lip and

$$\Delta p = p_m - p(t, 0) \quad (5.2)$$

is the pressure difference between the pressure in the mouth, p_m , and the pressure in the instrument mouthpiece, $p(t, 0)$.

Additional expressions are required to couple the reed to the instrument. McIntyre *et al.* [113] coupled excitation mechanisms to instruments by convolving the instrument reflection function with the flow that passes through the reed. This was later employed by Adachi and Sato for a trumpet player model [1, 2], among others. Here, we also use the flow passing through the reed to couple to the instrument but without the use of convolution, similar to applications using DWGs [149, 151]. The two approaches can be considered to be doing the same thing, but the method presented here can be considered as an IIR implementation, whereas the convolution would require an infinitely long FIR implementation. The pressure difference over the reed generates a volume velocity given by the Bernoulli equation

$$U_b = w[y + H_0]_+ \text{sign}(\Delta p) \sqrt{\frac{2|\Delta p|}{\rho_0}} \quad (5.3)$$

where w is an effective width of the reed, H_0 is the static equilibrium separation, $\text{sign}(\cdot)$ is the sign operator, and $[\cdot]_+ = \max(\cdot, 0)$ which removes any flow when the lips are closed¹. A volume flow is also generated by the motion of the reed

$$U_r = S_r \frac{dy}{dt} \quad (5.4)$$

We assume volume velocity is conserved so the total volume of air injected into the

¹It is interesting to note some conflict in the early literature on reeds where the experimental data showed different power laws relating the volume flow to the area and pressure difference [9]

instrument from the player is

$$Sv|_{z=0} = U_b + U_r \quad (5.5)$$

5.1.2 Energy analysis

Multiplying (5.1) by the first derivative of y and rearranging gives

$$\mu_r \frac{dy}{dt} \frac{d^2y}{dt^2} + \mu_r \sigma \left(\frac{dy}{dt} \right)^2 + \mu_r \omega_0^2 \frac{dy}{dt} y - \frac{dy}{dt} S_r \Delta p = 0 \quad (5.6)$$

Substituting (5.4) into this expression and using (5.5) gives

$$\mu_r \frac{dy}{dt} \frac{d^2y}{dt^2} + \mu_r \sigma \left(\frac{dy}{dt} \right)^2 + \mu_r \omega_0^2 \frac{dy}{dt} y + (U_b - Sv|_{z=0}) \Delta p = 0 \quad (5.7)$$

Using (5.2) gives

$$\mu_r \frac{dy}{dt} \frac{d^2y}{dt^2} + \mu_r \sigma \left(\frac{dy}{dt} \right)^2 + \mu_r \omega_0^2 \frac{dy}{dt} y + U_b \Delta p - Sv|_{z=0} (p_m - p(t, 0)) = 0 \quad (5.8)$$

Recalling that the power at the input of an acoustic tube is given by

$$\mathcal{B}'_{he} = -pSv|_{z=0} \quad (5.9)$$

and neglecting any losses within the acoustic tube or additional boundary conditions gives

$$\mu_r \frac{dy}{dt} \frac{d^2y}{dt^2} + \mu_r \sigma \left(\frac{dy}{dt} \right)^2 + \mu_r \omega_0^2 \frac{dy}{dt} y + \frac{d\mathcal{H}_{he}}{dt} - Sv|_{z=0} p_m + U_b \Delta p = 0 \quad (5.10)$$

Using (2.4) and rearranging produces

$$\frac{d}{dt} (\mathcal{H}_{he} + \mathcal{H}_{reed}) + \mathcal{Q}_{reed} + \mathcal{P}_{reed} = 0 \quad (5.11)$$

where

$$\mathcal{H}_{reed} = \frac{\mu_r}{2} \left(\left(\frac{dy}{dt} \right)^2 + \omega_0^2 y^2 \right) \geq 0 \quad (5.12a)$$

$$\mathcal{Q}_{reed} = \mu_r \left(\frac{dy}{dt} \right)^2 + w[y + H_0]_+ \sqrt{\frac{2}{\rho_0}} |\Delta p|^{3/2} \geq 0 \quad (5.12b)$$

$$\mathcal{P}_{reed} = -(U_b + U_r) p_m \quad (5.12c)$$

The energy stored in the reed, \mathcal{H}_{reed} , and the power dissipated, \mathcal{Q}_{reed} , are non-negative. Energy is injected into the system by the player, shown in the term \mathcal{P}_{reed} , but there is loss due to damping in the oscillator and due to the coupling between the reed and the instrument.

5.1.3 Numerical scheme

Discrete forms of (5.1)-(5.5) are [20]

$$\mu_r \delta_{tt} y + \mu_r \sigma \delta_t y + \mu_r \omega_0^2 \mu_t y = S_r \Delta p \quad (5.13a)$$

$$\Delta p = p_m - \mu_{t+} p_0 \quad (5.13b)$$

$$U_b = w[y + H_0]_+ \text{sign}(\Delta p) \sqrt{\frac{2|\Delta p|}{\rho_0}} \quad (5.13c)$$

$$U_r = S_r \delta_t y \quad (5.13d)$$

$$\mu_{z-} (S_{1/2} v_{1/2}) = U_b + U_r \quad (5.13e)$$

where $y^{n+1/2}$, $\Delta p^{n+1/2}$, $U_b^{n+1/2}$, and $U_r^{n+1/2}$ are all sampled on the half integer temporal grid. This superscript will be suppressed and assumed to be $n + 1/2$ unless otherwise stated for these variables.

Energy analysis

Multiplying (5.13a) by $\delta_t y$ and rearranging gives

$$\mu_r \delta_t y \delta_{tt} y + \mu_r \sigma (\delta_t y)^2 + \mu_r \omega_0^2 \delta_t y \mu_t y - S_r \delta_t y \Delta p = 0 \quad (5.14)$$

Using (5.13d) and (5.13e) gives

$$\mu_r \delta_t y \delta_{tt} y + \mu_r \sigma (\delta_t y)^2 + \mu_r \omega_0^2 \delta_t y \mu_t y + (U_b - \mu_{z-} (S_{1/2} v_{1/2})) \Delta p = 0 \quad (5.15)$$

and using (5.13b) and (5.13c)

$$\mu_r \delta_t y \delta_{tt} y + \mu_r \sigma (\delta_t y)^2 + \mu_r \omega_0^2 \delta_t y \mu_t y + U_b \Delta p - \mu_{z-} (S_{1/2} v_{1/2}) (p_m - \mu_{t+} p_0) = 0 \quad (5.16)$$

Recalling that the discrete power transfer at the entrance of the acoustic tube is given by

$$\mathbf{b}'_{he} = -\mu_{t+} p_0 \mu_{z-} (S_{1/2} v_{1/2}) \quad (5.17)$$

gives

$$\mu_r \delta_t y \delta_{tt} y + \mu_r \sigma (\delta_t y)^2 + \mu_r \omega_0^2 \delta_t y \mu_t y + U_b \Delta p - \mu_{z-} (S_{1/2} v_{1/2}) p_m + \delta_{t+} \mathbf{h}_{he} = 0 \quad (5.18)$$

Using (3.26a) and (3.26e) gives

$$\delta_{t+} (\mathbf{h}_{he} + \mathbf{h}_{reed}) + \mathbf{\Omega}_{reed} + \mathbf{p}_{reed} = 0 \quad (5.19)$$

where

$$\mathbf{h}_{reed} = \frac{\mu_r}{2} \left((\delta_t y)^2 + \omega_0^2 \mu_{t-} (y^2) \right) \geq 0 \quad (5.20a)$$

$$\mathbf{\Omega}_{reed} = \mu_r \sigma (\delta_t y)^2 + w[y + H_0]_+ \sqrt{\frac{2}{\rho_0}} |\Delta p|^{3/2} \geq 0 \quad (5.20b)$$

$$\mathbf{p}_{reed} = -(U_b + U_r) p_m \quad (5.20c)$$

Again, the stored energy in the reed and power dissipation are non-negative.

Update for reed coupling

The update for the reed position is given by

$$y^{n+3/2} = \alpha_r y^{n+1/2} + \beta_r y^{n-1/2} + \xi_r \Delta p^{n+1/2} \quad (5.21)$$

where

$$\alpha_r = \frac{4}{2 + k\sigma + k^2\omega_0^2} \quad (5.22a)$$

$$\beta_r = \frac{k\sigma - 2 - k^2\omega_0^2}{2 + k\sigma + k^2\omega_0^2} \quad (5.22b)$$

$$\xi_r = \frac{2k^2 S_r}{\mu_r(2 + k\sigma + k^2\omega_0^2)} \quad (5.22c)$$

To get the pressure difference across the reed (5.13a)-(5.13e) need to be combined, along with appropriate manipulations of the discrete operators. Using

$$\delta_{tt} = \frac{2}{k} (\delta_{t+} - \delta_{t-}), \quad \mu_{t+} = k\delta_{t+} + w_{t+} \quad (5.23)$$

allows us to rewrite (5.13a) as

$$a_1 \delta_{t+} y - a_2 \Delta p - a_3^n = 0 \quad (5.24)$$

where

$$a_1 = \frac{2}{k} + \sigma + k\omega_0^2 \geq 0, \quad a_2 = \frac{S_r}{\mu_r} \geq 0, \quad a_3^n = \left(\frac{2}{k} \delta_{t-} - \omega_0^2 w_{t-} \right) y \quad (5.25)$$

Substituting (5.13d) followed by (5.13e) gives

$$\frac{a_1}{S_r} (\mu_{z-} (S_{1/2} v_{1/2}) - U_b) - a_2 \Delta p - a_3^n = 0 \quad (5.26)$$

Recall that the lossless horn equation, (3.108), at $l = 0$ can be written as

$$\frac{\bar{S}_0}{\rho_0 c_0^2} \delta_{t+} p_0 = -\frac{2}{h} (S_{1/2} v_{1/2} - \mu_{z-} (S_{1/2} v_{1/2})) \quad (5.27)$$

Using $\delta_{t+} = \frac{2}{k} (\mu_{t+} - 1)$ and using (5.13b) gives

$$\mu_{z-} (S_{1/2} v_{1/2}) = b_1^n - b_2 \Delta p \quad (5.28)$$

where

$$b_1^n = S_{1/2} v_{1/2} + \frac{h \bar{S}_0}{\rho_0 c_0^2 k} (p_m - p_0), \quad b_2 = \frac{h \bar{S}_0}{\rho_0 c_0^2 k} \geq 0 \quad (5.29)$$

Using this expression in (5.26) and substituting (5.13c) gives

$$-c_1^n \text{sign}(\Delta p) |\Delta p|^{1/2} - c_2 \Delta p + c_3^n = 0 \quad (5.30)$$

where

$$c_1^n = w[y + H_0]_+ \sqrt{\frac{2}{\rho_0}} \geq 0, \quad c_2 = b_2 + \frac{S_r a_2}{a_1} \geq 0, \quad c_3^n = b_1^n - \frac{S_r a_3^n}{a_1} \quad (5.31)$$

Dividing by $-\text{sign}(\Delta p)$ gives the following quadratic equation in $|\Delta p|^{1/2}$

$$c_1^n |\Delta p|^{1/2} + c_2 |\Delta p| - \frac{c_3^n}{\text{sign}(\Delta p)} = 0 \quad (5.32)$$

Since $c_1^n, c_2 \geq 0$, real solutions are guaranteed if

$$\text{sign}(c_3^n) = \text{sign}(\Delta p) \quad (5.33)$$

resulting in

$$|\Delta p|^{1/2} = \frac{-c_1^n \pm \sqrt{(c_1^n)^2 + 4c_2 |c_3^n|}}{2c_2} \quad (5.34)$$

Taking the positive solution of the square root term guarantees the solution is positive. The pressure difference is then given by

$$\Delta p = \text{sign}(c_3^n) \left(\frac{-c_1^n + \sqrt{(c_1^n)^2 + 4c_2 |c_3^n|}}{2c_2} \right)^2 \quad (5.35)$$

5.1.4 Simulation

Simulations were performed for the lip reed model connected to a lossless cylinder of length 0.5 m and radius 0.005 m, terminated with a Dirichlet boundary condition at the end opposite the reed. The explicit horn equation scheme (3.108) was used to model propagation in the tube. Simulations were performed at 50 kHz and a temperature of 26.85°C. Lip parameters were: $S_r = 1.46 \times 10^{-5} \text{ m}^2$, $\mu_r = 5.37 \times 10^{-5} \text{ kg}$, $\sigma = 5$, $H_0 = 2.9 \times 10^{-4} \text{ m}$, $w = 1 \times 10^{-2} \text{ m}$, and $p_m = 3 \times 10^3 \text{ Pa}$.

Fig. 5.2 shows the reed displacement for $\omega_0 = 200\pi \text{ rad}\cdot\text{s}^{-1}$ where no self sustained oscillations occur. In this case, the reed is displaced by a constant amount and no musical note is produced. Fig. 5.3 shows the energy balance of this system, given as an extension of (3.75)

$$\mathfrak{h}_{sum}^{n+1} = \frac{\mathfrak{h}_{we}^{n+1} + \mathfrak{h}_{reed}^{n+1} - \mathfrak{h}_{we}^0 - \mathfrak{h}_{reed}^0 + k \sum_{q=0}^n \mathfrak{Q}_{reed}^{n+1/2} + \mathfrak{p}_{reed}^{n+1/2}}{[\mathfrak{h}_{we}^0 + \mathfrak{h}_{reed}^0]_2} \quad (5.36)$$

The energy balance is on the order of $\mathcal{O}(10^{-10})$.

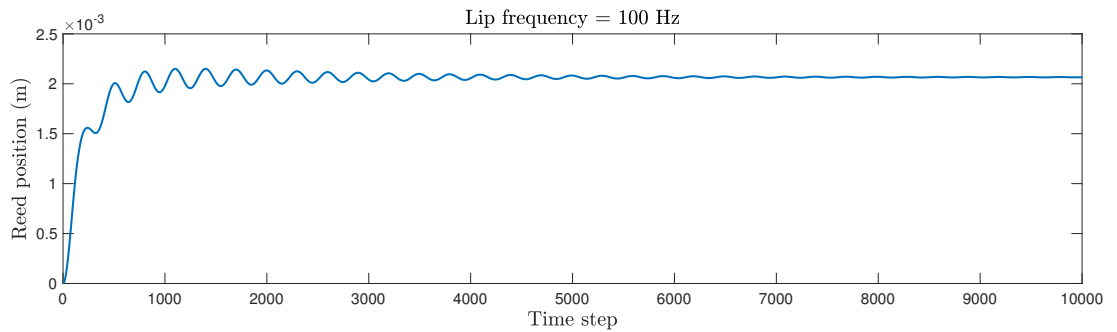


Figure 5.2: Displacement of the lip reed from equilibrium when no self sustained oscillation occurs.

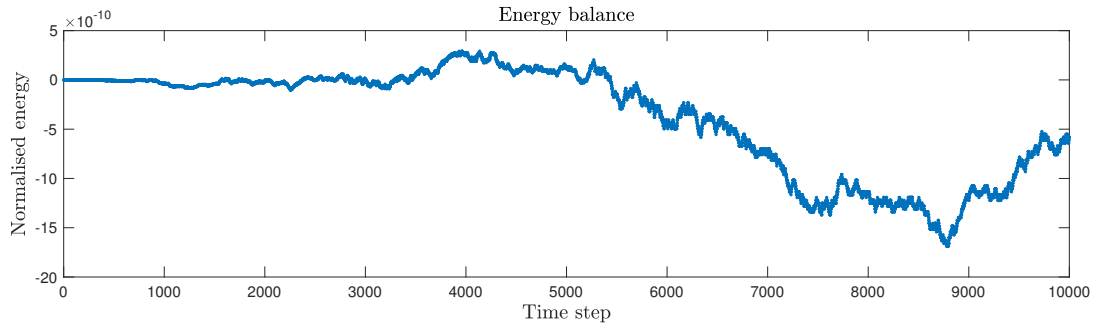


Figure 5.3: Energy balance of the system when no oscillation occurs.

Fig. 5.4 shows the reed displacement for $\omega_0 = 340\pi \text{ rad}\cdot\text{s}^{-1}$ where, after a transient stage, self sustained oscillations occur. Fig. 5.5 shows the corresponding energy evolution of the system; Fig. 5.6 shows the same plot but enlarged so as to see the variations in stored energy. Most of the energy is dissipated by the coupling between the reed and the acoustic tube, however, there is a clear periodic exchange of energy between the acoustic tube and the reed. The energy balance is shown in Fig. 5.7 for this configuration. The variation in the normalised energy balance is also on the order of 10^{-10} .

Both examples presented here display variations in energy that are above machine precision. This could be a result of rounding errors in the update scheme for the lip reed: there are several orders of magnitude difference between the energy stored in the tube and the reed. Torin [163] showed variations in the discrete energy of a simple harmonic oscillator were caused by floating point rounding errors when dividing by terms in the FDTD scheme; similar operations are seen in the lip coupling scheme. Such issues are interesting but are beyond the scope of this work.

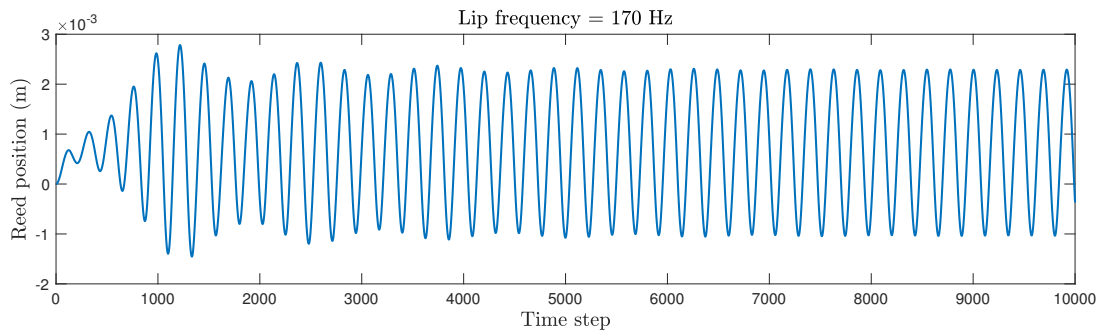


Figure 5.4: Displacement of the lip reed from equilibrium in the case of self sustained oscillation.

5.2 Valves

As previously mentioned in the introduction to this chapter, the pitch of a note produced by a brass instrument is determined by the coupling between the reed and the instrument's resonances. The lower resonances of an instrument are separated by large intervals, spanning several musical notes, meaning that the instrument bore profile must be modified to fill in

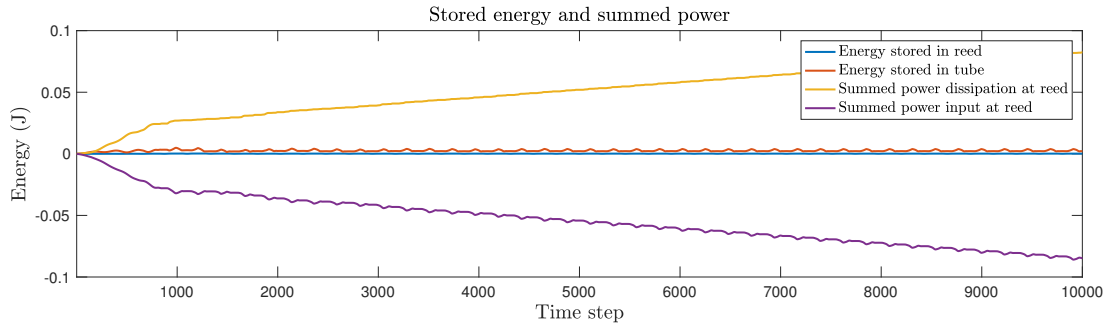


Figure 5.5: Energy evolution of the system when self sustained oscillation occurs. Stored energy in the reed (blue) and tube (red), summed power dissipation in reed (orange) and summed power input at reed (purple).

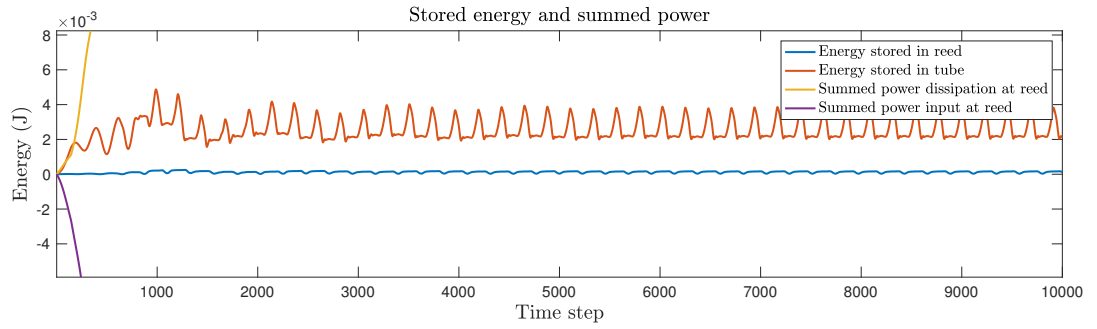


Figure 5.6: Energy evolution of the system when self sustained oscillation occurs. Stored energy in the reed (blue) and tube (red), summed power dissipation in reed (orange) and summed power input at reed (purple).

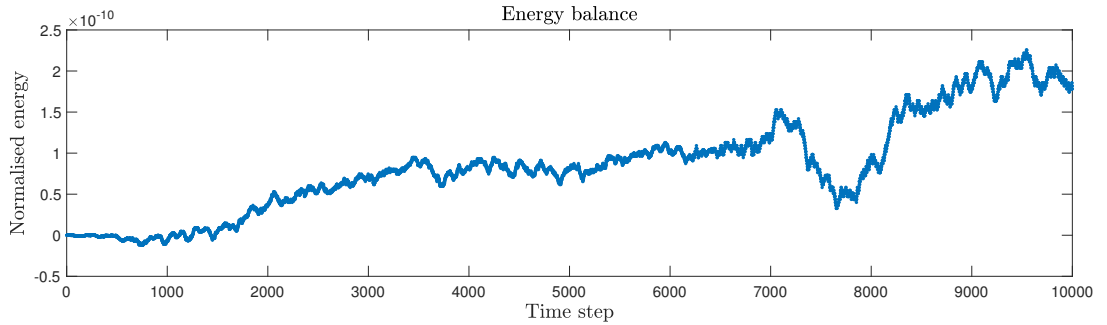


Figure 5.7: Energy balance for self sustained oscillating system.

these gaps. This can be done by changing the length of the air column. In woodwind instruments, tone holes are used to disrupt the pressure field in the tube and change the internal mode shapes. Trombones (and to some extent instruments with tuning slides) adjust the length of the air column by extending a moveable slide to make the instrument longer. Another method of lengthening the air column in a brass instrument is through the use of valves that divert air into longer, or shorter, pieces of tubing.

Simple treatment of changing notes using DWG methods involves storing the individual tube lengths corresponding to different pitches in separate delay lines [47]. However, this

approach does not allow for interactions between tube branches or include transient effects as the system is modified with time. Kemp *et. al.* [98] presented a time-domain model of an extending trombone slide that included doppler shift, although this was not used for sound synthesis purposes. Models for a single tone hole were presented by Keefe [93] and Dubos *et. al.* [50]; these have been extended to model the effect of several open tone holes in an instrument in the frequency domain [100, 101, 128] and time domain [20]. Modelling of tone holes has also been performed in three-dimensions by Giordano [68] and in two-dimensions by Allen and Raghuvanshi [4]. The latter team also used their system to model valves, but did not include interactions between the tubes that make up the valve system. Bilbao [22] presented a model that does allow for this interaction and is presented here.

A simplified schematic of a brass instrument valve is shown in Fig. 5.8. Three pieces of tubing are connected at a junction J : a main tube feeds into a default tube and a bypass tube. The default tube is the path that airflow can take when the valve is left in the neutral position; the bypass tube is the route air takes when the valve is depressed. This description extracts the most important behaviour but neglects the additional complexity of the bore profile in such valve sections.

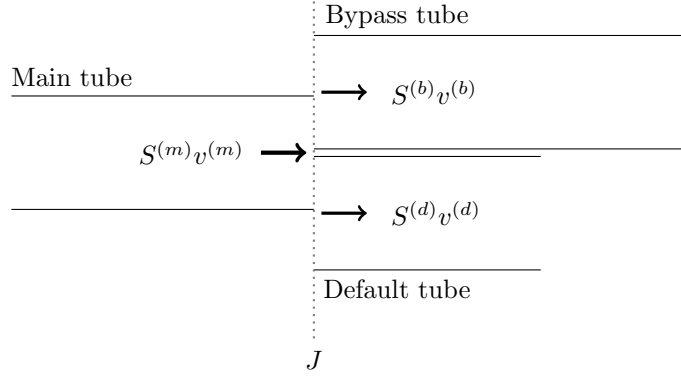


Figure 5.8: Schematic of a brass instrument valve. Three pieces of tubing are combined at J . The pressure at the junction is the same in each piece of tubing and the total volume velocity flow over the junction is conserved.

It is useful to consider each piece of tubing in its own spatial domain. The superscripts (m) , (d) , and (b) will refer to variables concerned with the main, default, and bypass tubes. The main tube lies over the spatial interval $\mathcal{D}_m = \{z \in \mathbb{R} \mid 0 \leq z \leq L_m\}$, the default tube over $\mathcal{D}_d = \{z \in \mathbb{R} \mid 0 \leq z \leq L_d\}$, and the bypass tube over $\mathcal{D}_b = \{z \in \mathbb{R} \mid 0 \leq z \leq L_b\}$. The values L_m , L_d , and L_b are the lengths of the respective pieces of tubing. The junction, J , is positioned at $z = L_m$ in \mathcal{D}_m for the main tube and $z = 0$ in \mathcal{D}_d and \mathcal{D}_b for the default and bypass tubes.

At the junction, the pressure is the same in each tube

$$p^{(m)}(t, L_m) = p^{(d)}(t, 0) = p^{(b)}(t, 0) = p^{(J)}(t) \quad (5.37)$$

Volume flow is also conserved across the junction so that

$$S^{(m)}(L_m)v^{(m)}(t, L_m) = S^{(d)}(0)v^{(d)}(t, 0) + S^{(b)}(0)v^{(b)}(t, 0) \quad (5.38)$$

These boundary conditions are the same as those shown in the coupling of DWGs in [150], although Smith did not use this formulation in the context of valve modelling. The surface areas of the default and bypass tubes at the junction can be written in terms of the surface area of the main tube at the junction

$$S^{(d)}(0) = q^{(d)} S^{(m)}(L_m), \quad S^{(b)}(0) = q^{(b)} S^{(m)}(L_m) \quad (5.39)$$

where $q^{(d)}$ and $q^{(b)}$ are control parameters relating to how much the valve is open. The following inequality must hold

$$q^{(d)} + q^{(b)} \leq 1 \quad (5.40)$$

If $q^{(d)} = 1$ and $q^{(b)} = 0$, air can only flow into the default tube from the junction; nothing passes into the bypass tube. If $q^{(d)} = 0$ and $q^{(b)} = 1$ then the opposite occurs.

For synthesis purposes, it is suitable to only use the equality

$$q^{(d)} + q^{(b)} = 1 \implies q^{(b)} = 1 - q^{(d)} = 1 - q \quad (5.41)$$

where q is a valve control parameter. However, for experiments the inequality must be used due to the geometry of the valve—see Fig. 5.9.

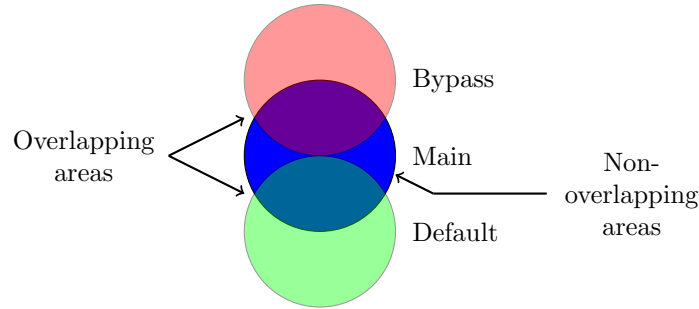


Figure 5.9: Overlapping circles representing the junction of a valve. The default (green) and bypass (red) tubes overlap the main tube (blue). However, it is clear that the total area of the main tube is not covered by the other tubes.

Energy

For simplicity, we will only consider the energy at the junction; there is no energy injected at the entrance of the tube at this point. Energy analysis on the main, default, and bypass tubes results in

$$\frac{d\mathcal{H}^{(m)}}{dt} + p^{(m)} S^{(m)} v^{(m)}|_{z=L_m} = 0 \quad (5.42a)$$

$$\frac{d\mathcal{H}^{(d)}}{dt} - p^{(d)} S^{(d)} v^{(d)}|_{z=0} = 0 \quad (5.42b)$$

$$\frac{d\mathcal{H}^{(b)}}{dt} - p^{(b)} S^{(b)} v^{(b)}|_{z=0} = 0 \quad (5.42c)$$

where

$$\mathcal{H}^{(m)} = \frac{1}{2\rho_0 c_0^2} \|\sqrt{S^{(m)}} p^{(m)}\|_{\mathcal{D}_m}^2 + \frac{\rho_0}{2} \|\sqrt{S^{(m)}} v^{(m)}\|_{\mathcal{D}_m}^2 \geq 0 \quad (5.43a)$$

$$\mathcal{H}^{(d)} = \frac{1}{2\rho_0 c_0^2} \|\sqrt{S^{(d)}} p^{(d)}\|_{\mathcal{D}_d}^2 + \frac{\rho_0}{2} \|\sqrt{S^{(d)}} v^{(d)}\|_{\mathcal{D}_d}^2 \geq 0 \quad (5.43b)$$

$$\mathcal{H}^{(b)} = \frac{1}{2\rho_0 c_0^2} \|\sqrt{S^{(b)}} p^{(b)}\|_{\mathcal{D}_b}^2 + \frac{\rho_0}{2} \|\sqrt{S^{(b)}} v^{(b)}\|_{\mathcal{D}_b}^2 \geq 0 \quad (5.43c)$$

$$(5.43d)$$

and only the power transfer at the tube junction has been taken into account. Using the pressure condition (5.37) gives

$$\frac{d\mathcal{H}^{(m)}}{dt} + p^{(J)} S^{(m)} v^{(m)}|_{z=L_m} = 0 \quad (5.44a)$$

$$\frac{d\mathcal{H}^{(d)}}{dt} - p^{(J)} S^{(d)} v^{(d)}|_{z=0} = 0 \quad (5.44b)$$

$$\frac{d\mathcal{H}^{(b)}}{dt} - p^{(J)} S^{(b)} v^{(b)}|_{z=0} = 0 \quad (5.44c)$$

Utilising conservation of volume velocity over the junction, (5.38), gives

$$\frac{d\mathcal{H}^{(m)}}{dt} + p^{(J)} \left(S^{(d)} v^{(d)}|_{z=0} + S^{(m)} v^{(m)}|_{z=0} \right) = 0 \quad (5.45)$$

Using (5.44b) and (5.44c) gives

$$\frac{d}{dt} \left(\mathcal{H}^{(m)} + \mathcal{H}^{(d)} + \mathcal{H}^{(b)} \right) = 0 \quad (5.46)$$

It is clear that the expression $\mathcal{H}^{(m)} + \mathcal{H}^{(d)} + \mathcal{H}^{(b)}$ is non-negative so coupling of the system in this way results in bounded solutions.

5.2.1 Numerical scheme

We now discretise the spatial domains for each tube section. The pressure lies over the spatial grids defined by: $d_m = \{l \in \mathbb{Z} \mid 0 \leq l \leq N_m\}$ in the main tube, $d_d = \{l \in \mathbb{Z} \mid 0 \leq l \leq N_d\}$ in the default tube, and $d_b = \{l \in \mathbb{Z} \mid 0 \leq l \leq N_b\}$ in the bypass tube. The velocity lies over the spatial grids defined by: $\bar{d}_m = \{l \in \mathbb{Z} \mid 0 \leq l \leq N_m - 1\}$ in the main tube, $\bar{d}_d = \{l \in \mathbb{Z} \mid 0 \leq l \leq N_d - 1\}$ in the default tube, and $\bar{d}_b = \{l \in \mathbb{Z} \mid 0 \leq l \leq N_b - 1\}$ in the bypass tube. The number of points in each tube are given, respectively, by $N_m = \text{floor}(L_m/h_m)$, $N_d = \text{floor}(L_d/h_d)$, and $N_b = \text{floor}(L_b/h_b)$, where the spacings h_m , h_d , and h_b all satisfy the Courant condition but are not necessarily of equal lengths. Temporal indices will be suppressed and are assumed to be at n for pressure variables and $n + 1/2$ for velocity variables, unless otherwise stated. The junction between the tubes lies at $l = N_m$ in d_m in the main tube and $l = 0$ in d_d and d_b for the default and bypass tubes.

The discrete forms of (5.37) - (5.39) are

$$p_{N_m}^{(m)} = p_0^{(d)} = p_0^{(b)} = p^{(J)} \quad (5.47a)$$

$$\mu_{z-} S_{N_m+1/2} v_{N_m+1/2}^{(m)} = \mu_{z-} S_{1/2}^{(d)} v_{1/2}^{(d)} + \mu_{z-} S_{1/2}^{(b)} v_{1/2}^{(b)} \quad (5.47b)$$

$$\bar{S}_0^{(d)} = q^{(d)} \bar{S}_{N_m}^{(m)}, \quad \bar{S}_0^{(b)} = q^{(b)} \bar{S}_{N_m}^{(m)} \quad (5.47c)$$

The discrete energy in each of the tubes is given by

$$\delta_{t+} \mathfrak{h}^{(m)} + p_{N_m}^{(m)} \mu_{z-} S_{N_m+1/2}^{(m)} v_{N_m+1/2}^{(m)} = 0 \quad (5.48a)$$

$$\delta_{t+} \mathfrak{h}^{(d)} - p_0^{(d)} \mu_{z-} S_{1/2}^{(d)} v_{1/2}^{(d)} = 0 \quad (5.48b)$$

$$\delta_{t+} \mathfrak{h}^{(b)} - p_0^{(b)} \mu_{z-} S_{1/2}^{(b)} v_{1/2}^{(b)} = 0 \quad (5.48c)$$

where

$$\mathfrak{h}^{(m)} = \frac{1}{2\rho_0 c_0^2} \left(\|\sqrt{\bar{S}^{(m)}} p^{(m)}\|^x \right)_{d_m}^2 + \frac{\rho_0}{2} \langle S^{(m)} v^{(m)}, w_{t-} v^{(m)} \rangle_{\bar{d}_m} \geq 0 \quad \text{if } \lambda_m \geq 1 \quad (5.49a)$$

$$\mathfrak{h}^{(d)} = \frac{1}{2\rho_0 c_0^2} \left(\|\sqrt{\bar{S}^{(d)}} p^{(d)}\|^x \right)_{d_d}^2 + \frac{\rho_0}{2} \langle S^{(d)} v^{(d)}, w_{t-} v^{(d)} \rangle_{\bar{d}_d} \geq 0 \quad \text{if } \lambda_d \geq 1 \quad (5.49b)$$

$$\mathfrak{h}^{(b)} = \frac{1}{2\rho_0 c_0^2} \left(\|\sqrt{\bar{S}^{(b)}} p^{(b)}\|^x \right)_{d_b}^2 + \frac{\rho_0}{2} \langle S^{(b)} v^{(b)}, w_{t-} v^{(b)} \rangle_{\bar{d}_b} \geq 0 \quad \text{if } \lambda_b \geq 1 \quad (5.49c)$$

Note that we only consider the energy at the junction and neglect any power changes at the far ends.

Using (5.47a) and (5.47b) allows us to combine all of the energies so that

$$\delta_{t+} \left(\mathfrak{h}^{(m)} + \mathfrak{h}^{(d)} + \mathfrak{h}^{(b)} \right) = 0 \quad (5.50)$$

The total energy of the system is non-negative, so solutions are bounded.

5.2.2 Update for coupling

We have shown that the specific discretisation of the coupling condition between tubes is stable, we now look at how to actually implement this scheme. Consider lossless wave propagation to begin with. We can write the pressure FDTD scheme of the horn equation, (3.108), of each tube at the junction as

$$\frac{\bar{S}_{N_m}^{(m)}}{\rho_0 c_0^2} \delta_{t+} p_{N_m}^{(m)} + \frac{2}{h_m} \left(\mu_{z-} S_{N_m+1/2}^{(m)} v_{N_m+1/2}^{(m)} - S_{N_m-1/2}^{(m)} v_{N_m-1/2}^{(m)} \right) = 0 \quad (5.51a)$$

$$\frac{\bar{S}_0^{(d)}}{\rho_0 c_0^2} \delta_{t+} p_0^{(d)} + \frac{2}{h_d} \left(S_{1/2}^{(d)} v_{1/2}^{(d)} - \mu_{z-} S_{1/2}^{(d)} v_{1/2}^{(d)} \right) = 0 \quad (5.51b)$$

$$\frac{\bar{S}_0^{(b)}}{\rho_0 c_0^2} \delta_{t+} p_0^{(b)} + \frac{2}{h_b} \left(S_{1/2}^{(b)} v_{1/2}^{(b)} - \mu_{z-} S_{1/2}^{(b)} v_{1/2}^{(b)} \right) = 0 \quad (5.51c)$$

It is clear that this form uses points outside of the domain of the tubes; see Fig. 5.10 for a representation of this. The boundary conditions previously specified allow us to couple the tubes. Using (5.47b) allows us to combine these equations, which, after rearranging, gives

$$\begin{aligned} \frac{h_m \bar{S}_{N_m}^{(m)}}{2\rho_0 c_0^2} \delta_{t+} p_{N_j}^{(m)} + \frac{h_d \bar{S}_0^{(d)}}{2\rho_0 c_0^2} \delta_{t+} p_0^{(d)} + \frac{h_b \bar{S}_0^{(b)}}{2\rho_0 c_0^2} \delta_{t+} p_0^{(b)} &= S_{N_m-1/2}^{(m)} v_{N_m-1/2}^{(m)} - S_{1/2}^{(d)} v_{1/2}^{(d)} \\ &\quad - S_{1/2}^{(b)} v_{1/2}^{(b)} \end{aligned} \quad (5.52)$$

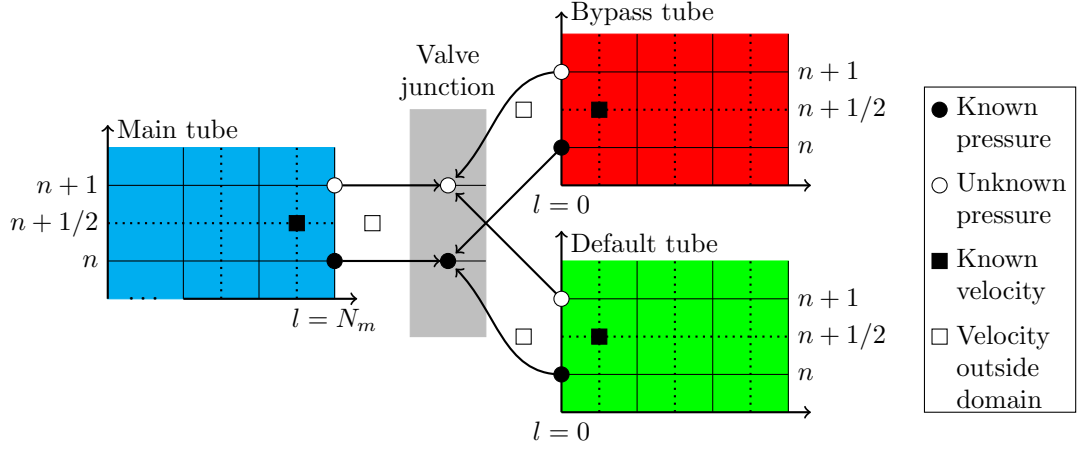


Figure 5.10: Schematic of the valve junction on the discrete grids. The pressure at the valve junctions is the same in each tube. There are velocities outside the domain, but these can be removed using continuity of volume velocity over the junction.

Rewriting this expression in terms of the pressure and main tube surface area at the junction using (5.47a) and (5.47c) produces

$$\left(h_m + h_d q^{(d)} + h_b q^{(b)}\right) \frac{\bar{S}_{N_m}^{(m)}}{2\rho_0 c_0^2} \delta_{t+p}^{(J)} = S_{N_m-1/2}^{(m)} v_{N_m-1/2}^{(m)} - S_{1/2}^{(d)} v_{1/2}^{(d)} - S_{1/2}^{(b)} v_{1/2}^{(b)} \quad (5.53)$$

Rearranging to give the value of $p^{(J),n+1}$ gives

$$p^{(J),n+1} = p^{(J),n} + \frac{2\rho_0 c_0^2 k}{\bar{S}_{N_m}^{(m)} (h_m + h_d q^{(d)} + h_b q^{(b)})} \left(S_{N_m-1/2}^{(m)} v_{N_m-1/2}^{(m)} - S_{1/2}^{(d)} v_{1/2}^{(d)} - S_{1/2}^{(b)} v_{1/2}^{(b)} \right) \quad (5.54)$$

5.2.3 Recombining tubes

In brass instruments the tubes in the valve sections must recombine to form a single air column, see Fig. 5.11. We define the new variables in the recombined tube using the superscript (m') and go straight into application in the discrete domain. The pressure in this new tube is defined over the discrete domain $d_{m'} = \{l \in \mathbb{Z} \mid 0 \leq l \leq N_{m'}\}$, where $N_{m'} = \text{floor}(L_{m'}/h_{m'})$, $L_{m'}$ is the length of the tube, and $h_{m'}$ is the step size used in the new domain. The velocity is defined over $\bar{d}_{m'} = \{l \in \mathbb{Z} \mid 0 \leq l \leq N_{m'} - 1\}$. The new junction, J' , combines the default and bypass tubes at $l = N_d$ in d_d and $l = N_b$ in d_b , respectively, to the recombined tube at $l = 0$ in $d_{m'}$.

The boundary conditions concerning pressure and volume velocity, (5.47a) and (5.47b), remain the same. However, implementation is modified since the side of the domain where the unknown points changes, resulting in a change of sign for the volume velocities. The pressure

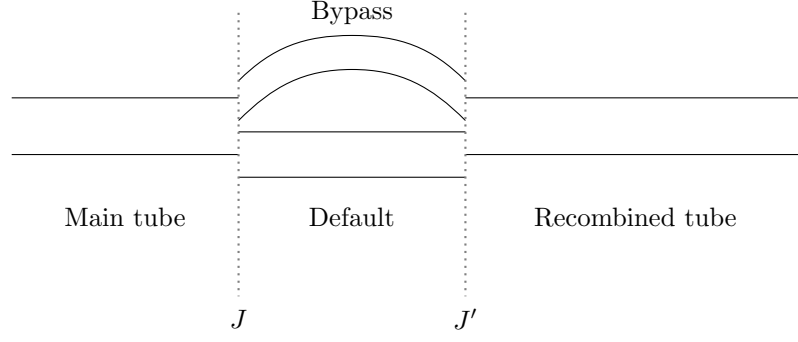


Figure 5.11: Schematic of a tube system that splits into two and then recombines back into one tube. Note that modelling of the bypass tube is done by assuming it is straight, its bent appearance in the figure is to show how the default and bypass tubes reconnect.

update at the recombining junction is given by

$$p^{(J'),n+1} = p^{(J'),n} - \frac{2\rho_0 c_0^2 k}{\bar{S}_0^{(m')} (h_{m'} + h_d q^{(d)} + h_b q^{(b)})} \left(S_{1/2}^{(m')} v_{1/2}^{(m')} - S_{N_d-1/2}^{(d)} v_{N_d-1/2}^{(d)} - S_{N_b-1/2}^{(b)} v_{N_b-1/2}^{(b)} \right) \quad (5.55)$$

Profile for default and bypass tubes

The cross-sectional area of the default and bypass tubes require modification at the tube ends on both the pressure and velocity grids. We state examples for the default tube but the discussion extends in the same way for the bypass tube.

On the pressure grid, (5.47c) holds for $\bar{S}^{(d)}$ at $l = 0$ and $l = N_d$. This is also the case the points on the particle velocity grid so that

$$S_{1/2}^{(d)} = \bar{S}_0^{(d)}, \quad S_{N_d-1/2}^{(d)} = \bar{S}_{N_d}^{(d)} \quad (5.56)$$

The remainder of the bore profile on the velocity grid is then sampled directly from the bore. The bore profile on the pressure grid is averaged from the neighbouring points on the velocity grid; see Fig. 5.12.

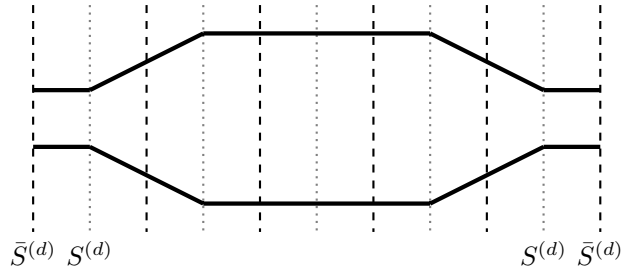


Figure 5.12: Profile of the default tube. Black dotted lines show the pressure spatial grid, grey dotted lines show the particle velocity grid, solid black lines show the bore profile.

For a real instrument geometry there are extra complications that should be noted. For typical audio sample rates, the length of the default tube section can only contain the

pressures at the junctions and one internal velocity field point. This results in a cylindrical profile with area $q^{(d)}S^{(m)}$. Due to the construction of the real instrument valve, the bypass tube has a section at either end that is a similar geometry to the default tube. This part is also cylindrical with areas that are scaled by the bypass tube opening but expand to the actual tube diameter over the interior of the tube.

5.2.4 Junction coupling using lossy propagation

The same boundary conditions can be applied to joining tubes modelled with lossy propagation. For example, the pressure update (3.164) that uses the Foster network approximation becomes

$$p^{(J),n+1} = \alpha_{N_m}^{(p)} p^{(J),n} + \beta^{(J),(p)} \left(S_{1/2}^{(d)} v_{1/2}^{(d)} + S_{1/2}^{(b)} v_{1/2}^{(b)} - S_{N_m-1/2}^{(m)} v_{N_m-1/2}^{(m)} \right) + \alpha_{0,N_m}^{(p)} p_0^{(J),n} + \sum_{q=1}^M \alpha_{q,N_m}^{(p)} \tilde{p}_q^{(J),n} \quad (5.57)$$

where only the volume velocity constant is modified

$$\beta^{(J),(p)} = - \frac{\rho_0 c_0^2 k}{\bar{S}^{(J)} (h_m + q^{(d)} h_d + q^{(b)} h_b) (1 + E_l \tilde{G}_l)} \quad (5.58)$$

The updates of the network variables, $p_0^{(J)}$ and $p_q^{(J)}$, at the junction remain the same as those defined in Chap. 3. At first it seems counter-intuitive that the inclusion of a branching tube to the visctherm model only requires modification of one term. However, for the Zwikker and Kosten model the attenuation processes are essentially local and would not be modified by neighbouring points.

5.2.5 Simulation results

Simulations were performed for the lossless system with tube lengths of $L_m = 1.3$ m, $L_d = 0.016$ m, $L_b = 0.2$ m, and $L_{m'} = 1$ m. The radii of each tube were 0.05 m. Simulations were performed at a sample rate of 50 kHz and for a duration of 10 s.

Fig. 5.13 shows the energy evolution of the lossless valve system when $q^{(d)} = 0.5$. Energy is transferred from one tube to the next as the wave propagates along the tube system and energy is conserved to numerical precision of the machine.

Fig. 5.14 shows simulation results for the lossy system² using the Foster loss model with $M = 4$. Input impedances were calculated for different values of $q^{(d)}$ using the procedure described in Sec. 3.4.3. The equality $q^{(b)} = 1 - q^{(d)}$ was used to set the bypass tube opening.

There is a reduction in the frequency of the input impedance peaks as $q^{(d)}$ reduces. For partially open configurations the input impedance peaks lie between the fully open and fully closed configurations and are unevenly spaced. Comparing to the fully open or fully closed configurations, the partially open systems appear to add some additional resonances either by introducing a new impedance peak, shown by the peak around 700 Hz, or by splitting the impedance peaks, such as those below 900 Hz. Modifying the valve opening changes the magnitude and position of these peaks, although the effect is more noticeable above 600 Hz.

²The results for the lossless system are similar to those presented here. However, using the lossy model gives a clearer indication on the effect of partial valve openings on the input impedance.

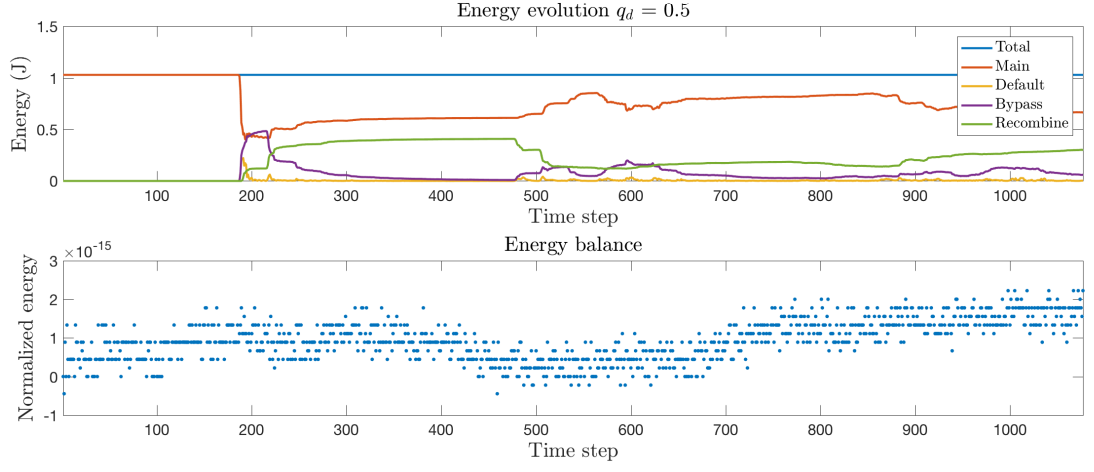


Figure 5.13: Top: Energy evolution of the system with $q^{(d)} = 0.5$: total energy (blue), main tube energy (red), default tube energy (yellow), bypass tube (purple), recombined tube (green). Bottom: energy balance for the whole system.

Modifying the resonances of the tube in this way not only changes the available frequencies at which the lip reed can oscillate at but also modifies the timbre of the note produced. The partial valve openings can create multiphonic sounds which will be explored in the next chapter. A short experimental study concerning partially open valves is presented in App. C.

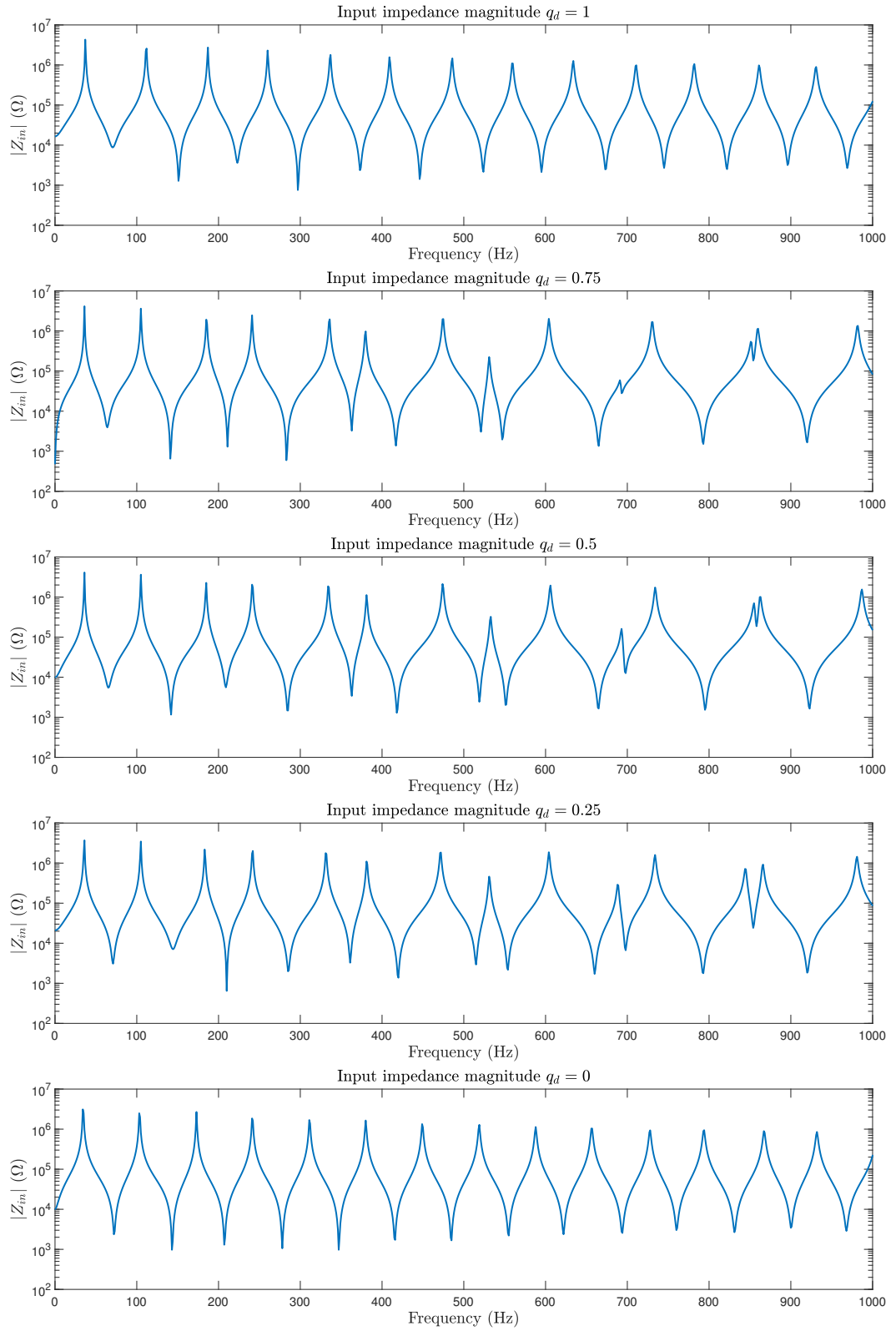


Figure 5.14: Input impedance calculations for the lossy valved tube system for different opening configurations. Top to bottom: Decreasing value of $q^{(d)}$ from 1 to 0 in increments of 0.25.

5.2.6 Time varying valves

We now look to the action of dynamic valves whose openings vary with time. We return to the single acoustic tube that lies over \mathcal{D} , whose cross-sectional area, $S(t, z)$, now varies with time. A suitable model taken from the literature on vocal tract modelling [134] is

$$\frac{1}{\rho_0 c_0^2} \partial_t (Sp) + \partial_t S + \partial_z (Sv) = 0, \quad \rho_0 \partial_t v + \partial_z p = 0 \quad (5.59)$$

which reduces to the normal horn equation, (2.49), when the cross-sectional area is constant over time. Taking the inner product of the first of (5.59) with p over the domain \mathcal{D} gives

$$\frac{1}{\rho_0 c_0^2} \langle p, \partial_t (Sp) \rangle_{\mathcal{D}} + \langle p, \partial_t S \rangle_{\mathcal{D}} + \langle p, \partial_z (Sv) \rangle_{\mathcal{D}} = 0 \quad (5.60)$$

Employing integration by parts (2.3) and using the second of (5.59) gives

$$\frac{1}{\rho_0 c_0^2} \langle p, \partial_t (Sp) \rangle_{\mathcal{D}} + \langle p, \partial_t S \rangle_{\mathcal{D}} + \rho_0 \langle \partial_t v, Sv \rangle_{\mathcal{D}} + \mathcal{B}_{he} = 0 \quad (5.61)$$

where \mathcal{B}_{he} is the same boundary term that is present for the static horn equation. This is important as it means that the same boundary conditions discussed in the previous sections can be applied when joining tubes together in valves.

We know that this system reduces to the horn equation when there is no time variation in the surface area so we should expect terms $\partial_t \|\sqrt{S}p\|_{\mathcal{D}}^2$ and $\partial_t \|\sqrt{S}v\|_{\mathcal{D}}^2$ to appear; this makes the derivations slightly easier if we already know what form to expect. Expanding these expressions for the time varying surface area case gives

$$\partial_t \|\sqrt{S}v\|_{\mathcal{D}}^2 = \langle \partial_t S, v^2 \rangle_{\mathcal{D}} + 2 \langle Sv, \partial_t v \rangle_{\mathcal{D}} \quad (5.62a)$$

$$\begin{aligned} \partial_t \|\sqrt{S}p\|_{\mathcal{D}}^2 &= \langle \partial_t S, p^2 \rangle_{\mathcal{D}} + 2 \langle Sp, \partial_t p \rangle_{\mathcal{D}} \\ &= \langle \partial_t S, p^2 \rangle_{\mathcal{D}} + 2 \langle p, \partial_t (Sp) - p \partial_t S \rangle_{\mathcal{D}} \\ &= 2 \langle p, \partial_t (Sp) \rangle_{\mathcal{D}} - \langle \partial_t S, p^2 \rangle_{\mathcal{D}} \end{aligned} \quad (5.62b)$$

Substituting these back into our main energy expression gives

$$\frac{d\mathcal{H}_{he}}{dt} + \mathcal{P}_{mov} + \mathcal{B}_{he} = 0 \quad (5.63)$$

where \mathcal{H}_{he} is the normal expression for energy stored in the acoustic tube but now with time varying $S(t)$

$$\mathcal{H}_{he} = \frac{1}{2\rho_0 c_0^2} \|\sqrt{S}p\|_{\mathcal{D}}^2 + \frac{\rho_0}{2} \|\sqrt{S}v\|_{\mathcal{D}}^2 \quad (5.64)$$

and

$$\mathcal{P}_{mov} = \langle \partial_t S, p \rangle_{\mathcal{D}} + \frac{1}{2\rho_0 c_0^2} \langle \partial_t S, p^2 \rangle_{\mathcal{D}} - \frac{\rho_0}{2} \langle \partial_t S, v^2 \rangle_{\mathcal{D}} \quad (5.65)$$

Discrete implementation

A discrete form of (5.59) is

$$\frac{1}{\rho_0 c_0^2} \delta_{t+} (\bar{S}p) + \delta_{t+} \bar{S} + \delta_{z-} (Sv) = 0, \quad \rho_0 \delta_{t-} v + \delta_{z+} p = 0 \quad (5.66)$$

where \bar{S}_l^n is sampled on the same spatial *and* temporal grid as the pressure and $S_{l+1/2}^{n+1/2}$ is sampled on the same spatial and temporal grid as the particle velocity.

The particle velocity update of the system remains as (3.109b) as in Chap. 3. The pressure update for a tube whose surface area varies is given by

$$p_l^{n+1} = \frac{\bar{S}_l^n p_l^n}{\bar{S}_l^{n+1}} - \frac{\rho_0 c_0^2 k}{h \bar{S}_l^{n+1}} \left(S_{l+1/2}^{n+1/2} v_{l+1/2}^{n+1/2} - S_{l-1/2}^{n+1/2} v_{l-1/2}^{n+1/2} \right) - \rho_0 c_0^2 \frac{\bar{S}_l^{n+1} - \bar{S}_l^n}{\bar{S}_l^{n+1}} \quad (5.67)$$

At a junction between tubes where the surface areas vary over time, the update is given by

$$\begin{aligned} p_J^{n+1} = & \frac{h_m + q^{(d),n} h_d + q^{(b),n} h_b}{h_m + q^{(d),n+1} h_d + q^{(b),n+1} h_b} p_J^n \\ & - \rho_0 c_0^2 \left(1 - \frac{h_m + q^{(d),n} h_d + q^{(b),n} h_b}{h_m + q^{(d),n+1} h_d + q^{(b),n+1} h_b} \right) \\ & + \frac{2\rho_0 c_0^2 k \left(S_{N_m-1/2}^{(m)} v_{N_m+1/2}^{(m),n+1/2} - S_{1/2}^{(d),n+1/2} v_{1/2}^{(d),n+1/2} - S_{1/2}^{(b),n+1/2} v_{1/2}^{(b),n+1/2} \right)}{\bar{S}_{N_m}^{(m)} (h_m + q^{(d),n+1} h_d + q^{(b),n+1} h_b)} \end{aligned} \quad (5.68)$$

where $q^{(d),n}$ and $q^{(b),n}$ are time varying openings of the default and bypass tubes. Note that $\bar{S}_{N_m}^{(m)} > 0$ to prevent singularities.

We can define an energy balance by taking the weighted inner product of the first of (5.66) with μ_{t+p} over d to produce

$$\frac{1}{\rho_0 c_0^2} \langle \mu_{t+p}, \delta_{t+} (\bar{S}p) \rangle_d^x + \langle \mu_{t+p}, \delta_{t+} \bar{S} \rangle_d^x + \langle \mu_{t+p}, \delta_{z-} (Sv) \rangle_d^x = 0 \quad (5.69)$$

Employing summation by parts, (3.28), and substituting the second of (5.66) results in

$$\frac{1}{\rho_0 c_0^2} \langle \mu_{t+p}, \delta_{t+} (\bar{S}p) \rangle_d^x + \langle \mu_{t+p}, \delta_{t+} \bar{S} \rangle_d^x + \rho_0 \langle \delta_t v, Sv \rangle_d^x + \mathfrak{h}_{he} = 0 \quad (5.70)$$

where \mathfrak{h}_{he} is the power change at the boundaries of the tube previously shown for the horn equation. This is important as it means the coupling conditions between the tubes remains the same, as in the continuous case.

We now investigate the first and third terms of (5.70). Neglecting the factor of $1/\rho_0 c_0^2$, the first term can be expanded as follows

$$\begin{aligned} \mu_{t+p} \delta_{t+} (\bar{S}p) &= \frac{1}{2k} (p^{n+1} + p^n) (\bar{S}^{n+1} p^{n+1} - \bar{S}^n p^n) \\ &= \frac{1}{2k} \left(\bar{S}^{n+1} (p^{n+1})^2 - \bar{S}^n (p^n)^2 + p^{n+1} p^n (\bar{S}^{n+1} - \bar{S}^n) \right) \\ &= \frac{1}{2} \delta_{t+} (\bar{S}p^2) + \frac{1}{2} \delta_{t+} \bar{S} (p, w_{t+p}) \end{aligned} \quad (5.71)$$

Neglecting the factor of ρ_0 , the third term of (5.70) can be modified with the addition of

zero

$$\begin{aligned}
\delta_{t+} v S v &= \frac{S^{n+1/2}}{2k} \left(v^{n+3/2} v^{n+1/2} - v^{n+1/2} v^{n-1/2} \right) \pm \underbrace{\frac{S^{n-1/2}}{2k} v^{n+1/2} v^{n-1/2}}_{+0} \\
&= \frac{1}{2k} \left(v^{n+3/2} S^{n+1/2} v^{n+1/2} - v^{n+1/2} S^{n-1/2} v^{n-1/2} + v^{n+1/2} v^{n-1/2} \left(-S^{n+1/2} + S^{n-1/2} \right) \right) \\
&= \frac{1}{2} \delta_{t+} (v w_{t-} (S v)) - \frac{1}{2} \delta_{t-} S v w_{t-} v
\end{aligned} \tag{5.72}$$

Using these expressions in our energy derivation results in

$$\delta_{t+} \mathfrak{h}_{he} + \mathfrak{p}_{mov} + \mathfrak{h}_{he} = 0 \tag{5.73}$$

where \mathfrak{h}_{he} is the normal expression for the energy stored in the horn equation but with time varying \bar{S} and S

$$\mathfrak{h}_{we}^n = \frac{1}{2\rho_0 c_0^2} \left(\|\sqrt{\bar{S}^n} p^n\|_d^\chi \right)^2 + \frac{\rho_0}{2} \langle v^{n+1/2}, w_{t-} (S^{n+1/2} v^{n+1/2}) \rangle_{\bar{d}} \tag{5.74}$$

and

$$\mathfrak{p}_{mov} = \langle \delta_{t+} \bar{S}, \mu_{t+} p \rangle_d^\chi + \frac{1}{2\rho_0 c_0^2} \langle \delta_{t+} \bar{S}, p w_{t+} p \rangle_d^\chi - \frac{\rho_0}{2} \langle \delta_{t-} S, v w_{t-} v \rangle_{\bar{d}} \tag{5.75}$$

We choose to use

$$\lambda \leq 1 \tag{5.76}$$

and

$$\bar{S}_l^n = \mu_{z-} S_{l+1/2}^{n+1/2} \tag{5.77}$$

Although we can define an energy balance, which is useful as a debugging tool, determining stability of this numerical scheme is still an open problem.

Simulation results

Fig. 5.15 shows the energy for the moving valve system with $q^{(d)}$ linearly changing from 1 to 0 over 0.1 s, this time with no volume velocity injected into the instrument. It is clear that moving the valves injects energy into the system—the motion of the valve acts as a volume velocity source. However, the energy balance of the system is shown to be conserved.

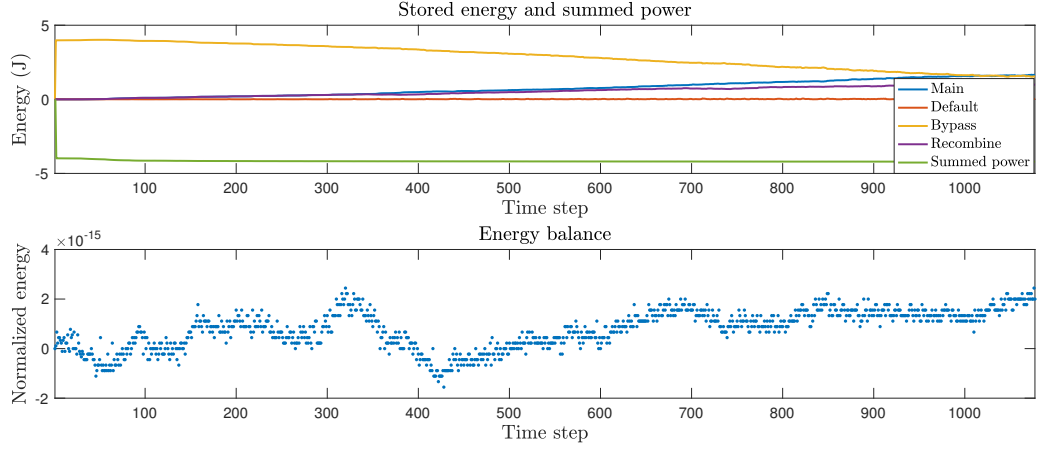


Figure 5.15: Top: Energy evolution of the valved system with time varying openings. Bottom: Energy balance of the system.

5.3 Conclusions

This chapter has presented the additional models required to make a virtual brass instrument.

A lumped one degree of freedom reed model with outward striking behaviour is chosen as the excitation mechanism for the virtual instrument. This model allows for a relatively small parameter space to produce sounds, whilst maintaining complex coupling behaviour with an acoustic tube. A numerical update is presented for this model along with discrete energy analysis. Simulations are performed that give examples of when the model produces, and also does not produce, self sustained oscillations. The numerical energy appears to vary above machine precision, but this could be a result of rounding errors previously discussed by Torin [163].

Whilst this simple lip reed model restricts the ability to shift whether the instrument plays above or below the instrument resonance, the motion of the reed is still, essentially, sinusoidal. The majority of harmonic generation occurs through the Bernoulli equation, given in (5.3). In terms of the resulting sound, adding additional degrees of freedom will not have much of a perceptible impact on the resulting sound, and will only add to overload the user with additional parameters.

Introducing valves allows for the resonances of the tube to be modified. A static model for a branching and recombining tube is presented with and without viscothermal losses. Boundary conditions that couple the sections of the valve together are derived from conservation of numerical energy, and the schemes are shown to be passive. Examples of input impedances for partially open valve configurations are then presented. The additional paths introduce resonances to the system which modify the timbre of the produced sound. The valve model is then extended to the case of time-varying valves. A numerical update and energy balance is presented, although the determination of stability is left as an open problem.

Chapter 6

A brass instrument synthesis environment

“I dream of instruments obedient to my thought and which with their contribution of a whole new world of unsuspected sounds, will lend themselves to the exigencies of my inner rhythm.”

— Edgard Varèse

We now have the individual components required to model a brass instrument: a generator, the lip reed; a variable resonator, the acoustic tube with time-varying valve sections; and a radiator, the radiation model. The next step is to forge these elements together to create a virtual instrument and determine how such an instrument is controlled; this is the subject of this chapter.

In this work brass instrument synthesis is performed using FDTD methods although several other approaches have been used historically to create virtual brass instruments. DWG methods were employed by Cook [47] in the ‘TBone’ workbench and were later implemented in the Yamaha VL1 synthesiser [144]. Modal methods were used in the MoReeSC framework [148], although this is intended for musical acoustics research rather than as a composer’s tool. A convolution modelling method was used in the BRASS project [170], which also included some nonlinear propagation effects. Allen and Raghuvanshi [4] used FDTD methods in a two-dimensional wave simulator to produce woodwind and brass instrument sounds, but they did not present any results for partially open valve configurations.

In this chapter, the structure of the synthesis code is presented. This is followed by a detailed discussion of the input files used to control the instrument along with examples of gestures that can be produced with the environment. A short playability study concludes the chapter. The synthesis environment described here has previously been discussed in [76], with details of the algorithm and code optimisation procedures in [75].

6.1 Structure of code

The synthesis environment was developed in MATLAB by the author and then optimised by James Perry of Edinburgh Parallel Computing Centre at the University of Edinburgh. The

original version used the loss model of Bilbao and Chick along with the RLC radiation impedance [24]. However, the discussion here will be general enough to apply to all of the models presented in this thesis. The general structure of the code is similar to that of Torin [163]; see Fig. 6.1 for a flow chart of this.

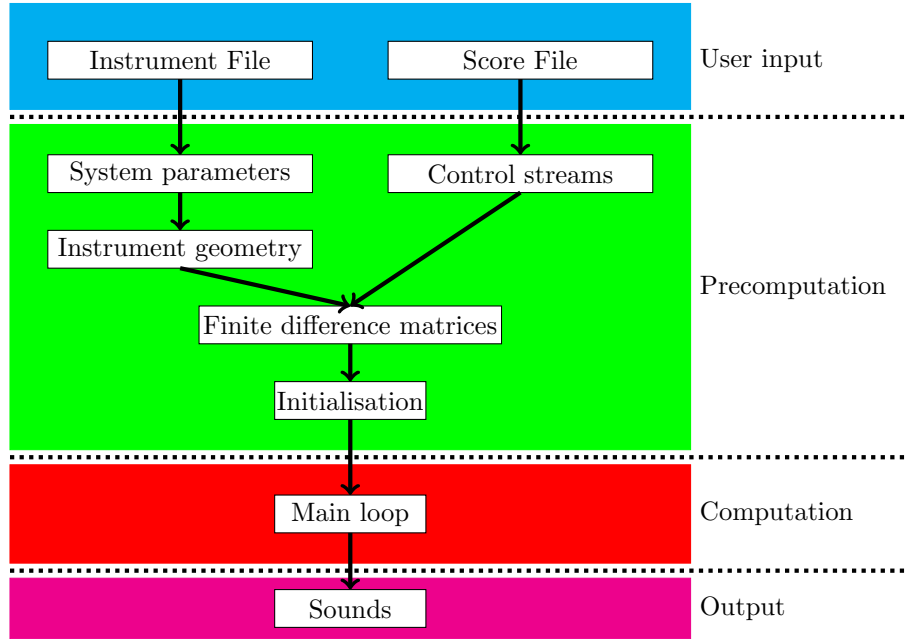


Figure 6.1: Structure of the brass instrument synthesis environment. Users specify instrument and score files (in blue rectangle) that are inputs to the code. These input files are then used in the precomputation stage (green rectangle) to calculate system parameters and control streams used in the main loop (red rectangle) where the system variables (acoustic pressure, particle velocity, lip position) are computed. The output (purple rectangle) is generated as a WAV file from the pressure at the end of the instrument.

6.1.1 Input files

The synthesis environment is controlled through separate instrument and score files described in detail in Sec. 6.2. The instrument file defines the instrument bore either from measurements of a real instrument or through a parameterised description of a synthetic bore. The score file indicates how the instrument is played by giving time varying parameters that control the lip dynamics and valve openings.

6.1.2 Precomputation

After selection of the input files, the brass environment precomputes the necessary matrices used in the main loop. This can be separated into several sections.

System parameters

Temporal step size is calculated from the sample rate. Thermodynamic constants are computed from a user selected temperature. Temporal step size and speed of sound are used

to compute a minimum spatial step size that satisfies the Courant condition. The spatial step size is modified so that an integer number of points define the tubes of the instrument.

Control streams

The control parameters, e.g. lip frequencies and valve openings, are given as break point functions in the score files (see Sec. 6.2). Interpolation is therefore required to sample these control parameters on the discrete temporal grid. Modulation of the control streams, if specified by the user, is applied here. The valve opening control stream is examined at this point to restrict values between 0 and 1. If the valve openings lie outside this range they are forced to the nearest limit.

Instrument geometry

If the custom instrument function is selected, the bore profile must be generated at this stage. For a valved instrument, there are multiple pieces of tubing that make up the entire instrument each requiring, in general, a distinct spatial step size for correct representation of the tube length. Using these spatial step sizes, discrete axial distance vectors can be constructed that the instrument bore is sampled on.

Finite-difference matrices

Matrices are constructed that approximate the operators in the PDE system and include effects due to boundary conditions and the shape of the instrument bore. These are used in the temporal loop.

Initialisation

The variables of the system are assigned memory prior to the start of the main temporal loop. Variables associated to propagation are stored in vectors of length equal to the discrete number of points in that domain. Boundary condition terms (lip position and network variables of the radiation model) are stored as single variables, one for each time step required in the individual update expressions.

6.1.3 Main loop

A temporal loop is performed to evolve the state variables at each time step. First, the pressure difference between the mouth and the instrument mouthpiece is computed. This is used to update the lip position and the pressure in the instrument mouthpiece. The pressure along the instrument bore is then updated, either by a loop over the spatial index or by matrix multiplication¹. The pressure at the radiating end of the instrument is computed and the network variables updated. Finally the particle velocity is updated along the length of the instrument. This process is repeated for the appropriate number of time steps.

¹In this work, software generated from the C programming language used a loop implementation. MATLAB allows both loop and matrix implementation, and is optimised for the latter.

6.1.4 Output sounds

For sound generation, the output signal is taken as the pressure at the end of the instrument, where the radiation model is applied. The output is normalised by the maximum absolute value of the time series, to avoid any distortion from clipping during playback, and saved as a WAV format file.

6.2 Control of instrument

We now look to how the virtual brass instrument can be controlled through the use of the input files. Users can describe the geometry of the instrument, through the use of the instrument file, and how the instrument is played, through the score file.

6.2.1 The instrument file

The instrument file allows the user to define the instrument geometry along with the sample rate the simulations are performed at and the temperature which defines the thermodynamic constants. Users can either input the profile of a real instrument using position-diameter pairs, or set the parameters that are used to create a custom instrument, discussed below. Positions of the valves are specified along with corresponding lengths of the default and bypass tubes.

Custom instrument function

The custom instrument function allows the user to design an instrument through parametrisation of the bore profile. The instrument as a whole can be split into three main sections: the mouthpiece, the central bore, and a flaring section. The mouthpiece is defined using half a period of a cosine function where the user specifies the length and diameter at the two ends of the mouthpiece. The bell is defined using a power of the axial distance; the user sets this power along with the final tube diameter. The central section of the instrument is defined by a series of concatenated tubes with differing profile set by the user. The choice of profiles is: cylindrical, conical, cosinusoidal ramp (similar to mouthpiece definition), and a sinusoidal bulge. Users specify the length of these sections along with the diameter of the end points. Fig. 6.2 shows three types of profiles in this middle section but in practice users can set as many as required, provided the length of all the sections fits the full length of the instrument.

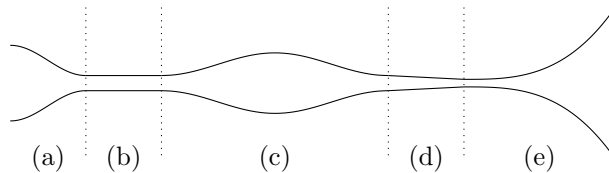


Figure 6.2: Example of an instrument constructed using the custom instrument function. Section (a) is the mouthpiece defined using a cosine, (b) a cylindrical segment, (c) is a bulge defined using the square of a sinusoid, (d) a converging conical section, and (e) is the flaring section defined using a power of the axial position.

6.2.2 The score file

The score file determines the overall duration of the simulation along with the time varying parameters used in the control of the instrument. The time varying parameters include the lip parameters (surface area, mass, damping, equilibrium separation, width, oscillation frequency), mouth pressure, and valve openings. Tab. 6.1 shows some example ranges of these control parameters to produce sound for a trumpet, found through a process of trial and error. The control parameters are given as time-value pairs that define a breakpoint function. Valve parameters specify the valve openings at each time instance.

Score parameter	Typical values for trumpet simulations
Length of simulation [s]	≥ 1
Effective lip area [m ²]	1.46×10^{-5}
Effective lip mass [kg]	5.37×10^{-5}
Lip damping	5
Lip equilibrium position [m]	2.9×10^{-4}
Effective lip width [m]	10^{-2}
Lip frequency [Hz]	400 – 1000
Mouth pressure [Pa]	$2.5 \times 10^3 - 5.0 \times 10^3$
Vibrato amplitude	0 – 0.05
Vibrato frequency [Hz]	0 – 7
Tremolo amplitude	0 – 0.2
Tremolo frequency [Hz]	0 – 7
Noise amplitude	0 – 0.05
Valve opening	0 – 1
Valve modulation frequency [Hz]	0 – 5
Valve modulation amplitude	0 – 0.5

Table 6.1: Parameters and typical values used in score file that plays a trumpet.

Modulation functions are also available for lip frequency, mouth pressure and valve openings.

Vibrato (lip frequency modulation) and tremolo (mouth pressure modulation)² are controlled by specifying an amplitude and rate of the modulation so that

$$f_{lip}^n \rightarrow f_{lip}^n (1 + A_v^n \sin(2\pi f_v^n n k)), \quad p_m^n \rightarrow p_m^n (1 + A_t^n \sin(2\pi f_t^n n k)) \quad (6.1)$$

where A_v^n and A_t^n are the amplitudes of the vibrato and tremolo, given as fractions of the static values, and f_v^n and f_t^n are the respective modulation frequencies. Noise can be added to the mouth pressure using

$$p_m^n \rightarrow p_m^n (1 + A_{noise}^n \theta^n) \quad (6.2)$$

where A_{noise}^n is the amplitude of the noise signal given as a fraction of the mouth pressure and θ^n generates a time series of numbers randomly generated between -1 and 1 .

Valve modulation is performed in a different manner—if the valve opening is set to zero, no modulation would occur using the modulation procedure for vibrato and tremolo. Instead,

²Here, tremolo denotes a loudness modulation rather than the performance direction to play a series of unmeasured, repeating notes.

valve modulation is performed by using

$$q^{(d),n} \mapsto q^{(d),n} + A_{valve}^n \sin(2\pi f_{valve}^n nk) \quad (6.3)$$

where f_{valve}^n is the valve modulation frequency and A_{valve}^n is the modulation amplitude given in terms of an actual valve opening.

All of the control parameters in the score files can be varied in time. However, in practice the lip area, mass, damping, equilibrium position and width remain constant.

6.2.3 Sound examples

We now give some examples of what types of gestures can be performed using the brass instrument synthesis tool. The instrument file was generated from measurements of a Smith Watkins trumpet provided by Dr. John Chick of the School of Engineering at the University of Edinburgh. Valves are positioned at 0.6 m, 0.63 m, and 0.69 m. Default tubes are all of length 0.02 m and bypass tubes are all of length 0.2 m.

Simulations were performed at a sample rate of 50 kHz. Lip parameters (area, mass, damping, equilibrium position, and width) are set to those in Tab. 6.1. Unless otherwise stated, the following parameter choice was used:

- A constant natural lip frequency of 550 Hz
- Pressure in the mouth increased from 0 Pa to 5×10^3 Pa over 10^{-4} s.
- Valves are assumed to be open, so the air column does not pass into the bypass tubes.
- No modulation of control parameters.

Peaks in spectrogram plots have been clipped to aid in viewing frequencies that are present in the sound. Yellow colours in the spectrogram denote regions where frequency content is strong, blue regions show where it is weak.

Simple gestures

Simple gestures can be performed by modifying the lip frequency to change note pitch or changing the mouth pressure to articulate notes. A linear sweep in lip frequency allows for an assessment of which lip frequencies produce notes when the instrument is in a static configuration. Fig. 6.3 shows the results of a simulation where the lip frequency begins at 220 Hz and linearly increases up to 1000 Hz over a duration of 3 s.

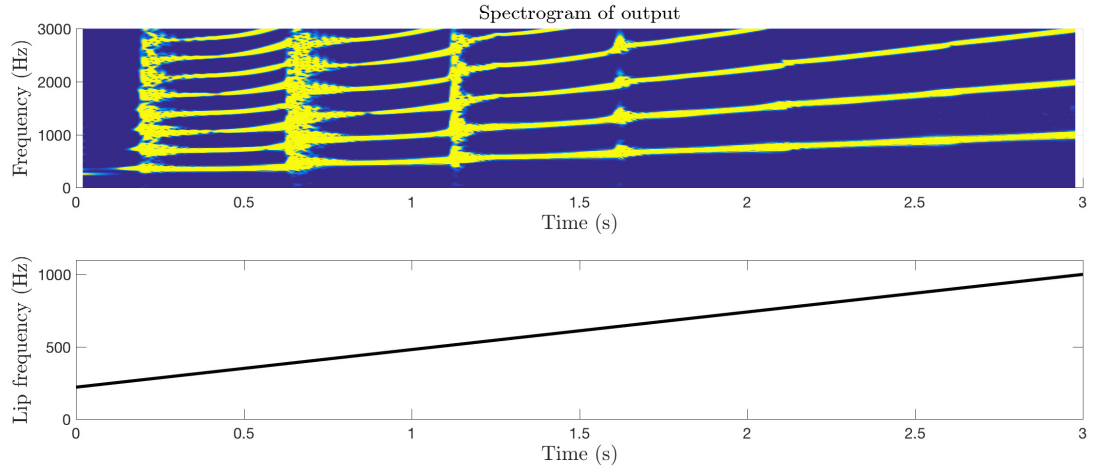


Figure 6.3: Top: Spectrogram of output sound when the lip frequency linearly changes from 220 Hz to 1000 Hz over 3 s. Bottom: The lip frequency as a function of time.

As the lip frequency increases, there is a gradual increase in the frequency of the spectrogram peaks of the produced sound. The spectrogram shows regions where the lips destabilise and then couple to a different instrument resonance; see just after 0.5 s, 1 s and 1.5 s. It should be noted that due to the nonlinear coupling between the reed and the instrument the lip frequency does not equal the fundamental frequency of the produced sound.

Separate notes can be produced through control of the mouth pressure. Fig. 6.4 shows an example where separate notes have been produced by linearly decreasing the end of the note from 5×10^3 Pa to 0 Pa over 0.1 s. Decreasing the mouth pressure stops the lips from being driven, which in turn stops the instrument producing sound.

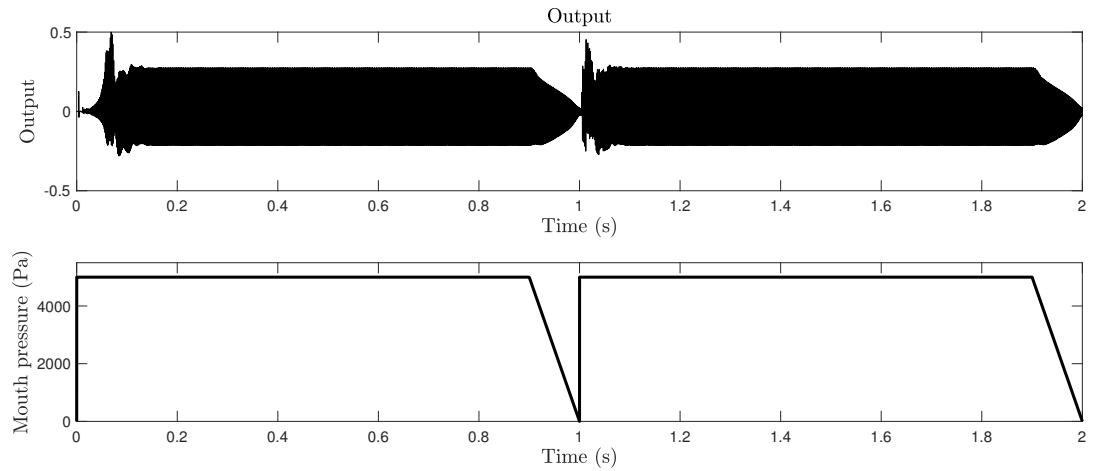


Figure 6.4: Top: Time series of output when two separate notes are played. Bottom: Corresponding mouth pressure as a function of time.

Modulating parameters

Fig. 6.5 shows results from a simulation where a vibrato of amplitude 0.05 and frequency of 7 Hz is applied to the lip frequency after 1 s. The peaks of the spectrogram of the output show modulation when vibrato is added to the note.

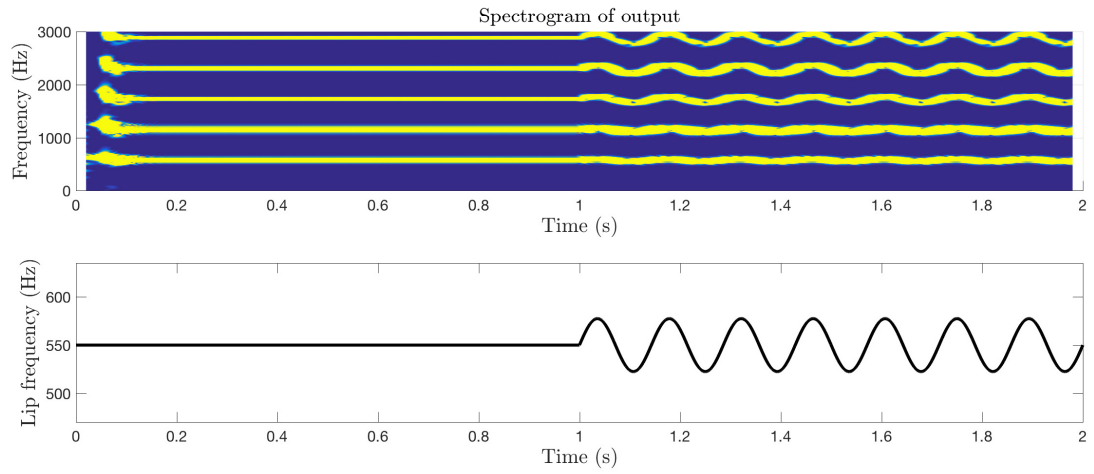


Figure 6.5: Top: Spectrogram of output sound when vibrato is added to the note after 1 s. Bottom: Lip frequency as a function of time. Lip frequency is constant for first second then modulation is added.

Fig. 6.6 shows simulation results where a tremolo of amplitude 0.2 and frequency of 7 Hz is applied to the mouth pressure after 1 s, with corresponding variations in the note's loudness shown in the output sound.

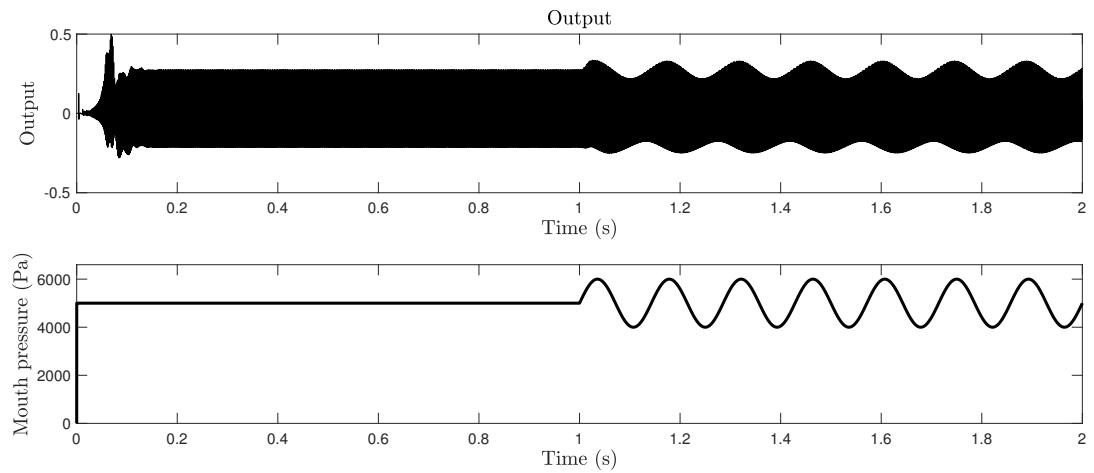


Figure 6.6: Top: Time series of output sound when tremolo is added. Bottom: Mouth pressure as a function of time. After the initial increase, the mouth pressure remains constant for the first second, after which the tremolo is added.

Fig. 6.7 shows the effect of adding noise of amplitude 0.05 to the mouth pressure after 1 s. An increase in non-harmonic frequency content is displayed in the spectrogram once noise is added.

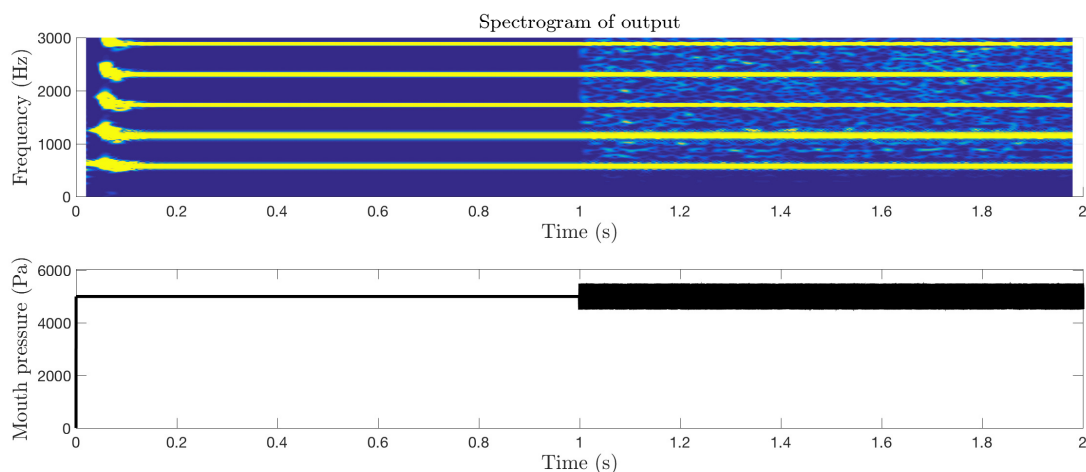


Figure 6.7: Top: Spectrogram of output sound when noise is added after 1 s. Bottom: Corresponding mouth pressure signal, with noise added after 1 s.

These specific examples lie to the more extreme effects of modulation. Simple treatment of these modulating parameters can result in ‘synthetic’ sounds as patterns in the sound are regularly repeated. This is not necessarily a negative result as users may wish to produce these types of sound. However, if the intended result requires something more ‘realistic’, then small variations must be carried out to make the sound constantly evolve. It is easier to do this with the modulating functions than to type out the individual lip frequency and pressure breakpoint functions.

Valve effects

Valves can be opened and closed over time to modify the resonances of the instrument. Fig. 6.8 shows the effect of changing the valve openings over time by closing successive valves at 2 s intervals whilst varying the lip frequency from 300 Hz to 700 Hz. Each time a valve is depressed, an additional piece of tubing is added to the air column that lowers the resonances of the instrument. This changes the available frequencies at which the lips couple to the instrument.

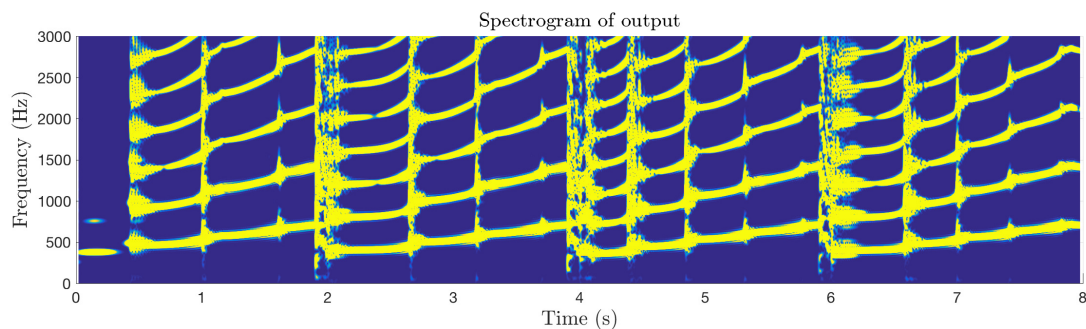


Figure 6.8: Spectrogram of output for repeated lip frequency sweeps from 300 Hz to 700 Hz over 2 s whilst changing valve configurations. At 2 s intervals, the next valve is depressed. This corresponds to a reduction in the lowest peak frequency shown in the spectrogram.

Setting the valves in a partially open configuration allows for the production of notes with a multiphonic timbre. Fig. 6.9 shows a comparison of the spectrum of a simulated note played using a fixed lip frequency and a) with all valves open and b) by using the partially open configuration of: $q^{(d)} = 0.7$ for the first valve, $q^{(d)} = 0.5$ for the second valve, and $q^{(d)} = 0.2$ for the third valve.

It is clear from the spectrum plot that the frequency content of the sound is modified when partial valve configurations are used. As the instrument resonances are different for the two valve configurations, the frequencies at which the lip oscillates at are different, despite using the same natural frequency. The magnitude of the spectrum is different for the two configurations, particularly between 2000 Hz and 2500 Hz where the partially open configuration has a lower value. This corresponds to the slightly muted characteristic of the sound produced in the partially open configuration, where there is a low presence of high frequency content.

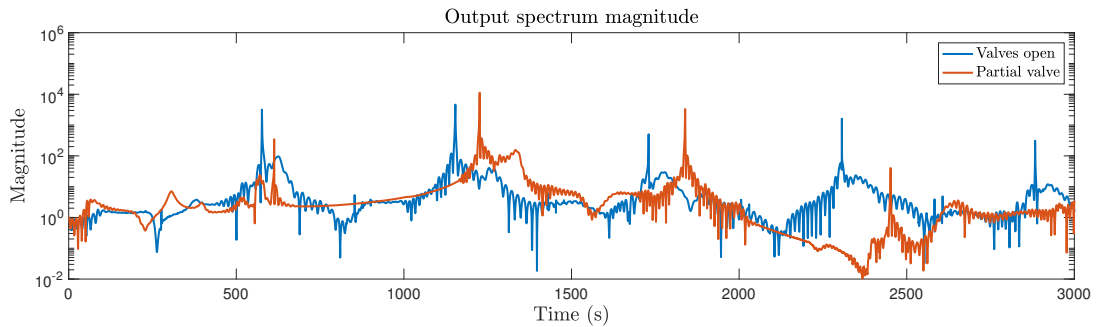


Figure 6.9: Spectrum of sounds produced with valves in open configuration (blue) and partially open configuration (red).

Valves can also be modulated over time. Fig. 6.10 shows the result of applying a modulation to the first valve of amplitude 0.25 and frequency 5 Hz, where all valve openings are set to a value of $q^{(d)} = 0.5$. As the valve is modulated, small variations in the frequency of the peaks of the spectrogram of the sound are observed.

6.2.4 Playability space

We have shown some of the capabilities of the brass instrument environment as a useable instrument. It is worth highlighting some issues to do with playability here.

A simple playability test can be performed by examining combinations of lip frequency and mouth pressure that produce a sustained note from the instrument, whilst keeping the other parameters in the score file constant. The space investigated consisted of lip frequencies between 50 Hz and 1 kHz, spaced at 10 Hz intervals, and mouth pressures between 2.5 kPa and 5.5 kPa, spaced at intervals of 0.5 kPa. The other score parameters were the same as those in Tab. 6.1. Additional inclusion criteria need to be specified as production of a sustained note can take over 1 s for some combinations of lip frequency and mouth pressure. Luce and Clark [110] measured the average transient responses in brass instruments as 0.05 ± 0.02 s. Experiments by Chick *et. al.* [43] showed that the variations in pitch in an instrument mouthpiece significantly reduce over a period of 0.04 s for a horn of length 1.8 m long. From these suggestions, the inclusion criteria for this test is that the sustained part of

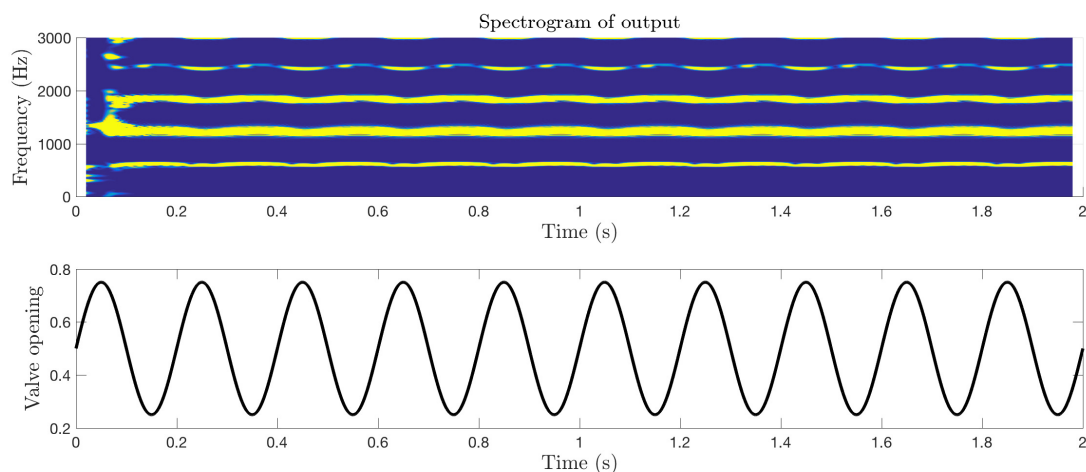


Figure 6.10: Top: Spectrogram of sound produced when first valve is modulated. Bottom: Time series of the first valve opening.

the note occurs in 0.07 s or less; see Fig. 6.11.

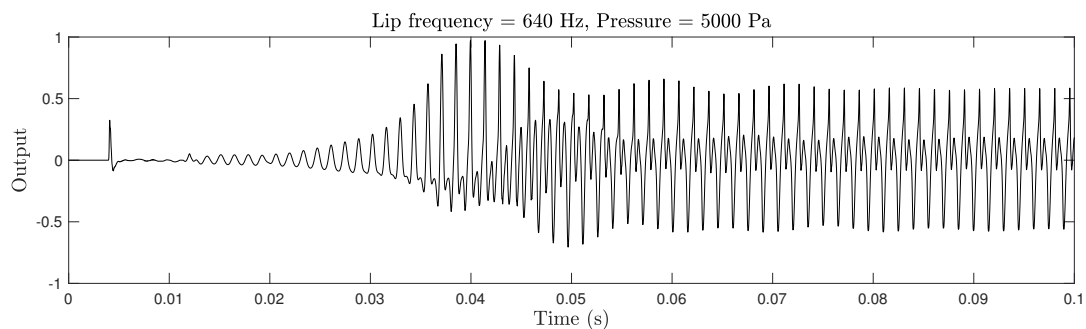


Figure 6.11: Example of a sound that fits the acceptance criteria. It is clear that the appearance of the repeated cycle that makes up the sustained part of the note occurs before 0.07 s.

Fig. 6.12 shows the playability space using the Smith Watkins trumpet bore. It is clear that there are regions in this space where sounds are not produced. As the mouth pressure increases, the number of lip frequencies that produce notes that fall within the selection criteria increases.

Although this type of study suggest possible combinations of lip frequency and mouth pressure that produce a sustained note, it does not give any information about the pitch of the produced note or its timbre. The particular choice of inclusion criteria eliminates many lip frequency/mouth pressure combinations that can produce a sustained note that takes longer to develop than 0.07 s. These omitted examples could have their note onsets digitally manipulated so that the timing would work in an electronic composition. However, the use of the shorter onset time allows for an objective inclusion criteria that is based on real systems.

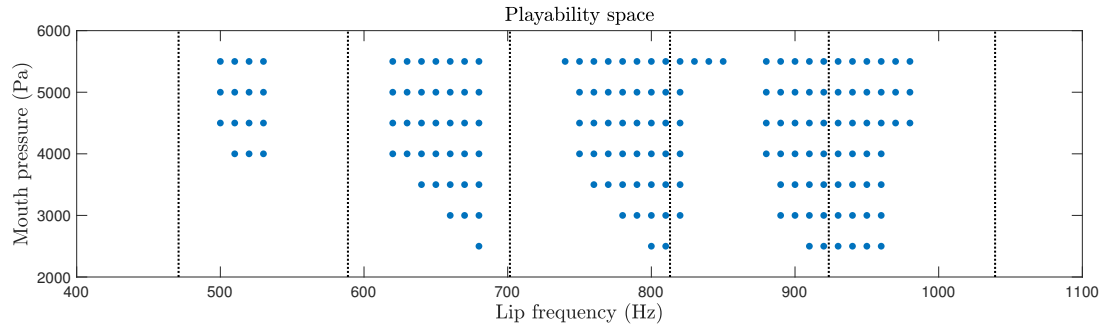


Figure 6.12: Playability space for Smith Watkins trumpet bore used in brass instrument environment. Points denote areas where a note is produced whose sustained part occurs in 0.07 s or less. Dashed vertical lines show where the instrument resonances lie.

6.3 Conclusions

Here we have presented the structure of the synthesis code along with descriptions of the input files. The synthesis code is controlled by an instrument and score file. Real instrument geometries can be specified but users also have the option to create their own custom instruments. All control parameters in the score file can be varied over time to produce a wide variety of gestures.

Act III

Nonlinear Acoustics

Chapter 7

Comparison of nonlinear propagation models

“All science is based on models, and every scientific model comprises three distinct stages: statement of well-defined hypotheses; deduction of all the consequences of these hypotheses, and nothing but these consequences; confrontation of these consequences with observed data.”

— Maurice Allais

A key playing feature of a brass instrument whose bore profile is predominantly cylindrical, such as the trombone, is the change in timbral quality between a note played at *piano* and *forté* dynamic levels. This change to what is labelled the ‘brassy’ regime is characterised by the generation of high frequency content in the sound spectrum of a loud note.

The environment presented in Chap. 6 uses a nonlinear coupling between the reed and the instrument; the Bernoulli flow generates additional harmonics beyond the sinusoidal motion of the reed opening. However, the propagation model is linear with frequency dependent losses. It was originally believed the coupling between the reed and the instrument was solely responsible for harmonic generation in brass instruments [10], but Beauchamp [11, 12] suggested that there were additional nonlinearities in the system. The work of Hirschberg *et al.* [88] discovered the presence of shock waves in trombones which could only be produced by nonlinear propagation within the instrument bore.

Such nonlinear effects allow for classification of brass instruments using an objective brassiness parameter [66, 67] that relates the nonlinear propagation behaviour of the instrument to that of a cylinder. Predictions of the brassiness parameter, however, are dependent on the model used to describe nonlinear propagation. The analysis of such models is inherently difficult, and simplifications have been applied to produce results. These simplifications, however, neglect some important behaviour—this is the subject of this chapter, the outline is as follows.

First, a review of nonlinear wave propagation is performed in the context of brass instrument acoustics. Then the Euler equations for a tube of varying cross-sectional area are presented followed by a discussion on common simplifications used in modelling applications. Two such models from the literature are presented and compared to the Euler equations.

Specific examples are then investigated: the scattering of waves due to changes in cross-sectional area and the interaction between forwards and backwards waves in a cylinder.

7.1 History of nonlinear propagation and brassiness

Beauchamp [11, 12] is often credited as the first to investigate the change in timbre when a brass instrument plays at high dynamic levels. He described this using a volume flow dependent low pass filter, whose cutoff frequency increased with dynamic level. However, the mechanism for this process was not described.

Hirschberg *et al.* [88] presented the first measurements showing a developing nonlinearity within the bore of a trombone, and similar results were later presented by Pandya *et al.* for the trumpet [130]. At high dynamic levels, a shock wave—a wave with a discontinuity in its profile—was seen to develop as disturbances travelled along the instrument. Importantly, the shock wave was seen to develop in the cylindrical portions of the instrument, indicating that trumpets and trombones, instruments with predominantly cylindrical bore profiles, would experience a developing brassiness as the dynamic level was increased. Instruments with a predominantly conical bore, such as the Saxhorns and Flugelhorns, do not have a developing brassiness as the increasing cross-section reduces the pressure, and therefore the overall nonlinearity in the system. A theoretical value for the distance over which a sinusoidal source develops into a shock in a lossless cylinder is [88]

$$L_{shock} \approx \frac{2\gamma P_0 c_{tot}}{(\gamma + 1) \max(dp_{in}/dt)} \quad (7.1)$$

where P_0 is atmospheric pressure, c_{tot} is the speed of sound in air, and $\max(dp_{in}/dt)$ denotes the maximum value of the temporal derivative of the driving pressure function.

Since brass instruments behave as radiators at high frequencies, Hirschberg *et al.* suggested that only the sound heard by the listener was affected by the nonlinearity; the player’s lips only interacted with the linear behaviour of the instrument. This led to several synthesis applications that used a mix of linear and nonlinear propagation models. Thompson and Strong [161] used a linear model of the instrument to simulate its reflection function. This was then used to separate forwards and backwards waves from experimentally measured mouthpiece pressures. The forward wave was then used to excite a nonlinear frequency domain propagation model based on the Burgers equation. A similar approach was adopted by Vergez and Rodet using the Burgers equation [169] and with an artificial distortion parameter [168]. In both cases this system was excited using a simple lip reed model.

Msallam *et al.* [123] used a nonlinear delay line representation in their synthesis work. As well as applying the nonlinearity to the output produced by a linear model, they also investigated the effect of using a nonlinear propagation model in the cylindrical portions of the resonator which produced more spectral enrichment than applying to only the forwards wave. This work still assumed that forwards and backwards waves were independent of each other. Kausel and Geyer [92] used a similar delay line approach but modified the wave speed based on the local pressure in DWGs to simulate nonlinear wave propagation, thus including some coupling between the waves. Allen and Raghuvanshi [4] used FDTD methods to directly simulate the two-dimensional wave equation to model wind instruments, but the local speed of sound had to be artificially limited to maintain the stability of simulations.

Additional models have been developed to describe nonlinear wave propagation in acoustic tubes. A common thread in these models is the use of separable, or uni-directional, waves. In this work, we will define separable waves as the solutions who travel in one direction only and who do not interact with waves travelling in the opposite direction. Of particular interest are the Burgers model, used, for example, by Lombard *et al.* [17, 107], and the generalised Burgers model developed by Menguy and Gilbert [114, 115]. Both of these models will be discussed in more detail in Sec. 7.3.1 and 7.3.2 respectively.

An application of these uni-directional theories is the classification of brass instruments in terms of their ‘Brassiness’, defined by an objective Brassiness parameter; see [33, 36, 44, 66, 67]. Experiments in brassiness look at how the spectral centroid, a measure of frequency content, of the wave changes as it propagates through the instrument. The brassiness parameter has been shown to correlate with this spectral enrichment, how the spectral centroid changes during propagation through the instrument, so a higher brassiness parameter will classify an instrument as having a brighter sound.

The calculation of the brassiness parameter requires defining an equivalent cylinder length over which the same amount distortion occurs as in the real instrument. The brassiness parameter is then given as the ratio of this cylinder length to an equivalent cone length that fits the instrument’s resonances. To determine the correct cylinder length requires accurate modelling of the nonlinear processes.

Of course, the development of shock waves is dependent on the shape of the original signal; recent work has returned to investigating this [135].

7.2 The Euler equations

A suitable model of nonlinear propagation in acoustic tubes is given by the Euler equations, which are derived from conservation laws. In one-dimension, the Euler equations are given as¹ [103]

$$\partial_t \rho_{tot} + \partial_z (\rho_{tot} v) = 0 \quad (7.2a)$$

$$\partial_t (\rho_{tot} v) + \partial_z (\rho_{tot} v^2) + \partial_z p_{tot} = 0 \quad (7.2b)$$

where the total density and pressure can be decomposed into static and oscillatory contributions so that $\rho_{tot} = \rho_0 + \rho$ and $p_{tot} = P_0 + p$, where ρ_0 and P_0 are the static components and ρ and p are the oscillatory parts. Note that the particle velocity is purely oscillatory; we assume no mean flow.

In this chapter, we shall again consider the finite spatial domain $z \in \mathcal{D} = \{z \in \mathbb{R} \mid 0 \leq z \leq L\}$, where the length of the tube L is considered to be shorter than the shock distance L_{shock} . The temporal domain shall be limited so that $0 \leq t < c_0 L$ so as not to include any reflections.

For a tube of varying cross-sectional area, the Euler equations are given by [102]

$$S \partial_t \rho_{tot} + \partial_z (S \rho_{tot} v) = 0 \quad (7.3a)$$

$$\partial_t (S \rho_{tot} v) + \partial_z (S \rho_{tot} v^2) + S \partial_z p_{tot} = 0 \quad (7.3b)$$

¹The Euler equations are usually accompanied by an energy evolution equation. We neglect that here as we will later relate pressure and density, therefore requiring only two PDEs to describe the system.

7.2.1 Adiabatic approximation

If we assume there is no heat transfer in the gas we can use the adiabatic gas law² to relate pressure and density [64]

$$p_{tot} = \kappa \rho_{tot}^\gamma, \quad \kappa = \frac{P_0}{\rho_0^\gamma} \quad (7.4)$$

This allows us to rewrite (7.3) in terms of the acoustic pressure and velocity

$$\partial_t p + v \partial_z p + \gamma (P_0 + p) \partial_z v + \gamma v (P_0 + p) \frac{S'}{S} = 0 \quad (7.5a)$$

$$\partial_t v + v \partial_z v + \frac{1}{\rho_0} \left(1 + \frac{p}{P_0}\right)^{-\frac{1}{\gamma}} \partial_z p = 0 \quad (7.5b)$$

It is clear that linearising these equations results in the horn equation, (2.49), since the linear speed of sound is given by [63]

$$c_0 = \sqrt{\frac{\gamma P_0}{\rho_0}} \quad (7.6)$$

This is an important feature to point out as the horn equation has been tested against experiments in the linear regime of playing. The Euler equations will therefore behave in a similar manner in the low amplitude limit.

7.2.2 Riemann invariants

The speed of sound in the nonlinear regime is given by [64]

$$c_{tot} = \sqrt{\frac{\gamma p_{tot}}{\rho_{tot}}} \quad (7.7)$$

When using the adiabatic approximation, (7.4), this results in a speed of sound given in terms of the pressure

$$c_{tot} = \sqrt{\gamma \kappa p_{tot}^{\frac{\gamma-1}{\gamma}}} \quad (7.8)$$

Replacing the total pressure in (7.5) with this definition of the speed of sound and combining the equations results in

$$(\partial_t + \underbrace{(v \pm c_{tot})}_{\phi^\pm} \partial_z) \left\{ v \pm \frac{2}{\gamma-1} c \right\} = \mp \frac{c_{tot} v}{S} \frac{dS}{dz} \quad (7.9)$$

where c is the deviation in the speed of sound so that $c_{tot} = c_0 + c$. In Chap. 2, similar analysis of the horn equation resulted in (2.51). The terms within $\{ \}$ of (7.9) are the Riemann invariants of the system. In the method of characteristics [103], these invariants remain constant as they travel along the characteristic curves defined by the PDE system. In

²The adiabatic gas law is typically used in the literature of brass instrument modelling. This describes a lossless process, however, when shocks develop the system is no longer lossless [143].

this case there are two invariants given by

$$\phi_{\pm} = v \pm \frac{2}{\gamma - 1} c \quad (7.10)$$

that travel in individual directions with speeds $v + c_{tot}$ and $v - c_{tot}$.

Let us first consider a cylinder, so that S is constant. The system is initialised so that ϕ^+ is zero and ϕ^- is a continuous, smooth function. This means that only the forwards propagating wave exists, simplifying the system to

$$(\partial_t + (v - c_{tot})\partial_z)\phi^- = 0 \quad (7.11)$$

This describes a propagating wave whose velocity depends on its own initial conditions. This means that different parts of the wave travel at different speeds, distorting the wave profile; see Fig. 7.1 for an example with an initial sinusoidal profile.

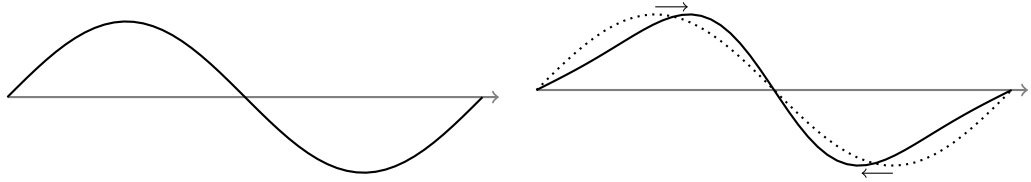


Figure 7.1: Left: A simple wave. Right: An example of distortion applied to the wave (solid line) with the original wave profile shown as reference (dotted line). Arrows show how the wave has been distorted, with positive values sped up, and negative values slowed down.

If this wave is allowed to travel for a sufficiently long period of time, the parts of the wave travelling at a higher velocity will catch up to those that were originally ahead of it. When this occurs, the solution becomes multivalued at the point of overlap and a shock develops. This creates issues when applying numerical methods to solving the systems both in terms of numerical stability and accuracy, as the shocks cannot be reasonably resolved on any grid; see the text of LeVeque for more on this subject [103].

Now consider the case when both invariants are initialised with smooth functions

$$(\partial_t + (v \pm c_{tot}))\phi_{\pm} = 0 \quad (7.12)$$

When ϕ_{\pm} are defined to be non-zero in separate regions then we can consider them in the same way as (7.11). However, once they overlap they interact with each other because the particle velocity and deviation in speed of sound are dependent on both invariants

$$v = \frac{1}{2}(\phi_+ + \phi_-), \quad c = \frac{\gamma - 1}{4}(\phi_+ - \phi_-) \quad (7.13)$$

There is now a coupling between the forwards and backwards waves. In the case of a tube with spatially varying bore profile, there is also an additional coupling due to the spatial derivative of the cross-sectional area in (7.9).

7.3 Uni-directional models

We now present two uni-directional nonlinear wave propagation models used in brass instrument modelling: the Burgers model and the generalised Burgers model. Typically these models are presented with terms associated with attenuation due to boundary layer effects, but these have been neglected here so as to focus only on the nonlinear behaviour.

7.3.1 Burgers model

The Burgers model is presented as

$$\left(\partial_t + \left(\frac{\gamma + 1}{2} v^\pm \pm c_0 \right) \partial_z \right) v^\pm = \mp \frac{c_0 v^\pm}{S} \frac{dS}{dz} \quad (7.14)$$

where $v^\pm(t, z)$ are the forwards and backwards velocity waves, the sum of which gives the total particle velocity [17, 107]. The forwards and backwards pressure waves, $p^\pm(t, z)$, in this model are assumed to be locally dependent on the particle velocity and given by the linear relationship

$$p^\pm = \pm \rho_0 c_0 v^\pm \quad (7.15)$$

resulting in

$$\left(\partial_t \pm \left(\frac{\gamma + 1}{2 \rho_0 c_0} p^\pm + c_0 \right) \partial_z \right) p^\pm = \mp \frac{c_0 p^\pm}{S} \frac{dS}{dz} \quad (7.16)$$

The model can be seen as a simplification to the Riemann invariants, (7.9), of the Euler equations (in fact, for a single travelling wave solution in a cylindrical tube, this is the result given by the Euler equations). The wave velocity is modified using the method of characteristics

$$v \pm c_{tot} \rightarrow \frac{\gamma + 1}{2} v^\pm \pm c_0 \quad (7.17)$$

see [51]. The cross-sectional area term on the right hand side of (7.14) can then be seen as neglecting higher order values of Mach number (see Sec. 7.3.2).

In [17] and [107] the travelling wave equation (7.14) is described as the Menguy-Gilbert model, discussed in the next section as the generalised Burgers model. This is not exactly the case: there are differences between the propagation terms of the two models and they are identified as distinct from each other in [112]. There is a similar presentation of the Burgers model in [66] to (7.16), but this citation includes a multiple of 1/2 on the right hand side of the equation. This is not present in [17, 106], therefore the models are considered as distinct.

7.3.2 Generalised Burgers model

The generalised Burgers model for propagation in acoustic tubes was first presented in [115] for cylindrical tubes and was extended in [114] for tubes with a varying cross-sectional area. This model is constructed by nondimensionalising the Euler equations using the Mach number

$$M = \frac{|v|_{max}}{c_0} \quad (7.18)$$

where $|v|_{max}$ represents the maximum absolute value of the particle velocity. The Mach number is a measure of the nonlinearity of the system. For musical acoustics applications it is

assumed that $M \ll 1$ so that the system can be described as weakly nonlinear.

Nondimensionalising the system using this parameter allows for simplifications, usually that terms of $\mathcal{O}(M^2)$ and above are neglected. This has the equivalent effect of linearising the right hand side (7.9) to be

$$(\partial_t + (v \pm c)\partial_z) \left\{ v \pm \frac{2}{\gamma - 1}c \right\} = \mp \frac{c_0 v}{S} \frac{dS}{dz} \quad (7.19)$$

The waves are still coupled via the propagation speed and the change in cross-sectional area, but the scattering occurs in a linear fashion.

After normalising the system, the Method of Multiple Scales (MMS) perturbation method is applied to develop a series of PDEs in a transformed coordinate system. The specific details of this perturbation method are out with the scope of this work but a brief discussion is required here; for more information on MMS see the text of Nayfeh [126] and the publications of Menguy and Gilbert [114, 115].

Perturbation methods assume that nonlinear behaviour can be included by introducing a small modification to known solutions to a similar linear system. For a nonlinear equation that does not have analytical solutions, we begin with a linear equation with similar properties and that has a known solution $f_l(t, z)$. The solution to the linear equation is modified by adding an additional perturbation function, $f_p(t, z)$, so that an approximation to the solution of the nonlinear system is

$$f_{nl} \approx f_l + M f_p \quad (7.20)$$

where it is common practice in fluid mechanics problems to use the Mach number as a weighting for the perturbation function. This combined solution can then be substituted into the nonlinear PDE system, which, by gathering like terms of powers of M , can be reduced to a simpler ODE system.

As well as introducing a perturbation to the solution, MMS uses transformed coordinates to separate the behaviour of the system into slow and fast scale processes. The fast scale processes are those that happen locally, such as the main propagation of waves within the fluid. The slow scale processes require larger time scales to become noticeable, such as the gradual distortion of the wave profile. As the change in cross-sectional area is assumed to be small, this effect is also treated as a slow scale process in the generalised Burgers model for wave propagation in acoustic tubes. By making this assumption, we are left with just the wave equation as the linear part of the problem, not the horn equation, which always results in separable wave solutions. The perturbed part of the solution then shows how these waves are distorted and how the magnitude is scaled by the cross-sectional area. This means that the wave coupling is completely neglected and no scattering is included in the model. In the normalised, modified coordinate system, the generalised Burgers model is presented as

$$\partial_\sigma q^\pm = \pm q^\pm \partial_{\theta^\pm} q^\pm \mp \frac{q^\pm}{2S} \frac{dS}{d\sigma} \quad (7.21)$$

where $q^\pm(\sigma, \theta^\pm)$ are the forwards and backwards travelling wave variables, treated as non-dimensionalised pressure waves, $\sigma = \omega \frac{\gamma+1}{2c_0} z$ is a scaled length coordinate and $\theta^\pm = \omega \left(t \mp \frac{x}{c_0} \right)$ are the characteristic variables of the waves. It should be noted that in [114, 115], the angular frequency is used as a normalisation parameter to describe effects

related to boundary layer losses that are neglected in this chapter; in practice, ω appears as a multiple of each term in the equation so can be factorised. To return to the normal time and space coordinates we use

$$\partial_\sigma = \frac{2}{\omega(\gamma+1)} (c_0 \partial_z \pm \partial_t), \quad \partial_{\theta^\pm} = \frac{\partial_t}{\omega} \quad (7.22)$$

which gives

$$\left(\left(1 - \frac{\gamma-1}{2} q^\pm \right) \partial_t \pm c_0 \partial_z \right) q^\pm = - \frac{c_0 q^\pm}{2S} \frac{dS}{dz} \quad (7.23)$$

The form of this wave equation is again different to the Euler equations. The nonlinearity is now a multiple of the temporal derivative, whereas it appears as a multiple of the spatial derivative in the Euler equations and the Burgers model. The sign of the cross-sectional area term on the right hand side is always negative, whereas it changes sign depending on the direction of wave propagation in the Euler and Burgers equations.

The wave variables, q^\pm , are related to the pressure and velocity by

$$p^\pm = \rho_0 c_0^2 q^\pm, \quad v^\pm = \pm c_0 q^\pm \quad (7.24)$$

The generalised Burgers equations can then be written in terms of pressure waves as

$$\left(\left(1 - \frac{\gamma-1}{2\rho_0 c_0^2} p^\pm \right) \partial_t \pm c_0 \partial_z \right) p^\pm = - \frac{c_0 p^\pm}{2S} \frac{dS}{dz} \quad (7.25)$$

7.4 Propagation behaviour in different models

It is clear there are differences between the Euler, Burgers, and generalised Burgers equations described in the previous section. The primary difference is that the Burgers and generalised Burgers models permit separable travelling wave solutions in all cases, whereas the Euler equations only permit these solutions under specific configurations.

It is clear that the Euler equations reduce to the Burgers equations for the case of a single travelling wave in a cylinder. However, when two travelling waves exist the two models differ as the Burgers model neglects the coupling of the two waves through the local wave speed.

The generalised Burgers model is significantly different from the Euler equations for a single travelling wave in a cylindrical tube as the nonlinearity is present in the time derivative instead of the spatial derivative.

In tubes of varying cross-section, both the Burgers and generalised Burgers equations differ from the Euler equations as they neglect any wave scattering in the tube. Ultimately, we must utilise numerical methods to study the difference between each model.

7.4.1 Numerical methods

We can compare the individual nonlinear acoustic tube models by using FDTD methods.

For the Euler equations we use the interleaved grids for pressure and velocity presented in

Chap. 3. We recall that the pressure and velocity are approximated by the grid functions

$$p_l^n \approx p(nk, lh), \quad l \in d = \{l \in \mathbb{Z} \mid 0 \leq l \leq N\} \quad (7.26)$$

$$v_{l+1/2}^{n+1/2} \approx v((n+1/2)k, (l+1/2)h), \quad l \in \bar{d} = \{l \in \mathbb{Z} \mid 0 \leq l \leq N-1\} \quad (7.27)$$

We shall only consider temporal indices so that $0 \leq n < N$. A discrete form of the Euler equations, (7.5), is

$$\delta_t p + \delta_z p \mu_z - \mu_t v + \gamma (P_0 + p) \mu_t - \delta_z v + \gamma (P_0 + p) \mu_t - \mu_z v \frac{\delta_z S}{S} = 0 \quad (7.28a)$$

$$\delta_t v + v \delta_z v + \frac{1}{\rho_0} \left(1 + \frac{\mu_t + \mu_z + p}{P_0} \right)^{-\frac{1}{\gamma}} \mu_t + \delta_z p = 0 \quad (7.28b)$$

which results in the following update equations

$$\begin{aligned} p_l^{n+1} = & p_l^{n-1} - \frac{k}{4h} (p_{l+1}^n - p_{l-1}^n) \left(v_{l+1/2}^{n+1/2} + v_{l-1/2}^{n+1/2} + v_{l+1/2}^{n-1/2} + v_{l-1/2}^{n-1/2} \right) \\ & - \frac{\gamma k}{h} (P_0 + p_l^n) \left(v_{l+1/2}^{n+1/2} - v_{l-1/2}^{n+1/2} + v_{l+1/2}^{n-1/2} - v_{l-1/2}^{n-1/2} \right) \\ & - \frac{\gamma k}{2h} (P_0 + p_l^n) \left(v_{l+1/2}^{n+1/2} + v_{l-1/2}^{n+1/2} + v_{l+1/2}^{n-1/2} + v_{l-1/2}^{n-1/2} \right) \frac{S_{l+1/2} - S_{l-1/2}}{\bar{S}_l} \end{aligned} \quad (7.29a)$$

$$\begin{aligned} v_{l+1/2}^{n+3/2} = & v_{l+1/2}^{n-1/2} - \frac{k}{h} v_{l+1/2}^{n+1/2} \left(v_{l+3/2}^{n+1/2} - v_{l-1/2}^{n+1/2} \right) \\ & - \frac{k}{\rho_0 h} \left(1 + \frac{p_{l+1}^{n+1} + p_l^{n+1} + p_{l+1}^n + p_l^n}{4P_0} \right)^{-\frac{1}{\gamma}} (p_{l+1}^{n+1} - p_l^{n+1} + p_{l+1}^n - p_l^n) \end{aligned} \quad (7.29b)$$

At present, it is not possible to show that this scheme is stable. However, when linearised, scheme (7.28) can be seen as the temporal average of the explicit scheme for the horn equation, (3.108). We therefore use the same relationship between the length spacing and the time step, $\lambda = c_0 k/h$. Convergence tests show consistency of scheme (7.28) over regions where a shock has yet to develop.

At $l = 0$ and $l = N$, the update for the velocity, (7.28b), requires points that lie outside of the domain. Rather than constructing additional boundary conditions, we use the linearised form of (7.28b) at these points in space

$$v_{l+1/2}^{n+3/2} = v_{l+1/2}^{n-1/2} - \frac{k}{\rho_0 h} (p_{l+1}^{n+1} - p_l^{n+1} + p_{l+1}^n - p_l^n) \quad (7.30)$$

The Burgers and generalised Burgers equations will use the following grid function to approximate the forwards pressure wave

$$p_l^{+,n} \approx p^+(nk, lh) \quad (7.31)$$

Typically, one-way advection equations would be implemented using upwind methods [103]. However, these schemes are uncentered; we wish to use centred schemes to match the form used for (7.28). The discrete form of the forwards Burgers pressure wave equation,

(7.16), is given by

$$\delta_t.p^+ + \left(\frac{\gamma+1}{2\rho_0 c_0} p^+ + c_0 \right) \delta_z.p^+ = -c_0 p^+ \frac{\delta_z.S}{\bar{S}} \quad (7.32)$$

resulting in the following update

$$p_l^{+,n+1} = p_l^{+,n-1} - \frac{k}{h} \left(\frac{\gamma+1}{2\rho_0 c_0} p^{+,n} + c_0 \right) (p_{l+1}^{+,n} - p_{l-1}^{+,n}) - \frac{2c_0 k}{h} p_l^{+,n} \frac{S_{l+1/2} - S_{l-1/2}}{\bar{S}_l} \quad (7.33)$$

The generalised Burgers equation is discretised using

$$\left(1 - \frac{\gamma-1}{2\rho_0 c_0^2} p^+ \right) \delta_t.p^+ + c_0 \delta_z.p^+ = -\frac{c_0 p^+}{2} \frac{\delta_z.S}{\bar{S}} \quad (7.34)$$

resulting in the update

$$p_l^{+,n+1} = p_l^{+,n-1} - \frac{c_0 k}{h} \left(1 - \frac{\gamma-1}{2\rho_0 c_0^2} p_l^{+,n} \right)^{-1} \left(p_{l+1}^{+,n} - p_{l-1}^{+,n} + p_l^{+,n} \left(\frac{S_{l+1/2} - S_{l-1/2}}{\bar{S}_l} \right) \right) \quad (7.35)$$

Again, at $l = 0$ and $l = N$, the schemes for the Burgers equation, (7.32), and the generalised Burgers equation, (7.35), require points outside of the domain. However, in this work the systems will always be excited by a pressure source at the boundaries, so we need not consider additional numerical boundary conditions.

7.4.2 Simulation results

Simulations were performed at a sample rate of 100 kHz in a tube of length 4 m. At $l = 0$, the pressure in each model was excited using a Hann pulse of width $T_{Hann} = 1/300$ s.

$$p_0^n = A_{in} p_{Hann}^n, \quad p_{Hann}^n = \begin{cases} 0.5 \left(1 - \cos \left(\frac{2\pi n}{K_{Hann}} \right) \right), & 0 \leq n \leq K_{Hann} \\ 0, & n > K_{Hann} \end{cases} \quad (7.36)$$

where A_{in} is the maximum excitation of the input signal and $K_{Hann} = \text{floor}(T_{Hann}/k)$ is the number of time steps corresponding to the width, T_{Hann} , of each pulse.

Each model used the same spatial step size calculated using a Courant number of $\lambda = 0.9$. This choice of Courant number was used to reduce the risk of instability in the simulations. A linear simulation using the explicit FDTD scheme for the horn equation, (3.108), was also performed under the same conditions for comparison.

Figs. 7.2-7.5 show snapshots of wave propagation simulated using the models described above under different configurations. Fig. 7.2 shows propagation in a cylinder using $A_{in} = 0.03P_0$. This corresponds to the upper pressures used in the spectral enrichment and brassiness investigations by Campbell *et al.* [33, 36, 67, 125]. The Euler and Burgers models behave identically, showing some wave steepening as the disturbance propagates along the tube. The generalised Burgers model shows little steepening relative to the linear propagation model.

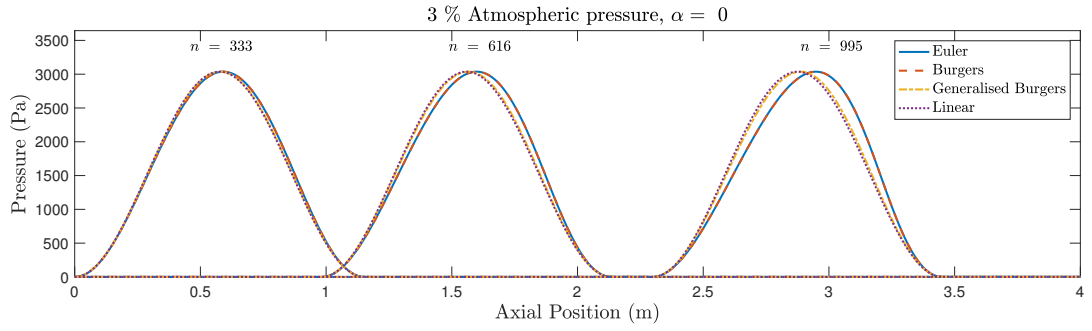


Figure 7.2: Propagation of a Hann pressure pulse of width $1/300$ s and amplitude 3 % of atmospheric pressure in a cylindrical tube modelled using the Euler equations (blue), Burgers equation (dashed red), generalised Burgers equation (dash-dot yellow), and the linear horn equation (dotted purple). Labels above peaks denote corresponding time steps.

Higher excitation pressures up to 4 % of atmospheric pressure are used in the investigations of Hirschberg *et al.* [88] and Rendon *et al.* [136]. Fig. 7.3, shows simulations of wave propagation in a cylinder excited with a signal whose maximum amplitude is $A_{in} = 0.05P_0$. This excitation amplitude is used in subsequent simulations. Again, the Euler and Burgers models behave identically. The generalised Burgers model displays some wave steepening but not to the same extent as the other nonlinear models.

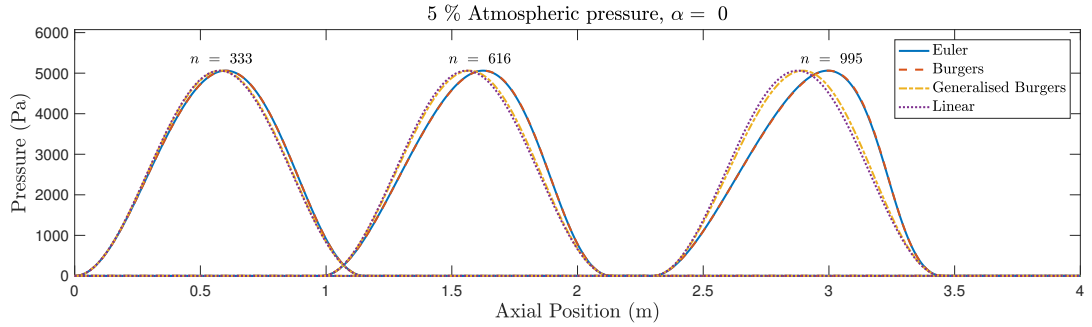


Figure 7.3: Propagation of a Hann pressure pulse of width $1/300$ s and amplitude 5 % of atmospheric pressure in a cylindrical tube modelled using the Euler equations (blue), Burgers equation (dashed red), generalised Burgers equation (dash-dot yellow), and the linear horn equation (dotted purple). Labels above peaks denote corresponding time steps.

Simulations using an exponential horn profile with flaring parameter $\alpha = 0.5 \text{ m}^{-1}$ and opening radius of $r_0 = 0.01 \text{ m}$ are shown in Fig. 7.4. We recall the surface area of an exponential horn is given by

$$S = S_0 e^{\alpha z} \quad (7.37)$$

There is more variation between the models when there is a change in cross-sectional area. The simulation using the Burgers model shows a larger reduction in the value of the pressure as it propagates along the horn. The generalised Burgers model appears to have reduced a similar amount as the Euler and linear horn equations, but again does not show a great deal of distortion. There is a small amount of scattering present in the simulations using the Euler and linear horn equations caused by the change in cross-sectional area. This isn't present in

the simulations using the Burgers and generalised Burgers models as these models are uni-directional and don't include any transfer of energy between the forwards and backwards waves.

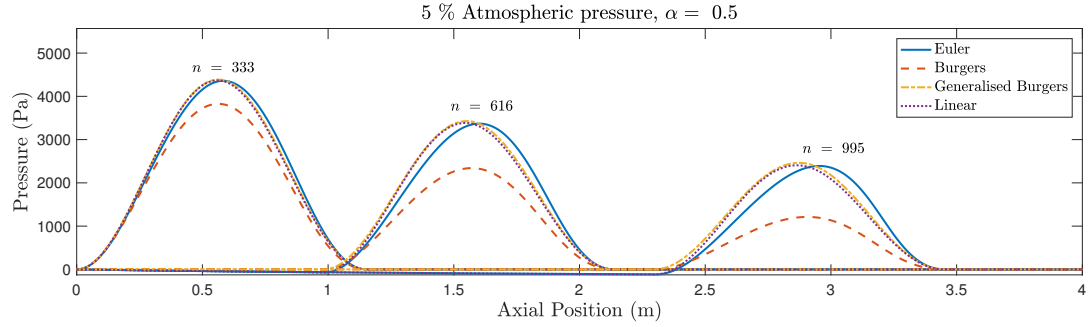


Figure 7.4: Propagation of a Hann pressure pulse of width $1/300$ s and amplitude 5 % of atmospheric pressure in an exponential horn with flaring parameter $\alpha = 0.5 \text{ m}^{-1}$ modelled using the Euler equations (blue), Burgers equation (dashed red), generalised Burgers equation (dash-dot yellow), and the linear horn equation (dotted purple). Labels above peaks denote corresponding time steps.

Simulations for an exponential horn with a larger flaring parameter, $\alpha = 1 \text{ m}^{-1}$, are shown in Fig. 7.5. The reduction in pressure profile of the Burgers model is greater in this configuration than in the previous case. The wave simulated using the generalised Burgers model is slightly larger in amplitude than the Euler and horn equation simulations, which are of similar magnitude and display the same scattering behaviour.

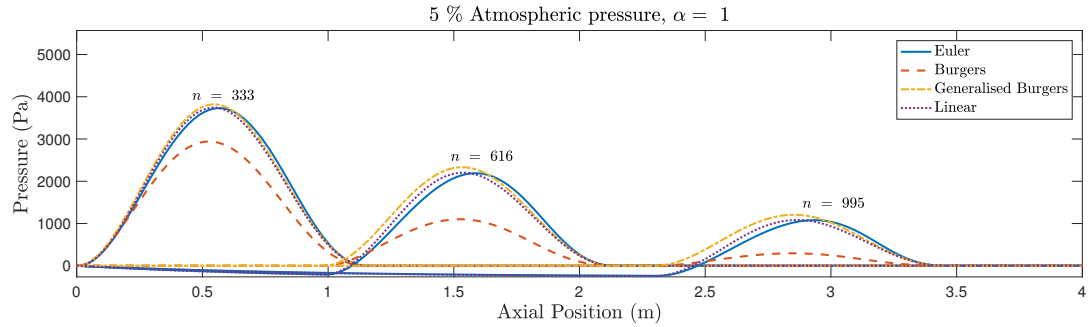


Figure 7.5: Propagation of a Hann pressure pulse of width $1/300$ s and amplitude 5 % of atmospheric pressure in an exponential horn with flaring parameter $\alpha = 1 \text{ m}^{-1}$ modelled using the Euler equations (blue), Burgers equation (dashed red), generalised Burgers equation (dash-dot yellow), and the linear horn equation (dotted purple). Labels above peaks denote corresponding time steps.

7.5 Effect of varying bore profile on linearised models

The simulation results presented in Figs. 7.4 and 7.5 show significant differences between the models when there is a change in cross-sectional area. We can investigate these effects further by performing dispersion analysis on the linearised forms of the Euler, Burgers, and generalised Burgers equations. We return to the domain of positive real numbers for time so

that $t \in \mathbb{R}^+$.

As noted earlier, the Euler equations, (7.5), reduce to the horn equation, which, we recall is given in transmission line form as

$$\text{Model 1 : } \partial_t p + \rho_0 c_0^2 \partial_z v + \frac{\rho_0 c_0^2 v}{S} \frac{dS}{dz} = 0, \quad \partial_t v + \frac{1}{\rho_0} \partial_z p = 0 \quad (7.38)$$

Linearising the Burgers model, (7.14), and using the linear relation between pressure and velocity, (7.15), results in

$$\text{Model 2 : } \partial_t p + \rho_0 c_0^2 \partial_z v + \frac{\rho_0 c_0^2 v}{S} \frac{dS}{dz} = 0, \quad \partial_t v + \frac{1}{\rho_0} \partial_z p + \frac{p}{\rho_0 S} \frac{dS}{dz} = 0 \quad (7.39)$$

Linearising the generalised Burgers model, (7.23), and using the relation between the forwards and backwards wave variables to pressure and velocity, (7.24), produces

$$\text{Model 3 : } \partial_t p + \rho_0 c_0^2 \partial_z v + \frac{c_0 p}{2S} \frac{dS}{dz} = 0, \quad \partial_t v + \frac{1}{\rho_0} \partial_z p + \frac{c_0 v}{2S} \frac{dS}{dz} = 0 \quad (7.40)$$

We have already shown in Chap. 2 that Model 1 does not permit separable wave solutions when there is a change in cross-sectional area. Model 2 can be rewritten in the form of a wave equation with wave variable Sp

$$\partial_{tt} (Sp) - c_0^2 \partial_{zz} (Sp) = 0 \quad (7.41)$$

The effect of the surface area for this model is to scale the pressure (or particle velocity) but does not create any scattering effects. This is clear when using the scaled pressure.

$$\tilde{p} = Sp \implies \partial_{tt} \tilde{p} - c_0^2 \partial_{zz} \tilde{p} = 0 \quad (7.42)$$

where \tilde{p} is the conserved quantity.

Model 3 can be rewritten in two separate advection equations using the variables q^+ and q^-

$$\partial_t (\sqrt{S} q^+) + c_0^2 \partial_z (\sqrt{S} q^+) = 0, \quad \partial_t \left(\frac{q^-}{\sqrt{S}} \right) - c_0^2 \partial_z \left(\frac{q^-}{\sqrt{S}} \right) = 0 \quad (7.43)$$

Again, there is no scattering due to the a change in cross-sectional area which only has the effect of scaling the wave variables. However, this scaling is different depending on which direction the wave is travelling in. Defining new scaled wave variables

$$\tilde{q}^+ = \sqrt{S} q^+, \quad \tilde{q}^- = \frac{q^-}{\sqrt{S}} \quad (7.44)$$

we can construct another wave equation

$$\partial_{tt}\tilde{q} - c_0^2\partial_{zz}\tilde{q} = 0 \quad (7.45)$$

where $\tilde{q} = \tilde{q}^+ + \tilde{q}^-$ is the conserved quantity. In this case, the process to retrieve the original wave variables is different for the forwards and backwards waves.

Immediately it is clear that the effect of scattering due to changes in the tube cross-section are neglected in models 2 and 3.

7.5.1 Dispersion analysis

Dispersion analysis can be performed on models 1-3 using an exponential horn. The system equations become:

Model 1

$$\partial_t p + \rho_0 c_0^2 \partial_z v + \rho_0 c_0^2 \alpha v = 0, \quad \partial_t v + \frac{1}{\rho_0} \partial_z p = 0 \quad (7.46)$$

Model 2

$$\partial_t p + \rho_0 c_0^2 \partial_z v + \rho_0 c_0^2 \alpha v = 0, \quad \partial_t v + \frac{1}{\rho_0} \partial_z p + \frac{\alpha p}{\rho_0} = 0 \quad (7.47)$$

Model 3

$$\partial_t p + \rho_0 c_0^2 \partial_z v + \frac{c_0 \alpha p}{2} = 0, \quad \partial_t v + \frac{1}{\rho_0} \partial_z p + \frac{c_0 \alpha v}{2} = 0 \quad (7.48)$$

Assuming harmonic solutions of the form

$$p = e^{j\omega t} e^{j\beta z} \quad (7.49)$$

allows for the determination of the dispersion relations.

The dispersion relation for Model 1, which we recall from Chap. 2, Sec. 2.3.1, is

$$\beta_1 = \frac{j\alpha \pm \sqrt{4\left(\frac{\omega}{c_0}\right)^2 - \alpha^2}}{2} \quad (7.50)$$

with phase and group velocities

$$v_{p1} = \pm \frac{2\omega}{\sqrt{4(\omega/c_0)^2 - \alpha^2}}, \quad v_{g1} = \pm \frac{c_0^2 \sqrt{4(\omega/c_0)^2 - \alpha^2}}{2\omega} \quad (7.51)$$

We recall that for Model 1, dispersion analysis shows that a) there is a cutoff frequency, $\alpha c_0/2$, below which waves cannot propagate, and b) that different frequency waves travel at different velocities due to the flaring parameter.

The dispersion relation for Model 2 is given by

$$\beta_2 = j\alpha \pm \frac{\omega}{c_0} \quad (7.52)$$

with phase and group velocities given by

$$v_{p2} = v_{g2} = \pm c_0 \quad (7.53)$$

A similar dispersion relation is found for Model 3

$$\beta_3 = \mp \frac{j\alpha}{2} \pm \frac{\omega}{c_0} \quad (7.54)$$

with phase and group velocities given by

$$v_{p3} = v_{g3} = \pm c_0 \quad (7.55)$$

It is clear that wave solutions to models 2 and 3 do not display any dispersion due to the change in cross-sectional area³. There is also no cutoff frequency in these models, meaning that the low frequency behaviour of models 2 and 3 is very different to that of Model 1.

The imaginary part of β_2 is twice the value in β_1 meaning that waves modelled using Model 2 will see a greater reduction in amplitude due to the increase in tube cross-section, as shown in the simulations in Figs. 7.4 and 7.5.

The magnitude of the imaginary part of β_3 is the same as in β_1 , but there is a change in sign for the first solution, corresponding to a solution travelling in the negative z direction. Considering $\alpha > 0$, this means that the backwards solution is travelling into a contracting tube. For Model 1, we would expect the pressure to increase as it is concentrated over a smaller surface area. However, for Model 3, the opposite happens and the acoustic pressure reduces.

7.5.2 Input impedances

The input impedances predicted by the linear models 1-3 can be calculated using their corresponding dispersion relations, in the same manner as presented in Chap. 2, Sec. 2.3.4. Fig. 7.6 shows the input impedances calculated using each model for an exponential horn of length 1 m and flaring parameter 1 m^{-1} terminated with a Dirichlet boundary condition.

The input impedance calculated using Model 1 has already been discussed in Chap. 2; we recall that the lower resonance peaks are raised in frequency relative to those of a cylinder of the same length. Models 2 and 3 do not exhibit this shift in lower resonances, in fact they are the same frequency as those of a cylinder. Whereas Model 2 still shows well defined peaks, the resonances of Model 3 are not sharply defined and tend to flatten out as the flaring parameter is increased.

³Note that we are discussing actual dispersion in the model, not any numerical dispersion created by a FDTD scheme.

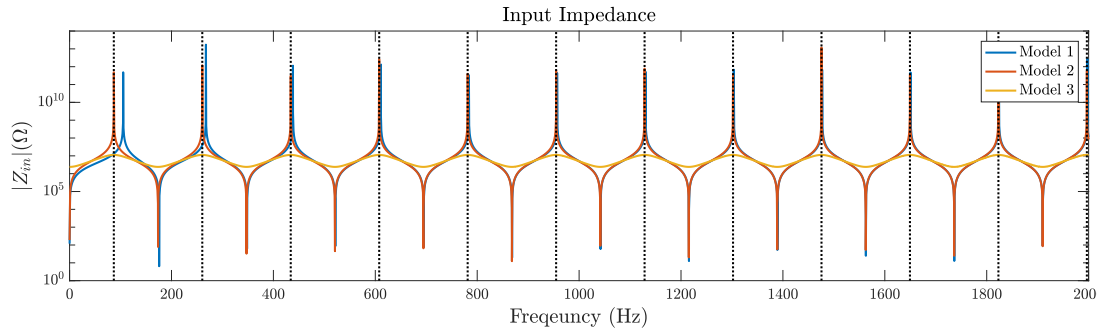


Figure 7.6: Input impedances calculated using models 1-3 for an exponential horn of length 1 m and flaring parameter 1 m^{-1} terminated with a Dirichlet boundary condition. Dashed black lines show the resonance frequencies of a cylinder of similar length.

7.6 Effect of coupling of forwards and backwards waves in a cylinder

We now look to investigate the importance of two waves interacting with each other in a cylinder caused by the nonlinearity in the Euler model. Consider a cylinder of length $L < L_{shock}$ that is excited at both ends by a pressure signal. We assume a finite time so that $0 \leq t < c_0 L$. At either end, the excitations can either have the same sign, a configuration we label ‘Test 1’, or the opposite sign, ‘Test 2’; see Fig. 7.7. Taking a pressure measurement at some point along the tube after the waves have crossed over each other allows for comparison between the two scenarios. If there is little or no difference between the measurements, then the coupling between the two waves can be neglected.

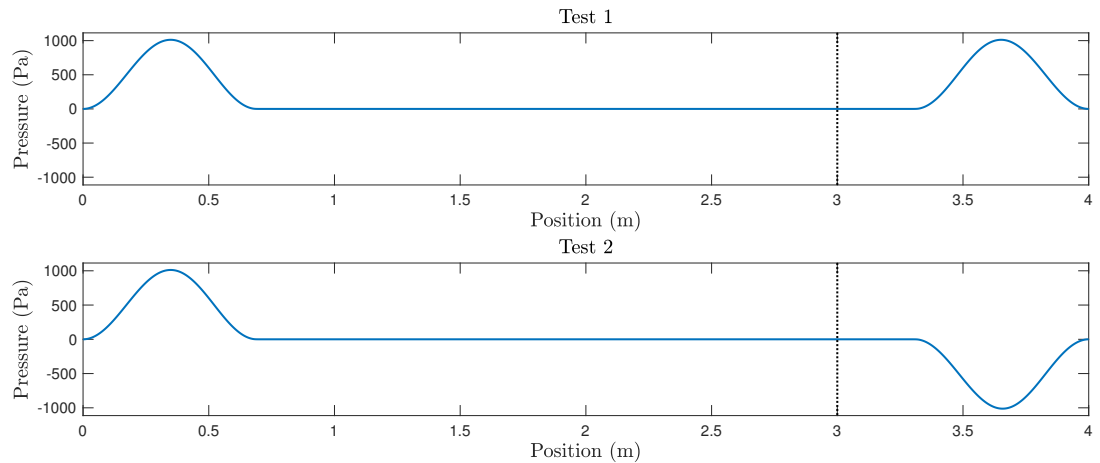


Figure 7.7: Top: Test case where the tube is excited with the same signal at both ends. Bottom: Test case where the tube is excited with signals of opposite signs at both ends. Dashed line shows where the output is taken.

7.6.1 Simulation results

Simulations are performed using the FDTD scheme (7.28) to solve the Euler equations at a sample rate of 100 kHz and Courant number of $\lambda = 0.9$ for several excitation signals and tube lengths. The measurement position is set to be 75 % along the tube length, with a simple linear interpolation performed if this position lies between grid points. Signals are truncated so that only the rightward travelling component is presented, with the signal length being 501 samples long, resulting in a frequency resolution of around 200 Hz. At the end points, the pressure is set by the driving pressures

$$p_0^n = A_{in} p_{Hann}^n \quad (7.56)$$

$$p_N^n = \begin{cases} A_{in} p_{Hann}^n, & \text{Test 1} \\ -A_{in} p_{Hann}^n, & \text{Test 2} \end{cases} \quad (7.57)$$

Fig. 7.8 show simulations for a 3 m long tube using $A_{in} = 0.05P_0$ and widths, T_{Hann} , of 1/300 s, 1/500 s, and 1/700 s, respectively. There is a clear shift in arrival time between the two test scenarios; pressure pulses of the same sign, shown in Test 1, arrive later than when they are of the opposite sign, shown in Test 2. However, the overall shape of the final pulse is similar in both cases. These results show that there is some effect due to the coupling of wave speeds in the cylinder.

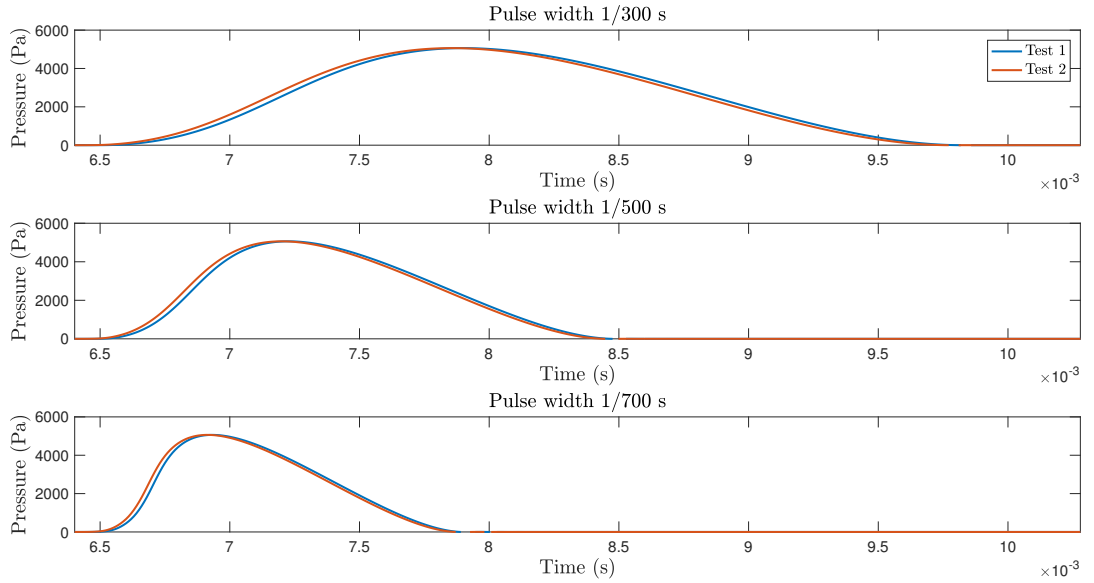


Figure 7.8: Pressure signals recorded 75 % along a tube of length 3 m when excited at both ends with Hann pulses of amplitude 5 % of atmospheric pressure, with the same sign, Test 1 (blue), and opposite sign, Test 2 (red). Top: Pulse width 1/300 s. Middle: Pulse width 1/500 s. Bottom: Pulse width 1/700 s.

To quantify these results, we compare them to the case where only the left hand side of the tube is excited; this mimics the effect of using a uni-directional model without introducing assumptions that modify the behaviour of the model. Let us label the output of this result y_0^n ,

and use y_1^n and y_2^n to denote the results from Tests 1 and 2 respectively. The percentage difference in the change of spectral content is given by

$$\Delta A_1 = 100 \left(\frac{|\mathfrak{F}(y_1)| - |\mathfrak{F}(y_0)|}{|\mathfrak{F}(y_0)|} \right), \quad \Delta A_2 = 100 \left(\frac{|\mathfrak{F}(y_2)| - |\mathfrak{F}(y_0)|}{|\mathfrak{F}(y_0)|} \right) \quad (7.58)$$

where we recall that $\mathfrak{F}()$ denotes the DFT of a signal. The percentage difference in phase, or angle, of these signals is given by

$$\Delta \theta_1 = 100 \left(\frac{\angle \mathfrak{F}(y_1) - \angle \mathfrak{F}(y_0)}{\angle \mathfrak{F}(y_0)} \right), \quad \Delta \theta_2 = 100 \left(\frac{\angle \mathfrak{F}(y_2) - \angle \mathfrak{F}(y_0)}{\angle \mathfrak{F}(y_0)} \right) \quad (7.59)$$

The change in spectral content for the simulations presented in Fig. 7.8 is shown in Fig. 7.9. For the shorter duration pulses of length 1/700 s and 1/500 s, ΔA_1 is positive—there is an increase in harmonic content in Test 1, where the interacting pressure pulses have the same sign, relative to the single wave. The value of ΔA_2 , on the other hand, is negative for this case. The absolute change in spectral content is less than 1 % for the 1/700 s pulse. There is a larger change in spectral content for the 1/500 s pulse of up to 5 %. For the widest pulse of duration 1/300 s, the change in harmonic content is less symmetric between tests 1 and 2 than for the shorter duration pulses. For ΔA_1 , the difference changes by up to ± 2 % whereas ΔA_2 has a maximum value of 4 % and a minimum of -11 %.

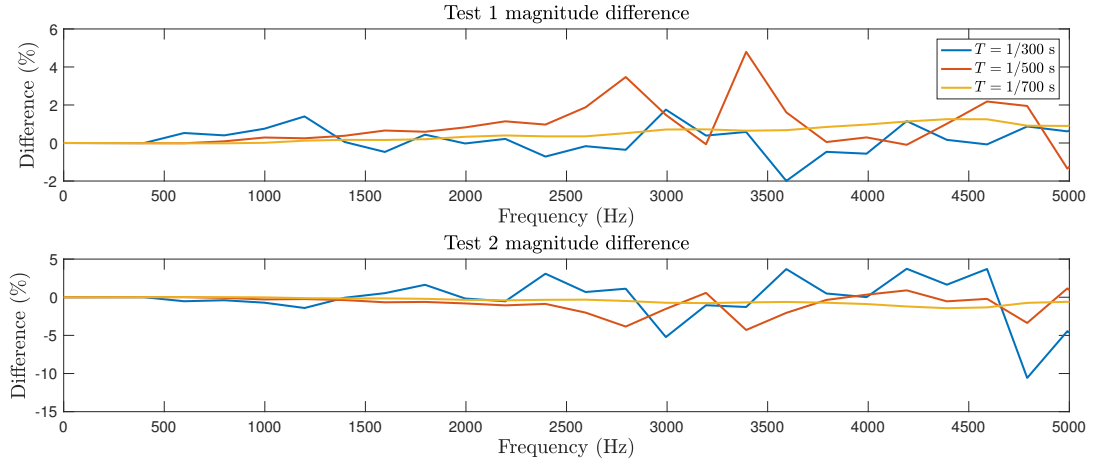


Figure 7.9: Percentage differences in magnitude of output relative to a single input. Top: Test 1 difference. Bottom: Test 2 difference.

The percentage difference in the angle of the DFT is shown in Fig. 7.10. $\Delta \theta_1$ is always negative, $\Delta \theta_2$ is always positive. This reflects what is shown in the time signals as the Test 2 results appear to arrive before the Test 1 results. As the pulse width is reduced, the values of $\Delta \theta_1$ and $\Delta \theta_2$ both approach zero.

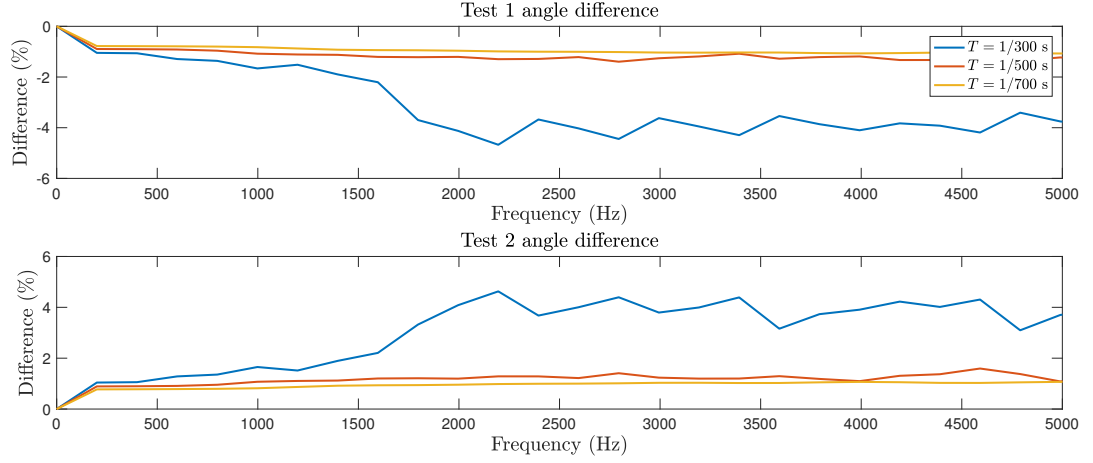


Figure 7.10: Percentage differences in angle of output relative to a single input. Top: Test 1 difference. Bottom: Test 2 difference.

We can describe these results in the following way. The narrowest pulse exhibits the smallest change due to interaction of waves because there is a shorter interaction time as the pulses pass over each other. The pulse of duration $1/500$ s has a longer time to overlap, so the change in spectral behaviour is greater. In Test 1, the pulses add together to create a larger local pressure and therefore a larger local speed of sound. This in turn increases the nonlinearity and would explain why there is an increase in harmonic content. For Test 2, the pulses cancel each other out, effectively reducing the nonlinearity in the region where the pulses overlap. This would explain why the harmonic content reduces for this case. This argument does not easily explain why the longest pulse of $1/300$ s does not present a systematic increase or decrease in harmonic content. This could be due to the low gradient of the pulse meaning that not enough distortion has occurred. There is a noticeable increase in the difference of the phase for this pulse in both test cases, corresponding to a longer overlap time.

Similar numerical experiments were performed for tubes of different lengths to investigate whether the amount that the pulse has distorted affects the interaction between the two waves. The spectrum magnitude and angle differences are shown in Figs. 7.11 and 7.12, respectively, for a pulse of width $1/500$ s. These results are similar to those shown in Figs. 7.9 and 7.10: ΔA_1 is generally positive and $\Delta \theta_1$ is negative; ΔA_2 is generally negative and $\Delta \theta_2$ is positive. However, these differences reduce as the tube length, and therefore the corresponding amount of distortion that occurs to the pulses, increases.

The smaller differences for larger tube lengths can be explained in a similar manner to the discussion above regarding pulse widths. As the pulse propagates along the tube, the maximum value of the pulse shifts towards the front of the wave. This means that when opposing waves overlap, the overall pressure profile is going to have a sharper peak than waves whose maxima lie more to their centre. The corresponding increase in local pressure occurs over a shorter period of time, meaning the increased (or decreased) nonlinearity occurs over a shorter period of time.

Magnitude differences for pulses of width $1/300$ s propagating in tubes of different length are shown in Fig. 7.13. There appears to be some symmetric behaviour between tests 1 and 2;

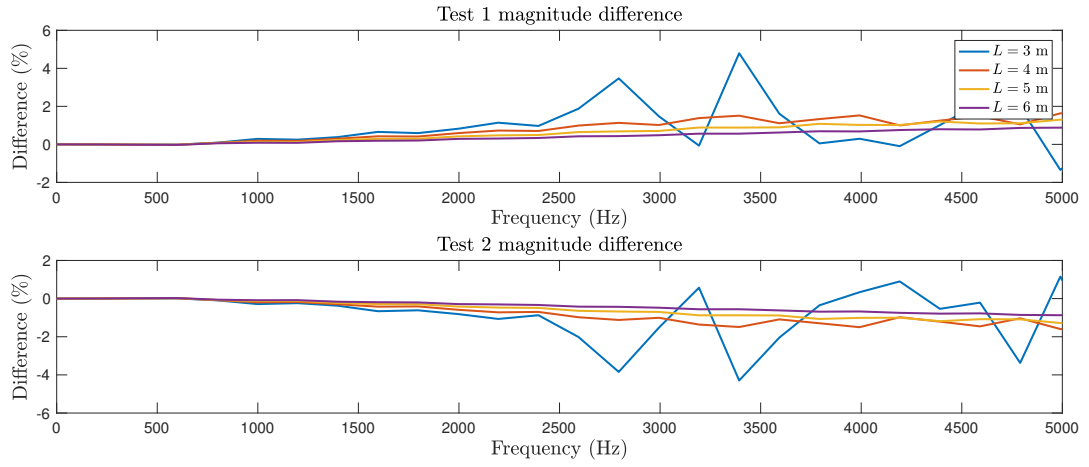


Figure 7.11: Percentage differences in magnitude of output relative to a single input for a pulse of width $1/500$ s for tubes of different lengths. Top: Test 1 difference. Bottom: Test 2 difference.

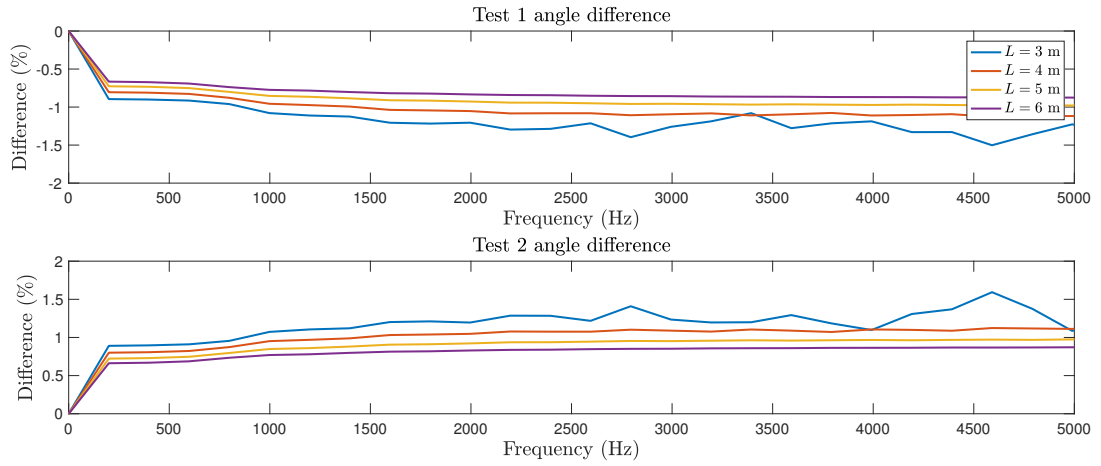


Figure 7.12: Percentage differences in angle of output relative to a single input for a pulse of width $1/500$ s for tubes of different lengths. Top: Test 1 difference. Bottom: Test 2 difference.

where results for Test 1 show a positive magnitude difference, results for Test 2 show a negative magnitude difference of similar magnitude and vice-versa. However, the difference in magnitude between the interacting and non-interacting waves does not decrease as the tube length increases. There appears to be a reduction in magnitude difference from a maximum of 4 % to just under 2 % as the tube length increases from 3 m to 5 m but results from the 6 m tube show an increased magnitude difference with a maximum of 25 % around 4200 Hz.

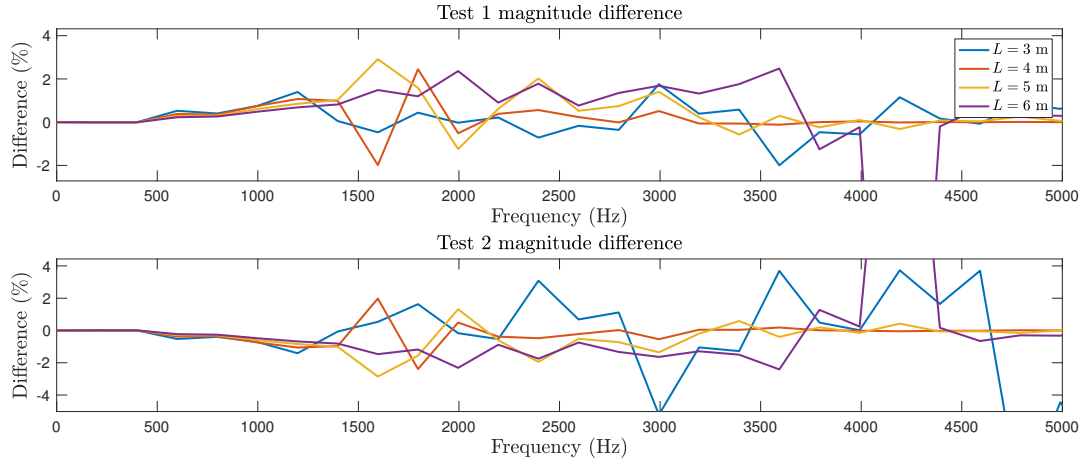


Figure 7.13: Percentage differences in magnitude of output relative to a single input for a pulse of width $1/300$ s for tubes of different lengths. Top: Test 1 difference. Bottom: Test 2 difference. For $L = 6$ m the differences go to 25 % for Test 1 and -25 % for test 2.

The angle differences for the pulses of width $1/300$ s are shown in Fig. 7.14. In general, $\Delta\theta_1$ and $\Delta\theta_2$ tend towards zero for the two test cases as the length of the tube increases. The notable exceptions are for the 4 m long tube above 3000 Hz, which increases the absolute values of these angle differences with frequency, and for the 5 and 6 m long tubes around 400 Hz, where a spike in angle difference is present but reduces as frequency increases.

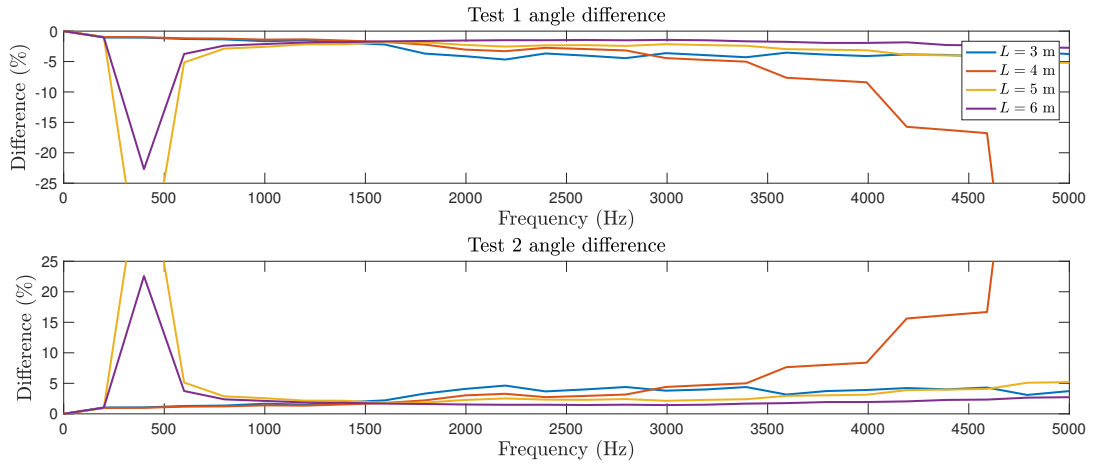


Figure 7.14: Percentage differences in angle of output relative to a single input for a pulse of width $1/300$ s for tubes of different lengths. Top: Test 1 difference. Bottom: Test 2 difference. For $L = 6$ m the differences go to 25 % for Test 1 and -25 % for test 2.

7.7 Conclusions

In this chapter we have investigated some of the models used to describe nonlinear propagation within acoustic tubes. In musical acoustics, this nonlinearity is important in describing the change in timbre when brass instruments are played at high dynamic levels.

The models in the literature stem from the Euler equations, with assumptions made that allow for separable solutions. However, it is clear from looking at the Riemann invariants of the Euler equations that separable solutions are not, in general, possible; there is a coupling between forwards and backwards waves through the wave speed and due to the change in cross-sectional area. To the author's knowledge, no one has investigated what effect neglecting this coupling has on wave propagation.

To investigate the differences in models, simulations were performed using simple finite difference schemes. It was shown that for a cylinder, the Burgers model distorts the same as for the Euler equations, whereas the generalised Burgers model shows significantly less distortion. For an exponential horn, the Burgers model shows a greater reduction in the pressure amplitude than that shown in the Euler model. The pressure amplitude produced by the generalised Burgers model is slightly larger than observed in the Euler model.

By linearising the models and performing dispersion analysis, it is clear that the extra reduction of the pressure amplitude observed in the Burgers model results from the linear effect of changing the cross-sectional area. This argument cannot be used to explain why the generalised Burgers model shows less reduction in amplitude as the imaginary part of the wave number is the same as for the horn equation. Instead, this effect could be described by the scattering that occurs in the Euler model. Since the peak amplitude of the Euler and horn equation simulations appear to be of a similar value, it could be that the extra reduction is caused by waves being scattered backwards, an effect that is not included in the uni-directional models.

Finally, the effect of coupling between forwards and backwards waves in a cylinder was investigated. This was done using simulations of a cylindrical tube excited at both ends with the same signal, but with inverted sign for one test case. Simulations for this study were done using just the Euler equations and results were compared against the case of a single propagating pulse. This removed any effects introduced by the other models to ensure a fair comparison when the waves interacted. It is clear that there is a small modification in the wave speed when waves interact with each other; if the pressure disturbances have the same sign they slow each other down, if the sign is opposite they speed each other up. The interaction also affects the amount of distortion that occurs—the same signs increase the nonlinearity whereas opposite signs can cancel each other out and reduce the nonlinearity. The overall effect on wave propagation is related to the amount of time that the disturbances interact with each other. The amount of distortion that has already occurred also appears to have an impact on the interaction.

The implications of this wave interaction are as follows. The scattering behaviour caused by changes in cross-sectional area is different between the models, leading to different resonance behaviour; the uni-directional models always produce the resonances of a cylinder. This is important from a physical modelling perspective as the virtual instruments synthesised using these methods will not have the same playable notes as a real tube with spatially varying cross-section. It should be noted, however, that other work using the uni-directional models

has often focussed on high frequency experiments where the scattering is less pronounced.

The amount of distortion between the propagation models is also different. Results from the Burgers model are identical to those of Euler model for the case of a cylinder when waves do not overlap. However, there is a deviation for non-cylindrical bore profiles, with the amplitude of the pressure in the Burgers model being reduced by a greater amount due to scaling over the cross-sectional area. It is clear that for an exponential horn the Euler equations still produce some distortion of the profile of the wave; this distortion will be weaker in Burgers model due to the lower pressure. The generalised Burgers model displays a significantly weaker distortion of waves than the Euler model for a cylindrical and exponential horn tube profile.

The simulations performed in this study did not include losses due to boundary layer effects, see Chap. 2. Since the strength of this loss mechanism increases with frequency, we would expect that at some point this will start to reduce the nonlinearity, and reduce the effect of the nonlinear interactions, provided the loss mechanism remains linear.

Act IV

Finale

Chapter 8

Conclusions and future work

The main objective of this thesis has been to develop a synthesis framework for the production of brass instrument sounds. This objective has been achieved; the algorithms presented in this work are stable, accurate, and efficient. In addition, the algorithms have been implemented in a virtual instrument environment, with the help of colleagues in Edinburgh Parallel Computing Centre, and used in several compositions by international musicians. In this chapter, we first summarise the contents of this thesis before moving onto how this research can be advanced.

8.1 Summary

In Chap. 2, the acoustic tube system was introduced in the continuous domain. The lossless system was first considered with the example of cylindrical tubes and then extended to tubes of varying cross-sectional area. Attenuation processes were included using approximations to the boundary layer loss model of Zwicker and Kosten—a review of frequency domain approximations was presented followed by the construction of an equivalent network model. This chapter introduced dispersion analysis as a method to characterise the behaviour of systems along with measures of the energy of the system. The dispersion analysis allows for a measure of accuracy of the numerical scheme and is also used in determining behaviour of the nonlinear models studied in Chap. 7. Energy analysis allows for the determination of system passivity and constitutes the first step in determining stability of numerical schemes.

In Chap. 3, the finite-difference time-domain method was introduced in the context of acoustic tube modelling. The energy methods described in the previous chapter were extended to the discrete case, and the passivity of a numerical scheme was used to show numerical stability. In addition, these energy methods also suggest strategies for implementing numerical boundary conditions. A conditionally stable explicit scheme with good dispersion characteristics and efficient implementation was compared to an unconditionally stable scheme constructed using the bilinear transform, a standard discretisation tool. The bilinear transform is unsuitable for the lossless part of the acoustic tube system due to the severity of numerical dispersion. However, its guaranteed passivity property was exploited for modelling attenuation processes, whilst the explicit scheme is used for accurate modelling of wave propagation. Schemes using both fractional derivatives and network approximations were presented for attenuation modelling, with the network

approaches requiring significantly less processing power.

The problem of radiation of sound from an acoustic tube was considered in Chap. 4. Modelling of sound radiation was approached in two separate manners: an approximation to the Levine and Schwinger radiation impedance using an equivalent electrical network, discretised using the bilinear transform, and direct simulation of the acoustic field outside the instrument. The network approximation is suitable for synthesis purposes due to its efficient implementation, but modelling the acoustic field outside of the instrument allows for the inclusion of mode conversion and additional effects concerning the acoustics of the performance space.

The remaining elements required for instrument emulation, the exciter and valve model, were presented in Chap. 5. The numerical energy analysis of an acoustic tube presented in Chap. 3 was used to determine suitable strategies to couple both the reed model to the acoustic tube and to connect three tubes together to form a valve. A single degree of freedom outward striking reed model was selected as the instrument sound generator, and an appropriate discretisation method was presented. The valve model was constructed using conservation of energy and momentum over the valve boundary and schemes were presented for the static lossless and lossy cases, as well as the time varying case.

Chap. 6 explored the possible uses of the virtual instrument. Simple gestures were presented that included time-varying parameters. A short playability study was performed to highlight the sensitivity of the performance parameter space.

Finally, a comparison of some commonly used nonlinear propagation models was performed in Chap. 7. Analysis of these models was performed using simulation frameworks based on schemes presented in Chap. 3 and using the dispersion analysis presented in Chap. 2. The effect of using unidirectional models was shown to be significant when a change in cross-sectional area was present. Changes in wave speed and distortion of solutions are observable due to interactions between forwards and backwards waves but it is not yet clear how important this is for the purposes of brass instrument synthesis.

8.2 Future work

There are several problems that could not be fully addressed in this work, a discussion of some future work follows.

Passivity of fractional derivative model

Throughout the course of this work there has been a focus on proving the passivity of the presented algorithms using energy methods, the one exception being the fractional derivative model derived in Sec. 3.5.1. Although we can determine stability properties for this model from frequency domain behaviour, that of positive realness and where the poles lie on the unit circle, we cannot derive this from the energy methods discussed in this thesis. One would expect that there would be a network representation of this model, for example a Cauer structure, for which it would be relatively straightforward to prove passivity using energy methods.

Approximating radiation models with electrical networks

The radiation impedance approximation used in this work was originally presented by Silva *et al.* [147], who used this model due to its amenability to numerical optimisation procedures. A similar form was used by Hélie and Rodet [83] to approximate their spherical radiation model. This would suggest some connection between these radiation models, and potentially others such as the plane piston [121] and those of Zorumski [181], where the RLC structure used in this work could be a low order expansion of a positive real network; higher order expansions would therefore improve the accuracy of simulations. These structures could then be optimised to fit the results gathered from the embedded system, improving the accuracy of the one-dimensional system with a smaller computational cost than the three-dimensional one.

Validating the valve model

The valve model presented in Chap. 5 allows for the production of interesting resonance behaviour in the virtual instrument. However, despite valves being an important feature of brass instruments, there is surprisingly little literature on the topic. Some preliminary experiments are described in App. C that investigate the behaviour of partially open valve configurations. A detailed study of wave propagation through the interior of the valve (potentially from a fluid dynamics perspective) in both static and time varying applications would be beneficial.

Other methods of changing instrument resonances

The valve is not the only method of modifying the internal geometry of a brass instrument. Trombones use a sliding tube to adjust the total length of the instrument, whilst many woodwind instruments employ tone holes to change pitch. The slide mechanism requires modification of the tube domain, either by introducing new grid points or extending spatial step sizes. However, it is not clear how to incorporate these processes in a stable manner and the extension of step sizes would reduce the available bandwidth of the simulations. Models for tone holes exist in the literature but often incorporate reactive (non-passive) elements which require careful numerical treatment. The incorporation of these additional features would make for a more flexible instrument.

Stable modelling of nonlinear propagation models

The numerical scheme used to model the Euler equations in Chap. 7 was suitable for the study of interacting waves in acoustic tubes. However, to the author's knowledge, this scheme cannot be shown to be stable using the energy methods used throughout this thesis. As such, we cannot determine stability conditions that would make the method suitable for synthesis purposes. Alternative geometric integration methods could be applied to other conserved quantities, such as the entropy of the system [159], but again issues arise as the nonlinearity develops. Of course, the introduction of boundary layer losses removes energy from the system but, as shown by Hirschberg *et al.* [88], shocks still develop in brass instruments. Along with stability issues, there are also problems with correctly representing the shock on a discrete grid as some numerical methods produce numerical dispersion that smears the shock front—useful in terms of simulation stability but detrimental for giving accurate solutions [103].

Appendix A

Circuit elements

In this short appendix, we highlight some fundamentals of circuit analysis that have been used in this work.

The three core elements of an electrical circuit are the resistor, inductor and capacitor [165, 174]; see Fig. A.1.

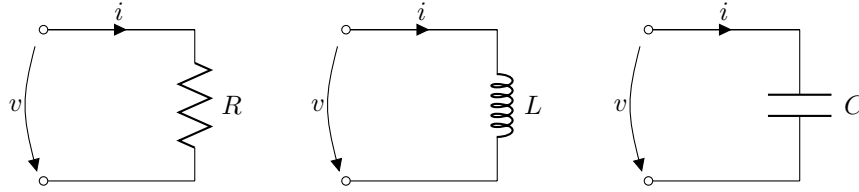


Figure A.1: One-port networks. Left: Resistor network. Middle: Inductor network. Right: Capacitor network.

A resistor, of resistance R , reduces the electric current flowing through it for a given potential difference and therefore takes energy out of the circuit as heat. A resistor can also be classified in terms of its gain, $G = 1/R$. A capacitor, of capacitance C , and inductor, of inductance L , store energy within them and in this work do not dissipate energy¹. The capacitor stores energy by holding charge on two adjacent plates whereas the inductor stores energy in the magnetic field surrounding the coil of wire it is constructed from.

The defining equations between the current, $i(t)$, and voltage, $v(t)$, over these network elements are given by [165]

$$\underbrace{v = Ri}_{\text{Resistor}}, \quad \underbrace{v = L \frac{di}{dt}}_{\text{Inductor}}, \quad \underbrace{v = \frac{1}{C} \int i dt}_{\text{Capacitor}} \quad (\text{A.1})$$

In the frequency domain these relations are

$$\hat{v} = R\hat{i}, \quad \hat{v} = j\omega L\hat{i}, \quad \hat{v} = \frac{1}{j\omega C}\hat{i} \quad (\text{A.2})$$

where $\hat{v}(\omega)$ and $\hat{i}(\omega)$ are the Fourier transforms of the voltage and current. The impedances of

¹In the real world of non-spherical chickens outside of the vacuum these circuit elements do contain a finite resistance.

these elements, that is the ratio of current to voltage over the elements, are given by

$$Z_R = R, \quad Z_L = j\omega L, \quad Z_C = \frac{1}{j\omega C} \quad (\text{A.3})$$

The admittance of each element is the inverse of the impedance

$$Y_R = \frac{1}{R} = G, \quad Y_L = \frac{1}{j\omega L}, \quad Y_C = j\omega C \quad (\text{A.4})$$

It is useful to use the Kirchoff's circuit laws for the analysis of more complex arrangements of network elements [73]. Kirchoff's current law is that *at any junction in a circuit, the sum of currents flowing into and out of the junction equals zero* or

$$\sum_{m=0}^M i_m = 0 \quad (\text{A.5})$$

Kirchoff's voltage law is that *the sum of voltages over a closed loop must equal zero*

$$\sum_{m=0}^M v_m = 0 \quad (\text{A.6})$$

See Fig. A.2 for a representation of these laws.

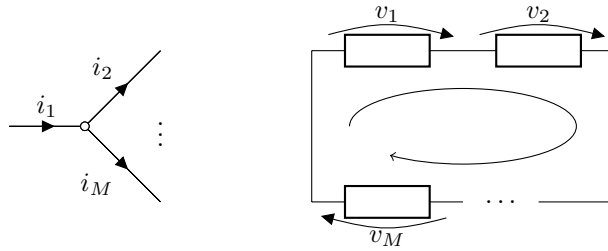


Figure A.2: Left: Currents into and out of a node. Right: The looped sum of voltages.

We can use Kirchoff's laws to determine the impedance and admittance of series and parallel networks; see Fig. A.3. For a network made up of M elements connected in series, the total impedance of the circuit is

$$Z = Z_1 + Z_2 + \cdots + Z_M \quad (\text{A.7})$$

Similarly, for M elements connected in parallel, the total admittance of the circuit is

$$Y = Y_1 + Y_2 + \cdots + Y_M \quad (\text{A.8})$$

We can label networks made up of particular elements by using the symbols in their name: RL networks contain only resistors and inductors, RC are made up of resistors and capacitors, LC are constructed from inductors and capacitors, and RLC contain all three elements.

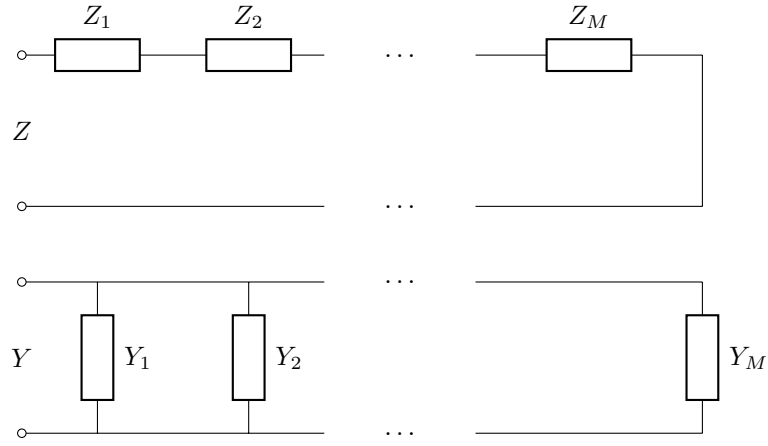


Figure A.3: Top: Circuit with elements connected in series. Bottom: Circuit with elements connected in parallel.

Equivalent circuits for acoustic systems

At first glance it may not be obvious how electrical network analysis can be of use to the practicing acoustician, so it will be enlightening to take a moment to address this. Consider a closed circuit containing a resistor, inductor, and capacitor connected in series shown in Fig. A.4.

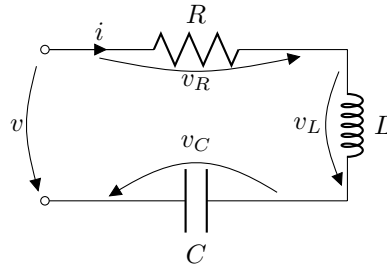


Figure A.4: An RLC circuit which has the same response as a simple harmonic oscillator with damping.

Taking the closed voltage loop around this circuit produces

$$v_L + v_R + v_C = v \implies L \frac{di}{dt} + Ri + \frac{1}{C} \int i dt = v \quad (\text{A.9})$$

where the current is equal across all circuit elements. If we assume that $v(t)$ is constant, the time derivative of this equation is

$$L \frac{d^2 i}{dt^2} + R \frac{di}{dt} + \frac{1}{C} i = 0 \quad (\text{A.10})$$

This is an ordinary differential equation that also describes the dynamics of the simple harmonic oscillator with damping. An inductor behaves like a mass, containing some inertia that resists motion or, in this case, changes to the electric current. The resistor acts like a damper in the simple harmonic oscillator, removing energy from the system. The capacitor

behaves like a spring, pushing the current in the opposite direction when it gains a charge.

We can also use network analogies for acoustic tubes [63]. Consider air in a small section of tubing of length ΔL and constant cross-sectional area S . The mass of the air is equal to $\Delta L S \rho_0$ meaning that the force acting on the air is

$$\rho_0 S \Delta L \frac{dv}{dt} = -S \Delta p \quad (\text{A.11})$$

where Δp is the difference in acoustic pressure between the two sides of the air and v is the particle velocity. Rearranging this equation and using the volume velocity, $U = Sv$ gives

$$-\Delta p = \frac{\rho_0 \Delta L}{S} \frac{dU}{dt} \quad (\text{A.12})$$

It is apparent that this description is similar to that of the voltage over an inductor, where the minus of the pressure difference across the tube is equivalent to the electric potential difference and the volume velocity is equivalent to the electric current. This means that an acoustic tube behaves like an inductor of inductance $\rho_0 \Delta L / S$. This analogy is only equivalent for low frequencies relative to the length of the tube but is a useful tool in acoustics.

Appendix B

Foster network element values

Recall the impedance of the Foster network is given by

$$Z_v^M = e^{a_0} + \sum_{q=1}^M \frac{e^{a_q} j\omega}{e^{b_q} + j\omega} \quad (\text{B.1})$$

B.1 Element values for continuous case

Here we present elements for the Foster network used to model viscous and thermal losses in the continuous domain.

$M = 4$	
E_R	0.0234494664073590
a_0	1.78673332377038
a_q	2.00382931898420, 3.14804951042440, 4.26150413518742, 5.50971380536713
b_q	3.39879310458637, 5.71032238039009, 7.95854733511626, 10.2448811301000
$M = 8$	
E_R	$5.07851108448002 \times 10^{-06}$
a_0	1.77626921138020
a_q	1.16947203816779, 1.63455222619591, 2.22808996187010, 2.80868696959160, 3.38432152205144, 3.96412484168712, 4.59313872296893, 5.69321545319216
b_q	2.83622816669839, 4.06100811397873, 5.21824406563471, 6.37563229181463, 7.52951817958072, 8.68261962284996, 9.85466844512209, 11.2408213780434
$M = 16$	
E_R	$1.88335259896002 \times 10^{-09}$
a_0	1.77617055460705
a_q	1.07101111930346, -0.191137256934357, -2.22953634694106, 1.16757650362629, 1.66903973571218, 2.07340818247316, 2.45430225714201, 2.82326302711027, 3.20075853542216, 3.58778174627400, 3.97118596901446, 3.31992288500898, 3.92720986887682, 2.30723002141302, 5.20175600836121, 13.2880886930482
b_q	2.80368863323309, 3.58176534709911, 3.58176534709918, 3.99610463720205, 4.80277903673739, 5.61822018775434, 6.42065124229265, 7.20347156389189, 7.97353741515494, 8.74240977325489, 9.51243176421373, 10.1896361251182, 10.3802224475833, 10.3802224475834, 11.2511443129779, 16.1294168496902

Table B.1: Foster element values when optimising using E_R for a tube of radius 0.005 m at 26.85° C over the frequency range 0.1 – 10 kHz.

$M = 4$	
E_M	0.0715786353463127
a_0	1.78951546246885
a_q	2.16943661559377, 3.45849867528497, 4.72224630727469, 6.56083118728158
b_q	3.54230512771505, 6.10613832356612, 8.63503593028419, 11.4369230510207
$M = 8$	
E_M	$3.02574820340624 \times 10^{-05}$
a_0	1.77634594834302
a_q	1.21795689259388, 1.79065106148618, 2.44955980938622, 3.09168299006462, 3.72826439347756, 4.37542420032459, 5.16877952981315, 7.21687325848349
b_q	2.85582406620587, 4.17355773792651, 5.45409713324216, 6.73606613886749, 8.01371812473195, 9.29168545594392, 10.6300369143409, 12.7756407005101
$M = 16$	
E_M	$5.18445861030921 \times 10^{-09}$
a_0	1.77617202016723
a_q	1.08365861138349, 1.12477948750744, 1.40845944720948, 1.85942844554413, 2.29454995017727, 2.66834447630448, 2.68811937341307, 2.84251699918943, 3.59998948569483, 4.08100455035118, 4.58449010348442, 5.32313671277967, 4.43502083478810, 6.98152719509852, 8.08233840300017, 11.8382444340280
b_q	2.80638898398790, 3.80345071146270, 4.53921311487309, 5.28632327535363, 6.07789421939354, 6.87599343819387, 7.57735113785327, 8.04471614010159, 8.72499399382516, 9.54537236402782, 10.4137737821984, 11.4133949247559, 12.3647128781383, 13.2694199447204, 16.0705166705316, 19.9800369207571

Table B.2: Foster element values when optimising using E_M for a tube of radius 0.005 m at 26.85° C over the frequency range 0.1 – 10 kHz.

$M = 4$	
$E_R =$	0.000141542510562678
a_0	2.56895852024480
a_q	2.64949367699711, 3.22982054694367, 3.93587280446617, 5.02394562987361
b_q	5.36449351366720, 6.83407959595604, 8.22900585988905, 9.78167541147680
$M = 8$	
E_R	$3.99781337238800 \times 10^{-08}$
a_0	2.39072893487651
a_q	2.15102947324571, 2.36815257481046, 2.75545270609303, 3.14972376266256, 3.53533745702292, 4.03733314014764, 5.18520009303550, 6.28892616777464
b_q	4.76875954807544, 5.86184446803226, 6.78331533424035, 7.65707903669578, 8.49572411718712, 9.33986959979712, 10.4669497561953, 13.1573441638063
$M = 16$	
E_R	$8.12541058964733 \times 10^{-12}$
a_0	2.26365426784080
a_q	1.83997418435759, 0.920452943638728, 1.49311893808675, 2.03637769782586, 2.17577282856170, 2.22897034234053, 2.63834315056954, 3.02500312860672, 3.33449922896188, 3.55097521394667, 3.64683211177011, 4.29760437361149, 4.30490487567676, 4.29059837456845, 3.98103941392489, 3.95880481718749
b_q	4.36612882657212, 5.16602396489476, 5.40775762815384, 6.03684009382674, 6.62885728933031, 7.11199723654211, 7.59243922608423, 8.15738597081932, 8.75139201571871, 9.33231489577200, 9.83318188398057, 10.3945896153586, 11.3316694308202, 11.3316694357558, 11.3316695631162, 11.3316695740028

Table B.3: Foster element values when optimising using E_R over a smaller frequency range for a tube of radius 0.005 m at 26.85° C over the reduced frequency range 20 Hz - 3 kHz.

$M = 4$	
E_M	0.00292405569458211
a_0	2.34766307840886
a_q	2.75636235102840, 3.49113805269408, 4.39152888271209, 6.31303994619724
b_q	5.11148131891873, 6.93271213517213, 8.66939248628015, 10.9760400605784
$M = 8$	
E_M	$2.92901975654115 \times 10^{-06}$
a_0	2.05492378788811
a_q	2.15796320342803, 2.42769393302163, 2.92603347210292, 3.46620375991204, 4.05373572096265, 4.94793064525109, 7.14033510305905, 0.425390103699538
b_q	4.20235209252206, 5.58875042436207, 6.71184100642302, 7.80374400862574, 8.90649235577635, 10.1562576278865, 12.4898544544823, 16.0338293462206
$M = 16$	
E_M	$5.13467272533272 \times 10^{-10}$
a_0	1.84523042820203
a_q	0.978598570821724, 0.610390905902404, 1.41269379178733, 1.71408606755416, 2.02246238922607, 2.30736365261612, 2.61757068069792, 2.98880213909959, 3.38663816791189, 3.76729088509325, 3.91813370682619, 4.83401760385133, 0.138658341528488, 6.65093866036470, 5.76744064476961, 5.17425387924675
b_q	3.29284207979976, 3.29288403065929, 4.35202258319201, 5.10456449178987, 5.82056267776754, 6.49684324910576, 7.14697466045120, 7.80680431173218, 8.50034240269842, 9.22234460481371, 9.89643622819650, 10.6211438212465, 11.5480572028912, 12.6217948634956, 12.6218124886916, 12.6218313956849

Table B.4: Foster element values when optimising using E_M for a tube of radius 0.005 m at 26.85° C over the reduced frequency range 20 Hz - 3 kHz.

B.2 Element values for discrete case

Here we present element values for the Foster network for viscous and thermal losses to be used in the discrete case. The functions have been optimised by pre-warping the angular frequency at a sample rate of 50 kHz. Recall that the pre-warped frequency is given by

$$\tilde{\omega}' = \frac{2}{k} \tan^{-1} \left(\frac{\omega k}{2} \right) \quad (\text{B.2})$$

$M = 4$	
E'_M	0.0949462118367476
a_0	1.79093241217392
a_q	2.21774119544845, 3.53504355037690, 4.83185854842939, 6.64025932147926
b_q	3.58977483976854, 6.21359662754855, 8.80260096873909, 11.6431597743201
$M = 8$	
E'_M	0.000641573586939728
a_0	1.77683207696528
a_q	1.36531177499111, 2.12114439455379, 2.89185539361509, 3.65093958860183, 4.42226341209098, 5.42645465366763, 3.90091429236591, 12.7743460756721
b_q	2.92770775765477, 4.47004911143952, 5.99369478960792, 7.51277808432381, 9.03348730169642, 10.6448301293608, 15.2214508864753, 18.5455246297529
$M = 16$	
E'_M	0.000349802524735779
a_0	1.77615317539466
a_q	1.10633531463411, 1.36236941583819, 1.83223005953335, 2.26436038812417, 2.54385001973642, 2.91163891261644, 3.60176303629582, 2.26051339836179, 4.20846521595365, 4.56589829859680, 4.81572728306258, 1.66279414507306, 3.46818783238449, 4.65013925527772, 6.00859131506436, 17.7759740465847
b_q	2.81315365903336, 3.89742994877119, 4.84400746181209, 5.77465110428627, 6.62622199124618, 7.37671923901475, 8.25914862942342, 9.35530147420441, 9.35530291195798, 10.7304632732496, 10.7304632757414, 16.6684144163614, 17.5730136833208, 18.1607921130290, 18.8327009237834, 23.5612132844038

Table B.5: Foster element values when optimising using E'_M for a tube of radius 0.005 m at 26.85° C over the pre-warped frequency range 0.1 – 10 kHz at a sample rate of 50 kHz.

$M = 4$	
E'_M	0.00929084924724041
a_0	2.44236974312547
a_q	2.93857509943753, 3.80626415894440, 4.92319050461018, 16.5624516922382
b_q	5.37218475536302, 7.35442924111783, 9.33154028303281, 21.7089231966319
$M = 8$	
E'_M	$3.52008223183838 \times 10^{-06}$
a_0	2.06645888670347
a_q	2.17841480671394, 2.45048715454489, 2.94835415197161, 3.49319854222213, 4.10348922337212, 5.16755939809455, 4.00430000497253, 15.3795286202532
b_q	4.23931674709201, 5.62870995450119, 6.75380891854883, 7.84836703302100, 8.96271626101145, 10.2919724072509, 13.1946488108175, 20.9549152866118
$M = 16$	
E'_M	$7.62125439714811 \times 10^{-08}$
a_0	1.90985046368390
a_q	1.81663954068205, 0.536368601929249, 0.436980756110944, 1.10335637104465, 2.00170278316213, 2.33253144555721, 2.68906252875716, 2.92931151549284, 3.26653718262055, 3.92836624630039, 3.70092722168874, 3.93142979868540, 3.99044225686261, 6.31113629994617, 6.43649290780868, 7.16006917490418
b_q	3.65958533096794, 4.84545510629187, 4.87459206592095, 4.91508859428561, 5.69023740044383, 6.40117613253956, 7.11316668007365, 7.79308097200874, 8.42114254390272, 9.17419515658121, 10.2560791756143, 10.2561415456023, 10.2561549651551, 13.2371018161500, 13.2378488945643, 13.2405893531275

Table B.6: Foster element values when optimising using E'_M for a tube of radius 0.005 m at 26.85° C over the pre-warped frequency range 20 Hz - 3 kHz at a sample rate of 50 kHz.

$M = 4$	
E'_M	1.22593380574525
a_0	-2.41998781013108
a_q	-0.849649872840543, 0.979862667053578, 2.82555593535784, 18.5427131525947
b_q	1.33447857934923, 5.03978465891827, 8.71835966169953, 26.0615486637585
$M = 8$	
E'_M	0.00490523564648042
a_0	-2.82447898096001
a_q	-2.33820672045830, -1.57840081667709, -0.671448908145540, 0.241673098913610, 1.15486750407413, 2.07293392472161, 3.14480055969493, 15.4829361443098
b_q	-0.790680087648193, 1.25128501779993, 3.09468026097488, 4.92522841659633, 6.75300303522660, 8.58160927832192, 10.4674610830690, 23.5090324114909
$M = 16$	
E'_M	0.000386692886726619
a_0	-2.82890826539225
a_q	-2.81212376884297, -2.36172064486213, -1.75942461079875, -1.12313365312854, -0.483746903294402, 0.154039963204909, 0.786922616903839, 1.41704831339022, 2.09037210174763, 3.09707034249958, -11.3725763984025, 0.962211184700942, 10.1089657554913, 17.5597311227531, 23.7025207935390, 34.9049244703962
b_q	-1.29194645855069, 0.312416743320408, 1.62753069876081, 2.91021502232840, 4.18951462489131, 5.46776181216450, 6.74234861658821, 8.01037714784997, 9.28887316962720, 10.7212417030777, 13.3876978872944, 17.7285990762499, 22.4661852641953, 28.4487717742128, 32.0582863389304, 44.8074401218128

Table B.7: Foster element values when optimising using E'_M for a tube of radius 0.05 m at 26.85° C over the pre-warped frequency range 0.1 – 10 kHz at a sample rate of 50 kHz.

$M = 4$	
E'_M	0.819929246258164
a_0	-4.06539981031461
a_q	-2.05283660403148, -0.402423555580136, 1.31194754722074, 3.28208410822298
b_q	0.285603342794180, 3.78650421679124, 7.21862529778111, 10.7613276998334

Table B.8: Foster element values when optimising using E'_M for a tube of radius 0.1 m at 26.85° C over the pre-warped frequency range 0.1 – 10 kHz at a sample rate of 100 kHz.

Appendix C

Experiments on brass instrument valves

The valves in instruments such as the trumpet allow for extensions in the range of notes available to the player. Despite their importance in performance, there is little in the way of either theoretical or experimental work on brass instrument valves. The main discussions of valves often revolve around the tuning concerns when multiple valves are depressed [34, 63]. To the author’s knowledge, the only experimental investigation on brass instrument valves was performed by Widholm, who investigated the use of the Viennese action in French horns in relation to slurred notes [176, 177].

This short appendix presents a simple experiment to investigate the effect of a brass instrument valve when it is set in a partially open configuration and comparisons are made to simulations. This work was first described in [77], although simulations were performed using scheme (3.157), the discrete form of the attenuation model of Bilbao and Chick.

C.1 Experimental set up

A simplified valved brass instrument was constructed to investigate the effects of partial openings. The third valve of a standard B♭ trumpet was removed from the original instrument and two cylindrical tubes were attached to either end. The valve in isolation is shown in Fig. C.1 and a schematic of the experimental set up is shown in Fig. C.2.



Figure C.1: A trumpet valve in isolation.

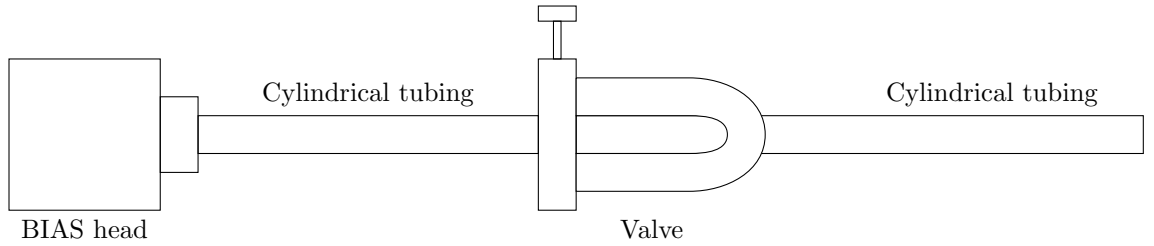


Figure C.2: Schematic of valve experiment

With the valve in an open configuration (so only air can flow through the default path), the total length of the instrument was 2492 mm. Fully depressing the valve extends the instrument length by 217 mm. The diameter of the tubing was 11.6 mm, which is close to the radius of the valve openings. Machined spacers were used to control the depression of the piston in 2 mm increments.

C.1.1 Results

Input impedance measurements were made using the BIAS capillary-based impedance measurement device [175, 178] for different configurations of the valve openings. Comparisons were made to simulations performed at 50 kHz for a duration of 1 s. In each tube, the explicit scheme using a fourth order Foster network approximation for attenuation, (3.161), was used to model propagation, and the lossy valve update (5.57) was used at the valve junctions. The system was terminated using scheme (4.14) to approximate the Levine and Schwinger radiation impedance. Simulated input impedances were gathered using the method described in Sec. 3.4.6.

For partially open configurations, the parameters $q^{(d)}$ and $q^{(b)}$ were given as the ratio of the area of the intersecting circles between the main tube and default and bypass tubes, respectively, to the area of the main tube. This also takes into account the separation between the default and bypass paths in the valve housing.

Figs. C.3 - C.8 show simulated and experimentally measured input impedances as the valve changes from a fully open configuration to a fully closed configuration. As the valve is closed, additional peaks are introduced to the input impedance as waves can travel through the system via a new path. The simulations show similar behaviour to the experimental measurements, but there is a large deviation in magnitude. There are several reasons for this. For the fully open and closed configurations, the simulations consistently over predict the input impedance peak magnitude compared to the experiment. As it was difficult to attach the valve to the main tubing, this could suggest that the seal was not secure, and leaks were present in the experimental set-up. There could also be some errors relating to measuring the geometry of the experiment. When the valve is fully closed, the simulation predicts peak positions at higher frequencies than those seen in the experiment whereas there is a better agreement between simulation and experiment for the fully open case. This suggests some error in measuring the bypass section of the valve.

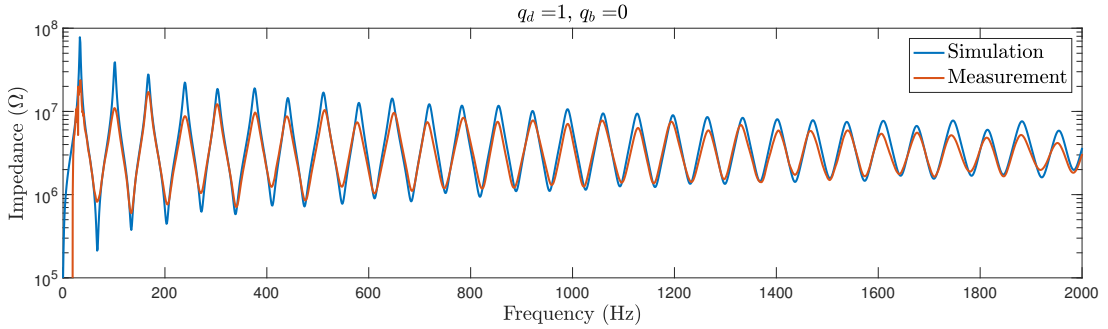


Figure C.3: Simulated and measured input impedance with the valve fully open.

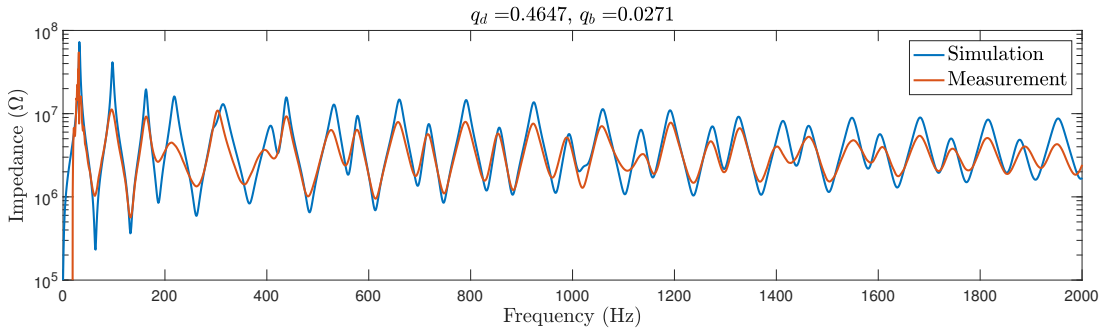


Figure C.4: Simulated and measured input impedance where 9 washers are used to keep the valve partially open.

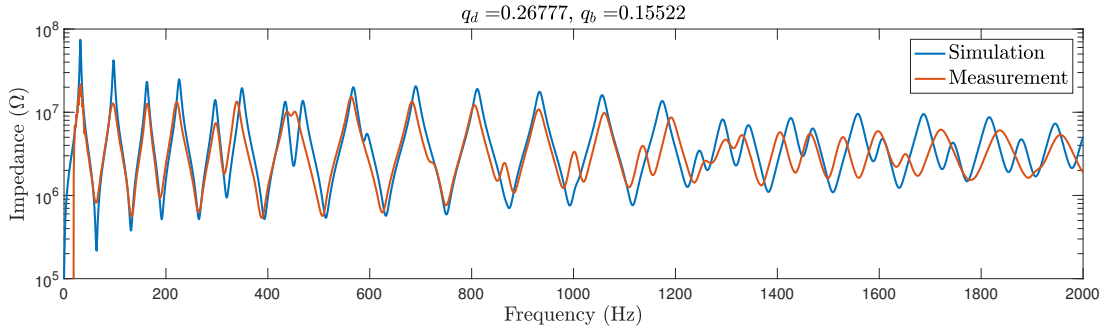


Figure C.5: Simulated and measured input impedance where 7 washers are used to keep the valve partially open.

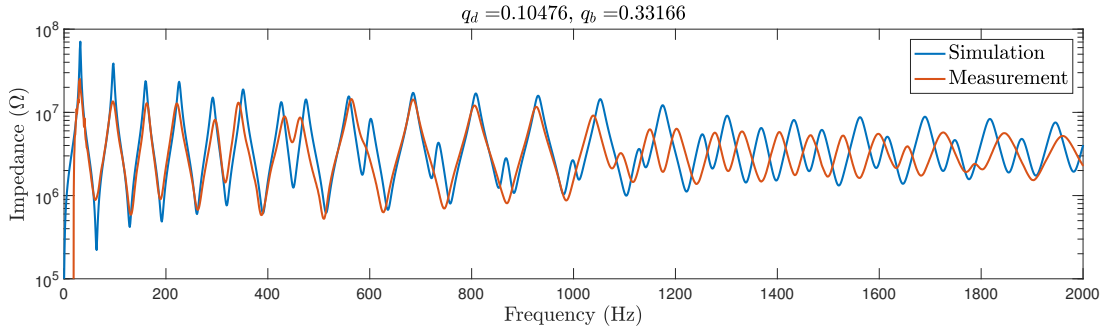


Figure C.6: Simulated and measured input impedance where 5 washers are used to keep the valve partially open.

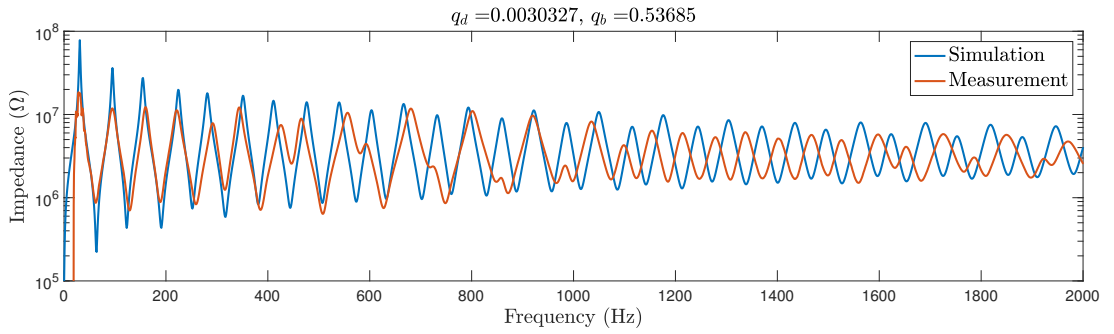


Figure C.7: Simulated and measured input impedance where 3 washers are used to keep the valve partially open.

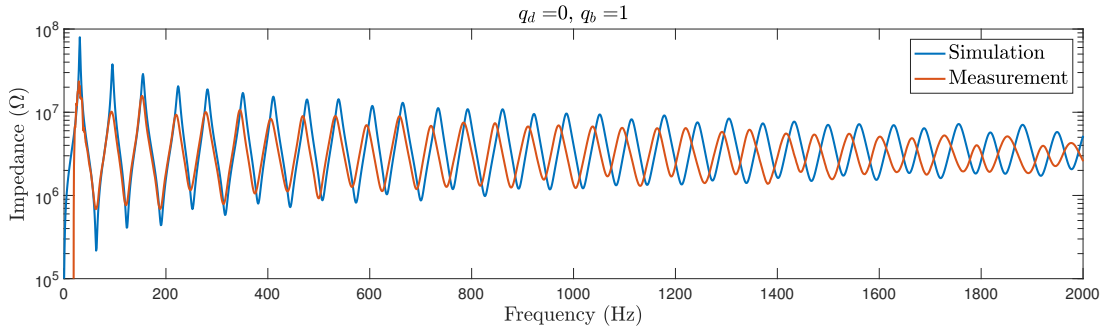


Figure C.8: Simulated and measured input impedance with the valve fully closed.

The shape of the valve junctions also introduces some error to the geometry of the system. Where the two tubes overlap, the area is no longer circular so the symmetry in the system breaks down. There are also uncertainties in calculating the values of $q^{(d)}$ and $q^{(b)}$. For example, Fig. C.9 shows the input impedance when 7 washers are used to open the valve but $q^{(b)}$ is multiplied by a factor of 0.45, so it is less than half the value used in Fig. C.5. This shows an improved agreement between simulated and experimental data and would suggest problems in determining the cross-sectional area at the valve junctions.

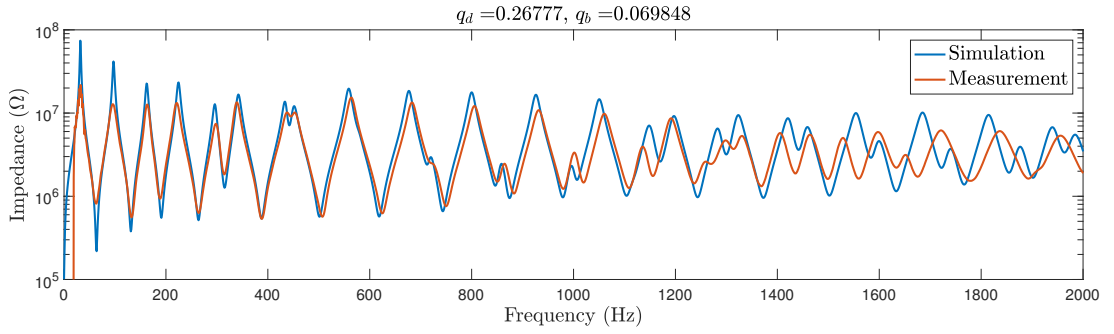


Figure C.9: Simulated and measured input impedance where 7 washers are used to keep the valve partially open. The value of $q^{(b)}$ has been modified in the simulation to better match the results of experiment.

Bibliography

- [1] S. Adachi and M. Sato. Time-domain simulation of sound production in the brass instrument. *Journal of the Acoustical Society of America*, 97(6):3850–3861, 1995.
- [2] S. Adachi and M. Sato. Trumpet sound simulation using a two-dimensional lip vibration model. *Journal of the Acoustical Society of America*, 99(2):1200–1209, 1996.
- [3] M. A. Al-Alaoui. Novel digital integrator and differentiator. *Electronics Letters*, 29(4):376–378, 1993.
- [4] A. Allen and N. Raghuvanshi. Aerophones in flatland: Interactive wave simulation of wind instruments. *ACM Trans. Graph.*, 34(4):134:1–134:11, July 2015.
- [5] N. Amir, H. Matzner, and S. Shtrikman. Acoustics of a flanged cylindrical pipe using singular basis functions. *Journal of the Acoustical Society of America*, 107(2):714–724, 2000.
- [6] N. Amir, V. Pagneux, and J. Kergomard. A study of wave propagation in varying cross-section waveguides by modal decomposition. part ii. results. *Journal of the Acoustical Society of America*, 101(5):2504–2517, 1997.
- [7] N. Amir, U. Shimony, and G. Rosenhouse. A discrete model for tubular acoustic systems with varying cross section - the direct and inverse problems. part 1: Theory. *Acustica*, 81(5):450–462, 1995.
- [8] F. Avanzini and M. van Walstijn. Modelling the mechanical response of the reed-mouthpiece-lip system of a clarinet. part i. a one-dimensional distributed model. *Acta Acustica united with Acustica*, 90:537–547, 2004.
- [9] J. Backus. Small-vibration theory of the clarinet. *Journal of the Acoustical Society of America*, 33(3):305–313, 1963.
- [10] J. Backus and T. C. Hundley. Harmonic generation in the trumpet. *Journal of the Acoustical Society of America*, 49(2):509–519, 1971.
- [11] J. W. Beauchamp. Analysis of simultaneous mouthpiece and output waveforms of wind instruments. In *Audio Engineering Society Convention 66*, Los Angeles, United States of America, May 1980.
- [12] J. W. Beauchamp. Wind instrument transfer responses. In *The 115th Meeting of the Acoustical Society of America*, Washington, United States of America, May 1988.

- [13] A. H. Benade. On the propagation of sound waves in a cylindrical conduit. *Journal of the Acoustical Society of America*, 44(2):616–623, 1968.
- [14] A. H. Benade. *Fundamentals of Musical Acoustics*. Dover, New York, second, revised edition, 1990.
- [15] A. H. Benade and E. V. Jansson. On plane and spherical waves in horns with nonuniform flare i. theory of radiation, resonance frequencies and mode conversion. *Acustica*, 31:79–98, 1974.
- [16] J.-P. Berenger. Three-dimensional perfectly matched layer for the absorption of electromagnetic waves. *Journal of Computational Physics*, 127(2):363–379, 1996.
- [17] H. Berjamine, B. Lombard, C. Vergez, and E. Cottanceau. Time-domain numerical modeling of brass instruments including nonlinear wave propagation, viscothermal losses, and lips vibration. *Acta Acustica united with Acustica*, 103:117–131, 2017.
- [18] D. P. Berners. *Acoustics and Signal Processing Techniques for Physical Modelling of Brass Instruments*. PhD thesis, Stanford University, 1999.
- [19] S. Bilbao. *Wave and Scattering Methods for Numerical Simulation*. John Wiley & Sons, Chichester, 2004.
- [20] S. Bilbao. Direct simulation of reed wind instruments. *Computer Music Journal*, 33(4):43–55, 2009.
- [21] S. Bilbao. *Numerical Sound Synthesis: Finite Difference Schemes and Simulation in Musical Acoustics*. John Wiley & Sons, Chichester, 2009.
- [22] S. Bilbao. Modelling of brass instrument valves. In *Proceedings of the 14th International Conference on Digital Audio Effects*, pages 337–343, Paris, France, September 2011.
- [23] S. Bilbao. Time domain simulation of brass instruments. In *Forum Acusticum*, Aalborg, Denmark, June 2011.
- [24] S. Bilbao and J. Chick. Finite difference time domain simulation for the brass instrument bore. *Journal of the Acoustical Society of America*, 134(5):3860–3871, 2013.
- [25] S. Bilbao and R. Harrison. Optimisation techniques for finite order viscothermal loss modelling in acoustic tubes. In *Proceedings of the International Symposium on Musical and Room Acoustics*, La Plata, Argentina, September 2016.
- [26] S. Bilbao and R. Harrison. Passive time-domain numerical models of viscothermal wave propagation in acoustic tubes of variable cross section. *The Journal of the Acoustical Society of America*, 140(1), 2016.
- [27] S. Bilbao, R. Harrison, J. Kergomard, B. Lombard, and C. Vergez. Passive models of viscothermal wave propagation in acoustic tubes. *The Journal of the Acoustical Society of America*, 138(2), 2015.
- [28] S. Bilbao, A. Torin, and V. Chatziioannou. Numerical modeling of collisions in musical instruments. *Acta Acustica united with Acustica*, 101:292–299, 2015.

- [29] B. Blackadar. *Operator Algebras: Theory of C-Algebras and von Neumann Algebras*, volume 122 of *Encyclopaedia of Mathematical Sciences*. Springer, Berlin, 2006.
- [30] J. F. Bonnans, J. C. Gilbert, C. Lemaéchal, and C. A. Sagastizábal. *Numerical Optimization: Theoretical and Practical Aspects*. Springer-Verlag, Berlin, second edition, 2006.
- [31] D. Botteldooren. Acoustical finite-difference time-domain simulation in a quasi-cartesian grid. *Journal of the Acoustical Society of America*, 95(5):2313–2319, 1994.
- [32] D. Botteldooren. Finite-difference time-domain simulation of low-frequency room acoustic problems. *Journal of the Acoustical Society of America*, 98(6):3302–3308, 1995.
- [33] M. Campbell, J. Chick, J. Gilbert, J. Kemp, A. Myers, and M. Newton. Spectral enrichment in brass instruments due to nonlinear sound propagation: a comparison of measurements and predictions. In *Proceedings of the International Symposium on Musical Acoustics 2014*, Le Mans, France, July 2014.
- [34] M. Campbell and C. Greated. *The Musician’s Guide to Acoustics*. Oxford, Oxford, 1987. Reprint 2001.
- [35] M. Campbell, C. Greated, and A. Myers. *Musical Instruments: History, Technology, & Performance of Instruments of Western Music*. Oxford, New York, 2004.
- [36] M. Campbell, M. Newton, J. Chick, A. Lopez-Carromero, and A. Myers. The influence of bore profile on spectral enrichment due to nonlinear sound propagation in brass instruments. In *Proc. of the International Symposium on Musical and Room Acoustics*, La Plata, Argentina, September 2016.
- [37] R. Caussé, J. Kergomard, and X. Lurton. Input impedance of brass musical instruments - comparison between experiment and numerical models. *Journal of the Acoustical Society of America*, 75(1):241–254, 1984.
- [38] A. Chaigne and A. Askenfelt. Numerical simulations of piano strings. i. a physical model for a struck string using finite difference methods. *Journal of the Acoustical Society of America*, 95(2):1112–1118, 1994.
- [39] L. Chaparro. *Signals and Systems Using {MATLAB}*. Academic Press, Oxford, second edition, 2015.
- [40] V. Chatziioannou and M. van Walstijn. Energy conserving schemes for the simulation of musical instrument contact dynamics. *Journal of Sound and Vibration*, 339:262–279, 2013.
- [41] Y. Chen and K. Moore. Discretization schemes for fractional-order differentiators and integrators. *IEEE Trans. Circuits Syst.*, 49(3):363–367, 2002.
- [42] Y. Chen, B. M. Vinagre, and I. Podlubny. Continued fraction expansion approaches to discretizing fractional order derivatives - an expository review. *Nonlinear Dynamics*, 38:115–170, 2004.

- [43] J. Chick, S. Bromage, and M. Campbell. Transient behaviour in the motion of the brass player's lips. In *Forum Acusticum*, Budapest, Hungary, August/September 2005.
- [44] J. P. Chick, S. M. Logie, M. Campbell, and J. Gilbert. Spectral enrichment and wall losses in trombones played at high dynamic levels. In *Proceedings of the Acoustics 2012 Nantes Conference*, Nantes, France, April 2012.
- [45] C. Chicone. *Ordinary Differential Equations with Applications*. Springer, New York, 2006.
- [46] R. Christensen. Modeling the effects of viscosity and thermal conduction on acoustic propagation in rigid tubes with various cross-sectional shapes. *Acta Acustica united with Acustica*, 97:193–201, 2011.
- [47] P. Cook. Tbone: An interactive waveguide brass instrument synthesis workbench for the next machine. In *Proceedings of the 1991 International Computer Music Conference*, pages 297–299, Montreal, Canada, October 1991.
- [48] R. Courant, K. Friedrichs, and H. Lewy. On the partial differential equations of mathematical physics. *IBM Journal of Research and Development*, 11(2):215–234, 1967. Originally published in 1928 as “Über die partiellen Differenzengleichungen der mathematischen Physik.” *Mathematische Annalen* 100(1):32–74.
- [49] Annie Cuyt. *Handbook of continued fractions for special functions*. [electronic resource]. Springer, Dordrecht, 2008.
- [50] V. Dubos, J. Kergomard, A. Kettabi, J. P. Dalmont, D. H. Keefe, and C. J. Nederveen. Theory of sound propagation in a duct with a branched tube using modal decomposition. *Acustica - Acta Acustica*, 85:153–169, 1999.
- [51] S. Earnshaw. On the mathematical theory of sound. *Philosophical Transactions of the Royal Society of London*, 150:133–148, 1860.
- [52] G. Eckel, F. Iovino, and R. Caussé. Sound synthesis by physical modelling with modalys. In *Proceedings of the International Symposium on Musical Acoustics*, pages 479–482, Dourdan, France, July 1995.
- [53] S. Elliot, J. Bowsher, and P. Watkinson. Input and transfer response of brass wind instruments. *Journal of the Acoustical Society of America*, 72:1747–1760, 1982.
- [54] M. Encina, J. Yuz, M. Zañartu, and G. Galindo. Vocal fold modeling through the port-hamiltonian systems approach. In *IEEE Conference on Control Applications*, Sydney, Australia, September 2015.
- [55] B. Engquist and A. Majda. Absorbing boundary conditions for the numerical simulation of waves. *Mathematics of Computation*, 31(139):629–651, 1977.
- [56] P. Eveno, J. P. Dalmont, R. Caussé, and J. Gilbert. Wave propagation and radiation in a horn: Comparisons between models and measurements. *Acta Acustica united with Acustica*, 98:158–165, 2012.

- [57] A. Falaize and T. Hélie. Passive simulation of electrodynamic loudspeakers for guitar amplifiers: a port - hamiltonian approach. In *Proceedings of the International Symposium on Musical Acoustics 2014*, Le Mans, France, July 2014.
- [58] A. Falaize and T. Hélie. Guaranteed-passive simulation of an electro-mechanical piano: A port-hamiltonian approach. In *Proc. of the 18th Int. Conference on Digital Audio Effects*, Trondheim, Norway, December 2015.
- [59] A. Falaize, N. Lopes, T. Hélie, D. Matignon, and B. Maschke. Energy-balanced models for acoustic and audio systems: a port - hamiltonian approach. In *Unfold Mechanics Colloquium*, Paris, France, September 2014.
- [60] A. Falaize-Skrzek and T. Hélie. Simulation of an analog circuit of a wah pedal: a port-hamiltonian approach. In *Audio Engineering Society Convention 135*, New York, USA, October 2013.
- [61] S. Farner, C. Vergez, J. Kergomard, and A. Lizée. Contribution to harmonic balance calculations of self-sustained periodic oscillations with focus on single-reed instruments. *Journal of the Acoustical Society of America*, 119(3):1794–1804, 2006.
- [62] A. Fettweis. Wave digital filters: Theory and practice. *Proceedings of the IEEE*, 74(2):270–327, 1986.
- [63] N. H. Fletcher and T. D. Rossing. *The Physics of Musical Instruments*. Springer, New York, second edition, 1998. Reprint 2005.
- [64] B. H. Flowers and E. Mendoza. *Properties of Matter*. John Wiley & Sons Ltd., Chichester, 1970. Reprint 1989.
- [65] V. Gerasik and M. Stastna. Complex group velocity and energy transport in absorbing media. *Physical Review E*, 81(5):056602, 2010.
- [66] J. Gilbert, D. M. Campbell, A. Myers, and R. W. Pyle. Differences between brass instruments arising from variations in brassiness due to nonlinear propagation. In *Proceedings of the International Symposium on Musical Acoustics*, Barcelona, Spain, September 2007.
- [67] J. Gilbert, L. Menguy, and M. Campbell. A simulation tool for brassiness studies(1). *Journal of the Acoustical Society of America*, 123(4):1854–1857, 2008.
- [68] N. Giordano. Nonlinear effects at woodwind toneholes. In *Proceedings of the International Symposium on Musical Acoustics 2014*, Le Mans, France, July 2014.
- [69] N. Giordano. Chaotic behaviour of the piccolo. In *Proc. of the 22nd International Congress on Acoustics*, Buenos Aires, Argentina, September 2016.
- [70] N. Giordano. Mode switching in an air-jet instrument. In *Proc. of the International Symposium on Musical and Room Acoustics*, La Plata, Argentina, September 2016.
- [71] B. Gustafsson, H-O. Kreiss, and J. Oliger. *Time Dependent Problems and Difference Methods*. John Wiley & Sons, Inc., New York, 1995.

- [72] H. Haddar, J. R. Li, and D. Matignon. Efficient solution of a wave equation with fractional-order dissipative terms. *Journal of Computational and Applied Mathematics*, 234(6):2003–2010, 2009.
- [73] D. Halliday, R. Resnick, and J. Walker. *Fundamentals of Physics*. John Wiley & Sons, Inc., New Jersey, United States, eighth edition, 2008.
- [74] B. Hamilton. *Finite Difference and Finite Volume Methods for Wave-Based Modelling of Room Acoustics*. PhD thesis, The University of Edinburgh, 2016.
- [75] R. Harrison, S. Bilbao, and J. Perry. An algorithm for a valved brass instrument synthesis environment using finite-difference time-domain methods with performance optimisation. In *Proceedings of the 18th International Conference on Digital Audio Effects*, Trondheim, Norway, November/December 2015.
- [76] R. L. Harrison, S. Bilbao, J. Perry, and T. Wishart. An environment for physical modeling of articulated brass instruments. *Computer Music Journal*, 29(4):80–95, 2015.
- [77] R. L. Harrison and J. Chick. A single valve brass instrument model using finite-difference time-domain methods. In *Proceedings of the International Symposium on Musical Acoustics.*, Le Mans, France, July 2014.
- [78] R. L. Harrison, B. Hamilton, and A. López-Carromero. Finite difference time domain simulation of a hybrid 1d/3d brass instrument model and comparison to measured radiation data. In *24th International Congress on Sound and Vibration*, July 2017.
- [79] T. Hélie. Unidimensional models of acoustic propagation in axisymmetric waveguides. *Journal of the Acoustical Society of America*, 114(5):2633–2647, 2003.
- [80] T. Hélie, T. Hézard, R. Mignot, and D. Matignon. One-dimensional acoustic models of horns and comparison with measurements. *Acta Acustica united with Acustica*, 99:960–974, 2013.
- [81] T. Hélie and D. Matignon. Diffusive representations for the analysis and simulation of flared acoustic pipes with visco-thermal losses. *Mathematical Models and Methods in Applied Sciences*, 16(4):503–536, 2006.
- [82] T. Hélie, R. Mignot, and D. Matignon. Waveguide modeling of lossy flared acoustic pipes: Derivation of a kelly-lochbaum structure for real-time simulations. In *IEEE Workshop on Applications of Signal Processing to Audio and Acoustics*, New Paltz, NY, October 2007.
- [83] T. Hélie and X. Rodet. Radiation of a pulsating portion of a sphere: Application to horn radiation. *Acta Acustica united with Acustica*, 89:565–577, 2003.
- [84] R. L. Higdon. Absorbing boundary condition for difference approximations to the multi-dimensional wave equation. *Mathematics of Computation*, 47(176):437–459, 1986.
- [85] R. L. Higdon. Numerical absorbing boundary condition for the wave equation. *Mathematics of Computation*, 49(179):65–90, 1987.

- [86] T. Hikichi, N. Osaka, and F. Itakura. Time-domain simulation of sound production of the sho. *Journal of the Acoustical Society of America*, 113(2):1092–1101, 2003.
- [87] L. Hiller and P. Ruiz. Synthesizing musical sounds by solving the wave equation for vibrating objects: Part i. *Journal of the Audio Engineering Society*, 17(1):462–470, 1971.
- [88] A. Hirschberg, J. Gilbert, R. Msallam, and A. P. J. Wijnands. Shock waves in trombones. *Journal of the Acoustical Society of America*, 99(3):1754–1758, 1996.
- [89] Roger A. Horn and Charles R. Johnson. *Topics in Matrix Analysis*. Cambridge University Press, Cambridge, 1991.
- [90] C. S. Jog and A. Nandy. Conservation properties of the trapezoidal rule in linear time domain analysis of acoustics and structures. *Journal of Vibration and Acoustics*, 137:1189–1198, 2015.
- [91] Gareth A. Jones and David Singerman. *Complex Functions: An Algebraic and Geometric Viewpoint*. Cambridge University Press, 1987.
- [92] W. Kausel and C. B. Geyer. Time domain simulation of standing waves in brass wind instruments taking non-linear wave steepening into account. In *Proceedings of the Stockholm Music Acoustics Conference*, Stockholm, Sweden, July/August 2013.
- [93] D. H. Keefe. Theory of the single woodwind tone hole. *Journal of the Acoustical Society of America*, 72:676–687, 1982.
- [94] D. H. Keefe. Acoustical wave propagation in cylindrical ducts: Transmission line parameter approximations for isothermal and nonisothermal boundary conditions. *Journal of the Acoustical Society of America*, 75(1):58–62, 1984.
- [95] D. H. Keefe and A. Barjau. Acoustic propagation in flaring, axisymmetric horns: II. numerical results, wkb theory, and viscothermal effects. *Acustica - Acta Acustica*, 85:285–293, 1999.
- [96] J. Kelly and C. Lochbaum. Speech synthesis. In *Proceedings of the Fourth International Congress on Acoustics*, Copenhagen, Denmark, September 1962.
- [97] J. Kemp, S. Bilbao, J. McMaster, and R. Smith. Wave separation in the trumpet under playing conditions and comparison with time domain finite difference simulations. *Journal of the Acoustical Society of America*, 134(2):1395–1406, 2013.
- [98] J. Kemp, A. López-Carromero, A. Wooley, and M. Campbell. Experimental investigation of doppler shift and infrasound generation during wave propagation within the bore of the trombone during slide movement. In *Proc. of the Third Vienna Talk on Music Acoustics*, Vienna, Austria, September 2015.
- [99] J. A. Kemp. *Theoretical and experimental study of wave propagation in brass musical instruments*. PhD thesis, The University of Edinburgh, 2002.
- [100] J. Kergomard. Regularity and irregularity in wind instruments with tone holes or bells. In *Proceedings of the International Symposium on Musical Acoustics 2014*, Le Mans, France, July 2014.

- [101] J. Kergomard and M. Pachebat. Low frequency coupling and mode interference in an homogenous lattice of finite length. In *Forum Acusticum 2014*, Krakow, Poland, September 2014.
- [102] P. G. LeFloch and M. Westdickenberg. Finite energy solutions to the isentropic euler equations with geometric effects. *Journal de Mathématiques Pures et Appliquées*, 88(2):389–429, 2007.
- [103] R. J. LeVeque. *Finite Volume Methods for Hyperbolic Problems*. Cambridge University Press, New York, 2002.
- [104] H. Levine and J. Schwinger. On the radiation of sound from an unflanged circular pipe. *Physical Review*, 73(4):383–406, 1948.
- [105] S. M. Logie. *An Acoustical Study of the Playing Characteristics of Brass Wind Instruments*. PhD thesis, The University of Edinburgh, 2012.
- [106] B. Lombard and J-F Mercier. Numerical modelling of nonlinear acoustic waves in a tube connected with helmholtz resonators. *Journal of Computational Physics*, 259:421–443, 2014.
- [107] B. Lombard, C. Vergez, and E. Cottenceau. Modélisation de la propagation non linéaire avec pertes viscothermiques: application à la famille des cuivres. In *Proceedings of the Congrès Français d’Acoustique (CFA)*, Poitiers, France, April 2014.
- [108] N. Lopes and T. Hélie. A power-balanced model of a valve exciter including shocks and based on a conservative jet for brass instruments: Simulations and comparison with standard models. In *Proceedings of the International Symposium on Musical Acoustics 2014*, Le Mans, France, July 2014.
- [109] N. Lopes and T. Hélie. Energy balanced model of a jet interacting with a brass player’s lip. *Acta Acustica united with Acustica*, 102:141–154, 2016.
- [110] D. Luce and M. Clark. Physical correlates of brass-instrument tones. *Journal of the Acoustical Society of America*, 42(6):1232–1243, 1967.
- [111] D. Matignon and T. Hélie. A class of damping models preserving eigenspaces for linear conservative port-hamiltonian systems. *European Journal of Control*, 19:486–494, 2013.
- [112] S. Maugeais and J. Gilbert. Nonlinear acoustic propagation applied to brassiness studies, a new simulation tool in the time domain. *Acta Acustica united with Acustica*, 103:67–79, 2017.
- [113] M. E. McIntyre, R. T. Schumacher, and J. Woodhouse. On the oscillations of musical instruments. *Journal of the Acoustical Society of America*, 74(5):1325–1345, 1983.
- [114] L. Menguy. *Propagation Acoustique Non Linéaire Dans Les Guides Monodimensionnels*. PhD thesis, Université du Maine, 2001.
- [115] L. Menguy and J. Gilbert. Weakly nonlinear gas oscillations in air-filled tubes; solutions and experiments. *Acustica - Acta Acustica*, 86:798–810, 2000.

- [116] R. Mignot, T. Hélie, and D. Matignon. Stable realization of a delay system modeling a convergent acoustic cone. In *16th Mediterranean Conference on Control and Automation*, Ajaccio, France, June 2008.
- [117] R. Mignot, T. Hélie, and D. Matignon. Acoustic modelling of a convex pipe adapted for digital waveguide simulation. In *Proceedings of the 13th International Conference on Digital Audio Effects*, Graz, Austria, September 2010.
- [118] R. Mignot, T. Hélie, and D. Matignon. Digital waveguide modeling for wind instruments: Building a state-space representation based on webster-lokshin model. *IEEE Transactions on Audio, Speech, and Language Processing*, 18(4):843–854, 2010.
- [119] D. Morrill. Trumpet algorithms for computer composition. *Computer Music Journal*, 1(1):46–52, 1977.
- [120] J. D. Morrison and J-M. Adrien. Mosaic: A framework for modal synthesis. *Computer Music Journal*, 17(1):45–56, 1993.
- [121] P. M. Morse. *Vibration and Sound*. Acoustical Society of America, New York, second edition, 1981. Reprint 1995.
- [122] P. M. Morse and K. U. Ingard. *Theoretical acoustics*. International series in pure and applied physics. McGraw-Hill, New York, 1968.
- [123] R. Msallam, S. Dequidt, R. Caussé, and S. Tassart. Physical model of the trombone including nonlinear effects. application to the sound synthesis of loud tones. *Acustica - Acta Acustica*, 86:725–736, 2000.
- [124] L. Muschietti and C. T. Dum. Real group velocity in a media with dissipation. *Physics of Fluids B*, 5(5):1383–1397, 1993.
- [125] A. Myers, R. W. Pyle, J. Gilbert, M. Campbell, J. P. Chick, and S. Logie. Effects of nonlinear sound propagation on the characteristic timbres of brass instruments. *Journal of the Acoustical Society of America*, 131(1):678–688, 2012.
- [126] A. H. Nayfeh. *Perturbation Methods*. John Wiley & Sons Inc, New York, 1973.
- [127] D. Noreland. A numerical method for acoustic waves in horns. *Acta Acustica united with Acustica*, 88:576–586, 2002.
- [128] D. Noreland, J. Kergomard, F. Laloë, C. Vergez, P. Guillemain, and A. Guilloteau. The logical clarinet: numerical optimisation of the geometry of woodwind instruments. *Acta Acustica united with Acustica*, 99(4):615–628, 2013.
- [129] J. O. D. Noreland, M. R. Udawalpola, and O. M. Berggren. A hybrid scheme for bore design optimization of a brass instrument. *Journal of the Acoustical Society of America*, 128(3):1391–1400, 2010.
- [130] B. H. Pandya, G. S. Settles, and J. D. Miller. Schlieren imaging of shock waves from a trumpet. *Journal of the Acoustical Society of America*, 114(6):3363–3367, 2003.
- [131] pBone. pbone plastic trombone: The worlds best selling trombone, July 2017. Last accessed July 2017.

- [132] A. D. Pierce. *Acoustics: An Introduction to Its Physical Principles and Applications*. Acoustical Society of America, New York, 1981. Reprint 1994.
- [133] pTrumpet. ptrumpet: World’s first all plastic trumpet, July 2017. Last accessed July 2017.
- [134] L. R. Rabiner and R. W. Schafer. *Digital processing of speech signals*. Prentice-Hall Inc., New Jersey, 1978.
- [135] P. L. Rendón, C. G. Malanche, and F. Oruña-Bustamente. Effect of input signal shape on the nonlinear steepening of transient acoustic waves in a cylindrical tube. In *Proc. of the 22nd International Congress on Acoustics*, Buenos Aires, Argentina, September 2016.
- [136] P. L. Rendón, F. Ordu na Bustamente, D. Narezo, and A. Pérez-López. Nonlinear progressive waves in a slide trombone resonator. *Journal of the Acoustical Society of America*, 127(2):1096–1103, 2010.
- [137] J. Resch. *Nonlinear Wave Propagation in Brass Instruments*. PhD thesis, The University of Waterloo, 2012.
- [138] J. Resch, L. Krivodonova, and J. Vanderkooy. A two-dimensional study of finite amplitude sound waves in a trumpet using the discontinuous galerkin method. *Journal of Computational Acoustics*, 22(3):145007, 2014.
- [139] O. Richards. *Investigation of the Lip Reed Using Computational Modelling and Experimental Studies with an Artificial Mouth*. PhD thesis, The University of Edinburgh, 2003.
- [140] K. F. Riley, M. P. Hobson, and S. J. Bence. *Mathematical Methods for Physics and Engineering*. Cambridge, Cambridge, third edition, 2006.
- [141] C. Roads. *The Computer Music Tutorial*. MIT Press, Cambridge, Massachusetts, 1996.
- [142] X. Rodet and C. Vergez. Nonlinear dynamics: From basic models to true musical-instrument models. *Computer Music Journal*, 23(3):35–49, 1999.
- [143] O. V. Rudenko and S. I. Soluyan. *Theoretical Foundations of Nonlinear Acoustics*. Nauka Press, Moscow, 1975. Trans. by R. T. Beyer, Consultants Bureau, New York, 1977.
- [144] M. Russ. Yamaha v11 virtual acoustic synthesizer. *Sound on Sound*, 1994. Available online https://web.archive.org/web/20150608005838/http://www.soundonsound.com/sos/1994_articles/jul94/yamahav11.html, Last accessed August 2017.
- [145] L. Savioja, T. J. Rinne, and T. Takala. Simulation of room acoustics with a 3-d finite difference mesh. In *Proceedings of the 1994 International Computer Music Conference*, Arhus, Denmark, September 1994.
- [146] G. P. Scavone. *An Acoustic Analysis of Single-Reed Woodwind Instruments with an Emphasis on Design and Performance Issues and Digital Waveguide Modeling Techniques*. PhD thesis, Stanford University, 1997.

- [147] F. Silva, Ph. Guillemain, J. Kergomard, B. Mallaroni, and A. N. Norris. Approximation formulae for the acoustic radiation impedance of a cylindrical pipe. *Journal of Sound and Vibration*, 322:255–263, 2009.
- [148] F. Silva, C. Vergez, P. Guillemain, J. Kergomard, and V. Debut. Moreesc: A framework for the simulation and analysis of sound production in reed and brass instruments. *Acta Acustica united with Acustica*, 100:126–138, 2014.
- [149] J. O. Smith. Efficient simulation of the reed-bore and bow-string mechanisms. In *Proceedings of the 1986 International Computer Music Conference*, pages 275–280, The Hague, Netherlands, October 1986.
- [150] J. O. Smith III. Musical applications of digital waveguides. Technical Report STAN-M-39, Center for Computer Research in Music and Acoustics, 1987.
- [151] J. O. Smith III. *Physical Audio Signal Processing*. Stanford, CA, 2004. Draft version. Available online at <http://ccrma.stanford.edu/~jos/pasp04/>, Last accessed August 2017.
- [152] T. Smyth and M. Rouhipour. Saxophone modelling and system identification. In *Proceedings of Meeting on Acoustics*, Montreal, Canada, June 2013.
- [153] Jan A. Snyman. *Practical Mathematical Optimization: An Introduction to Basic Optimization Theory and Classical and New Gradient-Based Algorithms*. Springer, New York, 2005.
- [154] M. R. Stinson. The propagation of plane sound waves in narrow and wide circular tubes, and generalisation to uniform tubes of arbitrary cross-sectional shape. *Journal of the Acoustical Society of America*, 89(2):550–558, 1991.
- [155] M. R. Stinson and Y. Champoux. Propagation of sound and the assignment of shape factors in model porous materials having simple pore geometries. *Journal of the Acoustical Society of America*, 91(2):685–695, 1992.
- [156] J. C. Strikwerda. *Finite Difference Schemes and Partial Differential Equations*. Society for Industrial and Applied Mathematics, Philadelphia, second edition, 2004.
- [157] J. W. Strutt. *The Theory of Sound Volume II*. Dover, New York, second edition, 1896. Reprint 1945.
- [158] M. Svärd and J. Nordström. Review of summation-by-parts schemes for initial-boundary-value problems. *Journal of Computational Physics*, 268:17–38, 2014.
- [159] E. Tadmor. Entropy stability for difference approximations of nonlinear conservation laws and related time-dependent problems. *Acta Numerica*, (12):451–512, 2003.
- [160] J. W. Thomas. *Numerical Partial Differential Equations: Finite Difference Methods*. Springer, New York, 1995.
- [161] M. W. Thompson and W. J. Strong. Inclusion of wave steepening in a frequency-domain model of trombone sound production. *Journal of the Acoustical Society of America*, 110(1):556–562, 2001.

- [162] S. C. Thompson, T. B. Gabrielson, and D. M. Warren. Analog model for thermoviscous propagation in a cylindrical tube. *Journal of the Acoustical Society of America*, 135(2):585–590, 2014.
- [163] A. Torin. *Percussion Instrument Modelling in 3D: Sound Synthesis Through Time Domain Numerical Simulation*. PhD thesis, The University of Edinburgh, 2015.
- [164] A. van der Schaft. Port-hamiltonian systems: an introductory survey. In *Proceedings of the International Congress of Mathematicians*, Madrid, Spain, August 2006.
- [165] M. E. van Valkenburg. *Introduction to Modern Network Synthesis*. John Wiley & Sons Inc, New York, 1960.
- [166] M. van Walstijn. Wave-based simulation of wind instrument resonators. *IEEE Signal Processing Magazine*, 21:21–31, 2007.
- [167] M. van Walstijn and M. Campbell. Discrete-time modelling of woodwind instrument bores using wave variables. *Journal of the Acoustical Society of America*, 113(1):575–585, 2003.
- [168] C. Vergez and X. Rodet. Dynamical systems and physical models of trumpet-like instruments. analytical study and asymptotical properties. *Acustica - Acta Acustica*, 86:147–162, 2000.
- [169] C. Vergez and X. Rodet. Trumpet and trumpet player: Model and simulation in a musical context. In *Proceedings of the 2001 International Computer Music Conference*, La Habana, Cuba, September 2001.
- [170] C. Vergez and P. Tisserand. The brass project, from physical models to virtual musical instruments: Playability issues. In R. Kronland-Martinet, T. Voinier, and S. Ystad, editors, *Lecture Notes in Computer Science: Computer Music Modeling and Retrieval*, volume 3902, pages 24–33. Springer, Berlin, September 2006.
- [171] B. Vinagre, I. Podlubny, A. Hernandez, and V. Feliu. Some approximations of fractional order operators used in control theory and applications. *Fractional Calculus and Applied Analysis*, 3(3):231–248, 2000.
- [172] S. Wang and G. Kreiss. Convergence of summation-by-parts finite difference methods for the wave equation. *Journal of Scientific Computing*, 71(1):219–245, 2017.
- [173] A. G. Webster. Acoustical impedance, and the theory of horns and of the phonograph. *Proceedings of the National Academy of Sciences of the United States of America*, 5(7):275–282, 1919.
- [174] L. Weinberg. *Network Analysis and Synthesis*. McGraw-Hill Book Company, Inc, New York, 1962.
- [175] G. Widholm. Brass wind instrument quality measured and evaluated by a new computer system. In *Proceedings of the 15th International Congress on Acoustics*, Trondheim, Norway, June 1995.

- [176] G. Widholm. The influence of valve mechanisms on the microstructure of slurs played with brass wind instruments. In *Proceedings of the International Symposium on Musical Acoustics*, Edinburgh, United Kingdom, August 1997.
- [177] G. Widholm. The vienna horn - a historic relict successfully used by top orchestras of the 21 century. In *Forum Acusticum*, Budapest, Hungary, August/September 2005.
- [178] G. Widholm, H. Pichler, and T. Ossmann. Bias: A computer-aided test system for brass wind instruments. In *Audio Engineering Society Convention 87*, New York, United States of America, October 1989.
- [179] K. S. Yee. Numerical solution of initial boundary value problems involving maxwell's equations in isotropic media. *IEEE Transactions on Antennas and Propagation*, 14(3):302–307, 1966.
- [180] U. Zölzer. *Digital Audio Signal Processing*. John Wiley & Sons Ltd, Chichester, second edition, 2008.
- [181] W. E. Zorumski. Generalized radiation impedances and reflection coefficients of circular and annular ducts. *Journal of the Acoustical Society of America*, 54(6):1667–1673, 1973.
- [182] C. Zwikker and C.W. Kosten. *Sound absorbing materials*. Elsevier Pub. Co., 1949.